Chair of Resource Mineralogy

Doctoral Thesis

A fundamentals mineralogical investigation of downhole cements within the context of Underground Hydrogen Storage

Dipl.-Ing. Thomas Sammer, BSc

October 2024

AFFIDAVIT

I declare on oath that I wrote this thesis independently, did not use any sources and aids other than those specified, have fully and truthfully reported the use of generative methods and models of artificial intelligence, and did not otherwise use any other unauthorized aids.

I declare that I have read, understood and complied with the "Preamble on Integrity in Academic Study, Teaching, and Research Operations" of the Montanuniversität Leoben.

Furthermore, I declare that the electronic and printed versions of the submitted thesis are identical in form and content.

Date

(The original signature is kept at the university)

DANKSAGUNG

An dieser Stelle möchte ich jenen Personen meinen aufrichtigen Dank aussprechen, die mich während meiner Forschungsreise unterstützt und zum Erfolg dieser Arbeit beigetragen haben.

Als aller erstes gilt mein Dank meinen beiden Betreuern Univ. Prof. Dr.phil. Johann Raith und Univ. Prof. Krishna Ravi, PhD für die Ermöglichung dieser Universitätsassistentenstelle, ihr Einverständnis diese Arbeit gemeinsam zu betreuen, die große Unterstützung während der Ausführung sowie ihre Bereitschaft immer, wenn nötig mit Rat und Tat zur Seite zu stehen. Besonderer Dank gilt meinem Hauptbetreuer und Doktorvater, Johann Raith für sein immer offenes Ohr, rasches und konstruktives Feedback, sowie die sehr persönliche Arbeitsatmosphäre.

Des Weiteren gilt mein Dank den Kollegen am Lehrstuhl für Rohstoffmineralogie Maik Zimmermann, Monika Feichter, Ronald Bakker und Federica Zaccarini für die Unterstützung bei der Proben-Präparation sowie im Labor. Besonderer Dank gilt auch Florian Altenberger und Ferdinand Hampl für anregende, aber auch unterhaltsame Diskussionen unter Gleichgesinnten. Ganz besonders zum Dank verpflichtet bin ich den Kollegen Arash Nasiri, Ibrahim Abu-Askar, Alexander Fine und Michael Prohaska des Lehrstuhls für Drilling and Completion Engineering für ihre Hilfe im Cementing Lab sowie die unzähligen wertvollen fachlichen Diskussionen.

Besonders bedanken möchte ich mich auch bei Univ. Prof. David Misch und den Mitarbeitern seiner Arbeitsgruppe Joel Bensing, Lukas Skerbisch und Xiangyun Shi für die Ermöglichung des Zugangs sowie die Unterstützung am Rasterelektronenmikroskop sowie die Hilfe bei den Autoklav-Versuchen und dem Image-Processing. Zum Dank verpflichtet bin ich auch den Kollegen Univ. Prof. Christian Teichert, Aleksandar Matkovic, Muhammad Khan und Nikolaos Kostoglou für ihre Bereitschaft zur Hilfe sowie wertvollen Beiträge zu einigen Publikationen.

Bedanken möchte ich mich auch bei Eva Caspari, Eva Wegerer, Franz Seidl, Franz Pusterwallner, Gerhard Hawranek und Fritz Kittinger sowie all jenen, deren Namen hier nicht genannt wurden, die jedoch auf ihre Weise zum erfolgreichen Abschluss dieser Dissertation beigetragen haben. Ihre Beiträge, sei es in Form von konstruktivem Feedback oder Unterstützung im Labor, waren unermesslich wertvoll und werden stets in bester Erinnerung bleiben.

Abschließend gilt mein besonderer Dank meinen Eltern für die Ermöglichung und finanzielle Unterstützung während meines Studiums, meinem Bruder für viele anregende Diskussionen, meinem Onkel sowie meinen Großeltern für die immerwährende Aufmunterung und last but not least meiner besseren Hälfte Katharina für ihre unermüdliche Unterstützung – DANKE!!!

Abstract

Underground hydrogen storage (UHS) offers significant potential for storing renewable energy, but the feasibility of this process also depends on the integrity of the cement sheaths used in boreholes when exposed to hydrogen. The integrity of these cements is crucial for ensuring both economical and safe storage of hydrogen. However, knowledge about the influence hydrogen might have on downhole materials and especially the cement sheath is scarce. In the geoenergy sector, downhole cements must be designed with low permeability and high mechanical durability, qualities that are deeply influenced by the material's microstructure. Enhancing these properties requires a detailed understanding of how different additives and preparation techniques tailor and respectively influence the microstructure once investigated in the lab. Advancements in high-resolution Scanning Electron Microscopes (SEM) have underscored the need for meticulous sample preparation to preserve fine microstructural features.

To assess the impact of hydrogen exposure on the commonly used class G cement, hydrothermal autoclave experiments were conducted. These experiments, coupled with X-ray diffraction, scanning electron microscopy, and nitrogen adsorption/desorption techniques, provided insight into the potential changes in the mineralogical phase composition and microstructure of the cement. The results indicate only minor alterations, such as the decomposition of monosulphate and the formation of ettringite, with the pore size distribution and overall porosity showing minimal change. These findings suggest that class G cement retains its structural integrity and phase composition under hydrogen exposure, reinforcing its suitability for UHS.

Addressing the demands of the geoenergy industry also requires exploring how modifications to class G cement can enhance its performance. The approach used in this study involved the incorporation of carbon black and silica fume to modify the microstructure. These additives were found to create a denser microstructure with reduced porosity while maintaining a similar pore size distribution. The introduction of carbon black resulted in a lower Young’s modulus, indicating increased plasticity, while silica fume increased both the mechanical strength and permeability of the cement with the second being undesirable.

In addition to exploring different mix formulations, the study of microstructural characteristics at the nanoscale has been greatly advanced by comparing different SEM sample preparation techniques. Specifically, state of the art resin-embedded polishing and novel Broad Ion Beam (BIB) milling were evaluated for their ability to preserve and reveal fine structural details in hydrated cement paste. SEM analysis, supported by image processing for porosity and pore geometry, and Atomic Force Microscopy (AFM) for surface roughness assessment, revealed that BIB milling was particularly effective in exposing nanoscale features such as gel porosity and the acicular morphology of calcium silicate hydrates. This technique produced pores with higher aspect ratios, while resin-embedded polishing achieved smoother vertical surfaces and more circular pores, indicating a better vertical surface roughness. These findings highlight the strengths and limitations of each preparation technique, offering critical insights into the preparation of cement samples for high-resolution SEM analysis.

In conclusion, this study provides a comprehensive understanding of the factors that influence the performance and durability of downhole cements, whether in the context of UHS or the broader geoenergy industry. The research demonstrates how careful cement slurry formulation and advanced analytical techniques can be combined to understand, evaluate and optimize cement performance in demanding environments.

Kurzfassung

Die unterirdische Wasserstoffspeicherung bietet erhebliches Potenzial zur Speicherung erneuerbarer Energien. Die Machbarkeit dieses Prozesses hängt jedoch auch von der Integrität der Zementummantelungen in Bohrlöchern gegen Wasserstoffexposition ab. Die Gewährleistung der strukturellen Integrität dieser Zemente ist entscheidend für eine wirtschaftliche und sichere Speicherung von Wasserstoff. Dennoch sind die Kenntnisse über den Einfluss von Wasserstoff auf Bohrlochmaterialien, insbesondere auf die Zementummantelung, begrenzt. Im Geoenergiesektor werden Bohrlochzemente mit geringer Permeabilität und hoher mechanischer Stabilität benötigt, Eigenschaften, die unter anderem auch von der Mikrostruktur des Materials abhängen. Eine Optimierung und methodische Untersuchung dieser Eigenschaften setzt ein detailliertes Verständnis der Wirkung von Zusatzstoffen zur Zementmixtur aber auch des Einflusses von Präparationstechniken auf Zementproben voraus. Fortschritte in der hochauflösenden Rasterelektronenmikroskopie (REM) haben die Bedeutung sowie Notwendigkeit einer optimierten und präzisen Probenpräparation zur Erhaltung kleinster mikrostruktureller Merkmale aufgezeigt.

Um den Einfluss von Wasserstoff auf Zement der Klasse G zu untersuchen, wurden hydrothermale Autoklav-Versuche durchgeführt, die durch Röntgendiffraktometrie, REM und Stickstoff-Adsorptions-/Desorptionsmessungen ergänzt wurden. Die Ergebnisse zeigen geringe Veränderungen in der mineralogischen Phasenzusammensetzung wie den Abbau von Monosulfat und die Bildung von Ettringit. Die Porengrößenverteilung und Gesamtporosität blieben nahezu unverändert. Diese Ergebnisse deuten darauf hin, dass Zement der Klasse G seine strukturelle Integrität und Phasenzusammensetzung unter Wasserstoffexposition beibehält, was seine Eignung für die unterirdische Speicherung von Wasserstoff bestätigt.

Um den Anforderungen der Geoenergieindustrie gerecht zu werden, wurde auch untersucht, wie Modifikationen von Zement der Klasse G dessen Leistungsfähigkeit verbessern könnten. Dafür wurden Carbon Black und Silica Fume als Zusatzstoffe beigemischt. Diese Zusätze führten zu einer dichteren Mikrostruktur mit reduzierter Porosität, wobei die Porengrößenverteilung unverändert blieb. Die Zugabe von Carbon Black reduzierte das Elastizitätsmodul und erhöhte die Plastizität, während Silica Fume sowohl die mechanische Festigkeit als auch die Permeabilität steigerte, wobei letzterer Effekt unerwünscht ist.

Zusätzlich zur Untersuchung unterschiedlicher Zementmixturen wurden verschiedene Präparationstechniken für hoch-auflösende REM-Untersuchungen auf ihre Eignung zur Darstellung mikrostruktureller Merkmale auf Nanometerebene untersucht.

Konventionelle Oberflächenpolitur mittels Harzimprägnierung wurde mit neuartigem Broad Ion Beam (BIB)-Milling hinsichtlich der Fähigkeit, feine strukturelle Details in hydratisiertem Zement zu erhalten, verglichen. Die REM-Untersuchung, unterstützt durch Bildverarbeitung zur Bestimmung der Porosität und Porengeometrie sowie Rasterkraftmikroskopie zur Bewertung der Oberflächenrauigkeit, zeigte, dass das BIB-Milling besonders effektiv war, um Merkmale im Nanometerbereich wie Gelporosität und die nadelige Morphologie von Calcium-Silikat-Hydraten darzustellen. Die Konventionelle Oberflächenpolitur mittels Harzimprägnierung führte zu glatteren Oberflächen mit niedrigerer Oberflächenrauheit. Diese

Erkenntnisse liefern wichtige Einsichten für die optimierte Präparation von Zementproben für hochauflösende REM-Analysen.
Zusammengefasst stellt diese Arbeit eine umfassende mineralogisch, mechanisch-physikalische Untersuchung der Faktoren dar, die die Leistung und Haltbarkeit von Bohrlochzementen beeinflussen, sei es im Zusammenhang mit der unterirdischen Speicherung von Wasserstoff oder der breiteren Geoenergieindustrie.

Table of contents

1 Introduction

Global warming caused by manmade climate change pressures current energy politics around the globe to enable a transition to a sustainable energy supply by substituting conventional fossil fuels with renewable energy sources [1–4]. This however, proposes a tremendous challenge since not only societal and economical but also technical obstacles need to be overcome since conventional fossil fuels are not just the backbone of our current energy structure, they also fuel our economy [5]. The supply of fossil fuels suffers from long-distance transport and is also a powerful leverage during military conflicts [6]. The most common renewable energy sources like solar or wind power would enable an autochthonous and independent electrical energy production of the individual states. Detrimentally, the production of electrical energy from solar or wind power depends on capricious weather conditions including seasonal, intermittent, and geographical constrains resulting in a fluctuating power supply [7]. The efficiency in the use of electrical energy produced from renewable energy sources highly depends on the balance of energy demand and energy production [8]. To overcome such fluctuations and thus addressing a significant challenge of the broad and feasible implementation of a sustainable energy transition, the long-time storage of electrical energy from renewable energy sources converted via electrolysis in a chemical energy form of hydrogen is becoming the centre of interest [9,10].

1.1 Problem definition

Nowadays, hydrogen is recognized as a promising way of storing excess energy derived from renewable sources due to its high energy density and lack of greenhouse gas emissions [11]. However, its low volumetric inferior calorific value compared to other common fuels (Figure 1) necessitates extensive storage volumes for a practical application [8,9,12,13]. Underground hydrogen storage (UHS), e.g., the utilization of natural geological reservoirs in the subsurface such as salt caverns, aquifers or depleted oil and gas fields, offer a solution to this requirement as potential storage sites [8,14–20]. Depleted oil or gas fields offer further advantages, despite the reservoirs being already well understood, existing infrastructure like boreholes and surface handling facilities could be widely used, thereby reducing initial investment costs. Boreholes play a crucial role by providing access to geological reservoirs, but they also present challenges as bottlenecks in any production or storage operations.

In simple terms, boreholes are lined with downhole materials, comprising a steel casing surrounded by a cement sheath filling the so-called annular space [21]. This way, cement, widely used in various compositions and nowadays a key construction material, is also finding applications in the geoenergy industry, including oil, gas, H_2-storage, carbon sequestration, and geothermal wells. The applied cement sheath ensures the mechanical strength of the borehole infrastructure and tightness, in other terms zonal isolation, against fluid migration. This is crucial for a safe and environmentally friendly energy production and storage [21]. Achieving zonal isolation, which separates fluids in one zone from another, requires low-permeability cement sheaths, especially under higher pressure-temperature conditions of the

subsurface formations encountered in the geoenergy industry. Simultaneously, the cement sheath must be mechanically durable to withstand the geothermal gradient, potential subsurface movements like earthquakes, or induced seismicity [22–26].

However, the impact that hydrogen might have on the mineralogical phase composition and subsequently on the physical and mechanical properties of downhole cement, potentially compromising the integrity of the cement sheath, is poorly understood [8,27]. Fundamental research is therefore essential for UHS, examining not only the integrity of reservoir and cap rocks [8,13,28–32], but also the downhole cement applied during the storage life of the well [8,33–35]. This becomes particularly critical once the injection scale is industrial, as there is a significant knowledge gap regarding the interaction between hydrogen and downhole cement, posing a substantial hazard to well integrity and thereof safety [21,23,24,26,36]. It is worth noting that various pilot hydrogen storage projects are already underway, contributing to the advancement of hydrogen utilization and storage technologies. Despite limited knowledge and experimental results on the effects of hydrogen on downhole cement [33,37,38], recent studies have undertaken thermodynamic modelling in this context [39,40]. These models suggest that certain redox-sensitive phases within the cement sheath are susceptible to hydrogen alteration due to its strong reducing character, potentially impacting the overall integrity of the well.

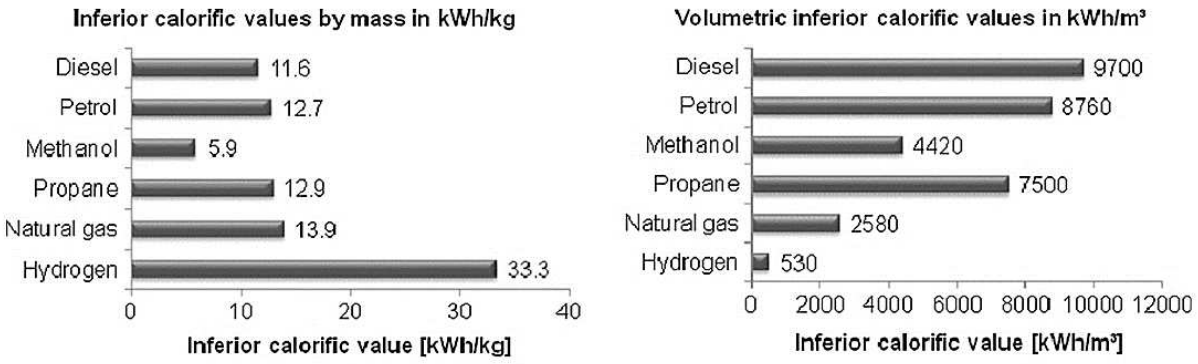

Figure 1: Mass and volume related inferior calorific values of common fuels at 200 bars and 25°C [41].

1.2 Aims and objectives

This PhD thesis is part of and funded by the Strategic Core Research Area SCoReA+ Hydrogen and Carbon of Montanuniversität Leoben, Austria. The aim of this thesis is to investigate hydrated cement pastes resembling cement sheaths used for downhole materials within the context of UHS. The focus is on fundamental questions regarding the mineralogical, mechanical, and physical characterisation and how these parameters interplay. Especially, potential hydrogen induced changes in the mineralogical phase composition of cement sheaths as well as the influence of those on mechanical, chemical, and physical parameters are of interest. This requires a suitable adaptation of mineralogical methods as well as for the sample preparation to obtain insightful results. Also, the tailoring of the mechanical and physical parameters of the hydrated cement paste using additives to prevent hydrogen permeation into the cement sheath and subsequent alteration is of interest. To fully assess the influence hydrogen has on a cement sheath in a realistic UHS storage operation, environmental aspects such as elevated pressure and temperature conditions encountered in subsurface storage sites as well as the presence of formation fluids or brines has to be considered during the design of experimental set ups. Therefore, a systematic and highly interdisciplinary approach between various chairs of Montanuniversität Leoben covering mineralogical, drilling engineering, geophysical, physical, material science and geoenergy competencies was implemented. To make the core results of the scientific work conducted within this thesis clearly visible the following three research questions are formulated:

1. **How can the sample preparation of hydrated cement pastes be advanced for microstructural investigations to fully utilize the potential of mineralogical methods for a holistic evaluation of cement sheaths? (Publication 1, [214])**

2. **What is the influence of certain additives added during the slurry mixing process on the mineralogical, mechanical, and physical properties of the hydrated cement paste and how can this be beneficial during UHS? (Publication 2, [215])**

3. **What is the influence of hydrogen on the mineralogical phase composition of downhole cement and subsequently on its integrity? What potential hydrogen induced geochemical reactions are likely to occur? (Publication 3, [216]).**

The results and findings of the scientific and experimental work carried out have been presented in several scientific publications. Therefore, this thesis is structured in a cumulative way. The core part, e.g., the results section (Chapter 4) is composed of three scientific, peer-reviewed publications [214-216]. In chapter 4 only a brief summary of publications 1 - 3 is presented; the complete publications formatted in the style of the publishing journal are added in Annex C.

To enable a systematic processing of the above formulated research questions five work packages (WP 1 – 5) were defined and deployed. The concept of technology readiness levels (TRL, Figure 2) [42] was implemented due to the fundamental nature of the research but also the very practical relevance of the issue. Work package 1 was set to start at a TRL of 1, and after the successful completion of autoclave experiments at the end of work package 5 a TRL of 4 was aimed to achieve (e.g., technological validity in the lab). In the following the content of the work packages is briefly described

- **WP 1: Literature study covering UHS as well as cement research, selection of a suitable cement type for investigation and development of an appropriate methodological approach (TRL 1).**
  A holistic literature study covering the topics UHS, cement mineralogy, cement – hydrogen interaction, as well as methods used for cement characterisation was carried out. class G cement, which is commonly deployed in geoenergy wells was selected for baseline investigations. A proper mixing, curing and storage procedure according to standardisations, to obtain comparable cement samples was established. An appropriate methodological approach was developed to characterise the cement in regard to its mineralogical phase composition, chemical, physical, and mechanical properties. Additionally, this approach was tailored to be able to detect potential hydrogen induced alterations of the previously named characteristics. The findings of WP1 served as input for WP2.
- **WP 2: Determination of the mechanical and physical properties and mineralogical characteristics of the selected cement. Evaluation of the influence of specific additives on the cement properties (TRL 2).**
  The initial properties such as mineralogical phase composition, chemical, physical, mechanical characteristics of the selected class G cement were determined based on the methodology approach developed in WP1. Suitable additives for mixing to the cement slurry, with the aim to reduce porosity and permeability as well as increase mechanical durability of the selected cement, were tested. Their influence on the above-mentioned properties was evaluated. The findings served as baseline data for WP4 and WP5.
- **WP 3: Thermodynamic modelling of the system cement – hydrogen as well as design and execution of first "bench top" experiments (TRL 3).**
  Thermodynamic modelling was executed to evaluate potential hydrogen induced reactions or changes in the mineralogical phase composition of the in WP1 selected class G cement and the in WP2 determined properties. Preliminary "bench top experiments" were designed and executed to create a first interaction of the selected cement with hydrogen. The findings served as input for the design and execution of autoclave experiments conducted in WP 4.
- **WP 4: Design and execution of initial, simplified autoclave experiments (TRL 4).**
  Autoclave experiments on a lab scale were designed using a "design of experiments" [43] approach. Under a defined atmosphere dried hydrated cement pastes were

brought into contact with hydrogen at different, for oil and gas reservoirs typical temperature and pressure conditions. After the experiments the cements were investigated using the methodological approach developed in in WP 1 and compared to the properties determined in WP2.

- **WP 5: Execution of autoclave experiments under reservoir like conditions, evaluation of the influence of brine (e.g., saturated cement) (TRL 4).**
  In a realistic UHS operation, the cement sheath is likely saturated by present formation fluids. Therefore, artificial brine was added to the autoclave environment to evaluate the influence that brines have on hydrogen reactivity and for better understanding the influence of capillarity within the pore space of cements. After the autoclave experiments, the cements were investigated using the developed approach of WP 1 and compared to the properties determined in WP2.

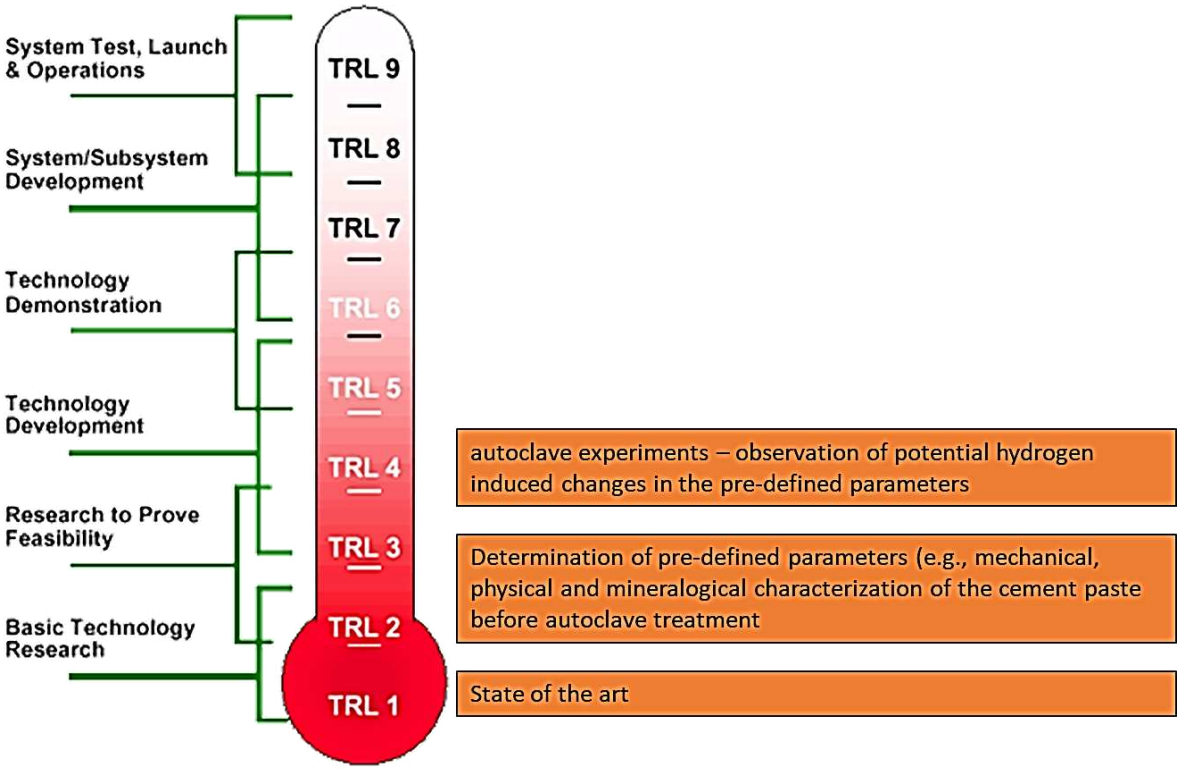

Figure 2: Concept of technology readiness levels (TRL) with the conducted work within this study[1].

[1]adapted after Wikipedia, https://de.wikipedia.org/wiki/Technology_Readiness_Level#/media/Datei:NASA_TRL_Meter.png – June 20244

2 Theoretical background

In this chapter first, a comprehensive review of the physical and chemical properties of molecular hydrogen and important aspects regarding elemental hydrogen reactivity within the context of underground hydrogen storage is presented. The following pages are inspired and based on the very detailed and comprehensive review paper by Zeng. et.al. 2023 [44]. Second, the concept of well integrity is laid out and the importance of cement as a downhole material as well as key mineralogical and structural aspects of cements are explained. For improving linguistic readability, paraphrasing and the search of information as well as references, artificial intelligence (ChatGPT V 3.5) was used occasionally (Table 5 in Annex A).

2.1 Physical and chemical properties of hydrogen

Hydrogen is a flammable, colourless, tasteless, odourless, non-toxic, non-corrosive, non-metallic gas. Under normal conditions, hydrogen exists as a dimerized molecule (H_2), a very inert, unreactive but highly explosive substance that can be considered as an ideal gas for a broad range of pressure (p) and temperature (T) conditions [45]. For temperatures below 20.27 K H_2 condenses into a clear and colourless liquid. At even lower T (14.02 K), H_2 transforms into a muddy condition called Slush bevor it crystallises into a solid with hexagonal densest packing [45]. The triple point of hydrogen is one of the fix points of the international temperature scale and lies at exactly 13.8033 K and 7.052 kPa [46]. The critical point lies at 33.18 K and 1.3 MPa [45]. The low reactivity of hydrogen gas is due to its strong H-H bonding with a dissociation energy of 435.7 kJ/mol and due to its nonpolar nature and its weak polarizability [45]. However, with increasing temperature or when activated by a catalyst (e.g., various metals), the reactivity of hydrogen increases significantly [45]. Due to its very small molecular size, hydrogen is characterized by a low viscosity, a large density difference compared to other gases [27], and high volatility [47]. The highly volatile character of hydrogen is reflected in a large diffusion coefficient of $5.13 * 10^{-9}$ m^2/s (in pure water at 25°C) [47].

Hydrogen is poorly soluble in water at normal p T conditions [48], on the other hand the large diffusion coefficient causes hydrogen to mix very rapidly with air, and also to escape very easily through the narrowest of gaps, which might be impermeable for other gases. In geological reservoirs, at higher temperatures, hydrogen might be considered generally more reactive, leading to the assumption of the occurrence of reactions between hydrogen and formation rocks as well as downhole materials [49]. Especially the strong reducing character of hydrogen might lead to redox reactions [45]. When it comes to diffusion or Darcy flow of hydrogen through reservoir and cap rocks and especially downhole materials such as the cement sheath, the degree of saturation as well as the salinity of the already present fluids in the pore space are main controlling factors [48,50,51] emphasizing the importance of understanding the effect capillarity has.

2.2 Role of hydrogen during Underground Hydrogen Storage

So far, most investigations concerning hydrogen behaviour during UHS have been conducted regarding its behaviour in combination with reservoir and cap rocks [44]. However, the fundamental chemical and physical principles are the same for the interaction with the cement sheath. Understanding the fundamental properties of hydrogen is crucial for the design and operation of underground hydrogen storage, significantly mitigating potential concerns regarding overall storage integrity [52–54].

In comparison to methane (CH_4), another commonly stored gas, H_2 has a higher heating value, e.g., energy density per mass (120–141.8 MJ/kg), making it an ideal fuel as an energy carrier [41]. However, the very low density of hydrogen and therefore the lower heating value per volume (10.8–12.7 MJ/m^3 compared to 35.8–39.8 MJ/m^3 of CH_4, Figure 1) implies the necessity of a tremendous volume of space to store H_2 [55]. Given the low critical temperature and pressure of hydrogen, large quantities of H_2 would be only storable in an energy efficient and cost-efficient way in the form of gas phase in subsurface formations [8,9,27,56–58]. The low density of H_2 also leads to an accumulated hydrogen cap below caprock, serving as a geologic seal for H_2 from escaping the storage site [59]. The denser cushion gas, e.g., CH_4 or N_2, would gather around H_2 in the form of a cushion gas plume to maintain enough formation pressure during H_2 withdrawal [58]. The viscosity of hydrogen is also less than the viscosity of CO_2 and CH_4, implying higher hydrogen mobility, expecting lower residual hydrogen trapped in the subsurface and higher reproduction efficiency [27]. The lower viscosity of hydrogen is helpful to suppress water coning issues [60]. However, the low viscosity of hydrogen could induce viscous fingering, leading to a certain amount of unrecoverable hydrogen [61]. Changes in pressure and temperature within the range of typical geological conditions, e.g., up to 200 MPa and 150°C have very limited effect on hydrogen viscosity (variation in the range of 9 - 11 * 10^6 Pa*s at pressure of 0.1 - 50 MPa and temperature of 25 - 120 °C [62]. Meanwhile, the cycling of H_2 during a storage process combined with pre-injected cushion gas and in-situ formation brine leads to complex multiphase flow behaviour [30].

2.3 Hydrogen solubility and dissociation in saline brines

In the context of underground hydrogen storage, the direct interaction of injected hydrogen with formation brine underscores the significance of understanding hydrogen solubility in subsurface porous media. This knowledge is crucial for monitoring and optimizing hydrogen mobility and reactivity [63,64]. As a non-polar gas, hydrogen exhibits minimal dissolution in water. At a temperature of 298 K and standard atmospheric pressure, the solubility of hydrogen in pure water is approximately 7.9 * 10^4 mol/kg$_w$ [63,64], slightly lower than the solubility of CH_4 (1.4 * 10^3 mol/kg$_w$) [65] but significantly lower than the solubility of CO_2 (> 0.033 mol/kg$_w$) [66]. Hydrogen solubility is influenced by pressure, temperature, and salinity; increasing pressure and decreasing temperature and salinity leads to higher solubility [48,64]. Bo et al. 2021 [29] simulated hydrogen solubility in saline brines with varying salinities, revealing a slight decrease in solubility of approximately 1 * 10^4 mol/kg$_w$) when increasing salinity from 5000 to 35,000 ppm. This finding is consistent with findings by Wiesenburg and Guinasso 1979 [64] and

Chabab et al. 2020 [67]. The exceptionally low solubility of hydrogen in saline brines suggests negligible hydrogen loss due to dissolution during underground hydrogen storage (UHS). The stability of hydrogen molecules further diminishes the dissociation of aqueous hydrogen in saline brines without minerals, as indicated by thermodynamic data from the WATEQ4F database associated with the PHREEQC geochemical solver [68]. The dissociation of aqueous hydrogen is defined by the reaction:

$$2H^+ + 2e^- = H_2 \quad \text{(Equation 1)}$$

The transition of hydrogen from the gas phase to the aqueous phase is described by:

$$H_{2(gas)} = H_{2(aqueous)} \quad \text{(Equation 2)}$$

as defined in the Lawrence Livermore National Laboratory database (LLNL) [68]. While the low solubility of hydrogen minimizes hydrogen loss through further dissociation, the nature of the host rock in UHS is crucial [44]. It not only influences petrophysical properties impacting hydrogen cycling but also dictates potential reactions between hydrogen and minerals like calcite, dolomite, siderite, pyrite, and others. These reactions involve redox processes, with hydrogen dissociation acting as an oxidation step, potentially leading to significant hydrogen loss, minerals dissolution, and impacting the stability and integrity of caprock, host rock and cement sheath in reservoirs [44].

2.4 Hydrogen diffusivity

From decades of studying petroleum systems two main mechanisms have been characterized to be mainly controlling the migration of fluids through an “impermeable” seal:

(1) molecular diffusion through the saturated pore space of the seal and
(2) compressible slow Darcy flow, e.g., upward diffusion through the seal medium [69].

The first process is ubiquitous but for most gases it is such a slow process that is only considered significant over geological timescales. However, the inherently low molecular weight of hydrogen leads to an increased diffusivity compared to other gases. In pure water at 298 K and standard pressure, the diffusion coefficient of hydrogen is approximately $5.13 * 10^9$ m^2/s [47], significantly surpassing the values for CO_2 ($1.6 * 10^9$ m^2/s) [70] and CH_4 ($1.85 * 10^9$ m^2/s) [71].
The second process depends strongly on geologic and hydrodynamic conditions of the system and the properties of the fluid [69]. To overcome the sealing capacity of the seal rock or the cement sheath a high enough pressure difference is needed. The magnitude of the necessary pressure difference is determined by the capillary forces and the wettability and contact angle of the fluids involved. The capillary forces across the interface of the wetting phase that saturates the seal (e.g., brine) and the nonwetting phase (e.g., hydrocarbons or hydrogen) are what define the sealing capacity of the seal [69].

2.4.1 Wettability and contact angle

The wettability of the H_2-brine-rock system has been investigated in several studies in recent years. For sandstones, it was found that the contact angle of a 10 wt% NaCl brine in the presence of hydrogen increases with rising temperature and pressure, revealing weakly water-wet to intermediate-wet hydrogen wettability under typical subsurface storage conditions [50,72–76]. Similar observations were made for carbonates, confirming an increasing hydrogen wettability with rising pressure and higher salinity [77,78].

2.4.2 Capillary pressure and interfacial tension

The capillary pressure prevents the penetration of the nonwetting fluids, such as hydrocarbons or hydrogen, into the sealing medium, hindering the loss of fluid through slow Darcy flow. Therefore, the characterization of capillary pressure in the hydrogen-water system under geological storage conditions is crucial for understanding hydrogen migration and assessing the capillary sealing capacity of caprock or cement sheath. Current studies suggest that the capillary pressure for the hydrogen-water-rock system increases as water saturation decreased [50]. Interestingly, unlike the CO_2-water system, changes in temperature and pressure seem to have minimal effects on capillary pressure suggesting that capillary pressure remains nearly constant across the pressure and temperature conditions relevant to UHS [50]. Figure 3 schematically illustrates the capillary sealing mechanism showing a pore with a curved interface between a wetting and nonwetting phase. Apart from capillary pressure, the interfacial tension between hydrogen and in-situ brine is another critical parameter influencing fluid flow and displacement impacting overall sealing and containment security. Several studies found that the interfacial tension decreases with increasing pressure and temperature but increases with decreasing salinity [73,74,79–82].

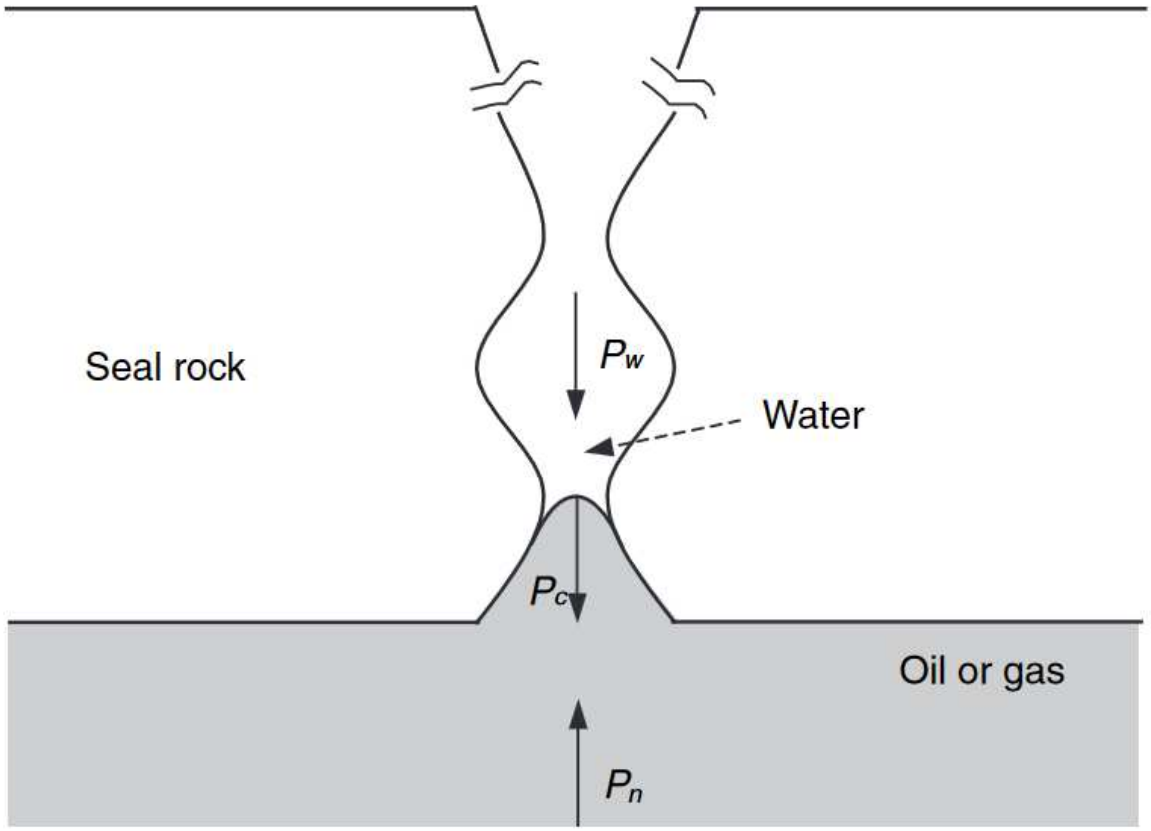

Figure 3: Illustration of the capillary sealing mechanism in a porous seal medium. P_w is the pressure of the wetting phase (e.g. brine), P_n is the pressure of the nonwetting phase (e.g., oil, natural gas, or hydrogen), P_c is the capillary pressure across the interface of the nonwetting/wetting phase. The non-wetting phase will only penetrate into the pore space once the pressure difference between the nonwetting and wetting phase exceed the capillary pressure [69].

2.5 Geochemical reactions

When hydrogen is introduced into subsurface porous media, it can potentially interact with specific mineral groups, particularly those prone to redox reactions. This interaction could directly affect the integrity and stability of the storage system. Several interactions between hydrogen and redox sensitive minerals might modify the physical (porosity, permeability) and physicochemical (wettability, contact angle, capillary pressure) properties as well as the mechanical strength of the caprock, reservoir rock and the wellbore, deteriorating storage capability and wellbore stability. Moreover, these geochemical reactions may modify in-situ brine geochemistry, creating a feedback loop that influences subsequent geochemical reactions and abiotic hydrogen loss [44,75]. Table 1 presents a summary of thermodynamic data for reductive dissolution of identified sensitive minerals from the thermodynamic LLNL database [68].

2.5.1 Sulfates

Reports on sulfate minerals dissolution induced by redox reactions with hydrogen come from both geochemical simulations and experimental observations [83–89]. The strong reducing character of hydrogen might reduce SO_4^{2-} from sulfate minerals like anglesite ($PbSO_4$), anhydrite ($CaSO_4$), gypsum ($CaSO_4.2H_2O$), barite ($BaSO_4$), and celestite ($SrSO_4$) to H_2S through the redox reaction:

$$SO_4^{2-} + 4H_2 \rightarrow H_2S + 2H_2O + 2OH^- \quad \text{(Equation 3)}$$

The generated H_2S can exist either in the gas phase or dissolve as an aqueous phase due to its high solubility [90] and it can further dissociate into HS^- and S^{2-}. Similar to carbonate minerals, the dissolution of sulfate minerals could have a partial impact on caprock integrity and rock mechanical behaviour as well as the integrity of the cement sheath since sulfates such as ettringite or aluminium-iron monosulfate (AFm) are main hydration products in common downhole cements [40,91].

2.5.2 Sulfides

Hydrogen induced pyrite (FeS_2) reduction was previously studied in several experiments [30,92,93] leading to the generation of pyrrhotite ($Fe_{1-x}S$) or troilite (FeS) as outlined in the idealised reaction:

$$FeS_2 + (1-x)H_2 = FeS_{(1+x)} + (1-x)H_2S \quad (0 < x < 0.125) \quad \text{(Equation 4)}$$

Generally, pyrite tends to be completely reduced by hydrogen to pyrrhotite within a short time interval at temperatures >90 °C and hydrogen partial pressures >100 kPa [89]. The rate of reduction is mainly controlled by pyrite solubility, however, at higher temperature and pressure, the reduction is driven by pyrrhotite precipitation. An alkaline environment, however, also facilitates pyrrhotite formation at low temperature and low H_2 partial pressure [94–97].

2.5.3 Fe^{3+}-bearing oxides

Minerals containing ferric iron, such as goethite [FeO(OH)] and hematite (Fe_2O_3), are susceptible to hydrogen induced reduction of Fe^{3+} to ferrous iron (Fe^{2+}). The oxide reduction process of e.g., hematite occurs in three sequential steps [98]:

$$Fe_2O_3 \rightarrow Fe_3O_4 \rightarrow FeO \rightarrow Fe \quad \text{(Equation 5)}$$

However, one has to mention that there is existing evidence that the reduction of Fe^{3+}-bearing oxides primarily occurs under elevated temperature conditions (300 to 700 °C) surpassing typical geological storage conditions [99–103]. The efficiency of these reduction reactions, however, might be catalysed by microorganisms as anaerobic bacteria play a vital role as catalysts, expediting redox processes by providing additional electrons [104–106].

Table 1: Thermodynamic reductive dissolution of identified sensitive minerals from the thermodynamic LLNL database [68].

Mineral	Reductive dissolution
Sulfates	
Anglesite	$PbSO_4 + 4H_2 = Pb^{2+} + H_2S + 2OH^- + 2H_2O$
Anhydrite	$CaSO_4 + 4H_2 = Ca^{2+} + H_2S + 2OH^- + 2H_2O$
Gypsum	$CaSO_4{:}2H_2O + 4H_2 = Ca^{2+} + H_2S + 2OH^- + 4H_2O$
Barite	$BaSO_4 + 4H_2 = Ba^{2+} + H_2S + 2OH^- + 2H_2O$
Celestite	$SrSO_4 + 4H_2 = Sr^{2+} + H_2S + 2OH^- + 2H_2O$
Sulfides	
Pyrite	$FeS_2 + H_2 = FeS + H_2S$
Oxides with Fe^{3+}	
Goethite	$2FeO(OH) + H_2 = 2Fe(OH)_2$
Hematite	$Fe_2O_3 + H_2 + H_2O = 2\ Fe(OH)_2$

2.6 Water geochemistry

2.6.1 pH

The pH serves as a crucial geochemical factor when it comes to the dissolution of mineral phases. Injecting H_2 into a depleted gas reservoir results in an pH increase to the range of 9 - 12 potentially altering sensitive minerals [29,30,83,107,108]. The pH elevation associated with hydrogen injection is primarily driven by reductive dissolution of carbonates, leading to the generation of additional OH^- ions [40,109]. A more alkaline environment can also facilitate the reduction of pyrite (FeS_2) to pyrrhotite (FeS) [30,93,95], along with the secondary dissolution of certain clays such as kaolinite and illite [110,111], potentially compromising reservoir integrity and stability. Given that the pH increase during UHS primarily influences interactions between sensitive minerals and stored hydrogen, it is anticipated that reservoirs with lithologies that contain fewer fractions of sensitive minerals may not experience a significant pH increase [29,109]. However, for carbonate reservoirs rich in calcite or dolomite, a more substantial pH increase may pose potential risks to storage integrity [108]. Consequently, sandstone reservoirs with limited amounts of sensitive minerals are considered most suitable for large-scale UHS to mitigate the impact of pH variation on storage integrity.

2.6.2 pE

The redox potential of a solution is directly correlated with the negative logarithm of its electron concentration, defined as pE [112]. In a simulation conducted by Zeng et al. [108] over an extended subsurface storage period in a carbonate reservoir, it was observed that the pE could significantly decrease to approximately -10.8 after 5 years (surface water typically has a pE of around 4), ultimately reaching values as low as -12. Similar to the pH increase observed during UHS, the decline in pE is attributed to redox reactions involving carbonate minerals. The highly negative pE indicates a strongly reductive environment, where CO_3^{2-}, HCO_3^-, SO_4^{2-}, and Fe^{3+} from minerals or aqueous ions undergo reduction to form CH_4, H_2S, and Fe^{2+}. A comparable outcome was documented by Jacquemet [109], who observed a pE decrease to approximately -11.3 in sandstone after reacting with hydrogen. A more negative pE signifies a higher reduction potential, indicating that chemical species are prone to gaining electrons and reducing to lower valence states in the presence of stored hydrogen.

2.6.3 Ion composition and concentration

The changes in ion composition and concentration before and after subjecting rocks or cement sheath to treatment with saline brine and hydrogen serves as an indicator of the extent of geochemical reactions, aiding in the assessment of storage integrity issues during UHS. Hassanpouryouzband et al. [113] conducted and extensive study, measuring the concentrations of Ca, K, Mg, Ba, Fe, S, Mn, and Ni before and after saturating sandstones with brine and either hydrogen or nitrogen. They observed minimal differences in water compositions for the sandstones treated with hydrogen compared to nitrogen. This suggests the absence of abiotic geochemical reactions for the tested sandstones within the experimental time scale indicating negligible dissolution or precipitation of minerals concluded by the lack of significant changes to the water chemistry.

2.7 Hydrogen as energy carrier

Access to affordable energy is a crucial success factor for any domestic economy as there is a clear connection between increasing prosperity with increasing energy consumption per capita [114]. In ancient times, societies relied on local resources such wood, and water until the steam engine fuelled by coal in the 19th century marked the beginning of industrialization [115]. In the 20th century, a transition from solid energy carriers to liquid fuels, like oil, and natural gas took place. This trend is set to be continued with hydrogen being considered a major future energy carrier (Figure 4) [116]. This transition is motivated by technological progress and innovation as well as a more responsible environmental thinking and the arising of a humanmade climate change. While the consumption of coal, oil, and gas releases CO_2 emissions into the atmosphere, the burning of hydrogen only produces water steam helping to reach a sustainable energy supply in the coming decades [115,116].
Since hydrogen is predominantly found on Earth in chemically bound forms, making it not a primary energy source but rather a chemical energy carrier, it has to be produced using renewable energy sources like solar energy, geothermal energy, or wind energy to make it a real sustainable energy option [117,118]. For a more efficient use of these renewable energy sources, an energy storage system is necessary due to the temporal and seasonal inconsistency between availability and demand [118]. Such an energy storage not only bridges supply gaps in time but also mitigates economic and political tensions caused by uneven distribution of resources through a more flexible energy market. In such a market, production and consumption are more decoupled and decentralized [119].

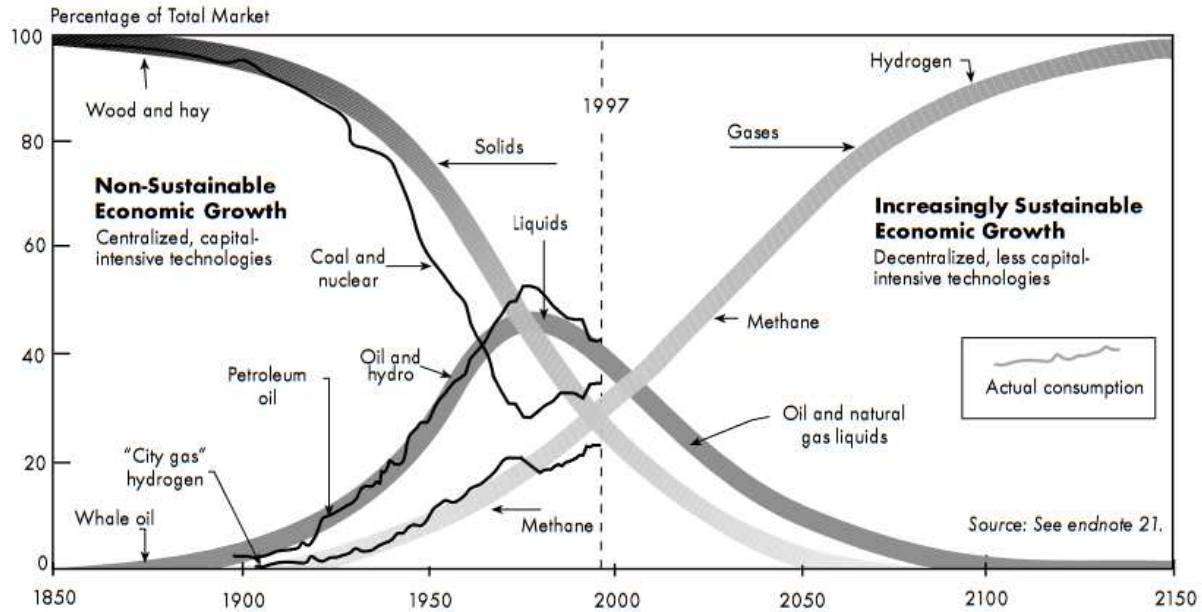

Figure 4: Schematic sketch of the development of the energy market and the importance of different energy carriers, from [116].

2.7.1 Hydrogen production

Processes for the production of hydrogen are well-developed and firmly established in the industry [118]. Depending on the production source the following “colours” of hydrogen can be distinguished [120,121]:

- Grey (produced from hydrocarbons with CO_2 as by-product, which is released, e.g., steam reforming)
- Blue (produced from hydrocarbons with CO_2 as by-product which is captured and used/stored, e.g., steam reforming)
- Pink (produced via water electrolysis powered by nuclear energy)
- Green (produced via water electrolysis powered with renewable energy)
- Gold (natural occurring hydrogen)

As of now, the production of grey or blue hydrogen by steam reforming is the cheapest and most widely applied technology [115,118]. However, especially in recent years technological advances regarding the efficiency of electrolysis cells helped to reduce the costs of green hydrogen production [117]. Gold hydrogen looks very promising and would be the most efficient way to use hydrogen as an energy carrier, however, only a handful of natural hydrogen reservoirs have been discovered world-wide so far and they are currently not yet considered an important option for hydrogen production [121,122]. However, exploration on natural occurring hydrogen commodities has not been done extensively in the past decades and discoveries of natural occurring hydrogen reservoirs were coincidentally [122].

2.7.1.1 Steam reforming

Steam reforming involves the conversion of hydrocarbons and alcohols into hydrogen, producing water vapor, carbon monoxide (CO), and carbon dioxide (CO_2) as byproducts [118]. Additionally, water vapor is used as an oxidizing agent to separate hydrogen from hydrocarbons. Natural gas, primarily methane-rich, is the most used source gas. For the reforming of methane, the following equation can be derived:

$$4CH_4 + 2H_2O \rightarrow CO + 3H_2 \qquad (\Delta H = 206\ kJ\ at\ 298\ K) \qquad \text{(Equation 6)}$$

Steam reforming of natural gas is well-established on an industrial scale and is widely used in petrochemical and fertilizer production. High conversion rates are achieved with high temperatures (typically 850°C), low pressures, a significant steam content, and the usage of iron or nickel as catalyst [123]. To obtain high-purity hydrogen, additional process steps, such as pressure swing adsorption or alkaline absorption gas washing, are often employed to decrease byproducts like CO, CO_2, and CH_4 to a few ppm [118].

2.7.1.2 Partial oxidation

Partial oxidation is another common and well-established industrial process that enables large scale hydrogen production from hydrocarbons by the partial oxidation of e.g., heavy oils or other hydrocarbons [118]. It efficiently produces syngas, a mixture of H_2 and CO, directly from coal or coke with a H_2/CO ratio of around 2, making it ideal for methanol synthesis. One can distinguish between non-catalytic partial oxidation, which is conducted at temperatures of 1200 – 1450 °C and pressures of 3 – 7.5 MPa, and catalytic partial oxidation which only requires temperatures around 1000 °C [118]. Overall efficiencies of partial oxidation are slightly below the methane steam reforming process, at approximately 50%. Other disadvantages are the high oxygen demand, catalyst deactivation due to carbon deposition, and a significant proportion of CO in the product gas, necessitating a potential shift reaction, and additional purification steps [118].

2.7.1.3 Water electrolysis

Electrolysis is the process of splitting a chemical compound under the influence of an electric current. In the case of water electrolysis, water molecules are split up into molecular hydrogen and oxygen [124]. When electrolysis is operated with electricity produced from renewable energy sources it does not release any CO_2, making it an attractive method for hydrogen production to store renewable power in a sustainable way [118]. It is particularly cost-effective when inexpensive electrical energy is available, and the produced pure oxygen can be economically utilized. Based on the construction of the electrolysis cell, one can distinguish between alkali electrolysis, proton exchange electrolysis (PEM) and solid oxide electrolyser cell (SOEC) technologies operating under low-temperature and high-temperature, low-pressure and high-pressure operation conditions [124].

The alkaline electrolysis (Figure 5) uses an alkaline electrolyte (e.g., water with salts like NaCl or KOH) in a vessel with two electrodes. Usual operation temperatures are between 70 and 90 °C, with a cell voltage of 1.85 - 2.05 V and current densities of 2 - 3 kA/m². The resulting purity is 99.9% for H_2 and 99.8% for O_2. The use of iridium dioxide catalysts as anode, platinum as cathode, and perfluorinated sulfonic acid-containing membranes as electrolyte has recently achieved efficiencies of 93% [124].

To overcome issues like partial load, low current density and low-pressure operation that plague the alkaline electrolyser, proton exchange electrolysis involving a proton exchange membrane was introduced [125]. The proton exchange membrane is placed between the anode and cathode acting as a solid electrolyte responsible for the conduction of protons allowing the separation of water molecules into very high purity gases of hydrogen and oxygen (Figure 5) [125]. One of the main advantages of this type of electrolysis cell is its ability to operate at high current densities, resulting in reduced operational costs. This is especially advantageous when coupled with dynamic energy sources such as renewables where sudden spikes in energy input would otherwise result in uncaptured energy [125].

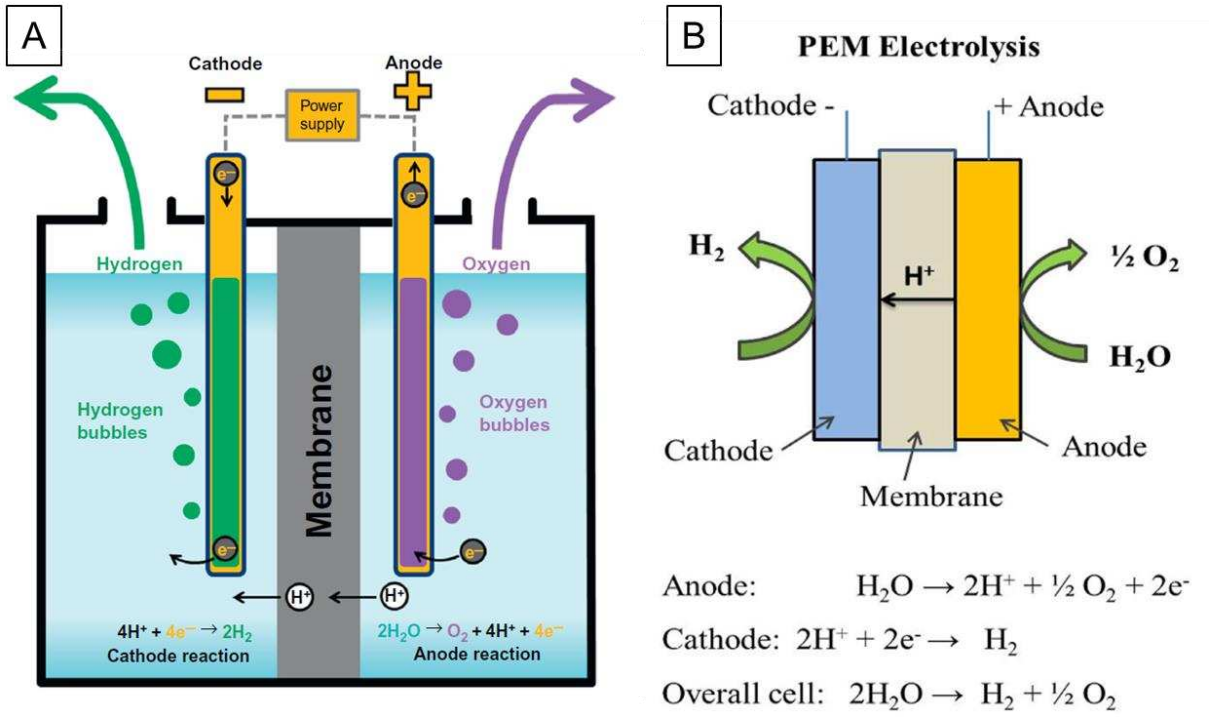

Figure 5: A: Arrangement and function of an alkaline electrolysis cell, from [124]. B: Arrangement and function of a proton exchange membrane electrolysis cell with chemical reactions occurring at the anode and cathode (from [125]).

A solid oxide electrolyser cell allows high-temperature electrolysis where water steam is split up into hydrogen and oxygen. Here, a porous solid oxide, e.g., ceramics are used as electrolyte (Figure 6). Typical operation temperatures are between 500°C and 850°C [125].

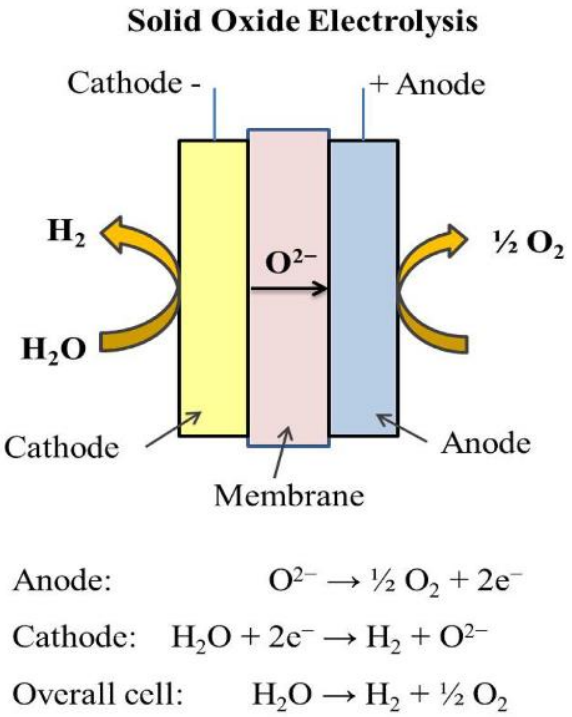

Figure 6: Arrangement and function of a solid oxide electrolysis cell with the chemical reactions occurring at the anode and cathode (from [125]).

2.7.2 Hydrogen storage

In the realm of hydrogen storage, both volumetric and gravimetric density are pivotal considerations, particularly for mobile and often stationary applications [8,9]. Throughout history, hydrogen storage has seen various methods, including high-pressure gas cylinders, cryogenic tanks for liquid hydrogen, adsorption on high-surface-area materials, absorption in host metals, chemical bonding in compounds, and even through the oxidation of reactive metals like Li, Na, Mg, Al, and Zn with water [9]. Traditionally, high-pressure gas cylinders, reaching up to 20 MPa, have been the go-to storage systems. In the renewable era, UHS stands out for its cost-effectiveness and scalability, attracting significant attention (Figure 7) [27,62,118,126]. UHS, not only offers safety advantages but also boasts extensive storage capacity, often surpassing surface storage methods by orders of magnitude [27,127]. Consequently, UHS is emerging as a fundamental component in the future hydrogen market chain.

There is already existing experience with the subsurface storage of hydrogen from the past century with the storage of town gas, a mixture of natural gas and hydrogen (51% H_2, 21% CH_4, 15% N_2, 9% CO) stored in salt caverns [13]. However, despite historical experience, concerns linger over hydrogen losses due to physical leakage and underground chemical reactions with reservoir rocks, cap rocks and downhole materials (see sections 2.2 – 2.6) [8]. Table 2 lists historic and contemporary UHS storage projects around the world reflecting the growing importance of a feasible and safe application of this research field.

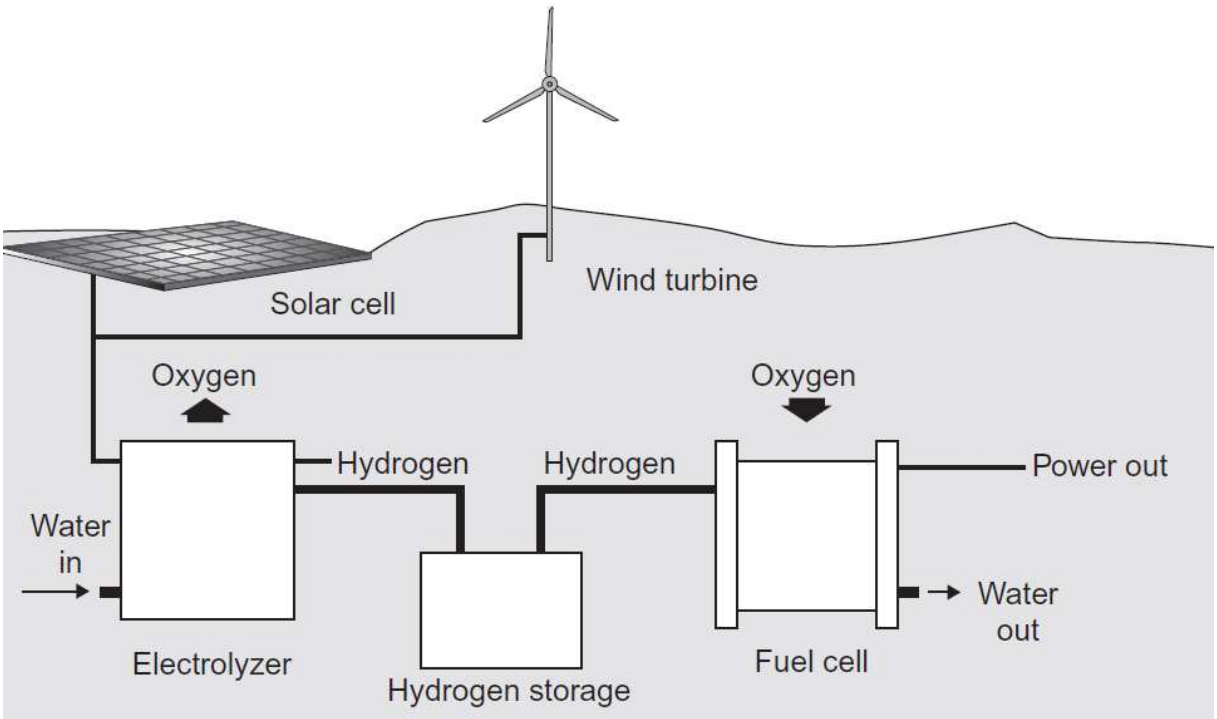

Figure 7: Concept of UHS combined with renewable energy sources, from [124].

Table 2: Listing of various historic and contemporary global UHS storage projects, based on [44].

Project	Country	Time	Type	Developer	Status
HyStorPor	United Kingdom	2019-2023	Porous rocks	Scotland Gas Network	Pilot and demonstration project
Teeside	United Kingdom	1972	Salt Dome	Sabic Petrochemicals	Existing UHS
Moss Bluff	United States of America	2007	Salt Dome	Praxair	Existing UHS
Spindletop	United States of America	2017	Salt Dome	Air Liquide	Existing UHS
ConocoPhillips Clemens Terminal	United States of America	1983	Salt Dome	ConocoPhillips and Praxair	Existing UHS
HyUnder	Europe	2013	Salt Dome	Fundación Hidrógeno, Aragón CENEX,	Pilot and demonstration project
Underground Sun Storage	Austria	2013	Porous Rocks	RAG Austria	Pilot and demonstration project
Vienna Basin Green Hydrogen Storage Project	Austria	2021	Porous Rocks	ADX Energy Ltd	Pilot and demonstration project
MefHySto Project	Europe	2019	NA	European Metrology Programme on Innovation and Research	Pilot and demonstration project
Large-Scale Energy Storage in Salt Caverns and Depleted Gas Fields	Netherlands	2019	Salt Dome	TNO	Pilot and demonstration project
HyPster	France	N/A	Salt Dome	Storengy	Pilot and demonstration project
HyChico	Argentina	N/A	Porous Rocks	Hychico Holding Group	Pilot and demonstration project

2.8 Well integrity

One key concept that needs to be accounted for to enable economic and safe hydrogen storage underground is well integrity. When talking about well integrity one refers to the ability of a well to allow the production or injection/storage of fluids in a controlled manner and preventing upward movement of fluids outside of the well [128]. ISO – 16530 defines well integrity as the "*containment and prevention of the escape of fluids to subterranean formations or surface with the application of technical, operational, and organizational methods to prevent the uncontrolled flow of fluids at the surface or across subsurface formations through the life cycle of the well*" [129]. A similar definition is found in NORSOK D-010 [130]. To ensure well integrity, modern wells are based on a multi-barrier concept, e.g., the interplay of so called well barrier elements which can be further grouped into primary barrier envelopes and secondary barrier envelopes (Table 3). These well barrier elements include various facets over the lifespan of a well including accountability, well operating processes, well service processes, tubing, cementing, annulus fluids, well head/tree, plug and abandonment (Figure 8). Once a well is installed, chemical and mechanical loads in the subsurface are exposed to the emplaced barrier elements, potentially reducing their effectiveness which might ultimately lead to the loss of integrity. Such loads might be amplified during the injection of hydrogen since the wells experience large temperature and pressure changes, higher injection pressures and reactions between hydrogen-brine mixtures with well components [131]. In the worst case, these enhanced loads lead to well integrity failure, meaning economic damage by the mean of hydrogen loss, environmental contamination, and safety hazards. Due to the interplay of several well barrier elements, the failure of one such barrier does not mean well integrity failure. However, it increases the load the next barrier element must withstand, potentially already affecting the economic operation of the well and leading to an increasing risk of well integrity failure. Therefore, one has to differentiate between the terms well integrity and structural integrity [132]. The failure of a barrier element compromises its structural integrity, however as long as this failure does not result in a blow out the well may not necessarily lose its integrity [132]. Therefore, well integrity is concerned with the safe, economic, and reliable containment of all well fluids throughout the life of a well.

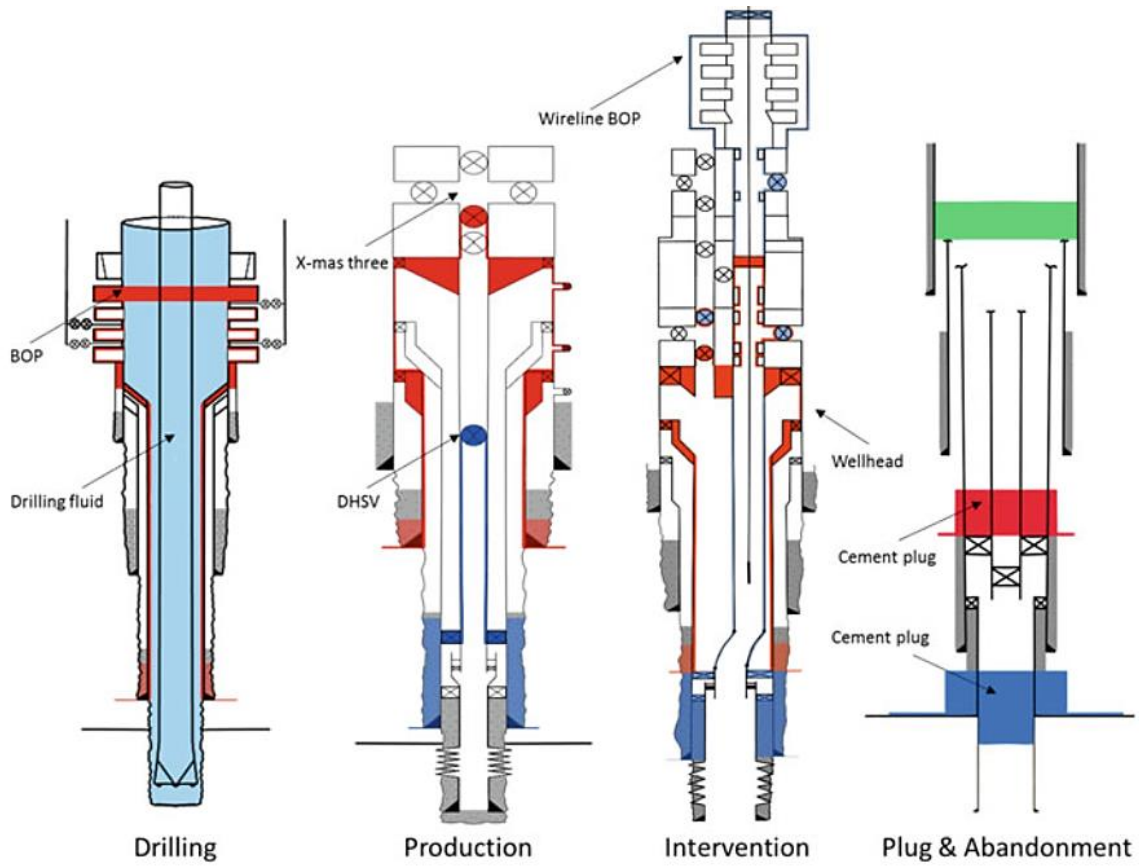

Figure 8: Illustration of the well integrity concept with different well barrier elements (e.g., red and blue) from the drilling phase to the plug and abandonment phase of the borehole, BOP = blow out preventer, DHSV = downhole safety valve, X-mas tree = assembly of valves, from [128].

Table 3: Examples of different well barrier elements during different phases of the well, from [128].

Example	Primary barrier envelope	Secondary barrier envelope
Drilling	Overbalanced mud with filter cake	Casing cement, casing, wellhead, blow out preventer
Production	Casing cement, casing, packer, tubing, downhole safety valve (DHSV)	Casing cement, casing, wellhead, tubing hanger, Christmas tree
Intervention	Casing cement, casing, deep-set plug, overbalanced mud	Casing cement, casing, wellhead, blow out preventer
Plug and abandonment	Casing cement, casing, cement plug	Casing cement, casing, cement plug

2.9 Cement used as downhole material

In the following chapter a comprehensive review of cement, from its manufacturing over its hydration reactions to potential hydrogen induced alterations once applied as downhole material, is presented. The following pages are based on the article of Scrivener and Snellings (2023) [133] which outlines the most important fundamentals for understanding cement as a construction and hydration material with added information from Bahafid (2017) [134] regarding microstructure development and the specific application area of ordinary Portland/ class G cement as downhole material.

Cement is a highly utilized and adaptable construction material with its roots ranging back to ancient times that has extended its applications into the contemporary geoenergy industry. There, cements serve as crucial well barrier elements to uphold well integrity. In the well construction process, a cement slurry is pumped in the before drilled hole to occupy the annular space between the steel casing and the adjacent rock formations of the wellbore [21]. The geothermal gradient and increasing hydrostatic pressure expose the curing cement sheath to diverse hydration conditions, impacting its mechanical and physical properties [22]. Once the slurry solidifies, the cement sheath must endure a spectrum of mechanical and thermal stresses throughout the well's entire lifespan, including the abandonment phase. Functioning as a pivotal well barrier element, the cement sheath has to fulfil three key roles to ensure well integrity [135]:

- **Zonal isolation:** This role stands out as the most crucial, involving the prevention of fluid mixing, such as e.g., gas and water from one zone, with oil from another.
- **Corrosion protection:** The cement sheath acts as a shield, impeding fluids from the surrounding formation to reach the casing and consequently preventing corrosion.
- **Mechanical support:** The cement sheath contributes to overall structural strength by offering indispensable support to the casing, enabling the well to withstand e.g., natural or induced seismicity.

The American Petroleum Institute Specification 10A [136] categorizes cements into different classes based on their bulk chemical and clinker composition (e.g., A, B, C, D, E, F, G, H) for well cementing applications. Class G, essentially ordinary Portland cement [137], emerges as the most commonly used cement. According to API Spec 10A, cement of Class G is defined as "*The product obtained by grinding Portland cement clinker, consisting essentially of hydraulic calcium silicates usually containing one or more forms of calcium sulfate as an interground additive. No additives other than calcium sulfate or water, or both, shall be interground or blended with the clinker during manufacture of Class G well cement*".

2.9.1 Portland cement

Portland cement stands out as one of the great human inventions, having found remarkable versatile success in various areas of application since its initial introduction in the early 19th century. Functioning as a mineral or inorganic powder, it solidifies upon mixing with water and binds aggregates such as sand, gravel, or crushed rock to form a robust, rock-like substance, e.g. mortar or concrete. The current annual global production of Portland cement is estimated at around 4.2 billion tonnes, representing over 99% of the worldwide cement market [138]. In the production process of Portland cement, limestone is combined with sources containing the elements Si, Al, and Fe to achieve a precisely defined raw meal composition. Due to the often-inherent impurity of the used limestone, the limestone itself, already contributes a portion of the required Si, Al, and Fe. To fine-tune the raw meal composition, clays or shale are traditionally added [133].

This mixture undergoes firing in a rotary kiln at a temperature of 1450 °C, resulting in the formation of the so-called clinker. In a Portland clinker, the following four clinker minerals are the major hydraulic phases and main constituents [139] (Table 4): alite constitutes approximately 65 wt.% of conventional Portland cement, belite is present at around 15 wt.%, aluminate and ferrite each account for about 10 wt.%. During the clinker firing, alite forms large, angular grains that have developed at the expense of belite, which forms rounded grains and the consumption of added free lime at the kiln's highest temperature section, above 1350 °C [133]. Both alite and belite are embedded in a melt phase, formed at temperatures surpassing 1338 °C. This melt phase plays a crucial role in expediting the high-temperature formation of alite by enhancing contact between solids and facilitating element diffusion through the melt phase [133]. Upon cooling, the melt phase crystallizes into aluminate and ferrite phases [140]. The preservation of "metastable" high-temperature clinker phases during cooling is pivotal for obtaining a reactive cement that gains strength rapidly once mixed with water [140]. Subsequently, the clinker is finely milled alongside a small amount of Ca sulfates (gypsum or anhydrite) to yield the final Portland cement product as a hydraulic binder [141].

The hardening of the obtained hydraulic binder is caused by a water-requiring reaction called hydration. The hydration process of Portland cement can be understood as a solution-precipitation process, as depicted in Figure 9 [142]. The high-temperature clinker minerals, initially unstable at ambient conditions, rapidly dissolve once in contact with water into the aqueous phase, leading to the precipitation of (meta-)stable cement hydrates from the supersaturated solution. These solid hydrates, with lower density than the clinker minerals, occupy the space once filled by water, creating extensive solid–solid interfaces (see Figure 9). The cohesion or strength of the binder primarily stems from the weak surface adhesive forces, such as Van der Waals forces, acting across these solid–solid interfaces [133].

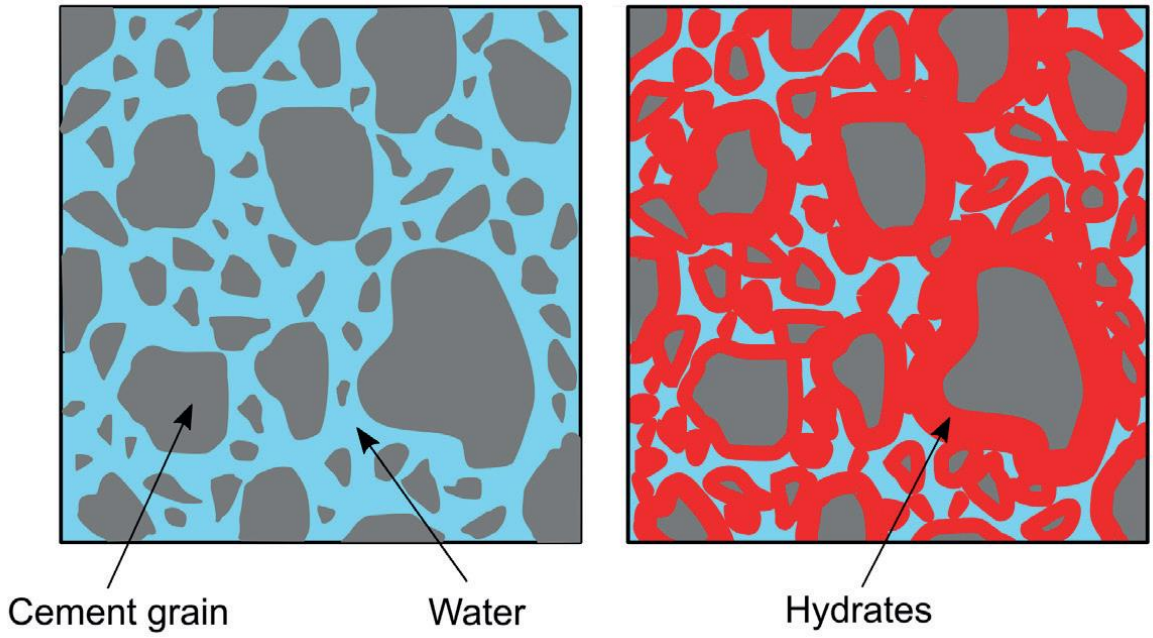

Figure 9: Sketch showing the dissolution – precipitation process of cement powder once in contact with water, from [133].

Since the chemical formulas of the clinker mineral phases and especially the hydration products can get lengthy, a simplified convention for naming cement phases based on their chemical composition has been in use for nearly a century now. This convention denotes a single capital letter to represent a specific oxide (Table 4) [143]. This allows the expression of lengthy chemical formulas in a condensed manner [144]. Per definition of a mineral [145], these clinker phases are not minerals from a historical point of view due to their artificial origin. However, certain phases formed during clinker production or cement hydration can also be found as minerals in nature. These minerals are predominantly formed in metamorphosed and metasomatized basaltic xenoliths, contact metamorphosed limestone, or skarn rocks. Noteworthy localities where such natural occurrences have been documented include Crestmore, California, USA [146], and the Hartrurim formation in the Maquarin area in Jordan [147] or basaltic vugs in the Eifel Mountains in Germany [148].

Table 4: List of phases in portland cement including the names used in industry, natural analogues known as minerals, cement notation and mineral chemical formula.

Name in cement industry	Mineral name	Cement notation	Mineral formula
Alite	Harturite	C_3S	Ca_3SiO_5
Belite	Larnite	C_2S	β-Ca_2SiO_4
Aluminate (Celite)	N/A	C_3A	$Ca_3Al_2O_6$
Ferrite	Brownmillerite	C_4AF	$Ca_4Al_2Fe_2O_{10}$
C-S-H	Tobermorite	C-S-H	$Ca_5Si_6O_{16}(OH)_{12}\cdot 4H_2O$
Portlandite	Portlandite	CH	$Ca(OH)_2$
Ettringite (AFt)	Ettringite	$C_3A\cdot 3C\$\cdot H_{32}$	$Ca_6Al_2(SO_4)_3(OH)_{12}\cdot 26H_2O$
Monosulfate (AFm)	Kuzelite	$C_3A\cdot C\$\cdot H_{12}$	$Ca_4Al_2(SO_4)(OH)_{12}\cdot 5.5H_2O$
Hemicarbonate	Hemicarbonate	$C_3A\cdot 0.5Cc\cdot H_{12}$	$Ca_4Al_2(CO_3)_{0.5}(OH)_{13}\cdot 5.5H_2O$
Monocarbonate	Monocarbonate	$C_3A\cdot Cc\cdot H_{11}$	$Ca_4Al_2(CO_3)(OH)_{12}\cdot 5H_2O$
Hydrotalcite	Hydrotalcite	M_6ACcH_{12}	$Mg_6Al_2(CO_3)(OH)_{16}\cdot 4H_2O$
Hydrogarnet	Katoite	C_3AH_6	$Ca_3Al_2O_6\cdot 6H_2O$
Cement notation	**Chemical Composition**		
C	CaO		
S	SiO_2		
A	Al_2O_3		
F	Fe_2O_3		
M	MgO		
H	H_2O		
Cc	CO_2		
$	SO_3		

2.9.1.1 Clinker phases

Alite

Alite (Ca_3SiO_3), a tricalcium silicate (C_3S), predominates in normal Portland cement clinker. It is the primary active component responsible for high hydration rates and strength development within the first days of mixing [149,150]. As a silicate with a nesosilicate structure, alite comprises a silicon atom bound to four oxygen atoms, forming a tetrahedral structure through covalent bonds $[SiO_4]^{4-}$. To achieve an electrical neutral compound, ionic bonds with metals (e.g., Ca, Mg, Fe) are formed [151]. Alite is also known to develop several polymorphs, e.g., compounds with the same chemical formula but different crystal structure. This polymorphism is notably influenced by temperature and impurities, impacting the orientation of silicate tetrahedra. At high kiln temperatures, C_3S exhibits rhombohedral (R) symmetry, transitioning to monoclinic (M1, M2, M3) and eventually triclinic (T1, T2, T3) symmetries during cooling (see Figure 10) [152–155]. However, to fully understand the crystal structure of alite polymorphs, additional research has to be carried out, as also other factors such as impurities of certain elements like Zn, P, Al, and Mg exert stabilization effects on different polymorphs [151,156]. Typically, rapidly cooled alite in Portland cement is monoclinic, with small amounts of Al and Mg substitutions in the C_3S crystal lattice stabilizing higher temperature monoclinic polymorphs [157]. Despite minor atom movements during the lowering of symmetry, the differences in hydrous reactivity between polymorphs are not significantly impactful [152]. Nevertheless, comprehending the crystal structures of major clinker phases sheds light on their reactivity disparities. C_3S exhibits higher reactivity compared to C_2S (belite) due to the presence of O^{2-} ions in its structure which is a unique characteristic among silicates, causing an open structure and distorted coordination of calcium atoms by oxygen [150].
Microscopically, alite crystals showcase idiomorphic, tabular, prismatic, compact, angular, or perfectly formed hexagonal shapes, with sizes varying between 25 and 65 µm [150]. Additionally, alite crystals may include inclusions of round, pre-formed belite and matrix phases (Figure 12). Belite can exist both as an inclusion within alite and as a coating enveloping the alite [158]. The extent of belite coating depends on the clinker composition, specifically the matrix composition in ordinary Portland cement. Apart from these structural aspects, alite also exhibits zoning, more prominent in poorly burned clinkers [158]. Furthermore, microcracks may be present in alite crystals, resulting from the rapid crystallization of the matrix, causing volume reduction and tensile stresses [158].

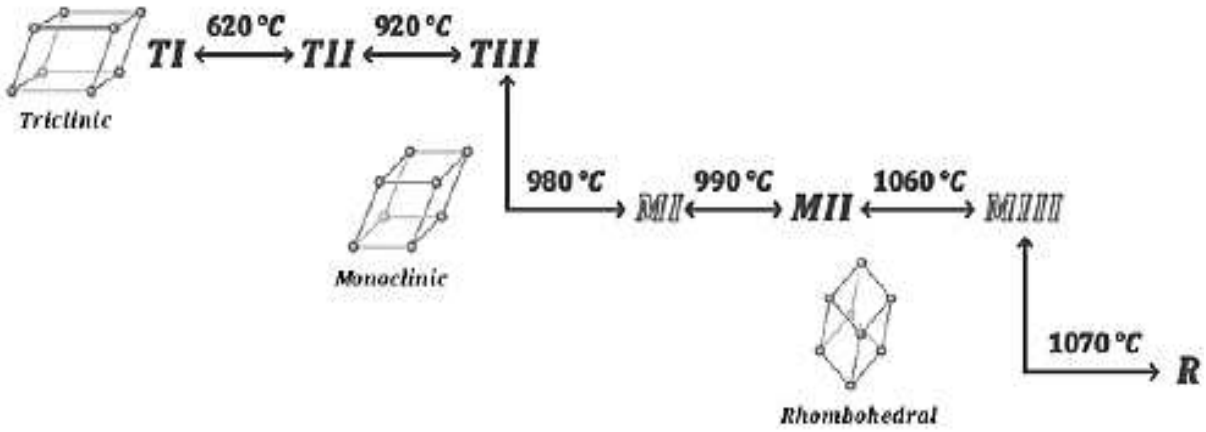

Figure 10: Polymorphism of alite; The triclinic compound T1 is attained at 620 °C during the cooling process to room temperature, with further transformations between 980 °C and 1060 °C to monoclinic and finally at 1070 °C to rhombohedral symmetry, from [159].

Belite

Dicalcium silicate, commonly known as belite (C_2S), is a clinker phase characterized by slow reactivity in early stages and a delayed setting time compared to alite. Despite this, it significantly contributes to the ultimate compressive strength of structures and enhances cement durability, imparting resistance to chemical attack and drying shrinkage within Portland cements [160]. The melting point of belite is at 2130 °C. From room temperature to its melting point, belite undergoes several phase transformations, resulting in five polymorphs within the α, β, and γ families, with the prevailing polymorph being β-C_2S [161]. In contrast to C_3S, the polymorphs of C_2S possess unique atomic arrangements and reactivities. At room temperature, γ-C_2S, also known as calcium olivine, is the stable polymorph, exhibiting minimal reactivity in Portland cement. Notably, γ-C_2S is undesirable during clinker formation due to its non-reactivity with water [162,163]. High-temperature polymorphs (α, α'H, α'L, and β) have less ideal close packing and lower density [161]. The lower monoclinic symmetry and more distorted coordination of calcium atoms correlate with higher reactivity [164]. Figure 11 illustrates the polymorphic transformations of dicalcium silicate.

Similar to alite, C_2S accommodates the incorporation of foreign ions to modify its activity [159]. For instance, impurities of e.g., P, Al, B, S, etc., have been studied for their effects on the reactivity of belite, with S showing varying impacts on hydraulic activity [151]. Solid solutions with ions like Al^{3+}, K^{+}, SO_4^{2-}, PO_4^{3-}, are common and stabilize higher temperature polymorphs [159].

Microscopically, belite crystals are characterized by either well-defined idiomorphic, glassy, or rounded shapes, sometimes displaying a distinct lamellar structure attributed to polymorphic twinning [158]. Twinning characteristics vary among polymorphs; for instance, α-belite exhibits no twinning and occurs mainly between the lamellae of β-belite. β-belite displays tight twinning, while γ-belite shows a somewhat broader twinning pattern. Inclusions of periclase (MgO) can also be present in belite crystals [158]. The size of belite varies depending on the firing temperature. Below 1300°C, crystal sizes range from 1 - 4 µm, whereas at higher temperatures at around 1500°C, they can reach sizes of 20 - 40 µm [158]. Additionally, the cooling rate plays

a crucial role in shaping belite. Slowly cooled clinker results in small, rounded particles dispersed within the interstitial components, often occurring as spot-like accumulations or individually scattered among other clinker phases [165].

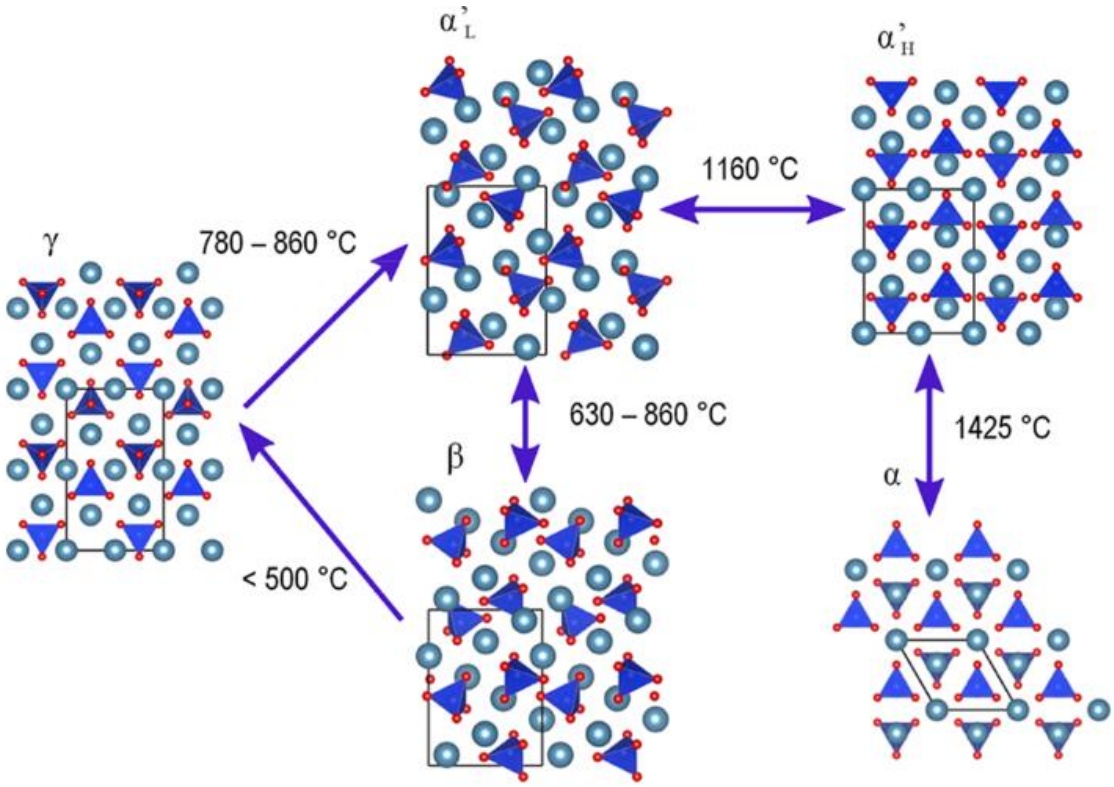

Figure 11: Polymorphs of belite and their T stability. α-belite forms at approximately 1425°C, β-belite at 670°C, and γ-belite at 830°C, from [161].

Aluminate (Celite)

The phase known as aluminate ($Ca_3Al_2O_6$) is a tricalcium aluminate (C_3A), that is known for its rapid reaction with water during hydration, contributing to an accelerated setting of the cement [150]. Aluminate displays polymorphs with isometric, tetragonal, monoclinic, and orthorhombic structures. In its crystalline form, aluminate manifests as small, xenomorphic to rectangular crystals, exhibiting a broad size range from 1 to 60 µm [166]. The aluminate crystals predominantly occupy interstitial spaces between the ferrite, alite, and belite phases, suggesting a late crystallization in the overall cement formation process (Figure 12) [158]. In contrast to these crystalline structures, aluminate can also be present in amorphous form [165].

Ferrite

Ferrite, a tetra calcium aluminoferrite (C_4AF, or $Ca_2(Al,Fe)^{3+}{}_2O_5$) can exhibit varying compositions based on the Al/Fe ratio. The setting speed of ferrite during hydration is notably diverse, influenced by its exact chemical composition. Generally, it is acknowledged that the setting speed is initially high and gradually decreases over time [150]. The prevailing crystal

system for ferrite is orthorhombic [166]. Ferrite can form small prismatic or dendritic crystals and, in some instances, may exhibit a fibrous habit. The crystals tend to form interstitially, between adjacent phases (Figure 12) [165]. Moreover, the cooling rate significantly impacts the crystal formation of ferrite. A slow cooling rate encourages a leafy form, moderate cooling results in a prismatic form, and rapid cooling favours a dendritic form. Under reflected light microscopy, ferrite is easily recognizable due to its higher reflectivity (Figure 12) [158].

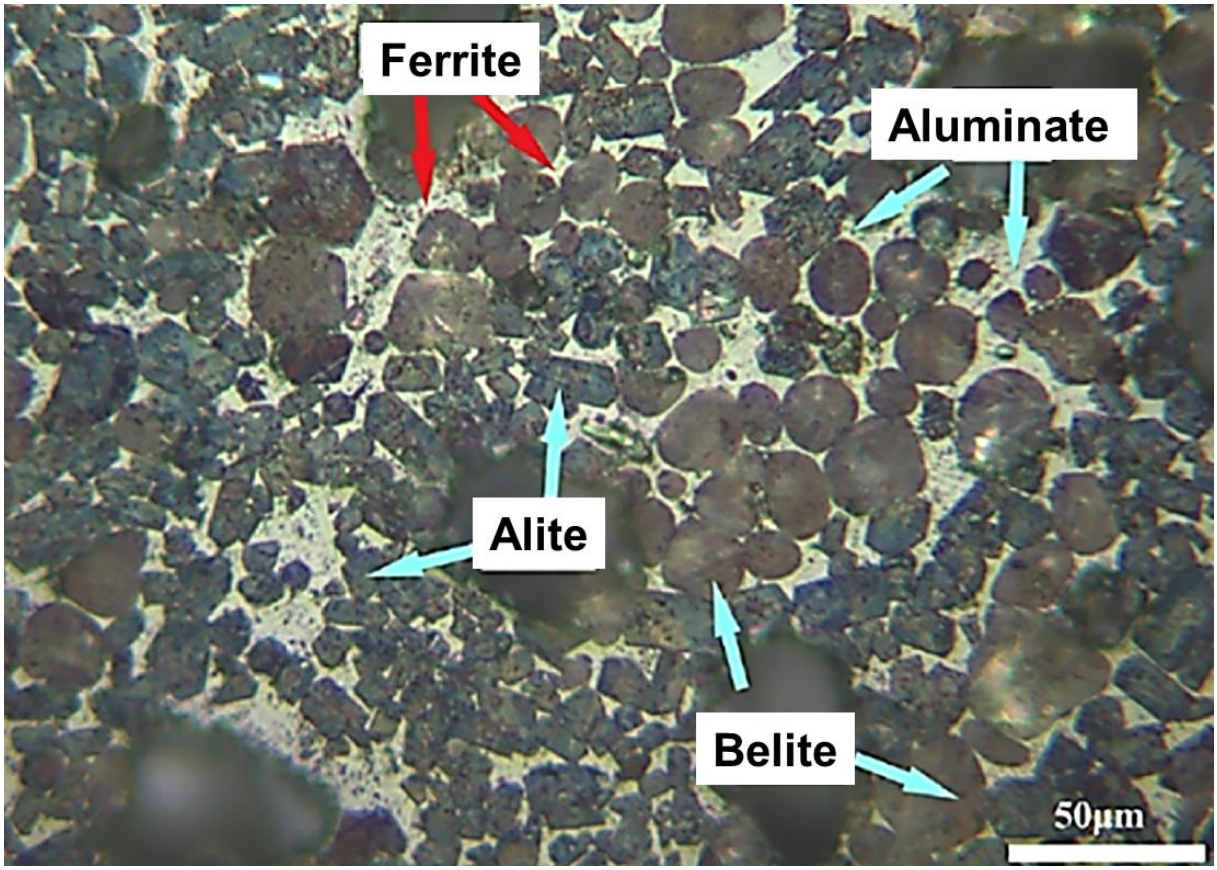

Figure 12: Reflected light microphotograph of cement clinker. The shape and colour of the four main clinker phases can be seen, from [167].

2.9.1.2 Portland cement hydration products

The hydration process of Portland cement is complex, involving various simultaneously occurring reactions of the clinker phases and gypsum with water [133]. As water interacts with the clinker phases in the cement, they undergo dissolution-precipitation reactions, resulting in the precipitation of hydrates on the grain surfaces [168]. Subsequently, through these dissolution-precipitation reactions, hydrates form and fill the space initially occupied by clinker phases and water (Figure 9). After the initial coating of the cement grains, the hydrates continue to gradually expand into available space [168,169]. Since the hydrates have significantly lower density than the anhydrous clinker phases the total volume of solids almost doubles due to hydration [133].

In the first hours of the hydration process, the hydration reactions of alite and aluminate predominantly cause the initial solidification of Portland cement. Belite and ferrite contribute significantly to the final solidification and strength development [150].

The hydration products of alite and belite, are so called calcium silicate hydrates characterised by variable stoichiometry and commonly referred to as C-S-H, as well as portlandite ($Ca(OH)_2$ or CH using the cement notation). C-S-H are crucial hydration products in Portland cement, characterized by an average stoichiometric composition of $C_{1.7}SH_4$ [133]. Concerning the crystal structure of C-S-H, it is best described as a nanocrystalline material that is lacking the long-range order of a well-crystallized phase. Tobermorite, a natural occurring mineral, was found to best resemble the defective nanocrystalline structure of C-S-H and is often used as an illustrative example for structural descriptions [170]. Tobermorite possesses a layered structure consisting of a distorted complex octahedral Ca-O layer with infinite chains of silicate tetrahedra on either side, following a “dreierkette” pattern (Figure 13) [170]. The interlayer is populated with additional H_2O and Ca^{2+} ions to balance the negative charge of the layers [171]. The Ca/Si ratio of tobermorite is 0.83 [133]. Introducing defects, such as the omission of silicate tetrahedra or chains and substitution of protons in the layer by Ca^{2+} ions, a Ca/Si ratio of 1.7 can be reached [170].

Portlandite, on the other hand, is a fully crystalline calcium hydroxide, often forming hexagonally shaped plates in hydrated cement paste.

The dissolution-precipitation reactions occurring during the hydration process of a cement powder, leading to the solidification of a cement slurry are presented in the following chapters.

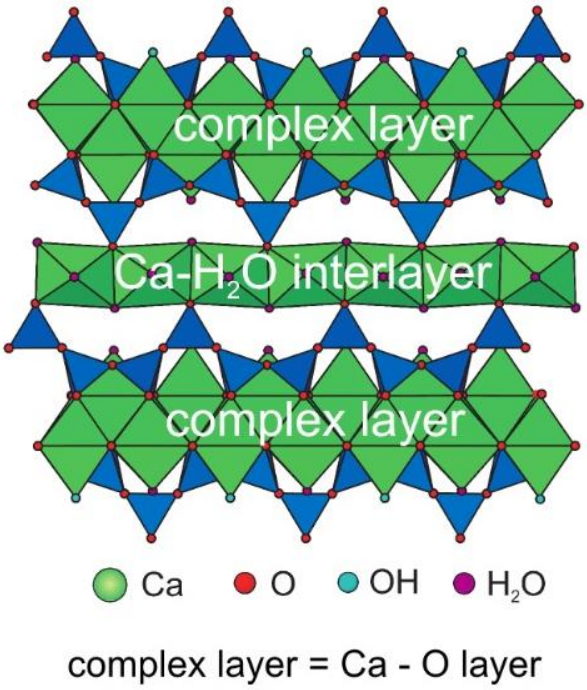

Figure 13: Crystal structure of tobermorite showing complex “dreierkette“ layers and Ca-H_2O interlayers, adapted from [172].

2.9.1.3 C_3S and C_2S hydration

The reactions described by equations 7 and 8 outline the hydration process of alite and belite. The hydration products of these two reactions are the amorphous C-S-H and crystalline portlandite. Since alite and belite are the main constituents of dry cement, their reaction products make up approximately 80% of the solidified cement paste and are thereof key aspects for the mechanical and physical parameters of solidified cements [173].
It is important to note that these reactions are approximations because the values of x and y are influenced by hydration conditions; i.e. pressure, temperature, water-to-cement ratio, relative humidity, age, particle size, presence of additives, and the inclusion of supplementary cementing materials into the C-S-H structure [134]. However, x is often considered to be 1.7, while y has a value of 4 [133].

$$C_3S + (3-x+y)H = C_x\text{-}S\text{-}H_y + (3-x)CH \quad \text{(Equation 7)}$$

$$C_2S + (2-x+y)H = C_x\text{-}S\text{-}H_y + (2-x)CH \quad \text{(Equation 8)}$$

2.9.1.4 C_3A and C_4AF hydration

The hydration reactions for C_3A and C_4AF, as presented in Equations 9 - 13, are more complicated and not as straight forward compared to those of C_3S and C_2S [22,174]. The products of these reactions result in the formation of various crystalline calcium aluminate hydrates (C-A-H) [133,150]. The specific hydrates formed from C_3A hydration depend on the presence and amount of gypsum, e.g., sulfate ions ($CaSO_4{\cdot}2H_2O$ or CSH_2 in cement notation) in the cement. When C_3A is hydrated in pure water, hydrogarnet C_3AH_6 is formed. However, this reaction releases a substantial amount of heat and causes rapid cement setting without significant strength development [150,173]. To prevent this unwanted outcome, gypsum is added to the initial cement clinker. The early hydration of C_3A in the presence of gypsum leads to the formation of ettringite ($Ca_6Al_2(SO_4)_3(OH)_{12}{*}26H_2O$ or $C_6A\$_3{\cdot}H_{32}$ in cement notation) which causes a delay of the initially rapid hydration of C_3A. Ettringite is a sulfate bearing, low-density calcium aluminate hydrate with a needle-like structure and three sulfate anions in its stoichiometric structure [22]. This is the cause why ettringite is often referred to as a tri-sulfate, or commonly referenced and abbreviated as AFt (aluminium-iron-tri-sulfate) in cement notations. When Fe^{3+} ions are present during the hydration process, e.g., from C_4AF, the substitution for Al^{3+} in the form of a solid solution is possible as well as the formation of iron hydroxides or iron-rich hydrogarnet [175].
As the hydration of C_3A in combination with gypsum progresses and sulfate ions become depleted, ettringite becomes unstable and transforms into a phase collectively known as the AFm phase (aluminium-iron-monosulfate) which has only one sulfate ion in its stoichiometry [133]. In the presence of small amounts of carbonate, precipitation of hemicarboaluminate ($C_3A0.5CcH_{12}$) and monocarboaluminate (C_3ACcH_{11}) can occur [176]. However, in general terms, both carbonate bearing phases are also attributed as AFm phase. The AFm phase can be thought of as an "anionic clay" or layered double hydroxide phases, sharing a common structure of positively charged $Ca_2Al(OH)_6^+$ layers and anion groups in between to balance the

charge [177]. AFm is characterized by hexagonal sheetlike crystal that reflect the layered crystal structure [177].
Recent advancements in determining consistent thermodynamic data on the solubility product of the hydration products allow thermodynamic models to make accurate predictions about the hydration product assemblage of Portland cement and various other hydraulic cements (Figure 14) [178].

C_3A reaction with no sulfate (formation of hydrogarnet):

$$2C_3A + 21H = C_3AH_9 + C_2AH_8 = 2C_3AH_6 + 9H \quad \text{(Equation 9)}$$

C_3A reaction with sulfate (formation of ettringite):

$$2C_3A + 2C\$H_2 + 26H = C_6A\$_3H_{32} \quad \text{(Equation 10)}$$

C_3A reaction after sulfate depletion (formation of AFm):

$$2C_3A + C_6A\$_3H_{32} + 4H = 3C_4A\$H_{12} \quad \text{(Equation 11)}$$

C_4AF reaction with sulfate (formation of iron-containing ettringite + iron-hydroxide):

$$C_4AF + 3C\$H2 + 21H = C_6(A,F)\$_3H_{32} + (F,A)H_3 \quad \text{(Equation 12)}$$

C_4AF sulfate depletion (formation of iron-containing AFm + iron-hydroxide):

$$C_4AF + C_6(A,F)\$_3H_{32} + 7H = 3C_4(A,F)\$_3H_{12} + (F,A)H_3 \quad \text{(Equation 13)}$$

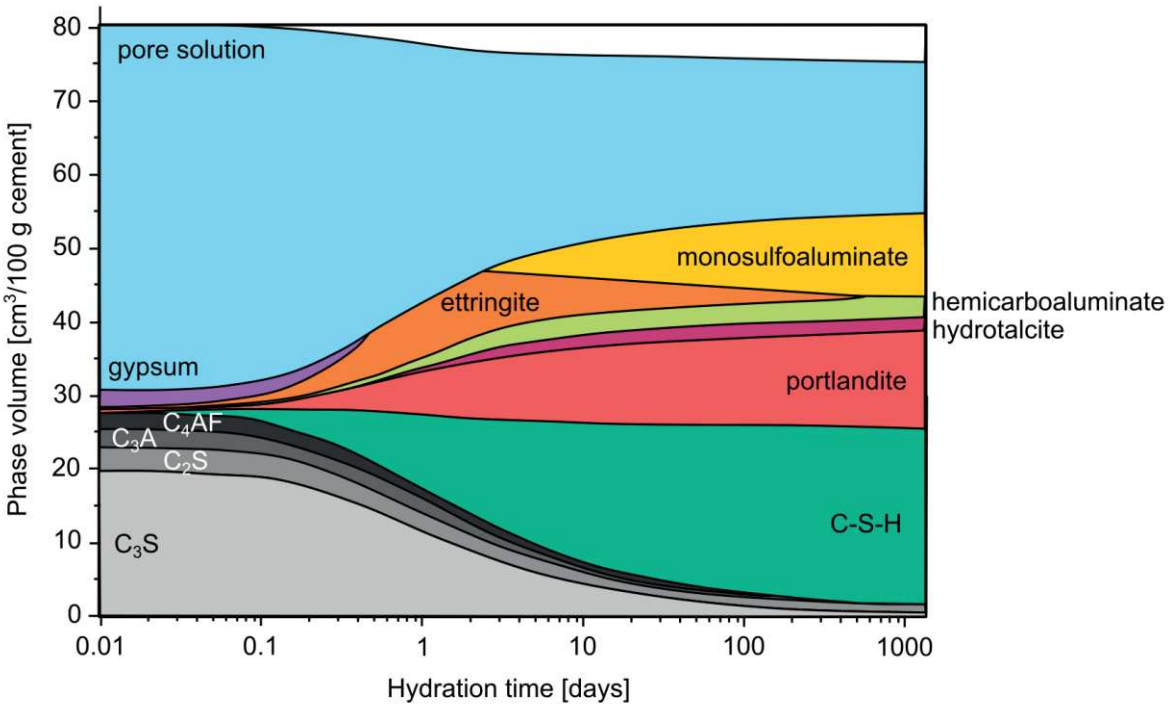

Figure 14: Thermodynamic modelling of the phase assemblage of Portland cement as a function of time, from [133].

2.9.1.5 Hydration kinetics

As mentioned above, cement hydration is the process of a series of successive dissolution-precipitation reactions [150]. These reactions release hydration heat, which can be measured using isothermal calorimetry. Such isothermal calorimetry experiments allow the distinctive recording of the hydration reactions, providing insights into the kinetics of these reactions [22]. The following list orders the hydration process into five essential stages based on kinetic findings of calorimetry experiments [169,179]:

1. **Pre-induction period:** the initial reaction that occurs when cement gets into contact with water. The duration of this period is a few minutes.
2. **Induction period:** slowdown in the hydration reactions before a significant increase in the reaction rate.
3. **Acceleration period:** this period takes several hours and is marked by a substantial release of heat. It is widely accepted that this heat release originates from nucleation and growth mechanisms of the hydration products.
4. **Deceleration period:** a significant decrease in the released heat is observed. This is likely caused by water depletion and associated with the challenge of the remaining water accessing still anhydrous grains that are surrounded by less permeable formed hydration products.
5. **Curing phase:** ongoing hydration that is primarily controlled by the diffusion of water through hydrates to further nucleate other grains in the anhydrous cement.

2.9.1.6 Microstructure of cement

As a result of the hydration process, the cured cement paste, e.g., the solidified cement sheath in boreholes, develops a highly intricate microstructure [180] that relies on curing conditions like pressure, temperature, and water content [134,181]. This is crucial as the physical and mechanical properties of hardened cement sheaths are determined by the resulting microstructure, thereby pointing out the importance of the curing conditions [134]. Over the past decade, various models have been proposed in an attempt to describe the microstructure of hydrated cement paste, with the Tennis and Jennings model being the most recent and comprehensive one [182,183].

Tennis and Jennings model

The Tennis and Jennings model, initially introduced as CM-I in the period 1994 - 2000 [182–184], was refined in 2008 and referred to as CM-II [185]. This model amalgamates elements from Feldman and Sereda's model [186,187] as well as Powers and Brownyard's model [188,189], two previous models for the description of microstructure in cement pastes. With the use of small angle neutron and X-ray scattering techniques, CM-II allows the conceptualization of the cement paste as a colloid composed of globules that aggregate to form the nano-porous C-S-H network [185]. The proposed C-S-H globule morphology [190] is illustrated in Figure 15. These globules are equiaxed particles with approximately 5 nm in diameter, displaying the above described sheet-like structure of tobermorite (Figure 13) [144]. The globules possess internal surface water and water-filled porosity which can be divided into three types (Figure 15) [185,190]:

- **Physically adsorbed water**: Water adhering to the outer surface, forming a monolayer coverage on the C-S-H globules.
- **Physically bound water**: Water arranged within the globules, occupying the interlayer spaces.
- **Chemically bound water**: Water bound within C-S-H sheets in the form of hydroxyl groups (OH^-).

In the Jennings model four pore types are described [174,184,185] (Figure 16):

- **Interlayer spaces and intraglobular pores (IGP):** both have sizes below 1 nm. The removal of water from interlayer spaces results in the collapse of the globule, whereas water removal from IGP does not induce any volume changes in the globule.
- **Small gel pores (SGP):** pores filled with water trapped between the globules, percolating towards the outer regions, with a characteristic size of 1 to 3 nm in diameter.
- **Large gel pores (LGP):** Resulting from the overlap of globular flocks, these pores have a characteristic size ranging from 3 to 12 nm in diameter.
- **Capillary pores:** pores filled with free water and are not intrinsic to the C-S-H, with sizes larger than 10 nm [174].

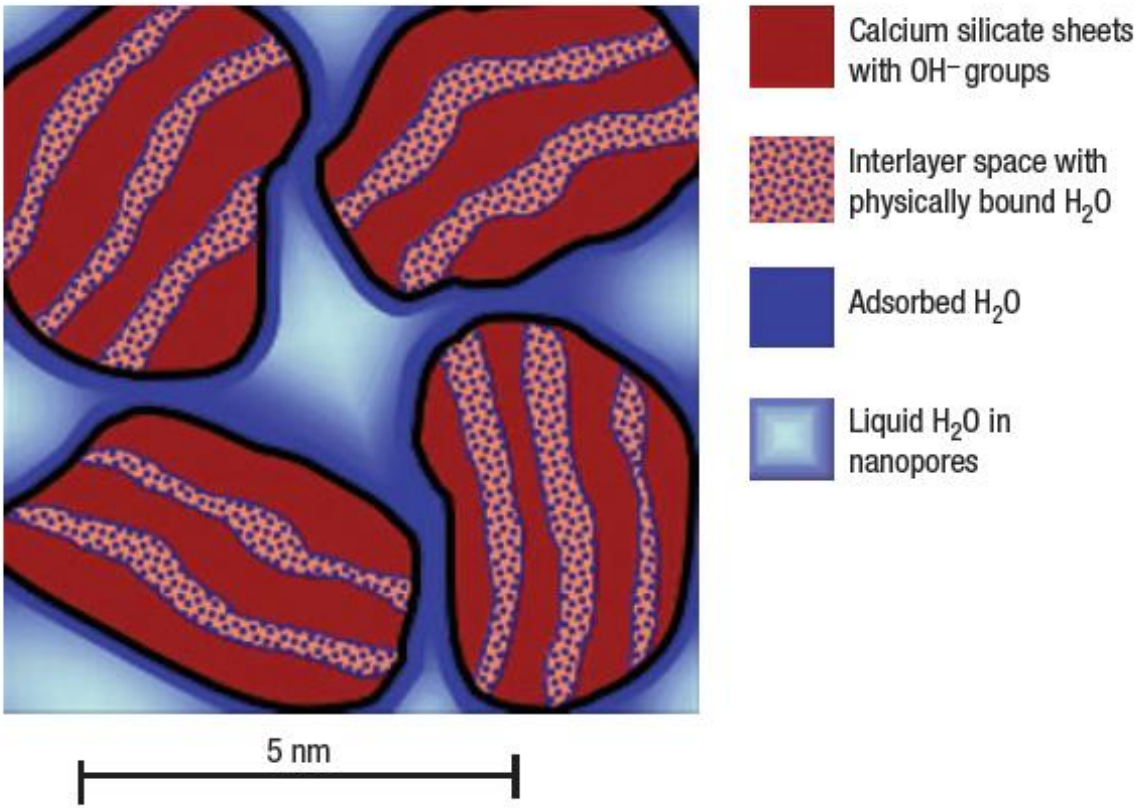

Figure 15: Morphology of the C-S-H globules with the three types of water present in C-S-H, from [190].

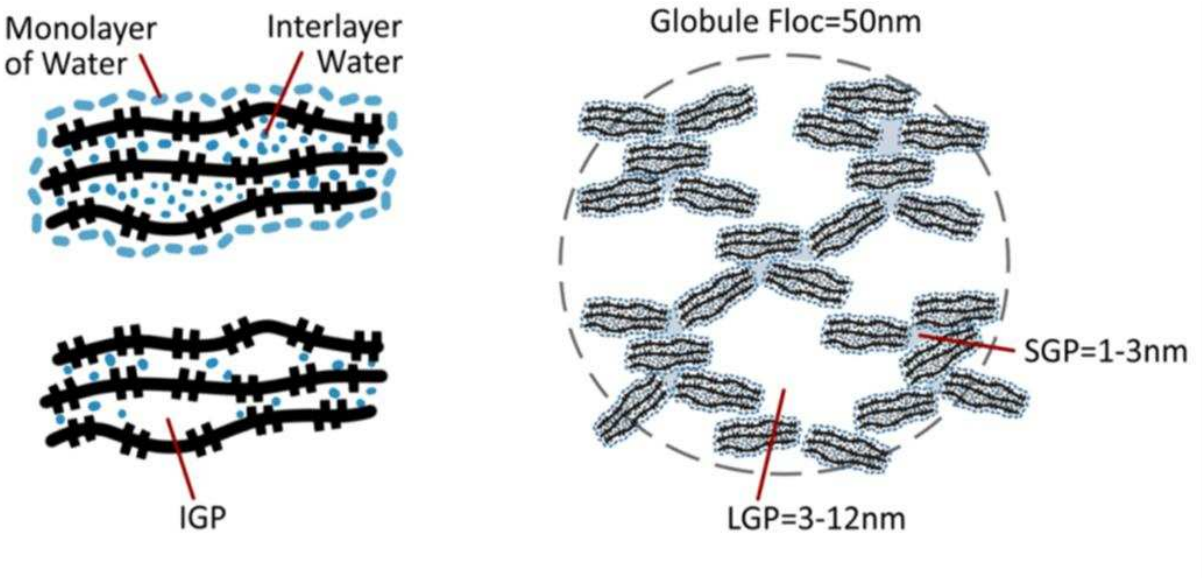

Figure 16: Types of pores in a hydrated cement paste, IGP: intraglobular pores, SGP: small gel porosity, LGP: large gel porosity, from [185].

2.9.1.7 Evidence of two C-S-H types

The distinction between two types of C-S-H phases is caused in the need of explaining various measurement inconsistencies in cementitious materials. For example, accurate porosity measurements of hydrated cement pastes are challenging, mainly due to the above-described incorporation of water molecules into the C-S-H structure. The obtained values depend on the applied technique and yield significant differences. A detailed discussion about the differences in common methods is presented in [180].

Similar challenges are encountered in measuring the specific surface area (SSA). For instance, a distinction must be made between SSA measured by water or nitrogen and their variation with the water-to-cement ratio [182,183]. The fact that water SSA measurements yield higher values than nitrogen SSA measurements indicates that water can penetrate a larger number of pores, while nitrogen cannot [180]. The pore region within C-S-H that nitrogen can penetrate is referred to as low density (LD) C-S-H, and the other pore region accessible only to water is referred to as high density (HD) C-S-H [134].

Additionally, the existence of C-S-H packing in two densities was also observed in several other studies by a variety of methods. For example, Small-Angle Neutron Scattering (SANS) facilitated the tracking of surface area development during hydration [191]. The combined measurements of SSA and heat release for a cement paste in the initial hours of hydration indicated that the SSA of early hydration products is higher than that of products formed later, [191]. In contrast, the HD C-S-H, filling the space at later ages, does not contribute to the measured SSA of the cement paste. Furthermore, nano-indentation experiments confirmed the existence of two C-S-H types with different elastic properties [192–194]. SEM micrographs revealed two C-S-H morphologies, a more and less dense C-S-H [195]. TEM experiments also detected two C-S-H types assigned to inner and outer products. The inner product grows at the surface of anhydrous grains, while the outer product grows at the inner product surfaces with a fibrillar morphology and fills the porous space [22, 196].

In summary, based on the CM-II findings, C-S-H is perceived as an assembly of globules packing together in two different densities, composing the two C-S-H regions: HD C-S-H and LD C-S-H that form the C-S-H gel. In conclusion, this chapter emphasizes that the CM-II model is an assumption of how the microstructure of cement pastes can be understood. However, it is crucial to note that there are parts of this model that are still under discussion. For a more detailed discussion of models describing cement pastes, the reader is referred to elsewhere [22,181,187,197–201].

2.9.2 Supplementary cementitious materials (SCMs)

Supplementary cementitious materials are a wide variety of both natural and technogenic materials (byproducts from various industries) with specific characteristics used in cementitious and concrete mixtures to improve specific properties of the hardened product [202]. SCMs are mainly used to improve sustainability of cement products by reducing the carbon footprint but also to enhance the long term performance of cement, mortar or concrete [203–205]. Typical and most common SCMs are:

- **fly ash** (a by-product of coal combustion in power plants)
- **ground granulated blast furnace slag** (a by-product of iron and steel manufacturing)
- **silica fume** (amorphous SiO_2, a by-product of silicon metal or ferrosilicon alloy production)
- **natural pozzolans** (volcanic ash or calcined clay such as metakaolin)
- **calcium carbonate**

The addition of SCMs into cementitious mixtures offers a wide range of improved properties such as increased compressive or flexural strength, improved durability by densifying the microstructure, reduced heat reduction during hydration and therefore mitigation of thermal cracking, reduced permeability, improved sulfate resistance, the mitigation of alkali-silica reaction and environmental sustainability [203]. These beneficial effects are a result of the interaction of the added SCM via the various chemical processes that occur during the hydration of cementitious materials such as Portland cement. Understanding the mechanisms of SCMs involves considering their chemical composition and physical characteristics. Important effects of SCMs are [202]:

- **pozzolanic reaction:** SCMs, such as fly ash or silica fume contain reactive silica that reacts with calcium hydroxide (e.g., portlandite) to additional C-S-H, leading to a denser microstructure and improving mechanical strength.
- **filler effect:** some SCMs contain very fine particle sizes, filling the voids between cement particles resulting in a denser structure and improved mechanical strength or reduced permeability.
- **water demand reduction:** some SCMs can chemically bind excess water in the cementitious mixture, reducing the free water content available for the hydration process. This leads to a lower water to cement ratio (w/c) improving workability without compromising mechanical strength and a reduced permeability.
- **hydration heat reduction:** SCMs can mitigate the heat generated during the hydration process, preventing thermal cracking.
- **alkali-silica reaction mitigation:** silica rich SCMs, such as fly ash or silica fume, can react with alkalis present in the cement, reducing the potential for alkali-silica-reaction, which can lead to expansion and cracking of the hardened paste over time.

- **sulfate resistance:** the addition of specific SCMs leads to the formation of stable compounds that resist the deleterious effects of sulfate ions. This is particularly important in environments where sulfates are present, e.g., oil or gas wells.

2.9.3 Cement degradation due to hydrogen

Analysing the cement sheath in a well is a vital aspect of assessing the integrity of the wellbore, taking into account potential deterioration from both mechanical and chemical perspectives [21,206]. Due to variations in gas volume and thermal expansion during underground hydrogen storage, mechanical degradation arises from exposure to severe loading conditions, such as pressure fluctuations [206]. The impact of chemical degradation depends on reactions like corrosion, leaching, and potential hydrogen-induced reduction of cement compounds, weakening its mechanical strength.

Understanding how hydrogen interacts with cement not just as pure gas but also in the presence of in-situ brine is crucial for evaluating cement degradation during UHS projects [207]. Despite its significance, there is a scarcity of experimental findings on cement degradation involving hydrogen. Some experiments suggest a reduction in the compressive strength of the cement sheath due to the development of hydrogen bubbles observed with a CT scan, initiated by the reductive dissolution of redox-sensitive minerals like hematite (Fe_2O_3) and the formation of mackinawite (FeS) [208]. These findings align with thermodynamic modelling indicating reductive dissolution of hematite and ettringite, leading to the formation of mackinawite (FeS) and magnetite (Fe_3O_4) (Figure 17) [33,39,40]. This indicates that cement degradation due to geochemical reactions with hydrogen is primarily linked to redox-sensitive phases within the cement sheath. However, their proportion in the phase composition of ordinary downhole cement is relatively small, raising questions about the severity of hydrogen-induced reductive dissolution and its impact on the cement sheath's integrity. Nevertheless, the accuracy of such thermodynamic models depends on the quality and availability of thermodynamic data and hence of the database used and justify the need for experimental verification such as done in this PhD thesis. Recent investigations indicate that the extent of hydrogen induced redox reactions in previous modelling studies (Figure 17) [39,40] might have been overestimated due to the use of non-modified thermodynamic databases [209,210]. Accurate and updated experimental data are crucial for refining existing thermodynamic databases, ensuring the reliability of predictions and models in this intricate field. Progress in this direction will significantly contribute to advancing our understanding of subsurface processes involving hydrogen and minerals [44]. Therefore, further research is urgently needed to comprehensively understand hydrogen-mineral interactions under in-situ conditions, and a holistic assessment of the issue, combining insights from thermodynamic modelling and experimental data, is essential.

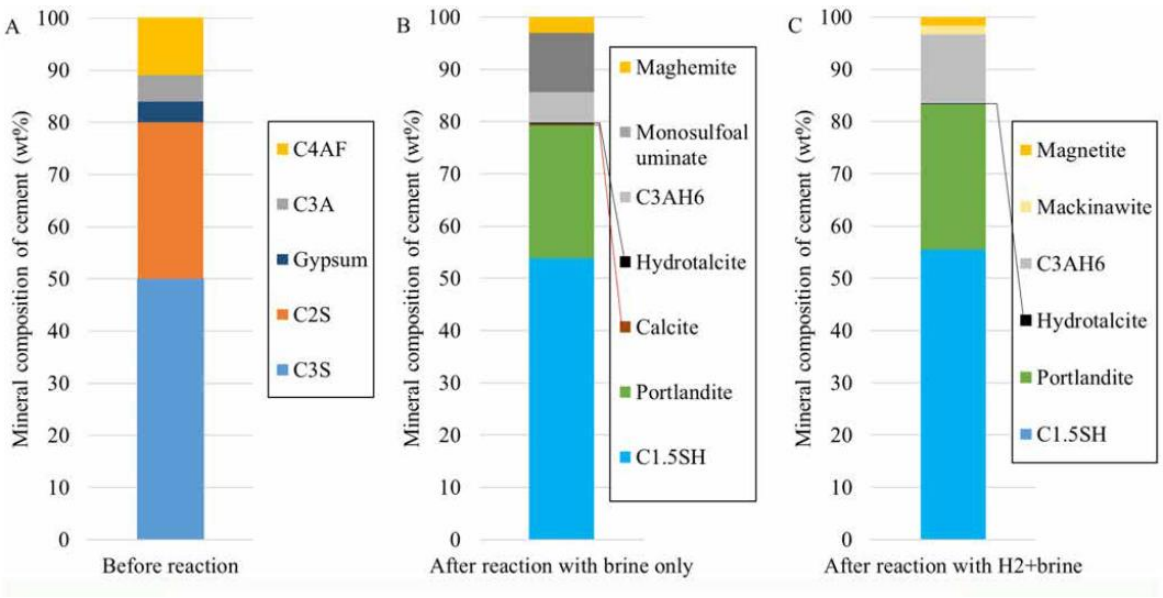

Figure 17: Thermodynamic modelling indicating hydrogen induced changes in the mineralogical phase composition of a modelled cement sheath caused by redox reactions, from [40]

3 Samples and Methods

3.1 Samples

For all experimental runs and investigations, a high sulfate resistant cement class G black label from Dyckerhoff with a gypsum and aluminate (C_3A) content < 3 mass% was used as base cement (see product data sheet Figure 19). All samples were mixed according to API Spec 10A with equipment complying the requirements stated in this specification [136]. All mixing was done in the cementing lab of the Chair of Drilling and Completion Engineering, Department Geoenergy, Montanuniversität Leoben (Figure 18). The exact slurry formulations of the individual investigations can be found in the method and sample section of each publication of this thesis (see Annex C). After mixing, the cement slurries were poured into cylindrical moulds with varying length and diameters made from brass or self-casted polyvinyl chloride (PVC) cylinders attached to a rubber base as moulds. For curing, the samples were placed in a water bath in a sealed container for 28 days at room temperature. After 28 days the cylinders were demoulded, and stored in a desiccator before the samples were further processed as needed for the follow-up investigations.

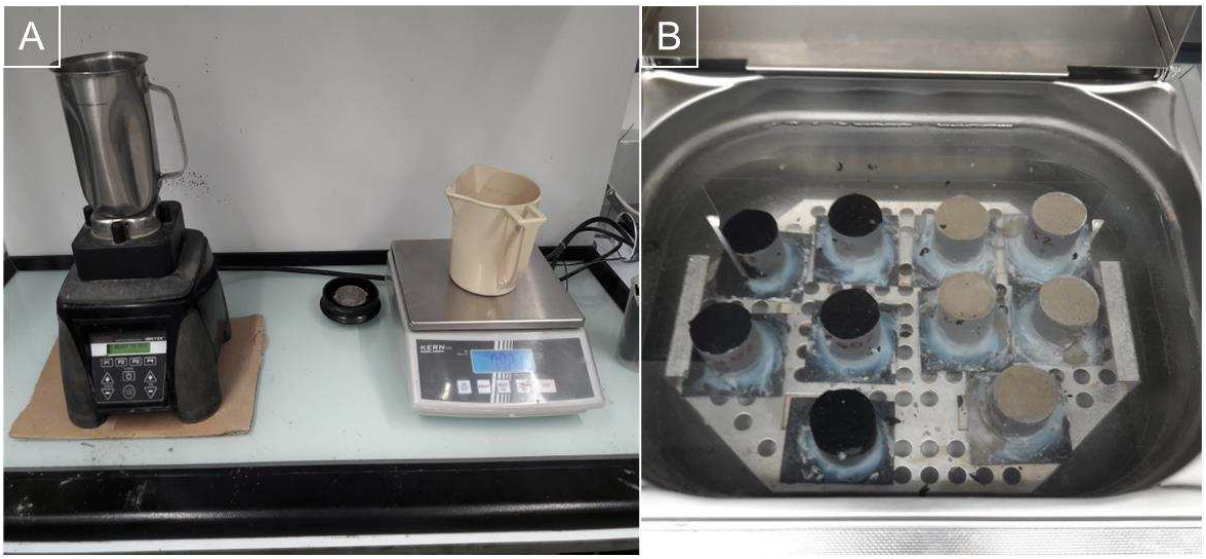

Figure 18: A: Mixing equipment in the cementing lab of the Chair of Drilling and Completion Engineering used for the mixing, B: curing of the cement samples investigated in this study.

All shipments from 01.01.2021 to 01.04.2021

Chemical composition:	Typical data	Specification API Spec 10A
MgO, %	**0,9**	≤ 6,0
SO3 , %	**2,7**	≤ 3,0
Loss on ignition, %	**1,4**	≤ 3,0
Insoluble residue, %	**0,56**	≤ 0,75
Tricalcium silicate (C3S), %	**51**	≥ 48 / ≤ 65
Tricalcium aluminate (C3A) , %	**2,5**	≤ 3
Since TM is 0,80 (> 0,64):		
(C4AF + 2 x C3A), %	**22,3**	≤ 24
Na2O-equivalent, %	**0,63**	≤ 0,75

Physical properties:

(44% BWOC mix water, neat)

Specific Surface Area (Blaine), m^2/kg	**323**	NR
Absolute grain density, g/cm^3	**3,18**	NR
Slurry density, kg/l	**1,91**	NR
Free Fluid, %	**1,9**	≤ 5,9
Compressive strength 8h/38°C, psi	**520**	≥ 300
Compressive strength 8h/60°C, psi	**2160**	≥ 1500

Thickening Time (TT), Neat

API Sch. 5 (Depth: 8.000ft, BHCT: 52°C)

Consistency after 30 min, Bc	**14**	≤ 30
Time to 30 Bc, min	**68**	≥ 30
Thickening time (Time to 100 Bc), min	**101**	≥ 90 / ≤ 120

Figure 19: Product data sheet with chemical and physical properties of the used cement class G from Dyckerhoff.

3.2 Experimental methods

In the following, all experimental methods, used for a detailed mechanical and physical characterization and exposure to various hydrogen containing environments of the investigated cement pastes are described. Obviously not all methods have been applied to the whole set of casted cement pastes, as they are very time consuming. Therefore, it is important to note that a more detailed description of the experimental procedures can be found in the sample and methods section of the journal publications related to this thesis (see Annex C).

3.2.1 Compressive strength

For investigating the uniaxial compressive strength, a Quasar 200 machine from Galdabini located at the Chair of Drilling and Completion Engineering, Montanuniversität Leoben was used. The mode of the measurement was axial displacement control (API RP 10B) with a speed of 0.5 mm/min until the samples failed. The load and deformation of the samples were recorded and converted into stress and strain. The stress/strain curve was displayed for evaluating the mechanical behaviour of the sample and for calculating Young´s modulus. The dimensions of the investigated samples were 2.54 cm in dimeter and 5.08 cm in length. The test procedure followed ASTM C39.

3.2.2 Tensile strength

For investigating the tensile strength, a Quasar 200 machine from Galdabini located at the Chair of Drilling and Completion Engineering, Montanuniversität Leoben was used according to ASTM C496. The mode of the measurement was axial displacement control (API RP 10B) with a speed of 0.5 mm/min until the samples failed. The load and deformation of the samples were recorded and converted into stress and strain. The dimensions of the samples were 5.08 cm in diameter and 2.54 cm in length.

3.2.3 N_2 sorption

Low pressure gas sorption experiments were executed with an Autosorb iQ3 gas sorption analyser from Anton Paar Quanta Tec located at the Chair of Physics, Montanuniversität Leoben, using N_2 of ultra-high purity (99.999%) as adsorbate. For this investigation first, a fine sample powder suitable for analytics had to be obtained. Before the actual measurement, 0.4 g of powdered sample were outgassed under vacuum (10^{-6} mbar) for 24 h at 40°C. N_2 adsorption/desorption isotherms were recorded at 77 K in a relative pressure (P/P_0) range from 10^{-3} to 0.99. Pore volume, pore size distribution from 3 nm to 100 nm, using Barrett-Joyner-Halenda (BJH) method and surface area using multi point Brunauer-Emmett-Teller (BET) method of the samples were obtained.

3.2.4 Permeability

N_2 gas permeability was determined of cylindrical samples with the dimensions of 2.54 cm in diameter and 5.08 cm in length at ambient temperature. A Gasperm Steady State Gas Permeameter from Vinci Technologies located at the Chair of Applied Geophysics,

Montanuniversität Leoben, was used with the low flow and high-pressure measurement condition and a radial confining pressure of 0.8 MPa. For each sample cylinder the N_2 gas flow was constantly increased manually until a constant flow was established. After achieving constant flow for the first time, the flow was then again increased for four more times, with recording the pressure every time the flow became constant again. Considering the non-Darcy flow in tight cement sheaths, the effect of gas slippage was accounted through Klinkenberg correction and permeability was calculated by the corresponding software from Vinci Technologies.

3.2.5 Hg-Porosimetry

Mercury Intrusion Porosimetry (MIP) measurements were conducted at the Chair of Geology, Friedrich-Alexander-Universität Erlangen. A Quantachrome Poremaster for Windows Data Report, version 8.00, was used. The mercury surface tension was 0.485 N/m and the contact angle to the pore surface 140°. Here, approximately 1.3 g of crushed and dried slices were placed in the sample chamber and analysed by increasing the pressure gradually up to a maximum pressure of 410 MPa. Using Washburn equation, the pore size distribution from pores in the size of mm down to 3 nm was obtained. Additionally, total porosity, density and surface area were recorded.

3.2.6 He-Pycnometry

He-Pycnometry was applied to measure skeletal density of the cement paste samples. Therefore, powders of the samples were measured with a helium Ultrapycnometer 1000 from Quantachrome located at the Chair of Physical Chemistry, Montanuniversität Leoben.

3.2.7 Autoclave experiments

To allow the exposure of the investigated cement pastes to hydrogen and hydrogen containing atmospheres autoclave experiments were conducted. The rationale of this autoclave experiments was to compare non-treated cement paste samples with those exposed to hydrogen and hydrogen containing atmospheres at well-defined p T conditions that enables the identification of potential hydrogen induced alteration. First, an experimental set was conducted at ambient T and elevated p under pure hydrogen atmosphere. In subsequent experimental runs also the influence of higher T and the presence of brines was evaluated. Even though the initial experimental conditions are not considered to be reflective for real in suite p & T conditions during UHS, it was still considered insightful for a better fundamental understanding of the so far poorly known system hydrogen – cement. For the later runs the p & T conditions were chosen to be reflective of UHS subsurface storage conditions; p of 80 bar and T up to 80°C, reflecting depth of ~ 2 km were applied. For ambient T, specific custom designed autoclaves with a diameter of ~ 3 cm and 20 cm length, e.g., a total volume of 141 mL, were used, for elevated T, autoclaves from Carl Roth of the type IV made of stainless steel of the grade V4A were used. The dimensions of this type were slightly larger with a diameter of ~ 4 cm and a length of ~ 30 cm with a total volume of 500 mL. For heating up, an appropriate heating device with incorporated T monitoring was used (Figure 20).

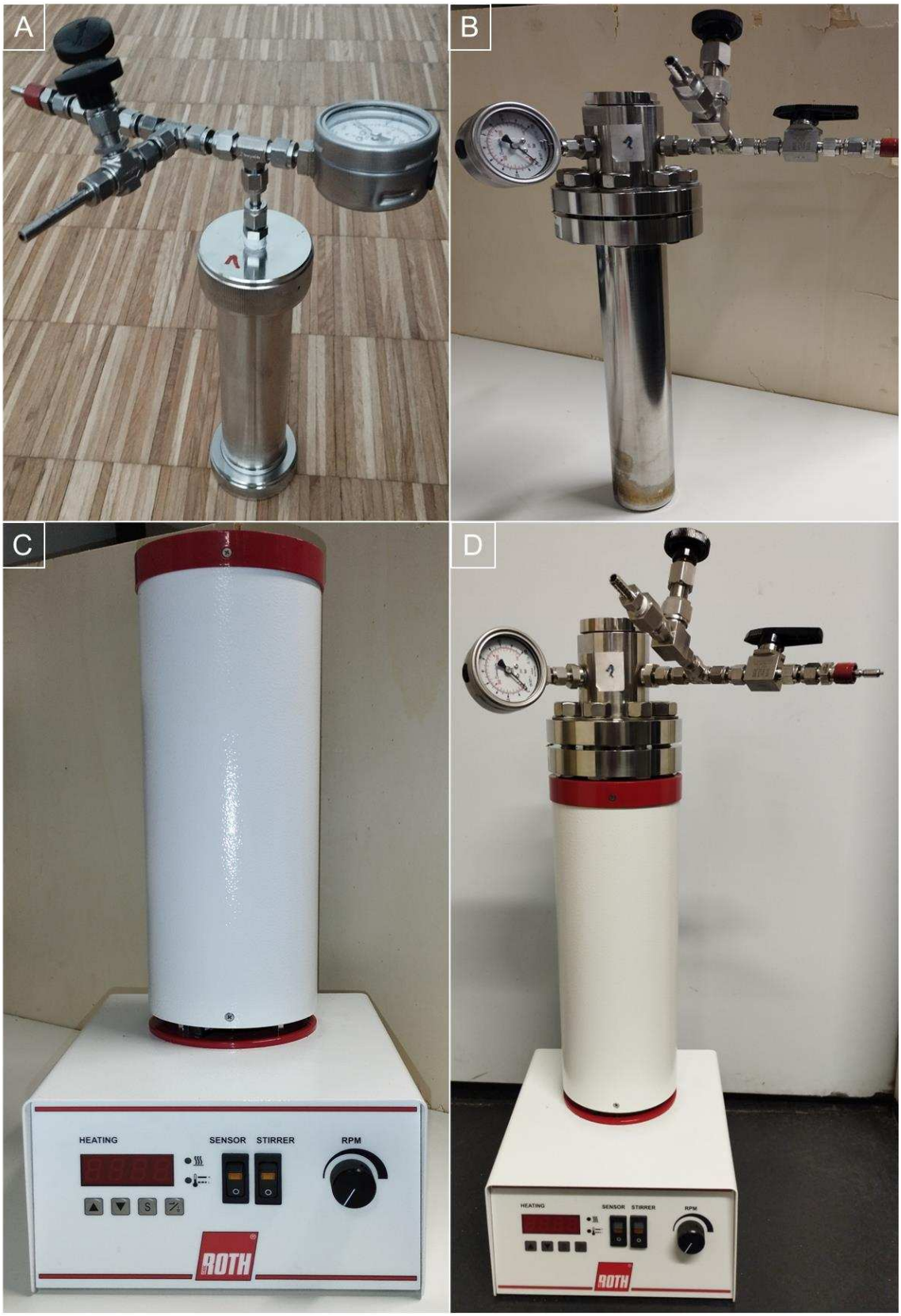

Figure 20: Autoclaves used within this study, A: custom designed autoclaves for ambient T experimental runs, B: Carl Roth type IV autoclave for elevated T experimental runs, C: corresponding heating system, D: Carl Roth type IV placed within the heating device

Since the conducted autoclave experiments take long time (several weeks to several months) and only a limited number of autoclaves were available, a precise planning and high organizational working was required. Therefore, the concept of design of experiments was implemented. Design of experiments (Doe) is the careful statistical planning of experiments that enables an efficient workflow guaranteeing usable results from experimental runs [43]. In this specific case, a distinction between so called “pre-defined parameters” and “factors” was done. The “pre-defined parameters” contained such things as the water to cement (w/c) ratio of the mixed slurry, the addition of supplementary cementitious materials (SCMs, e.g., silica fume, carbon black) to the slurry, as well as the obtained mechanical, physical, and mineralogical properties of the baseline samples. As “factors”, e.g., parameters of the experimental run that can be varied, T and p conditions of the autoclave experiments as well as the hydrogen containing atmosphere (dry or wet H2) were defined. This allows the observation of any changes of the “pre-defined parameters” in the system (e.g., every individual autoclave run) that can be related to a specific cause (e.g., factor) (Figure 21).

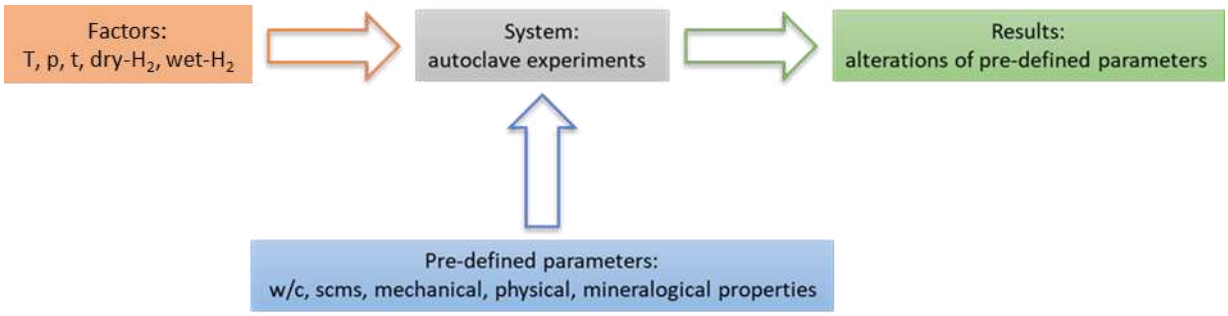

Figure 21: design of experiments approach for the systematic conduction of autoclave experiments; T = temperature, p = pressure, t = duration of the autoclave experiment, dry-H_2 = pure hydrogen atmosphere during the autoclave experiment, wett-H_2 = brine-hydrogen atmosphere during the autoclave experiment, c/w = water to cement ratio of the cement paste, scms = supplementary cementitious materials.

3.3 Analytical methods

In the following, all analytical methods, used for a detailed mineralogical characterization of the investigated cement pastes are described. Obviously not all methods have been applied to the whole set of casted cement pastes, as they are often expensive or very time consuming. A more detailed description of the experimental procedures can be found in the sample and methods section of the journal publications related to this thesis (see Annex C).

3.3.1 X-ray diffraction (XRD)

Powdered sample material was measured with a Panalytical XPert 3 Powder Diffractometer located at the Chair of Energy Geosciences, Montanuniversität Leoben, operating at 40 kV and 40 mA, using Cu Kα (1.5 Å) as radiation source at a step size of 0.004° per second in the 2θ range of 2.5° - 70°.

3.3.2 Field emission scanning electron microscope (FE-SEM)

A TESCAN CLARA field emission scanning electron microscope (FE-SEM) located at the Chair of Functional Materials and Materials Systems, Montanuniversität Leoben, equipped with the TESCAN Essence Image Snapper software, version 1.0.8.0, was used for capturing and stitching of high-resolution images. Both backscattered (BSE) and secondary (SE) electron images were obtained. The acceleration voltage was set at 10 kV and the beam current at 1 nA. To obtain a conducting surface and minimize charging effects, the samples were coated with gold using a Cressington Sputter Coater 108 Auto with 30 seconds sputtering time.

3.3.3 Electron probe micro analyser (EPMA)

A JEOL superprobe JXA 8200 located at the Chair of Resource Mineralogy, Montanuniversität Leoben, equipped with 5 spectrometers and a tungsten cathode was used. The acceleration voltage and beam current were set at 15 kV and 10 nA, respectively with a beam diameter of 1 µm. The polished samples were carbon coated with a 15 nm thin layer to ensure a conductive surface and allow wavelength dispersive spectrometry (WDS) analysis of the material. For every measurement, background correction and ZAF correction was applied and the detection limit (D.L.) for each measured element was calculated with equation 14 automatically by the software.

$$D.L. = z/m \sqrt{(2 * Ibg/tbg)} \qquad \text{(Equation 14)}$$

With z and m being factors for confidence levels and calculation in mass% respectively and Ibg and tbg being the intensity of the background in counts per second and the time of background counting.

3.3.4 Simultaneous thermal analysis (STA)

A combined measurement of thermogravimetry (TG) and differential scanning calorimetry (DSC) was carried out using a TG-DSC Apparatus STA 449 C from Netzsch located at the Chair of Process Technology and Industrial Environmental Protection, Montanuniversität Leoben. The samples were measured in powdered form. TG allows to measure changes of mass of a material during progressive heating as a function of temperature. Changes in mass are a result of degradation, removal of water (e.g., dehydration) and oxidation of components within the material. DSC is a thermo-analytical technique allowing to differentiate between exothermal and endothermal reactions recorded via TG.

3.3.5 Atomic force microscopy (AFM)

Atomic force microscopy uses a cantilever probe with a sharp tip that is moved across the sample to obtain a high-resolution three dimensional (3D) topographical information of the sample surface on the nanometre scale. The deflection of the cantilever during the contact with the specimen surface is recorded, and a topographical representation of the surface as z(xi, yj) = z(r) is generated. A AIST NT AFM system located at the Chair of Resource Mineralogy, Montanuniversität Leoben, was used in tapping mode and under ambient conditions. Nu Nano SCOUT probes were employed with nominal spring constant 42 N/m, resonant frequency ~350 kHz, and tip diameter < 20 nm.

3.4 Thermodynamic modelling with the freeware Gibbs Energy Minimization Selector (GEMS)

Thermodynamic modelling has proven to be a reliable and vital tool for the prediction of the mineralogical phase composition of hydrated cement paste [178,211]. However, an essential prerequisite to obtain reliable modelling results is the availability of accurate and complete thermodynamic databases as the thermodynamic data of the substances, phases and their (dissolved-) compounds, is the basis for the modelled occurrence of the individual mineralogical phases [212]. This is particularly important for phases such as AFm, or ettringite which can form solid solutions. The occurrence of solid solutions leads to different solubility products of the phase dependent on its exact chemical composition. Therefore, it is of outmost importance to have accurate thermodynamic data available when performing such modelling on particularly cementitious materials. When coupled with experimental investigations, insight from thermodynamic modelling can be a good first estimate for the evaluation of the experimental results.

In this study the freeware GEMS v.3 [213] with the cemdat18 database [212] was used. GEMS is a geochemical modelling code which computes phase assemblages and speciation in a complex chemical system from its total bulk elemental composition assuming thermodynamic equilibrium [212]. First, the initial hydrated composition was modelled for an ordinary Portland cement followed by the addition of hydrogen to the system. In GEMS the chemical interactions between the solids, solid solutions, and aqueous electrolyte are considered simultaneously and the speciation of the dissolved species as well as the kind and amount of stable solid phases are calculated based on their thermodynamic data. This allows the prediction of the composition of solid solutions and the coexisting liquid phase based on the bulk chemical composition, a feature only available in GEMS [211]. For the required chemical input information, average chemical bulk composition of Portland cement was assumed [150].

4 Results

4.1 Summary publication 1

***Thomas Sammer**, Xiangyun Shi, Muhammad Zubair Khan, Aleksandar Matkovic, Christian Teichert, Johann G. Raith, 2024, Influence of broad ion beam polishing on the surface roughness of hydrated cement paste and its implications on microstructural analysis, Cement and Concrete Research, Volume 182;*
published 2nd June 2024, DOI: 10.1016/j.cemconres.2024.107555.

This publication [214] presents results of WP 1 and deals with research question 1 focusing on advancements in the preparation techniques for high-resolution SEMs. With recent improvements in SEM technology, it is crucial to enhance preparation methods to fully exploit their capabilities, particularly in preserving nanometre-sized structural features. The study compares state-of-the-art resin-embedded polishing with a novel Broad Ion Beam (BIB) milling technique for hydrated cement paste. SEM investigations are aided by image processing to analyse porosity and pore geometry, along with a comprehensive quantitative analysis of surface roughness based on AFM scans. BIB milling allows for detailed examination of nano structural features like gel porosity and the acicular morphology of C-S-H, which are challenging to observe in resin embedded material. Additionally, BIB milling provides enhanced visualization of pore shapes and edges, making subsequent image processing and analysis easier compared to resin embedding, which often presents difficulties due to resin presence. Segmented pores from BIB SEM images exhibit higher aspect ratios compared to resin-embedded samples, where circularity of pores seems to be an artifact. However, BIB milling preparation may introduce cracks due to the brittle nature of hydrated cement paste, potentially biasing results. Surface roughness analysis shows that conventional polishing results in a smoother vertical surface compared to BIB milling, but BIB milling introduces higher lateral fluctuations. The study concludes that while BIB milling has advantages for enhancing microstructural investigations, it also has drawbacks such as potential sample cracking, emphasizing the need to carefully consider the method's suitability for specific research goals.

Contribution of the doctoral candidate: Conceptualization, methodology, resources, investigation, writing-original draft. The doctoral candidate casted the samples and conducted the sample preparation as well as the SEM investigations. He took part in the evaluation and interpretation of the AFM and image processing steps and linked the findings to each other. As the first and corresponding author, the doctoral candidate prepared the initial draft and final version of the paper and took care of the review process.

4.2 Summary publication 2

Thomas Sammer, *Arash Nasiri, Nikolaos Kostoglou, Krishna Ravi, Johann G. Raith, 2024, Insight into carbon black and silica fume as cement additives for geoenergy wells: linking mineralogy to mechanical and physical properties, C – Journal of Carbon Research, 10, 71;* **published 8th August 2024, DOI:10.3390/c10030071.**

This publication [215] presents results of work packages 1 and 2 and deals with research question 2, focusing on the mineralogical, mechanical, and physical properties of cement sheaths used in the geoenergy sector. It examines how the additives carbon black and silica fume influence these properties.

The study compares four samples of class G cement with formulations containing carbon black or silica fume, aiming to optimize performance. The addition of these additives notably alters the microstructure and affects modal and chemical phase composition. Silica fume, for instance, increases the C-S-H content while decreasing the portlandite content. EPMA measurements reveal increased sulphur integration into the C-S-H phase and a lowered Ca/Si ratio. Additionally, addition of silica fume results in a much denser and more granular microstructure of the C-S-H matrix with supressed formation of phases with acicular morphology. Moreover, the mechanical strength increased but also a more brittle behaviour of the cement sheath was observed. Conversely, adding carbon black increases the Ca/Si ratio, stabilizing low-density C-S-H phases, and alters mechanical properties in a way that could benefit cement sheaths in resisting lateral stress. Adjusting the water-to-cement ratio does not visibly affect the microstructure but does reduce porosity and enhance mechanical strength. These findings underscore the complexity of cement sheaths and emphasize the necessity of a comprehensive, interdisciplinary approach incorporating mineralogical methods for their evaluation.

Contribution of the doctoral candidate: Conceptualization, methodology, resources, investigation, writing-original draft. The doctoral candidate conducted the experiments, took part in the evaluation and interpretation, and linked the findings of the different methods to each other. As the first and corresponding author, the doctoral candidate prepared the initial draft and the final version of the paper and took care of the review process.

4.3 Summary publication 3

***Thomas Sammer**, Nikolaos Kostoglou, Krishna Ravi & Johann Raith, 2024, Hydrogen induced changes in the phase composition and micro-structure of downhole cements: fundamental research within the context of underground hydrogen storage, International Journal of Hydrogen Energy, Volume 89,*
published 4th November 2024, DOI: 10.1016/j.ijhydene.2024.09.449

This publication [216] presents the results of work packages 4 and 5 and deals with research question 3, focusing on underground hydrogen storage and its potential for enhancing renewable energy efficiency and overcoming seasonal limitations. While underground hydrogen storage holds promise, research must address not only the integrity of reservoir and cap rocks but also the interaction of hydrogen with the cement sheath in borehole annular spaces to ensure feasibility and safety. However, there is a notable knowledge gap regarding the potential deteriorating effects of hydrogen on the cement sheath and subsequently on well integrity. The study conducts hydrothermal autoclave experiments to assess changes in the mineralogical composition of hydrated class G cement exposed to various hydrogen-containing environments and how these changes affect cement properties. X-ray diffraction and scanning electron microscopy, along with nitrogen adsorption/desorption experiments, are employed. The results show minor mineralogical changes, such as monosulfate decomposition and ettringite formation, with negligible alterations in pore structure observed through nitrogen adsorption/desorption. This suggests that hydrogen exposure does not significantly impact the mineralogical composition or pore structure of the cement sheath, with other factors like temperature and brine presence likely exerting a more significant influence. However, these conclusions are specific to the low permeable class G cement tested within this study under the experimental conditions.

Contribution of the doctoral candidate: Conceptualization, methodology, resources, investigation, writing-original draft. The doctoral candidate casted the samples, conducted the autoclave experiments and the mineralogical investigations. He took part in the evaluation and interpretation of the nitrogen sorption experiments and linked the findings of the different methods to each other. As the first and corresponding author, the doctoral candidate prepared the initial draft and the final version of the paper and took care of the review process.

4.4 Thermodynamic modelling with GEMS

Figure 22 presents the results of the thermodynamic modelling carried out in work package 3 of this study using the GEMS software with the cemdat18 database. The modelling indicates that certain redox-sensitive phases within hardened downhole cement are susceptible to hydrogen alteration caused by the strong reducing character of hydrogen. Especially ferric iron and sulfate bearing phases like brownmillerite, monosulfoaluminate (AFm) and ettringite (AFt) are altered, resulting in the formation of magnetite and iron sulphides (e.g., troilite, FeS). Also, the C-S-H content is increased while the portlandite content shows only minor changes. The porosity is also slightly increased. The increase in porosity can be explained by higher densities of the newly developed phases (5.2 g/cm³ for magnetite, 4.8 g/cm³ for troilite) compared to the smaller densities of ettringite or AFm (both < 2g/cm³). An increase in porosity could indicate deteriorated mechanical and physical integrity of the cement sheath since higher porosity values could lead to higher permeability, meaning that the cement sheath can no longer ensure tightness of the well. In general rock mechanical terms, higher porosity often also means less mechanical strength.

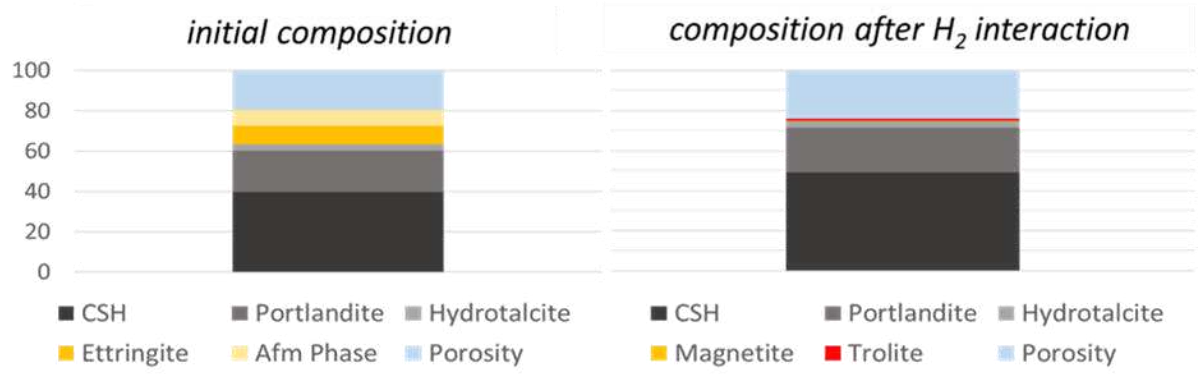

CSH	39.74	CSH	49.1
Portlandite	20.4	Portlandite	22.3
Hydrotalcite	3.31	Hydrotalcite	3.3
Ettringite	9.14	Magnetite	0.3
AFm	7.81	Troilite	0.7
Porosity	19.6	Porosity	24.3
	100		100

Figure 22: Results (%) of thermodynamic modelling using the software GEMS and cemdat18 database.

4.5 List of conference contributions related to this thesis.

Sammer, T., 2022, A fundamentals investigation of underground hydrogen storage with emphasis on the interactions between hydrogen and downhole cement. 1st Symposium on H_2 and C Initiative of the Rectorate of Montanuniversität Leoben (Oral Presentation), Leoben, Austria, 27th of June 2022.

Sammer, T., Nasiri, A., Feichter, M. & Ravi, K., 2022, Tackling challenges concerning the integrity of downhole cement/rock during underground gas storage: an interdisciplinary approach. Pangeo Austria (Poster presentation), Leoben, Austria, 10th to 13th of September 2022.

Sammer, T., Ravi, K. & Raith, J., 2022, A fundamentals mineralogical investigation of downhole cements within the context of underground hydrogen storage. Pangeo Austria (Oral Presentation), Leoben, Austria, 10th to 13th of September 2022.

Sammer, T., 2022, Effect of Hydrogen on Downhole Cements. Well Integrity Workshop of the Well Integrity Platform of the Drilling and Completion Engineering Chair (Poster & Oral Presentation), Leoben, Austria, 18th to 20th of October 2022.

Sammer, T., 2023, A fundamentals mineralogical investigation of downhole cements within the context of underground hydrogen storage. 2nd Symposium on H_2 and C Initiative of the Rectorate of Montanuniversität Leoben (Poster Presentation), Leoben, Austria, 10th and 11th of July 2023.

Sammer, T., Ravi, K. & Raith, J., 2023, A fundamentals mineralogical investigation of downhole cements within the context of underground hydrogen storage. Goldschmidt 2023 Conference (Poster Presentation), Lyon, France, 9th to 14th of July 2023.

Sammer, T., Ravi, K. & Raith, J., 2023, Hydrogen induced changes in the mineralogical phase composition of downhole cements: fundamental research within the context of underground hydrogen storage. MinWien (Oral Presentation), Vienna, Austria, 17th to 21st of September 2023.

Sammer, T., 2024 Hydrogen induced changes in the phase composition and micro-structure of downhole cements: fundamental research within the context of underground hydrogen storage. 4th annual Well Integrity Workshop of the Well Integrity Platform of the Drilling and Completion Engineering Chair (Poster Presentation), Leoben, Austria, 23rd to 25th of April 2024.

Selected posters related to this thesis are shown in annex B.

5 Conclusion and outlook

To reduce anthropogenic carbon emissions and alleviate global warming while meeting the global energy demand, fossil fuels need to be successively replaced by renewable energy sources. However, the generated capacity of renewable energy sources such as wind or solar is either seasonal or affected by weather fluctuations, hindering their efficiency. To overcome this limitations hydrogen is considered a promising and sustainable storage medium for excess energy produced by renewables. Large scale underground hydrogen storage (UHS) is considered a safe and economic storage option to really replace fossil fuels enabling seasonal balance of supply and demand. Currently, there is only a small number of operating UHS sites, limiting experience and understanding of UHS, impeding the successful industrial implementation on a large-scale. Storage integrity for both the reservoir but also the downhole infrastructure is one of the main concerns in UHS. These concerns are associated with geochemical reactions, including the role of dissolution/precipitation of sensitive minerals. Especially hydrogen induced cement degradation would lead to an unstable wellbore endangering an environmentally friendly, safe, and economic UHS operation. Compared to other commonly stored gases such as N_2, CO_2 or CH_4, hydrogen is a strong reducing agent that can transfer electrons to other ions, triggering redox reactions of sensitive minerals in the downhole cement sheath. However, based on the results of thermodynamic models, the degree of hydrogen induced cement degradation is minor. To fully evaluate the feasibility of UHS, it is essential that the results of thermodynamic modelling are confirmed by experimental findings as well. This PhD thesis aims to contribute to better understand fundamental questions regarding the mineralogy of downhole cement under the influence hydrogen. Therefore, autoclave experiments supported by mineralogical investigations were carried out. Within the scope of this thesis three research questions were formulated and set to be answered.

Research question 1:

How can the sample preparation of hydrated cement pastes be advanced for microstructural investigations to fully utilize the potential of mineralogical methods for a holistic evaluation of cement sheaths?

Evaluating the mineralogical properties of hydrated cement pastes, e.g., cement sheath in boreholes, contributes to a holistic and comprehensive investigation of the fundamental processes of various influences that might act on the cement sheath. However, due to the small and often amorphous character of the most prevalent phases in hydrated cement pastes, the application of mineralogical methods is challenging. A very common and established method for the mineralogical evaluation of cements is scanning electron microscopy. Usually, fractured, or polished surfaces are investigated. However, due to the rough surface characteristics of fractured surfaces only secondary electron imaging is feasible limiting

conclusions to morphological features only. Also, fractured surfaces are considered non-representative since cracks propagate through the weakest portion of the material. Polished sample surfaces on the other hand, however, allow the collection of electron back scatter diffraction patterns, chemical analysis through EDS or WDS, as well as image analysis providing valuable information about porosity or pore size distribution. Therefore, it is crucial that also the preparation techniques are improved since defects in polishing can result in misconceptions during microstructural studies. This is even more important since the technical capabilities of modern high-resolution SEM instruments equipped with a field emission gun improved significantly over the last decade, now allowing a more detailed study of even nanometre scale features. Hence, in publication 1 state-of-the-art resin-embedded polishing of hydrated cement paste was compared with a novel Broad Ion Beam (BIB) -milling process. For quantitative comparison, microstructural investigations carried out by SEM enhanced with image processing were employed to determine key parameters such as porosity, pore size distribution, pore circularity and aspect ratio. Furthermore, the resulting surface roughness of both polishing techniques was evaluated by a comprehensive surface roughness analysis applying height-difference function and height-height-correlation function analysis on AFM surface scans. The BIB-milled sample facilitated the detailed study of nano-microstructural features such as gel porosity and the acicular morphology of C-S-H, a level of detail not achievable in the resin-embedded sample. Furthermore, the BIB-milled sample exhibited enhanced visualization of pore shapes and edges, making SEM images easier to process in subsequent image processing and analysis. In contrast, the resin-embedded, conventionally polished sample presented very low porosity values, making it challenging for image processing. This was mainly caused by the presence of resin causing difficulties in the segmentation of pore space and masking the true shape of the pores. This emphasizes the necessity and advantages of a resin free polishing process. However, the surface roughness analysis applied on AFM scans revealed that conventional polishing leads to an overall much smoother vertical surface roughness (156 nm) compared to BIB-milling (388 nm). The level of lateral fluctuations indicated by the lateral correlation lengths is also increased by the BIB-milled method (e.g., 1.47 compared to 2.12 µm). The jaggedness of the conventionally polished surface, indicated by the roughness parameter α is only slightly decreased when changing from conventional polishing to BIB-milling.

The findings of publication 1 highlight the advantages and drawbacks of BIB-milling as an advanced sample preparation method for SEM microstructural investigations, compared to the resin-embedded, conventional polishing approach. The findings also point out that advanced polishing techniques for cementitious materials still need to be further developed in the future and they emphasize an imperative need for an improved, resin free polishing technique for cementitious materials.

Research question 2:

What is the influence of certain additives added during the slurry mixing process on the mineralogical, mechanical, and physical properties of the hydrated cement paste and how can this be beneficial during UHS?

The geoenergy industry has high demands on cements used for the cement sheath, be it for oil, gas, geothermal or UHS wells. Once the cement slurry is placed in the annular space, the hardened cement sheath must be mechanically durable while also being very low permeable. Therefore, to enhance the performance of downhole cements, SCMs are often added to the slurry mixture to tailor specific properties. The underlying process for the improvement of physical and mechanical properties is often caused by a change in the mineralogical phase composition of the downhole cement. To fundamentally understand the effect certain additives have it is important to apply mineralogical investigations for a comprehensive evaluation. Therefore, in the study of publication 2, the influence of silica fume as a common additive and carbon black as an innovative additive on mineralogical, physical, and mechanical characteristics of cement class G was evaluated. The aim was to provide a better and holistic understanding of how changes in the mineralogical phase composition can be related to improvements of physical and mechanical properties.

Adding silica fume increases the content of C-S-H phases and reduces the portlandite content. The disappearance of the specific AFm sulfate phase indicate minor changes in the mineralogical phase composition. Due to the small particle size and high surface area of silica fume the hydration kinetics of the cement paste are enhanced at early age, promoting C-S-H nucleation. Also, the rate of capillary water consumption is increased, affecting the hydration process of the C-S-H due to the lack of water filled space for C-S-H growth, promoting the development of granular C-S-H. Similar observations can be made for the microstructure of samples containing carbon black. Although, carbon black is assumed to be chemically inert it might physically block the free water filled space, preventing the growth of needle like C-S-H microstructure, and reducing porosity. Mineral chemical analysis showed that the Ca/Si ratio of the C-S-H matrix decreased due to the addition of silica fume. Moreover, the study shows that silica fume causes higher C-S-H content leading to increased mechanical strength, increased bulk density and reduced porosity. The addition of carbon black results in a higher Ca/Si ratio of the C-S-H phase indicating the prolonged stability of low-density C-S-H phases. Also, UCS and Young's modulus decreased but tensile strength increased. For the geoenergy industry, this is highly valuable as a cement sheath that is less brittle is more resistant to withstand lateral forces within the well. Both additives also reduced porosity and indicated a reduction of matrix permeability, which are crucial physical parameters of a downhole cement sheath to ensure tightness during any storage or production process. The findings of publication 2 highlight the complexity of the interplay of various properties of cement sheaths and their characterisation. Only a holistic and interdisciplinary approach with application of a wide spectrum of different methods can lead to reasonable interpretation and fundamental understanding of the results.

Research question 3:

What is the influence of hydrogen on the mineralogical phase composition of downhole cement and subsequently on its integrity? What potential hydrogen induced geochemical reactions are likely to occur?

To enable UHS in the foreseeable future, still technical and scientific challenges need to be overcome. Fundamental research must focus on the integrity of the reservoir and cap rocks but also on the cement sheath applied in the annular space of boreholes upon interaction with hydrogen. Especially, the evaluation of the cement sheath is important as there is still a severe knowledge gap regarding the possible deteriorating effect of hydrogen. This is particularly important as the cement sheath acts as a key part for well integrity ensuring a safe, economically, and environmentally friendly storage and production process of any gases stored underground.

Various studies published in recent years applying thermodynamic modelling suggest low reactivity of downhole cement with hydrogen gas. However, the strong reducing character of hydrogen has the potential to trigger redox reactions of sulfate and Fe^{3+} bearing phases, leading to minor changes in the mineralogical phase composition. Thermodynamic models are strongly dependent on the quality of the databases used and only simulate the situation in thermodynamic equilibrium. Therefore, modelling results need to be verified with experimental findings. Within the scope of this thesis, autoclave experiments on a lab scale were conducted to evaluate the deteriorating influence that hydrogen has on the cement sheath.

In the results published in publication 3, hydrogen exposed cement samples were evaluated regarding 1) changes in the mineralogical phase composition and 2) the influence of changes in the phase composition on the physical properties of the cement.

XRD analysis revealed some minor changes in the phase composition by decomposition of the AFm phase and the formation of ettringite. In experimental runs done at 80 °C ettringite was absent due to its thermal decomposition at higher temperatures and a hemi-carbonate phase was observed instead. In experimental runs involving an autoclave atmosphere of a hydrogen – brine mixture, hexagonal, platy crystals of a chlorine bearing Ca-Al-hydrate formed. However, their formation is attributed to solubility-precipitation processes and not caused by hydrogen.

For the evaluation of physical properties, nitrogen adsorption/desorption measurements @ 77K were carried out to identify potential changes in porosity, pore size distribution and pore structure. No hydrogen induced alteration of physical properties was observed.

In summary, the findings of publication 3 confirm that the exposure of hydrated cement pastes to hydrogen does not lead to substantial changes in the mineralogical phase composition and results in unaltered physical properties. Redox reactions, caused by the strong reducing character of hydrogen, that were predicted by various studies performing thermodynamic modelling, leading to at least minor changes in the phase composition were not observed during this study. This emphasizes the relative unreactive nature of downhole cements against hydrogen allowing the assumption that also the mechanical properties of the cement should remain unchanged. However, these findings are only valid for the investigated cement mixture

and the evaluated experimental conditions. Further research needs to consider long term hydrogen exposure, different slurry formulations and elevated curing conditions of the cement. Furthermore, considering the accuracy of thermodynamic models, the existing geochemical database needs to be updated by e.g., calibrating the equilibrium constant or the reaction enthalpy.

The findings of this doctoral thesis emphasize that mineralogical methods are a powerful tool and enable a holistic evaluation of downhole cements used for the cement sheath in boreholes. The presented mineralogical approach enables a better understanding of the fundamental interplay of mechanical, physical, and mineralogical properties of the cement sheath. Alongside the contribution of the advancement of sample preparation to enable the full potential of mineralogical tools (e.g., SEM) and the evaluation of tailoring certain properties of the cement sheath by adding SCMs, especially the experimental work investigating the integrity of downhole cements against hydrogen for UHS applications is of great practical and industrial relevance. This is particularly important as the findings contribute significantly to overcome the existing knowledge gap regarding the alteration potential hydrogen has on the cement sheath. Such fundamental research is an underlying part for enabling large scale hydrogen storage contributing to the successful transition to a climate neutral energy future.

6 Directories

6.1 List of abbreviations

$	Sulphur in chemical cement notation
%	Percent
°C	Degree Celsius
µm	Micrometre
3D	Three dimensional
A	Ampere
AFM	Atomic Force Microscopy
API	American Petroleum Institute
ASTM	American society for Testing and Materials
bar	Bar (unit for pressure)
BET	Brunauer-Emmett-Teller
BIB	Broad Ion Beam
BJH	Barrett-Joyner-Halenda
Cc	Carbonate
cm	Centimetre
CT	Computer Tomography
D.L.	Detection Limit
DHSV	Down hole safety valve
Doe	Design of experiment
DOI	Digital Object Identifier
DSC	Differential scanning calorimetry
e.g.	Exempli gratia
EPMA	Electron probe micro analysis
FE-SEM	Field emission scanning electron microscopy
g	Gramm
G	Giga
GEMS	Gibbs energy minimization selector
HD	High density
IGP	Intraglobular pores
ISO	International Organisation for standardization
J	Joule
K	kelvin
kg	Kilogram
kHz	Kilo hertz

km	Kilometre
L	Litre
LD	Low density
LGP	Large gel pores
LLNL	Lawrence Livermore National Laboratory
m	Metre
M	Mega
M1	Monoclinic
m²	Square metre
m³	Cubic metre
mass%	Mass percent
mbar	Milli bar
min	Minute
MIP	Mercury intrusion porosimetry
mL	Millilitre
mm	Milli metre
mol	Mole
N	Newton
n.A.	Not available
nA	Nano Ampere
nm	Nanometre
NORSOK	Norwegian shelf´s competitive position
p	Pressure
Pa	Pascal
P_c	Capillary pressure
pE	Value for electron concentration
PEM	Proton exchange membrane
pH	*pondus hydrogenii*
PhD	Philosophiae doctor
P_n	Pressure non wetting fluid
ppm	Parts per million
PVC	Polyvinylchlorid
P_w	Pressure wetting fluid
R	Rhombohedral
s	Second
SANS	Small Angle Neutron Scattering
SCMs	Supplementary cementing materials
SCoReA$^+$	Strategic Core Research Area Hydrogen & Carbon
SEM	Scanning Electron Microscopy
SGP	Small gel pores
SOEC	Solid Oxide Electrolyser Cell

Spec	Specification
SSA	Specific Surface Area
STA	Simultaneous Thermal Analysis
T	Temperature
T1	triclinic
TEM	Transmission electron microscopy
TG	Thermal gravimetry
TRL	Technology readiness level
UHS	Underground hydrogen storage
USA	United States of America
V	Volt
w	Water
w/c	Water to cement ratio
WDS	Wavelength dispersive spectroscopy
WP	Work package
wt%	Weight percent
XRD	X-ray diffraction
ZAF	Atomic number,- absorption,- excitation- effect
α	Alpha
β	Beta
γ	Gamma
ΔH	Enthalpy change

6.2 List of phases/minerals

AFm	$Ca_4Al_2(SO_4)(OH)_{12}*5.5H_2O$ (=Monosulfate)
AFt	$Ca_6Al_2(SO_4)_3(OH)_{12}*26H_2O$ (=Ettringite)
Alite	Ca_3SiO_5
Aluminate	$Ca_3Al_2O_6$
Anglesite	$PbSO_4$
Anhydrite	$CaSO_4$
Baryte	$BaSO_4$
Belite	β-Ca_2SiO_4
Brownmillerite	$Ca_4Al_2Fe_2O_{10}$ (=Ferrite)
C_2S	β-Ca_2SiO_4 (=Belite in cement notation)
C_3A	$Ca_3Al_2O_6$ (=Aluminate in cement notation)
C_3S	Ca_3SiO_5 (=Alite in cement notation)
C_4AF	$Ca_4Al_2Fe_2O_{10}$ (=Ferrite in cement notation)
C-A-H	$Ca_5Al_6O_{16}(OH)_{12}*4H_2O$
Calcite	$CaCO_3$
celestite	$SrSO_4$
Celite	$Ca_3Al_2O_6$ (=Aluminate)
C-S-H	$Ca_5Si_6O_{16}(OH)_{12}*4H_2O$
Dolomite	$CaMg(CO_3)_2$
Ettringite	$Ca_6Al_2(SO_4)_3(OH)_{12}*26H_2O$
Ferrite	$Ca_4Al_2Fe_2O_{10}$
Free lime	CaO
Goethite	$FeO(OH)$
Gypsum	$CaSO_4{:}2H_2O$
Harturite	Ca_3SiO_5 (=Alite)
Hematite	Fe_2O_3
Hemicarbonate	$Ca_4Al_2(CO_3)_{0.5}(OH)_{13}*5.5H_2O$
Hydrogarnet	$Ca_3Al_2O_6*6H_2O$
Hydrotalcite	$Mg_6Al_2(CO_3)(OH)_{16}*4H_2O$
Illite	$(K,H_2O)Al_2(Si_3Al)O_{10}(H_2O,OH)_2$
Kaolinite	$Al_2Si_2O_5(OH)_4$
Katoite	$Ca_3Al_2O_6*6H_2O$ (=Hydrogarnet)
Kuzelite	$Ca_4Al_2(SO_4)(OH)_{12}*5.5H_2O$ (=AFm / Monosulfate)
Larnite	β-Ca_2SiO_4 (=Belite)
Mackinawite	$(Fe,Ni)_9S_8$
Magnetite	Fe_3O_4
Monocarbonate	$Ca_4Al_2(CO_3)(OH)_{12}*5H_2O$
Monosulfate	$Ca_4Al_2(SO_4)(OH)_{12}*5.5H_2O$

Periclase	MgO
Portlandite	$Ca(OH)_2$
Pyrite	FeS_2
Pyrrhotite	$Fe_{1-x}S$
Tobermornite	$Ca_5Si_6O_{16}(OH)_{12}*4H_2O$ (=C-S-H)
Troilite	FeS

6.3 List of chemical elements and compounds

Al	Aluminium
B	Boron
Ba	Barium
C	Carbon
Ca	Calcium
CH_4	Methane
Cl	Chlorine
CO	Carbon monoxide
CO_2	Carbon dioxide
CO_3^{2-}	Carbonate ion
e^-	Electron
Fe	Iron
Fe^{2+}	Ferrous iron
Fe^{3+}	Ferric iron
H	Hydrogen
H_2	Molecular hydrogen gas
H_2O	Water
HCO_3^-	Hydrogen carbonate
He	Helium
Hg	Mercury
K	Potassium
KOH	Potassium hydroxide
Li	Lithium
Mg	Magnesium
Mn	Manganese
N	Nitrogen
N_2	Molecular nitrogen gas
Na	Sodium
NaCl	Sodium chloride, halite
Ni	Nickel
O	Oxygen
O_2	Molecular oxygen gas
OH^-	Hydroxide ion
P	Phosphorus
PO_4^{3-}	Phosphate
S	Sulphur
S^{2-}	Sulphide
Si	Silicon

SiO_4^{4-}	Silicate tetrahedron
$SO4^{2-}$	Sulfate
Zn	Zinc

6.4 Tables

6.5 Figures

6.6 Equations

7 References

[1] European green deal: Delivering on our targets, Publications Office of the European Union, Luxembourg, 2021.

[2] J.H. Williams, R.A. Jones, B. Haley, G. Kwok, J. Hargreaves, J. Farbes, M.S. Torn, Carbon-Neutral Pathways for the United States, AGU Advances 2 (2021).

[3] L. Wen, Z. Li, Provincial-level industrial CO_2 emission drivers and emission reduction strategies in China: Combining two-layer LMDI method with spectral clustering, The Science of the total environment 700 (2020) 134374.

[4] H. Lee, K. Calvin, D. Dasgupta, G. Krinner, A. Mukherji, P.W. Thorne, C. Trisos, J. Romero, P. Aldunce, K. Barrett, G. Blanco, W.W. Cheung, S. Connors, F. Denton, A. Diongue-Niang, D. Dodman, M. Garschagen, O. Geden, B. Hayward, C. Jones, F. Jotzo, T. Krug, R. Lasco, Y.-Y. Lee, V. Masson-Delmotte, M. Meinshausen, K. Mintenbeck, A. Mokssit, F.E. Otto, M. Pathak, A. Pirani, E. Poloczanska, H.-O. Pörtner, A. Revi, D.C. Roberts, J. Roy, A.C. Ruane, J. Skea, P.R. Shukla, R. Slade, A. Slangen, Y. Sokona, A.A. Sörensson, M. Tignor, D. van Vuuren, Y.-M. Wei, H. Winkler, P. Zhai, Z. Zommers, J.-C. Hourcade, F.X. Johnson, S. Pachauri, N.P. Simpson, C. Singh, A. Thomas, E. Totin, P. Arias, M. Bustamante, I. Elgizouli, G. Flato, M. Howden, C. Méndez-Vallejo, J.J. Pereira, R. Pichs-Madruga, S.K. Rose, Y. Saheb, R. Sánchez Rodríguez, D. Ürge-Vorsatz, C. Xiao, N. Yassaa, A. Alegría, K. Armour, B. Bednar-Friedl, K. Blok, G. Cissé, F. Dentener, S. Eriksen, E. Fischer, G. Garner, C. Guivarch, M. Haasnoot, G. Hansen, M. Hauser, E. Hawkins, T. Hermans, R. Kopp, N. Leprince-Ringuet, J. Lewis, D. Ley, C. Ludden, L. Niamir, Z. Nicholls, S. Some, S. Szopa, B. Trewin, K.-I. van der Wijst, G. Winter, M. Witting, A. Birt, M. Ha, J. Kim, E.F. Haites, Y. Jung, R. Stavins, D.J.A. Orendain, L. Ignon, S. Park, Y. Park, A. Reisinger, D. Cammaramo, A. Fischlin, J.S. Fuglestvedt, J.R. Matthews, C. Péan, IPCC, 2023: Climate Change 2023: Synthesis Report. Contribution of Working Groups I, II and III to the Sixth Assessment Report of the Intergovernmental Panel on Climate Change [Core Writing Team, H. Lee and J. Romero (eds.)]. IPCC, Geneva, Switzerland, Intergovernmental Panel on Climate Change (IPCC), 2023.

[5] World Energy Outlook 2023, OECD, 2023.

[6] C. Zou, Q. Zhao, G. Zhang, B. Xiong, Energy revolution: From a fossil energy era to a new energy era, Natural Gas Industry B 3 (2016) 1–11.

[7] D. Heide, L. von Bremen, M. Greiner, C. Hoffmann, M. Speckmann, S. Bofinger, Seasonal optimal mix of wind and solar power in a future, highly renewable Europe, Renewable Energy 35 (2010) 2483–2489.

[8] V. Reitenbach, L. Ganzer, D. Albrecht, B. Hagemann, Influence of added hydrogen on underground gas storage: a review of key issues, Environ Earth Sci 73 (2015) 6927–6937.

[9] A. Züttel, Hydrogen storage methods, Die Naturwissenschaften 91 (2004) 157–172.

[10] T.T. Le, P. Sharma, B.J. Bora, V.D. Tran, T.H. Truong, H.C. Le, P.Q.P. Nguyen, Fueling the future: A comprehensive review of hydrogen energy systems and their challenges, International Journal of Hydrogen Energy 54 (2024) 791–816.

[11] K. Sordakis, C. Tang, L.K. Vogt, H. Junge, P.J. Dyson, M. Beller, G. Laurenczy, Homogeneous Catalysis for Sustainable Hydrogen Storage in Formic Acid and Alcohols, Chemical reviews 118 (2018) 372–433.
[12] D. Pudlo, L. Ganzer, S. Henkel, M. Kühn, A. Liebscher, M. de Lucia, M. Panfilov, P. Pilz, V. Reitenbach, D. Albrecht, H. Würdemann, R. Gaupp, The H2STORE Project: Hydrogen Underground Storage – A Feasible Way in Storing Electrical Power in Geological Media?, in: M.Z. Hou, H. Xie, P. Were (Eds.), Clean Energy Systems in the Subsurface: Production, Storage and Conversion, Springer Berlin Heidelberg, Berlin, Heidelberg, 2013, pp. 395–412.
[13] P. Carden, L. Paterson, Physical, chemical and energy aspects of underground hydrogen storage, International Journal of Hydrogen Energy 4 (1979) 559–569.
[14] A. Amid, D. Mignard, M. Wilkinson, Seasonal storage of hydrogen in a depleted natural gas reservoir, International Journal of Hydrogen Energy 41 (2016) 5549–5558.
[15] N. Heinemann, M.G. Booth, R.S. Haszeldine, M. Wilkinson, J. Scafidi, K. Edlmann, Hydrogen storage in porous geological formations – onshore play opportunities in the midland valley (Scotland, UK), International Journal of Hydrogen Energy 43 (2018) 20861–20874.
[16] N.S. Muhammed, B. Haq, D. Al Shehri, A. Al-Ahmed, M.M. Rahman, E. Zaman, A review on underground hydrogen storage: Insight into geological sites, influencing factors and future outlook, Energy Reports 8 (2022) 461–499.
[17] N.S. Muhammed, M.B. Haq, D.A. Al Shehri, A. Al-Ahmed, M.M. Rahman, E. Zaman, S. Iglauer, Hydrogen storage in depleted gas reservoirs: A comprehensive review, Fuel 337 (2023) 127032.
[18] M. Perera, A review of underground hydrogen storage in depleted gas reservoirs: Insights into various rock-fluid interaction mechanisms and their impact on the process integrity, Fuel 334 (2023) 126677.
[19] W.T. Pfeiffer, S. Bauer, Subsurface Porous Media Hydrogen Storage – Scenario Development and Simulation, Energy Procedia 76 (2015) 565–572.
[20] R. Tarkowski, Underground hydrogen storage: Characteristics and prospects, Renewable and Sustainable Energy Reviews 105 (2019) 86–94.
[21] E.B. Nelson, Well cementing, Elsevier, Amsterdam, New York, New York, NY, USA, 2010.
[22] S. Bahafid, S. Ghabezloo, M. Duc, P. Faure, J. Sulem, Effect of the hydration temperature on the microstructure of Class G cement: C-S-H composition and density, Cement and Concrete Research 95 (2017) 270–281.
[23] A.-P. Bois, M.-H. Vu, S. Ghabezloo, J. Sulem, A. Garnier, J.-B. Laudet, Cement Sheath Integrity for CO_2 Storage – An Integrated Perspective, Energy Procedia 37 (2013) 5628–5641.
[24] G. Carter, K. Slagle, A Study of Completion Practices To Minimize Gas Communication, Journal of Petroleum Technology 24 (1972) 1170–1174.
[25] S. Ghabezloo, J. Sulem, S. Guédon, F. Martineau, J. Saint-Marc, Poromechanical behaviour of hardened cement paste under isotropic loading, Cement and Concrete Research 38 (2008) 1424–1437.

[26] D.C. Levine, E.W. Thomas, H.P. Bezner, G.C. Tolle, Annular Gas Flow After Cementing: A Look At Practical Solutions, in: All Days, SPE, 1979.
[27] D. Zivar, S. Kumar, J. Foroozesh, Underground hydrogen storage: A comprehensive review, International Journal of Hydrogen Energy 46 (2021) 23436–23462.
[28] L. Hashemi, M. Blunt, H. Hajibeygi, Pore-scale modelling and sensitivity analyses of hydrogen-brine multiphase flow in geological porous media, Scientific reports 11 (2021) 8348.
[29] Z. Bo, L. Zeng, Y. Chen, Q. Xie, Geochemical reactions-induced hydrogen loss during underground hydrogen storage in sandstone reservoirs, International Journal of Hydrogen Energy 46 (2021) 19998–20009.
[30] N. Hassannayebi, S. Azizmohammadi, M. de Lucia, H. Ott, Underground hydrogen storage: application of geochemical modelling in a case study in the Molasse Basin, Upper Austria, Environ Earth Sci 78 (2019).
[31] S. Henkel, D. Pudlo, L. Werner, F. Enzmann, V. Reitenbach, D. Albrecht, H. Würdemann, K. Heister, L. Ganzer, R. Gaupp, Mineral Reactions in the Geological Underground Induced by H_2 and CO_2 Injections, Energy Procedia 63 (2014) 8026–8035.
[32] J.P. Bensing, D. Misch, L. Skerbisch, R.F. Sachsenhofer, Hydrogen-induced calcite dissolution in Amaltheenton Formation claystones: Implications for underground hydrogen storage caprock integrity, International Journal of Hydrogen Energy 47 (2022) 30621–30626.
[33] A. Al-Yaseri, A. Fatah, L. Zeng, A. Al-Ramadhan, M. Sarmadivaleh, Q. Xie, On hydrogen-cement reaction: Investigation on well integrity during underground hydrogen storage, International Journal of Hydrogen Energy 48 (2023) 35610–35623.
[34] U.M. Angst, M.R. Geiker, A. Michel, C. Gehlen, H. Wong, O.B. Isgor, B. Elsener, C.M. Hansson, R. François, K. Hornbostel, R. Polder, M.C. Alonso, M. Sanchez, M.J. Correia, M. Criado, A. Sagüés, N. Buenfeld, The steel–concrete interface, Mater Struct 50 (2017).
[35] A. Nasiri, K. Ravi, M. Prohaska-Marchried, M. Feichter, J. Raith, C. Coti, E. Baronio, C. Busollo, A. Mantegazzi, V. Pozzovivo, S. Pruno, An Interdisciplinary Approach to Investigate the Cement Integrity for Underground Hydrogen Storage Wells, in: Day 1 Mon, June 05, 2023, SPE, 2023.
[36] R. Kiran, C. Teodoriu, Y. Dadmohammadi, R. Nygaard, D. Wood, M. Mokhtari, S. Salehi, Identification and evaluation of well integrity and causes of failure of well integrity barriers (A review), Journal of Natural Gas Science and Engineering 45 (2017) 511–526.
[37] Z. Shi, K. Jessen, T.T. Tsotsis, Impacts of the subsurface storage of natural gas and hydrogen mixtures, International Journal of Hydrogen Energy 45 (2020) 8757–8773.
[38] E.R. Ugarte, D. Tetteh, S. Salehi, Experimental studies of well integrity in cementing during underground hydrogen storage, International Journal of Hydrogen Energy 51 (2024) 473–488.
[39] N. Jacquemet, P. Chiquet, A. Grauls, Hydrogen Reactivity with (1) a Well Cement - PHREEQC Geochemical Thermodynamics Calculations, in: 1st Geoscience & Engineering in Energy Transition Conference, European Association of Geoscientists & Engineers, 2020, pp. 1–5.

[40] L. Zeng, M. Sarmadivaleh, A. Saeedi, A. Al-Yaseri, C. Dowling, G. Buick, Q. Xie, Thermodynamic Modelling on Wellbore Cement Integrity During Underground Hydrogen Storage in Depleted Gas Reservoirs, in: Day 2 Tue, October 18, 2022, SPE, 2022.
[41] F. Crotogino, R. Hammelmann, Wasserstoff-Speicherung in Salzkavernen zur Glättung des Windstromangebots, KBB Underground Technologies GmbH (2007).
[42] ERATO, The TRL Scale as a Research & Innovation Policy Tool, ERATO Recommendations, 2014.
[43] K. Siebertz, D. van Bebber, T. Hochkirchen, Statistische Versuchsplanung, Springer Berlin Heidelberg, Berlin, Heidelberg, 2017.
[44] L. Zeng, M. Sarmadivaleh, A. Saeedi, Y. Chen, Z. Zhong, Q. Xie, Storage integrity during underground hydrogen storage in depleted gas reservoirs, Earth-Science Reviews 247 (2023) 104625.
[45] Ullmann's encyclopedia of industrial chemistry, 7th ed., Wiley-VCH, Weinheim, Wiley online library, 2010.
[46] M. McGlashan, The international temperature scale of 1990 (ITS-90), The Journal of Chemical Thermodynamics 22 (1990) 653–663.
[47] R.T. Ferrell, D.M. Himmelblau, Diffusion coefficients of hydrogen and helium in water, AIChE Journal 13 (1967) 702–708.
[48] D. Li, C. Beyer, S. Bauer, A unified phase equilibrium model for hydrogen solubility and solution density, International Journal of Hydrogen Energy 43 (2018) 512–529.
[49] Rohöl-Aufsuchungs Aktiengesellschaft, AXIOM angewandte Prozesstechnik GesmbH, Verbund AG, Montanuniversität Leoben, Universität für Bodenkultur Wien, Energieinstitut an der Johannes Kepler Universität Linz, Underground Sun Storage: Chemical storage of renewable energy in porous subsurface reservoirs with exemplary testbed, Wien, 2017.
[50] A.E. Yekta, J.-C. Manceau, S. Gaboreau, M. Pichavant, P. Audigane, Determination of Hydrogen–Water Relative Permeability and Capillary Pressure in Sandstone: Application to Underground Hydrogen Injection in Sedimentary Formations, Transp Porous Med 122 (2018) 333–356.
[51] M. Panfilov, Physicochemical Fluid Dynamics in Porous Media: Applications in Geosciences and Petroleum Engineering, 1st ed., Wiley-VCH, Weinheim, 2018.
[52] R. Azin, A. Nasiri, A.J. Entezari, G.H. Montazeri, Investigation of Underground Gas Storage in a Partially Depleted Gas Reservoir, in: All Days, SPE, 2008.
[53] D.J. Evans, R.A. Chadwick (Eds.), Underground gas storage: Worldwide experiences and future development in the UK and Europe, 2009.
[54] J. Zhang, Y. Tan, T. Zhang, K. Yu, X. Wang, Q. Zhao, Natural gas market and underground gas storage development in China, Journal of Energy Storage 29 (2020) 101338.
[55] V. Reitenbach, D. Albrecht, L. Ganzer, Influence of hydrogen on underground gas storage; literature study, DGMK, Hamburg, 2014.
[56] A. Lord, Overview of geologic storage of natural gas with an emphasis on assessing the feasibility of storing hydrogen, 2009.

[57] R. Tarkowski, Perspectives of using the geological subsurface for hydrogen storage in Poland, International Journal of Hydrogen Energy 42 (2017) 347–355.
[58] D.D. Papadias, R.K. Ahluwalia, Bulk storage of hydrogen, International Journal of Hydrogen Energy 46 (2021) 34527–34541.
[59] Iglauer, Optimum geological storage depths for structural H_2 geo-storage, J. Petrol. Sci. Eng. 109498 (2021).
[60] V.S. Rajan, R.W. Luhning, Water Coning Suppression, Journal of Canadian Petroleum Technology 32 (1993).
[61] L. Paterson, The implications of fingering in underground hydrogen storage, International Journal of Hydrogen Energy 8 (1983) 53–59.
[62] N. Heinemann, J. Alcalde, J.M. Miocic, S.J.T. Hangx, J. Kallmeyer, C. Ostertag-Henning, A. Hassanpouryouzband, E.M. Thaysen, G.J. Strobel, C. Schmidt-Hattenberger, K. Edlmann, M. Wilkinson, M. Bentham, R. Stuart Haszeldine, R. Carbonell, A. Rudloff, Enabling large-scale hydrogen storage in porous media – the scientific challenges, Energy & Environmental Science 14 (2021) 853–864.
[63] O.M. Suleimenov, R.E. Krupp, Solubility of hydrogen sulfide in pure water and in NaCl solutions, from 20 to 320°C and at saturation pressures, Geochimica et Cosmochimica Acta 58 (1994) 2433–2444.
[64] D.A. Wiesenburg, N.L. Guinasso, Equilibrium solubilities of methane, carbon monoxide, and hydrogen in water and sea water, Journal of Chemical & Engineering Data 24 (1979) 356–360.
[65] Z. Duan, N. Møller, J. Greenberg, J.H. Weare, The prediction of methane solubility in natural waters to high ionic strength from 0 to 250°C and from 0 to 1600 bar, Geochimica et Cosmochimica Acta 56 (1992) 1451–1460.
[66] Z. Duan, R. Sun, An improved model calculating CO_2 solubility in pure water and aqueous NaCl solutions from 273 to 533 K and from 0 to 2000 bar, Chemical Geology 193 (2003) 257–271.
[67] S. Chabab, P. Théveneau, C. Coquelet, J. Corvisier, P. Paricaud, Measurements and predictive models of high-pressure H_2 solubility in brine (H_2O+NaCl) for underground hydrogen storage application, International Journal of Hydrogen Energy 45 (2020) 32206–32220.
[68] Parkhurst, Description of input and examples for PHREEQC version 3: A computer program for speciation, batch-reaction, one-dimensional transport, and inverse geochemical calculations (2013).
[69] S. LI, M. DONG, Z. LI, Huang, Qing., Nickel, Gas breakthrough pressure for hydrocarbon reservoir seal rocks: implications for the security of long-term CO2 storage in the Weyburn field, Geofluids 5 (2005) 326–334.
[70] A. Tamimi, E.B. Rinker, O.C. Sandall, Diffusion Coefficients for Hydrogen Sulfide, Carbon Dioxide, and Nitrous Oxide in Water over the Temperature Range 293-368 K, J. Chem. Eng. Data 39 (1994) 330–332.
[71] P.A. Witherspoon, D.N. Saraf, Diffusion of Methane, Ethane, Propane, and n-Butane in Water from 25 to 43°, J. Phys. Chem. 69 (1965) 3752–3755.

[72] S. Iglauer, M. Ali, A. Keshavarz, Hydrogen Wettability of Sandstone Reservoirs: Implications for Hydrogen Geo-Storage, Geophys Res Lett 48 (2021).
[73] S. Higgs, Y. Da Wang, C. Sun, J. Ennis-King, S.J. Jackson, R.T. Armstrong, P. Mostaghimi, In-situ hydrogen wettability characterisation for underground hydrogen storage, International Journal of Hydrogen Energy 47 (2022) 13062–13075.
[74] M. Ali, B. Pan, N. Yekeen, S. Al-Anssari, A. Al-Anazi, A. Keshavarz, S. Iglauer, H. Hoteit, Assessment of wettability and rock-fluid interfacial tension of caprock: Implications for hydrogen and carbon dioxide geo-storage, International Journal of Hydrogen Energy 47 (2022) 14104–14120.
[75] A.E. Yekta, M. Pichavant, P. Audigane, Evaluation of geochemical reactivity of hydrogen in sandstone: Application to geological storage, Applied Geochemistry 95 (2018) 182–194.
[76] M. Ali, N. Yekeen, N. Pal, A. Keshavarz, S. Iglauer, H. Hoteit, Influence of pressure, temperature and organic surface concentration on hydrogen wettability of caprock; implications for hydrogen geo-storage, Energy Reports 7 (2021) 5988–5996.
[77] M. Hosseini, J. Fahimpour, M. Ali, A. Keshavarz, S. Iglauer, Hydrogen wettability of carbonate formations: Implications for hydrogen geo-storage, Journal of Colloid and Interface Science 614 (2022) 256–266.
[78] H. Esfandyari, M. Sarmadivaleh, F. Esmaeilzadeh, M. Ali, S. Iglauer, A. Keshavarz, Experimental evaluation of rock mineralogy on hydrogen-wettability: Implications for hydrogen geo-storage, Journal of Energy Storage 52 (2022) 104866.
[79] M. Hosseini, J. Fahimpour, M. Ali, A. Keshavarz, S. Iglauer, H2−brine interfacial tension as a function of salinity, temperature, and pressure; implications for hydrogen geo-storage, Journal of Petroleum Science and Engineering 213 (2022) 110441.
[80] Y.F. Chow, G.C. Maitland, J.M. Trusler, Interfacial tensions of (H_2O + H_2) and (H_2O + CO_2 + H_2) systems at temperatures of (298–448) K and pressures up to 45 MPa, Fluid Phase Equilibria 475 (2018) 37–44.
[81] B. Pan, X. Yin, S. Iglauer, Rock-fluid interfacial tension at subsurface conditions: Implications for H_2, CO_2 and natural gas geo-storage, International Journal of Hydrogen Energy 46 (2021) 25578–25585.
[82] N. Yekeen, A. Al-Yaseri, B.M. Negash, M. Ali, A. Giwelli, L. Esteban, J. Sarout, Clay-hydrogen and clay-cushion gas interfacial tensions: Implications for hydrogen storage, International Journal of Hydrogen Energy 47 (2022) 19155–19167.
[83] C. Hemme, W. van Berk, Hydrogeochemical Modeling to Identify Potential Risks of Underground Hydrogen Storage in Depleted Gas Fields, Applied Sciences 8 (2018) 2282.
[84] A. Lassin, M. Dymitrowska, M. Azaroual, Hydrogen solubility in pore water of partially saturated argillites: Application to Callovo-Oxfordian clayrock in the context of a nuclear waste geological disposal, Physics and Chemistry of the Earth, Parts A/B/C 36 (2011) 1721–1728.
[85] Henkel, Effects of H2 and CO2 Underground Storage in Natural Pore Reservoirs-Findings by SEM and AFM Techniques, the Third Sustainable Earth Sciences

Conference and Exhibition, European Association of Geoscientists & Engineers (2015) 1.

[86] S. Flesch, D. Pudlo, D. Albrecht, A. Jacob, F. Enzmann, Hydrogen underground storage—Petrographic and petrophysical variations in reservoir sandstones from laboratory experiments under simulated reservoir conditions, International Journal of Hydrogen Energy 43 (2018) 20822–20835.

[87] I.M. Cozzarelli, J.M. Suflita, G.A. Ulrich, S.H. Harris, M.A. Scholl, J.L. Schlottmann, S. Christenson, Geochemical and Microbiological Methods for Evaluating Anaerobic Processes in an Aquifer Contaminated by Landfill Leachate, Environ. Sci. Technol. 34 (2000) 4025–4033.

[88] L. Truche, G. Berger, C. Destrigneville, A. Pages, D. Guillaume, E. Giffaut, E. Jacquot, Experimental reduction of aqueous sulphate by hydrogen under hydrothermal conditions: Implication for the nuclear waste storage, Geochimica et Cosmochimica Acta 73 (2009) 4824–4835.

[89] L. Truche, M.-C. Jodin-Caumon, C. Lerouge, G. Berger, R. Mosser-Ruck, E. Giffaut, N. Michau, Sulphide mineral reactions in clay-rich rock induced by high hydrogen pressure. Application to disturbed or natural settings up to 250 °C and 30 bar, Chemical Geology 351 (2013) 217–228.

[90] J.J. Carroll, A.E. Mather, The solubility of hydrogen sulphide in water from 0 to 90°C and pressures to 1 MPa, Geochimica et Cosmochimica Acta 53 (1989) 1163–1170.

[91] F. Crotogino, Large-scale hydrogen storage, Storing Energy 2nd ed. (2022) 613-632.

[92] A.J. Hall, Pyrite-pyrrhotine redox reactions in nature, Mineral. mag. 50 (1986) 223–229.

[93] L. Truche, G. Berger, C. Destrigneville, D. Guillaume, E. Giffaut, Kinetics of pyrite to pyrrhotite reduction by hydrogen in calcite buffered solutions between 90 and 180°C: Implications for nuclear waste disposal, Geochimica et Cosmochimica Acta 74 (2010) 2894–2914.

[94] T. Wiltowski, C.C. Hinckley, G.V. Smith, T. Nishizawa, M. Saporoschenko, R.H. Shiley, J.R. Webster, Kinetics and mechanisms of iron sulfide reductions in hydrogen and in carbon monoxide, Journal of Solid State Chemistry 71 (1987) 95–102.

[95] J.M. Lambert, G. Simkovich, P.L. Walker, The kinetics and mechanism of the pyrite-to-pyrrhotite transformation, Metall Mater Trans B 29 (1998) 385–396.

[96] M. Didier, L. Leone, J.-M. Greneche, E. Giffaut, L. Charlet, Adsorption of hydrogen gas and redox processes in clays, Environmental Science & Technology 46 (2012) 3574–3579.

[97] H. Moslemi, P. Shamsi, F. Habashi, Pyrite and pyrrhotite open circuit potentials study: Effects on flotation, Minerals Engineering 24 (2011) 1038–1045.

[98] W.K. Jozwiak, E. Kaczmarek, T.P. Maniecki, W. Ignaczak, W. Maniukiewicz, Reduction behavior of iron oxides in hydrogen and carbon monoxide atmospheres, Applied Catalysis A: General 326 (2007) 17–27.

[99] O.E. Lebedeva, W.M. Sachtler, Enhanced Reduction of Fe_2O_3 Caused by Migration of TM Ions out of Zeolite Channels, Journal of Catalysis 191 (2000) 364–372.

[100] H.-Y. Lin, Y.-W. Chen, C. Li, The mechanism of reduction of iron oxide by hydrogen, Thermochimica Acta 400 (2003) 61–67.

[101] E.R. Monazam, R.W. Breault, R. Siriwardane, Kinetics of Hematite to Wüstite by Hydrogen for Chemical Looping Combustion, Energy & Fuels 28 (2014) 5406–5414.
[102] G. Munteanu, L. Ilieva, D. Andreeva, Kinetic parameters obtained from TPR data for α-Fe2O3 and systems, Thermochimica Acta 291 (1997) 171–177.
[103] E.T. Turkdogan, J.V. Vinters, Gaseous reduction of iron oxides: Part I. Reduction of hematite in hydrogen, Metall Trans 2 (1971) 3175–3188.
[104] A.B. Dohrmann, M. Krüger, Microbial H2 Consumption by a Formation Fluid from a Natural Gas Field at High-Pressure Conditions Relevant for Underground H2 Storage, Environmental Science & Technology 57 (2023) 1092–1102.
[105] N. Dopffel, S. Jansen, J. Gerritse, Microbial side effects of underground hydrogen storage – Knowledge gaps, risks and opportunities for successful implementation, International Journal of Hydrogen Energy 46 (2021) 8594–8606.
[106] Gniese, Relevance of Deep-Subsurface Microbiology for Underground Gas Storage and Geothermal Energy Production (2014) 95.
[107] L. Zeng, M. Hosseini, A. Keshavarz, S. Iglauer, Y. Lu, Q. Xie, Hydrogen wettability in carbonate reservoirs: Implication for underground hydrogen storage from geochemical perspective, International Journal of Hydrogen Energy 47 (2022) 25357–25366.
[108] L. Zeng, A. Keshavarz, Q. Xie, S. Iglauer, Hydrogen storage in Majiagou carbonate reservoir in China: Geochemical modelling on carbonate dissolution and hydrogen loss, International Journal of Hydrogen Energy 47 (2022) 24861–24870.
[109] N. Jacquemet, P. Chiquet, A. Grauls, Hydrogen Reactivity with (2) an Aquifer - PHREEQC Geochemical Thermodynamics Calculations, in: 1st Geoscience & Engineering in Energy Transition Conference, European Association of Geoscientists & Engineers, 2020, pp. 1–5.
[110] S.A. Carroll, J.V. Walther, Kaolinite dissolution at 25 degrees 60 degrees and 80 degrees C, American Journal of Science 290 (1990) 797–810.
[111] J. Ganor, J.L. Mogollón, A.C. Lasaga, The effect of pH on kaolinite dissolution rates and on activation energy, Geochimica et Cosmochimica Acta 59 (1995) 1037–1052.
[112] T.V. Suslow, Oxidation-Reduction Potential (ORP) for Water Disinfection Monitoring, Control, and Documentation, University of California, Agriculture and Natural Resources, 2004.
[113] A. Hassanpouryouzband, K. Adie, T. Cowen, E.M. Thaysen, N. Heinemann, I.B. Butler, M. Wilkinson, K. Edlmann, Geological Hydrogen Storage: Geochemical Reactivity of Hydrogen with Sandstone Reservoirs, ACS Energy Lett. 7 (2022) 2203–2210.
[114] M. Su, Q. Wang, R. Li, L. Wang, Per capita renewable energy consumption in 116 countries: The effects of urbanization, industrialization, GDP, aging, and trade openness, Energy 254 (2022) 124289.
[115] C. Winter, The hydrogen energy economy: an address to the World Economic Forum 2004, International Journal of Hydrogen Energy (2004).
[116] S. Dunn, Hydrogen futures: toward a sustainable energy system, International Journal of Hydrogen Energy 27 (2002) 235–264.

[117] M.M. Aba, I.L. Sauer, N.B. Amado, Comparative review of hydrogen and electricity as energy carriers for the energy transition, International Journal of Hydrogen Energy 57 (2024) 660–678.

[118] A.M. Abdalla, S. Hossain, O.B. Nisfindy, A.T. Azad, M. Dawood, A.K. Azad, Hydrogen production, storage, transportation and key challenges with applications: A review, Energy Conversion and Management 165 (2018) 602–627.

[119] J.O. Abe, A. Popoola, E. Ajenifuja, O.M. Popoola, Hydrogen energy, economy and storage: Review and recommendation, International Journal of Hydrogen Energy 44 (2019) 15072–15086.

[120] J. Incer-Valverde, A. Korayem, G. Tsatsaronis, T. Morosuk, “Colors” of hydrogen: Definitions and carbon intensity, Energy Conversion and Management 291 (2023) 117294.

[121] R. Blay-Roger, W. Bach, L.F. Bobadilla, T.R. Reina, J.A. Odriozola, R. Amils, V. Blay, Natural hydrogen in the energy transition: Fundamentals, promise, and enigmas, Renewable and Sustainable Energy Reviews 189 (2024) 113888.

[122] E. Frery, L. Langhi, M. Maison, I. Moretti, Natural hydrogen seeps identified in the North Perth Basin, Western Australia, International Journal of Hydrogen Energy 46 (2021) 31158–31173.

[123] A. ERSOZ, Investigation of hydrocarbon reforming processes for micro-cogeneration systems, International Journal of Hydrogen Energy 33 (2008) 7084–7094.

[124] P. Breeze, Hydrogen Energy Storage, in: Power System Energy Storage Technologies, Elsevier, 2018, pp. 69–77.

[125] S. Shiva Kumar, V. Himabindu, Hydrogen production by PEM water electrolysis – A review, Materials Science for Energy Technologies 2 (2019) 442–454.

[126] Y. Chen, X. Jin, L. Zeng, Z. Zhong, M. Mehana, W. Xiao, W. Pu, K. Regenauer-Lieb, Q. Xie, Role of large-scale underground hydrogen storage and its pathways to achieve net-zero in China, Journal of Energy Storage 72 (2023) 108448.

[127] C. Sambo, A. Dudun, S.A. Samuel, P. Esenenjor, N.S. Muhammed, B. Haq, A review on worldwide underground hydrogen storage operating and potential fields, International Journal of Hydrogen Energy 47 (2022) 22840–22880.

[128] M. Khalifeh, A. Saasen, Introduction to Permanent Plug and Abandonment of Wells, Springer International Publishing, Cham, 2020.

[129] DIN 16530, DIN EN ISO 16530-1:2017-11, Erdöl- und Erdgasindustrie_- Bohrungsintegrität_- Teil_1: Lebenszykluslenkung (ISO_16530-1:2017); Deutsche Fassung EN_ISO_16530-1:2017, nur auf CD-ROM, Beuth Verlag GmbH, Berlin.

[130] Norsk Sokkels Konkuranseposisjon, NORSOK D 010 2013: WELL INTEGRITY IN DRILLING AND WELL OPERATIONS, 2013.

[131] J. Iyer, G. Lackey, L. Edvardsen, A. Bean, S.A. Carroll, N. Huerta, M.M. Smith, M. Torsæter, R.M. Dilmore, P. Cerasi, A Review of Well Integrity Based on Field Experience at Carbon Utilization and Storage Sites, International Journal of Greenhouse Gas Control 113 (2022) 103533.

[132] M. Anunciação Jaculli, N. Choueri Jr, C.R. Da Mata, A.G. Aparecida Silva Leite, J.R. Pelaquim Mendes, D. Colombo, Well safety and integrity evaluation of offshore wells: A

review of past, present, and future, Journal of Petroleum Science and Engineering 212 (2022) 110329.
[133] K.L. Scrivener, R. Snellings, The Rise of Portland Cements, Elements 18 (2022) 308–313.
[134] S. Bahafid, A multi-technique investigation of the effect of hydration temperature on the microstructure and mechanical properties of cement paste. PhD Thesis, Paris, 2017.
[135] A. Lavrov, Physics and Mechanics of Primary Well Cementing, Springer International Publishing, Cham, 2016.
[136] American Petroleum Institute, API Spec 10A, 2022.
[137] C01 Committee, Specification for Portland Cement, ASTM International, West Conshohocken, PA.
[138] USGS, Mineral Commodity Summaries, 2021.
[139] P.E. Stutzman, Microscopy of Clinker and Hydraulic Cements, Reviews in Mineralogy and Geochemistry 74 (2012) 101–146.
[140] F.P. Glasser, The Burning of Portland Cement, in: Lea's Chemistry of Cement and Concrete, Elsevier, 1998, pp. 195–240.
[141] G.C. Bye, Portland cement: Composition, production and properties, 2nd ed., Thomas Telford, London, 1999.
[142] K. Scrivener, A. Ouzia, P. Juilland, A. Kunhi Mohamed, Advances in understanding cement hydration mechanisms, Cement and Concrete Research 124 (2019) 105823.
[143] R. Benedix, Bauchemie: Einführung in die Chemie für Bauingenieure, 3rd ed., Teubner, Wiesbaden, 2005.
[144] H. Pöllmann, R. Snellings, L. Valentini, Cement and Concrete—Past, Present, and Future, Elements 18 (2022) 295–299.
[145] E.H. Nickel, International Mineralogical Association, Commission on New Minerals and Mineral Names: Definition of a mineral, Mineralogy and Petrology 55 (1995) 323–326.
[146] H.E. Pemberton, Minerals of California, Springer US, Boston, MA, 1982.
[147] Y. Vapnik, V.V. Sharygin, E.V. Sokol, R. Shagam, Paralavas in a combustion metamorphic complexHatrurim Basin, Israel, in: G.B. Stracher (Ed.), Geology of Coal FiresCase Studies from Around the World, Geological Society of America, 2007.
[148] B. Engelhaupt, W. Schüller, Mineral Reich Eifel, 1st ed., Christian Weise Verlag, München, 2015.
[149] X. Li, X. Shen, M. Tang, X. Li, Stability of Tricalcium Silicate and Other Primary Phases in Portland Cement Clinker, Ind. Eng. Chem. Res. 53 (2014) 1954–1964.
[150] H.F.W. Taylor, Cement chemistry, 2nd ed., Telford Publ, London, 2003.
[151] H.-M. Ludwig, W. Zhang, Research review of cement clinker chemistry, Cement and Concrete Research 78 (2015) 24–37.
[152] A. Bazzoni, S. Ma, Q. Wang, X. Shen, M. Cantoni, K.L. Scrivener, The Effect of Magnesium and Zinc Ions on the Hydration Kinetics of C 3 S, J American Ceramic Society 97 (2014) 3684–3693.

[153] M.-N. de Noirfontaine, F. Dunstetter, M. Courtial, G. Gasecki, M. Signes-Frehel, Polymorphism of tricalcium silicate, the major compound of Portland cement clinker, Cement and Concrete Research 36 (2006) 54–64.

[154] K. Urabe, T. Shirakami, M. Iwashima, Superstructure in a Triclinic Phase of Tricalcium Silicate, J American Ceramic Society 83 (2000) 1253–1258.

[155] F. Dunstetter, M.-N. de Noirfontaine, M. Courtial, Polymorphism of tricalcium silicate, the major compound of Portland cement clinker, Cement and Concrete Research 36 (2006) 39–53.

[156] Á.G. de La Torre, R.N. de Vera, A.J. Cuberos, M.A. Aranda, Crystal structure of low magnesium-content alite: Application to Rietveld quantitative phase analysis, Cement and Concrete Research 38 (2008) 1261–1269.

[157] I. Maki, K. Fukuda, H. Yoshida, J. Kumaki, Effect of MgO and SO 3 on the Impurity Concentration in Alite in Portland Cement Clinker, J American Ceramic Society 75 (1992) 3163–3165.

[158] D. Campbell, Microscopical Examination and Interpretation of Portland Cement and Clinker, Portland Cement Association, Skokie, Ilinois, USA, 1999.

[159] N. Betancur-Granados, Alternative Production Processes of Calcium Silicate Phases of Portland Cement: A Review, CERJ 5 (2018).

[160] N.B. Singh, S. Rai, N. Singh, Highly Reactive β-Dicalcium Silicate, J American Ceramic Society 85 (2002) 2171–2176.

[161] P. Rejmak, J.S. Dolado, M.A.G. Aranda, A. Ayuela, First-Principles Calculations on Polymorphs of Dicalcium Silicate—Belite, a Main Component of Portland Cement, The Journal of Physical Chemistry C 123 (2019) 6768–6777.

[162] A. Wesselsky, O.M. Jensen, Synthesis of pure Portland cement phases, Cement and Concrete Research 39 (2009) 973–980.

[163] N.A. Yamnova, N.V. Zubkova, N.N. Eremin, A.E. Zadov, V.M. Gazeev, Crystal structure of larnite β-Ca2SiO4 and specific features of polymorphic transitions in dicalcium orthosilicate, Crystallogr. Rep. 56 (2011) 210–220.

[164] Q. Wang, H. Manzano, Y. Guo, I. Lopez-Arbeloa, X. Shen, Hydration Mechanism of Reactive and Passive Dicalcium Silicate Polymorphs from Molecular Simulations, The Journal of Physical Chemistry C 119 (2015) 19869–19875.

[165] A.B. Poole, I. Sims, Concrete petrography: A handbook of investigative techniques, 2nd ed., CRC Press, Boca Raton, 2016.

[166] S.N. Ghosh, Portland Cement Phases: Polymorphism, Solid Solution, Defect Structure and Hydraulicity, in: Advances in Cement Technology, Elsevier, 1983, pp. 289–305.

[167] Y. Shao, X. Lu, Q. Li, Y. Dong, L. Zhang, C. Jiang, P. Du, X. Cheng, Study on the preparation and sulfate resistance of Portland cement clinker with the high Fe/Al ratio of ferrite phase, Cement and Concrete Composites 134 (2022) 104699.

[168] S. Lesko, E. Lesniewska, A. Nonat, J.C. Mutin, J.P. Goudonnet, Investigation by atomic force microscopy of forces at the origin of cement cohesion, Ultramicroscopy 86 (2001) 11–21.

[169] K.L. Scrivener, A. Nonat, Hydration of cementitious materials, present and future, Cement and Concrete Research 41 (2011) 651–665.

[170] I.G. Richardson, The calcium silicate hydrates, Cement and Concrete Research 38 (2008) 137–158.

[171] E. Bonaccorsi, S. Merlino, A.R. Kampf, The Crystal Structure of Tobermorite 14 Å (Plombierite), a C–S–H Phase, J American Ceramic Society 88 (2005) 505–512.

[172] J.E. Rossen, Composition and morphology of C-A-S-H in pastes of alite and cement blended with supplementary cementitious materials, Lausanne, EPFL, 2014.

[173] K.L. Scrivener, P. Juilland, P.J. Monteiro, Advances in understanding hydration of Portland cement, Cement and Concrete Research 78 (2015) 38–56.

[174] H.M. Jennings, J.J. Thomas, D. Rothstein, J.J. Chen, Cements as Porous Materials, in: F. Schth, K.S.W. Sing, J. Weitkamp (Eds.), Handbook of Porous Solids, Wiley-VCH Verlag GmbH, Weinheim, Germany, 2002, pp. 2971–3028.

[175] B.Z. Dilnesa, B. Lothenbach, G. Le Saout, G. Renaudin, A. Mesbah, Y. Filinchuk, A. Wichser, E. Wieland, Iron in carbonate containing AFm phases, Cement and Concrete Research 41 (2011) 311–323.

[176] K. de Weerdt, M.B. Haha, G. Le Saout, K.O. Kjellsen, H. Justnes, B. Lothenbach, Hydration mechanisms of ternary Portland cements containing limestone powder and fly ash, Cement and Concrete Research 41 (2011) 279–291.

[177] T. Matschei, B. Lothenbach, F.P. Glasser, The AFm phase in Portland cement, Cement and Concrete Research 37 (2007) 118–130.

[178] B. Lothenbach, M. Zajac, Application of thermodynamic modelling to hydrated cements, Cement and Concrete Research 123 (2019) 105779.

[179] J.W. Bullard, H.M. Jennings, R.A. Livingston, A. Nonat, G.W. Scherer, J.S. Schweitzer, K.L. Scrivener, J.J. Thomas, Mechanisms of cement hydration, Cement and Concrete Research 41 (2011) 1208–1223.

[180] K. Scrivener, R. Snellings, B. Lothenbach (Eds.), A practical guide to microstructural analysis of cementitious materials, CRC Press, Boca Raton, Florida, 2016.

[181] J.J. Beaudoin, R. Alizadeh, A discussion of the paper “Refinements to colloidal model of C–S–H in cement: CM-II” by Hamlin M. Jennings, Cement and Concrete Research 38 (2008) 1026–1027.

[182] P.D. Tennis, H.M. Jennings, A model for two types of calcium silicate hydrate in the microstructure of Portland cement pastes, Cement and Concrete Research 30 (2000) 855–863.

[183] H.M. Jennings, P.D. Tennis, Model for the Developing Microstructure in Portland Cement Pastes, J American Ceramic Society 77 (1994) 3161–3172.

[184] H.M. Jennings, A model for the microstructure of calcium silicate hydrate in cement paste, Cement and Concrete Research 30 (2000) 101–116.

[185] H.M. Jennings, Refinements to colloid model of C-S-H in cement: CM-II, Cement and Concrete Research 38 (2008) 275–289.

[186] R.F. Feldman, P.J. Sereda, A model for hydrated Portland cement paste as deduced from sorption-length change and mechanical properties, Mater Struct 1 (1968) 509–520.

[187] R.F. Feldman, P.J. Sereda, A new Model for Hydrated Portland Cement and its practical implications, Engineering Journal (Canada) (1970).

[188] T. Powers, T. Brownyard, Studies of the Physical Properties of Hardened Portland Cement Paste, JP 43 (1946).

[189] T.C. POWERS, Structure and Physical Properties of Hardened Portland Cement Paste, J American Ceramic Society 41 (1958) 1–6.

[190] A.J. Allen, J.J. Thomas, H.M. Jennings, Composition and density of nanoscale calcium-silicate-hydrate in cement, Nature materials 6 (2007) 311–316.

[191] J. Thomas, H. Jennings, A. Allen, The surface area of cement paste as measured by neutron scattering: evidence for two C-S-H morphologies, Cement and Concrete Research 28 (1998) 897–905.

[192] G. Constantinides, F.-J. Ulm, The effect of two types of C-S-H on the elasticity of cement-based materials: Results from nanoindentation and micromechanical modeling, Cement and Concrete Research 34 (2004) 67–80.

[193] G. Constantinides, F.-J. Ulm, K. van Vliet, On the use of nanoindentation for cementitious materials, Mater Struct 36 (2003) 191–196.

[194] O. Bernard, F.-J. Ulm, E. Lemarchand, A multiscale micromechanics-hydration model for the early-age elastic properties of cement-based materials, Cement and Concrete Research 33 (2003) 1293–1309.

[195] S. Diamond, The microstructure of cement paste and concrete—a visual primer, Cement and Concrete Composites 26 (2004) 919–933.

[196] S. Bae, R. Taylor, D. Shapiro, P. Denes, J. Joseph, R. Celestre, S. Marchesini, H. Padmore, T. Tyliszczak, T. Warwick, D. Kilcoyne, P. Levitz, P.J. M Monteiro, Soft X-ray Ptychographic Imaging and Morphological Quantification of Calcium Silicate Hydrates (C–S–H), J American Ceramic Society 98 (2015) 4090–4095.

[197] J.J. Beaudoin, R. Alizadeh, A discussion of the paper “A multi-technique investigation of the nanoporosity of cement paste” by Hamlin M. Jennings, Jeffrey J. Thomas, Julia S. Gevrenov, Georgios Constantinides and Franz-Josef Ulm, Cement and Concrete Research 37 (2007) 1373.

[198] A. Muller, K.L. Scrivener, A.M. Gajewicz, P.J. McDonald, Use of bench-top NMR to measure the density, composition and desorption isotherm of C–S–H in cement paste, Microporous and Mesoporous Materials 178 (2013) 99–103.

[199] A. Valori, P.J. McDonald, K.L. Scrivener, The morphology of C–S–H: Lessons from 1H nuclear magnetic resonance relaxometry, Cement and Concrete Research 49 (2013) 65–81.

[200] P.F. Faure, S. Rodts, Proton NMR relaxation as a probe for setting cement pastes, Magnetic resonance imaging 26 (2008) 1183–1196.

[201] F.H. Wittmann, Interaction of Hardened Cement Paste and Water, J American Ceramic Society 56 (1973) 409–415.

[202] M. Juenger, J.L. Provis, J. Elsen, W. Matthes, R.D. Hooton, J. Duchesne, L. Courard, H. He, F. Michel, R. Snellings, N. de Belie, Supplementary Cementitious Materials for Concrete: Characterization Needs, MRS Proc. 1488 (2012).

[203] S.H. Kosmatka, M.L. Wilson, Design and control of concrete mixtures: The guide to applications, methods, and materials, 15th ed., Portland Cement Association, Skokie, Ill., 2011.

[204] M. Schneider, M. Romer, M. Tschudin, H. Bolio, Sustainable cement production—present and future, Cement and Concrete Research 41 (2011) 642–650.

[205] K.L. Scrivener, R.J. Kirkpatrick, Innovation in use and research on cementitious material, Cement and Concrete Research 38 (2008) 128–136.

[206] E.R. Ugarte, S. Salehi, A Review on Well Integrity Issues for Underground Hydrogen Storage, Journal of Energy Resources Technology 144 (2022).

[207] R.B. Pernites, A.K. Santra, Portland cement solutions for ultra-high temperature wellbore applications, Cement and Concrete Composites 72 (2016) 89–103.

[208] A. Hussain, H. Al-Hadrami, H. Emadi, F. Altawati, S.R. Thiyagarajan, M. Watson, Experimental Investigation of Wellbore Integrity of Depleted Oil and Gas Reservoirs for Underground Hydrogen Storage, in: Day 2 Tue, May 03, 2022, OTC, 2022.

[209] J. Tremosa, R. Jakobsen, Y. Le Gallo, Assessing and modeling hydrogen reactivity in underground hydrogen storage: A review and models simulating the Lobodice town gas storage, Front. Energy Res. 11 (2023).

[210] O. Gelencsér, C. Árvai, L.T. Mika, D. Breitner, D. LeClair, C. Szabó, G. Falus, Z. Szabó-Krausz, Effect of hydrogen on calcite reactivity in sandstone reservoirs: Experimental results compared to geochemical modeling predictions, Journal of Energy Storage 61 (2023) 106737.

[211] B. Lothenbach, T. Matschei, G. Möschner, F.P. Glasser, Thermodynamic modelling of the effect of temperature on the hydration and porosity of Portland cement, Cement and Concrete Research 38 (2008) 1–18.

[212] B. Lothenbach, D.A. Kulik, T. Matschei, M. Balonis, L. Baquerizo, B. Dilnesa, G.D. Miron, R.J. Myers, Cemdata18: A chemical thermodynamic database for hydrated Portland cements and alkali-activated materials, Cement and Concrete Research 115 (2019) 472–506.

[213] D.A. Kulik, T. Wagner, S.V. Dmytrieva, G. Kosakowski, F.F. Hingerl, K.V. Chudnenko, U.R. Berner, GEM-Selektor geochemical modeling package: revised algorithm and GEMS3K numerical kernel for coupled simulation codes, Comput Geosci (2012).

[214] T. Sammer, X. Shi, M.Z. Khan, A. Matkovic, C. Teichert, J.G. Raith, Influence of broad ion beam polishing on the surface roughness of hydrated cement paste and its implications on microstructural analysis, Cement and Concrete Research 182 (2024) 107555

[215] T. Sammer, A. Nasiri, N. Kostoglou, K. Ravi, J.G. Raith, Insight into Carbon Black and Silica Fume as cement additives for geoenergy wells: linking mineralogy to mechanical and physical properties, C 10, 71 (2024)

[216] T. Sammer, N. Kostoglou, K. Ravi, J.G. Raith, Hydrogen induced changes in the phase composition and micro-structure of downhole cements: fundamental research within the context of underground hydrogen storage, International Journal of Hydrogen Energy 89 (2024) 1166-1175

Annex A

Table 5: declaration of AI usage.

Object	Share AI content (in %)	Tool/ version	Annotation
Improving linguistic readability and paraphrasing	< 5	ChatGPT, V 3.5	N/A Chapter 2, 4 and 5
Researching literature and information	< 1	ChatGPT, V 3.5	Help for finding information and literature, but the central statements were worked out independently, Chapter 2.9.2 (SCMs)

Annex B

Tackling challenges concerning the integrity of downhole cement/rock during underground gas storage: an interdisciplinary approach.

Thomas Sammer[a], Arash Nasiri[b], Monika Feichter[a], Krishna Ravi[b]

[a]Chair of Resource Mineralogy, Montanuniversität Leoben, Peter-Tunner Straße 5, 8700 Leoben
[b]Chair of Drilling and Completion Engineering, Montanuniversität Leoben, Parkstraße 27/III, 8700 Leoben
email: thomas.sammer@unileoben.ac.at

Introduction and Objective:

Current energy politics aim for an environmentally sustainable and secure energy supply resulting in the substitution of conventional fossil fuels by renewable energy sources. This is accelerated by the necessity of reducing greenhouse gas emissions to combat climate change. To overcome weather and seasonal fluctuations in the energy production from e.g., wind or solar sources the promotion of large-scale and secure storage of energy carrying gases is a necessity.

One promising way of storing nowadays important gases (e.g., H_2, CH_4, CO_2) is underground gas storage (UGS, Fig. 1-A). UGS is the concept of using natural geological bodies in the underground as potential storage sites. Potential applications of UGS are power to gas (PTG, Fig. 1-B), large scale safe hydrogen storage (UHGS) or carbon capture and storage (CCS).

Geological bodies suitable for UGS are aquifers, salt caverns and depleted oil and gas fields with the latter ones making up the majority (Fig. 1-C). Other advantages of depleted fields are that already existing infrastructure, e.g., boreholes and surface handling facilities, can be widely used. Moreover, the reservoirs are already well understood. However, to make UGS a feasible process, fundamental research investigating not just the integrity of reservoir and cap rocks, but also downhole cements applied in boreholes during the storage life of the well are essential. This is particularly important once the injection scale is industrial, as there is a severe knowledge gap regarding the interaction of these fluids with the downhole cement, which is a significant element for the well integrity and therefore safety.

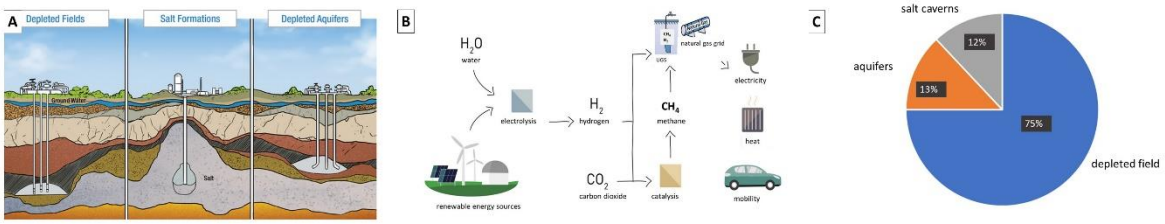

*Figure 1: **A**: schematic overview of the principle of Underground Gas Storage (UGS) within different geological bodies, from www.danaenergy.com ; **B**: schematic illustration of the principle of Power To Gas (PTG), modified after www.interconnector.de and www.fraunhofer.de; **C**: relative quantities of geological bodies suitable for UGS, modified after Tarkowski 2019;*

Methodology:

The presented study is an interdisciplinary approach among geoscientists and drilling engineers at Montanuniversität Leoben trying to link potential gas induced changes in the mineralogical phase composition of reservoir rocks and downhole cements to changes in their physical and mechanical parameters. In various projects a collection of siliciclastic sedimentary rocks as well as downhole cements were investigated. Important investigated parameters were permeability and porosity as well as compressive and tensile strength (Fig. 2-B). The mineralogical methods applied were XRD, EPMA, SEM (Fig. 2-D) and optical microscopy. Using mathematical models to correlate the density, p-wave velocity and compressive strength, ultrasonic measurements (Fig. 2-C) were conducted to provide insight regarding the potential damage to the samples. The rationale of the investigations is to compare non-treated samples (baseline) with those exposed to well-defined gas compositions for longer time spans. The experiments were done using hydrothermal autoclaves (100 bar, ambient temperature, Fig. 2-A) and individual experimental runs lasted 3 to 4 weeks.

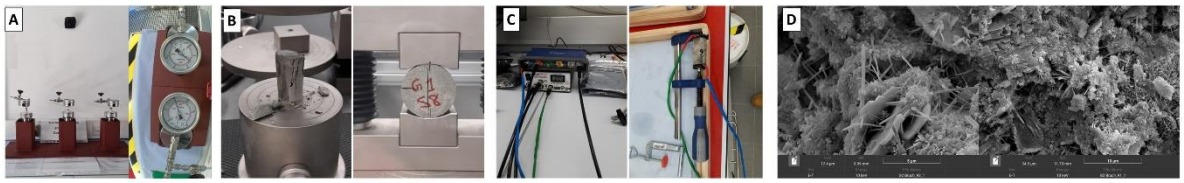

*Figure 2: **A**: images of the autoclaves used within these studies; **B**: set up for the mechanical testing (uniaxial compressive strength and tensile strength); **C**: set up of the ultrasonic measurements; **D**: FE-SEM investigations deliver high resolution images of the microstructure of downhole cements down to nanometer scale and the characteristics of the mineral phases composing them;*

Selected Results:

Fig. 3-A shows XRD diffractograms of baseline downhole cement (sample 1 & 2) compared to a downhole cement treated with CO_2 (sample 3). A clear change in the phase composition was observed. Ettringite and the clinker phases alite and belite disappeared and the formation of calcium carbonates and calcium sulphates was observed. Elemental mappings with EPMA (Fig. 3-B) allow the location of mineral phases likely susceptible to alterations caused by treatment with the above-mentioned gases (e.g., sulphur bearing phases like ettringite or monsulphate (Afm) (Fig. 3-B left) or ferric iron containing phases like brownmillerite (Fig. 3-B right).

Elemental mappings before and after autoclave experiments can be a powerful visualisation tool to support XRD data. Fig. 3-C demonstrates the correlation among the Ultrasonic P-wave velocity (UWV), Uniaxial Compressive Strength (UCS) and hydration age of different cement samples with various recipes. Using the proper correlation, density (ρ) can replace the hydration age, and hence a generic function of UCS was developed with respect to UWV and density. This function, as proof of concept shows that the non-destructive UWC reading could indeed be used to quantitatively monitor the compressive strength of cementitious materials.

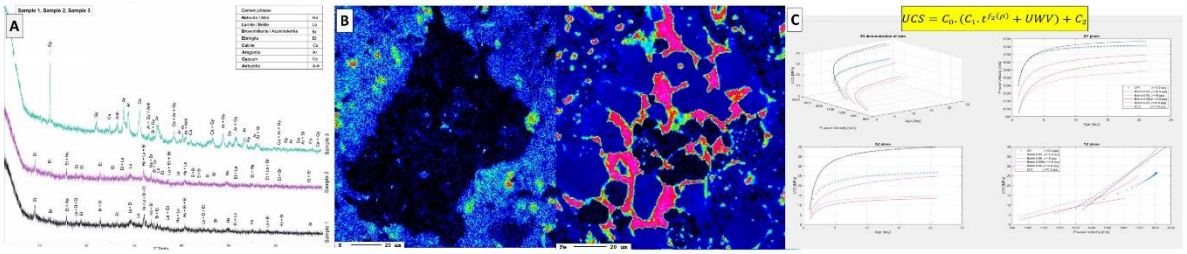

*Figure 3: **A**: XRD diffractogram of untreated and CO2 treated downhole cement; **B**: elemental mappings of S and Fe obtained with EPMA; **C**: developed correlation between UWV, UCS and ρ; C_0,C_1 & C_2 cement specific coefficients dependent on composition;*

References:
www.danaenergy.com
www.interconnector.de
www.ise.fraunhofer.de

R. Tarkowski, 2019, Underground hydrogen storage: Characteristics and prospects, Renewable and Sustainable Energy Reviews 105;

Poster presented at Pangeo 2022, 10th – 13th of September 2022.

dpe DEPARTMENT PETROLEUM ENGINEERING

MONTAN UNIVERSITÄT

Effect of Hydrogen on Downhole Cements

A fundamentals mineralogical investigation of downhole cements within the context of underground hydrogen storage

Introduction

Hydrogen is nowadays commonly considered a promising way of storing energy from renewable energy sources, helping overcome capricious weather as well as seasonal variations, hence increasing the efficiency of renewable energy sources. Underground Hydrogen Storage (UGHS) promises great potential due to vast storage capacities. However, to make UGHS a feasible process, fundamentals research investigating not just the integrity of reservoir and cap rocks, but also downhole materials used in boreholes against hydrogen is essential. Especially the effect hydrogen might have on the mineralogical phase composition and subsequently on physical and mechanical parameters of downhole cement is still very scarcely known. This research, which is part of a PhD programme of Montanuniversität Leoben on H_2 production and storage, aims to contribute to a better fundamental understanding of this issue.

Methodology

The rationale of this project is to link the mineralogical phase composition determined by basic mineralogical methods (XRD, FE-SEM, EPMA) to physical and mechanical properties. The physical properties investigated are porosity, pore size distribution and permeability, using Hg-porosimetry, N_2 sorption and nitrogen permeation. Mechanical properties investigated are compressive and tensile strength as well as hardness measurements of the individual mineralogical phases using nanoindentation. To investigate the influence hydrogen might have on these fundamental properties of downhole cement, autoclave experiments are planned to be carried out in the future where cement samples are treated for 3-4 weeks at defined T & p conditions and compared afterwards with the above-mentioned baseline investigations. Thermodynamic modelling was performed using the software GEMS (Gibbs Energy Minimization Selector) to evaluate whether a hydrogen-induced reaction in cements at thermodynamic equilibrium is possible at all.

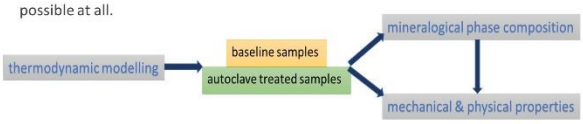

Results

First a proper preparation concept of cement samples for different mineralogical investigations had to be established since cements are very sensitive and easily altered during sample preparation. It was found that for optical investigation with a FE-SEM, looking at a fresh fractured surface (images below) yielded the best results, displaying very small, needle and platy like shapes of the different phases in the cement.

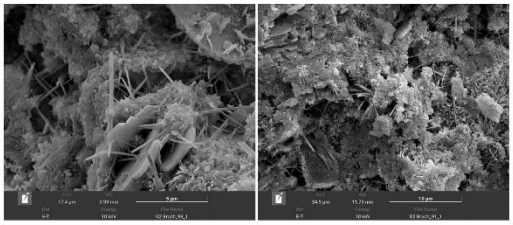

Thermodynamic modelling indicates that sulphate and ferric iron bearing phases like ettringite, Afm or the clinker phase ferrite are susceptible to hydrogen alteration, resulting in the formation of magnetite and iron sulfides (see graph below). Elemental mappings obtained by EPMA are a powerful tool to identify and localize above mentioned phases in the samples.

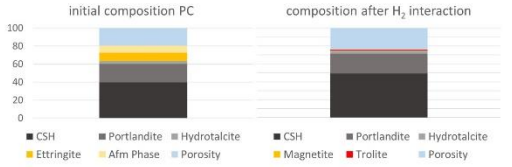

CSH	39.74
Portlandite	20.4
Hydrotalcite	3.31
Ettringite	9.14
Afm	7.81
Porosity	19.6
	100

CSH	49.1
Portlandite	22.3
Hydrotalcite	3.3
Magnetite	0.3
Troilite	0.7
Porosity	24.3
	100

Conclusion and outlook

- ❑ FE-SEM of fractured surface delivers high resolution images of the real characteristics of the nanostructure of cements
- ❑ Thermodynamic modelling indicates hydrogen induced changes
- ❑ EPMA elemental mapping can be a strong tool to identify sulphate and ferric iron bearing phases susceptible to hydrogen alteration as indicated by thermodynamic modelling
- ❑ In a next step autoclave experiments are conducted, and the hydrogen treated samples are compared to the baseline investigations

Thomas Sammer
Chair of Resource Mineralogy
At MUL since: 2021

Research Interests: mineralogy, applied mineralogy, sustainable energy production and storage,

WIP WELL INTEGRITY PLATFORM dpe

dpe.ac.at

Thomas Sammer
thomas.sammer@unileoben.ac.at

Chair of Resource Mineralogy,
Montanuniversität Leoben

RESOURCE MINERALOGY

Poster presented at the 3rd annual Well Integrity Workshop of the Well Integrity Platform of the Drilling and Completion Engineering Chair, 18th – 20th of October 2022.

A fundamentals mineralogical investigation of downhole cements within the context of Underground Hydrogen Storage

T. Sammer[1], K. Ravi[2], J. G. Raith[1];

[1]Chair of Resource Mineralogy, [2]Chair of Drilling and Completion Engineering, Montanuniversität Leoben, Austria
thomas.sammer@unileoben.ac.at

Introduction

Current energy politics aim for an environmentally sustainable and secure energy supply resulting in the substitution of conventional fossil fuels by renewable energy sources. To overcome weather and seasonal fluctuations in the energy production from e.g., wind or solar sources the promotion of large-scale and secure storage of green energy is a necessity. Hydrogen is nowadays commonly considered a promising way of storing energy from renewable energy sources, hence increasing their efficiency. Underground Hydrogen Storage (UHS) e.g., the idea of using natural geological bodies in the underground like aquifers, salt caverns or depleted oil and gas fields, promises great potential due to vast storage capacities (Fig. 1). However, to make UHS a feasible process, fundamentals research investigating not just the integrity of reservoir and cap rocks, but also downhole cements applied in boreholes during the storage life of the well against hydrogen is essential. This is particularly important once the injection scale is industrial, as there is a sever knowledge gap regarding the effect hydrogen might have on the mineralogical phase composition and subsequently on physical and mechanical parameters of downhole cement, which is a significant element for the well integrity and therefore safety. This research, which is part of a PhD programme of Montanuniversität Leoben on H_2 production and storage, aims to contribute to a better fundamental understanding of this issue.

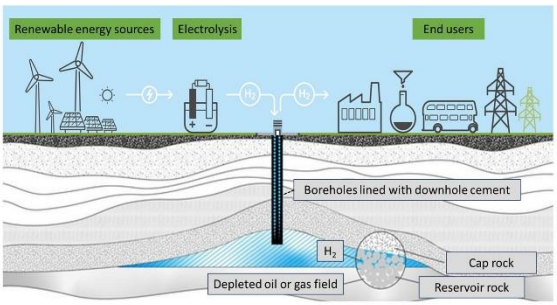

Figure 1: schematic concept of Underground Hydrogen Storage

Methodology

The presented study is an interdisciplinary approach among geoscientists and drilling engineers at Montanuniversität Leoben trying to link potential hydrogen induced changes in the mineralogical phase composition of downhole cements to changes in physical and mechanical properties (Fig. 2). Therefore, applied mineralogical methods are: XRD, FE-SEM and EPMA. The physical and mechanical properties investigated are porosity, pore size distribution and permeability, using Hg-porosimetry, N_2 sorption and nitrogen permeation as well as compressive and tensile strength, respectively. The rationale of the investigations is to compare non-treated samples (baseline) with those exposed to hydrogen for 3 - 4 weeks at well-defined p & T conditions using hydrothermal autoclaves. Additionally, thermodynamic modelling was performed using the software GEMS (Gibbs Energy Minimization Selector) to evaluate whether a hydrogen-induced reaction in cements at thermodynamic equilibrium is possible at all.

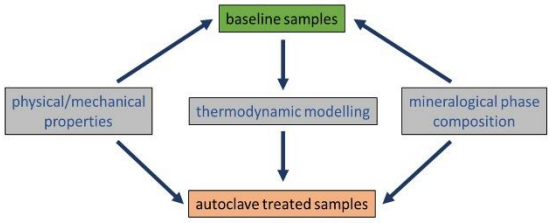

Figure 2: Methodology of the presented study

Results

Thermodynamic modelling (Fig. 3) indicates that certain redox-sensitive phases within hardened downhole cement are susceptible to hydrogen alteration caused by the strong reducing character of hydrogen. Especially ferric iron and sulphate bearing phases like brownmillerite, monosulfoaluminate (AFm) and ettringite (AFt) are altered, resulting in the formation of magnetite and iron sulphides.

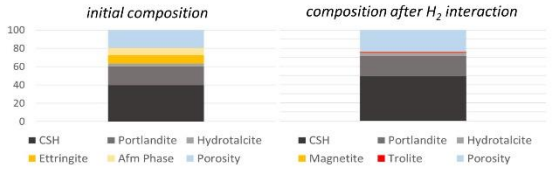

CSH	39.74
Portlandite	20.4
Hydrotalcite	3.31
Ettringite	9.14
Afm	7.81
Porosity	19.6
	100

CSH	49.1
Portlandite	22.3
Hydrotalcite	3.3
Magnetite	0.3
Troilite	0.7
Porosity	24.3
	100

Figure 3: results of thermodynamic modelling

X-ray Diffraction (XRD) measurements indicate the absence of AFm phase and the formation of ettringite within the hydrogen treated sample (Fig. 4). According to the results of thermodynamic modelling, ettringite should also be absent. This contradiction is not yet fully understood. Maybe thermodynamic equilibrium was not reached during H_2 treatment.

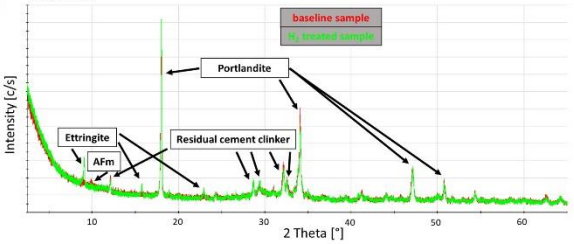

Figure 4: XRD data of baseline and hydrogen treated sample

SEM-EDS analysis show the formation of iron sulphides within the H_2 treated sample (Fig. 5). Even though only minor amounts of small (<3 µm) grains are found, this confirms the results of thermodynamic modelling.

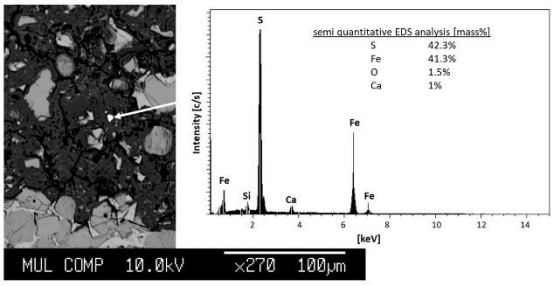

Figure 5: SEM - EDS analysis of hydrogen treated sample

Conclusion

- Thermodynamic modelling indicates hydrogen induced changes in the mineralogical phase composition of downhole cements.
- XRD indicates the absence of AFm phase in hydrogen treated samples.
- SEM-EDS analysis confirm the formation of iron sulphides as indicated by modelling

This research activity has received funding from Montanuniversität Leoben and is part of the Strategic Core Research Area SCoRe A+ Hydrogen and Carbon

SCoRe A+ Strategic Core Research Area Hydrogen and Carbon

Poster presented at Goldschmidt 2024, 9th -14th of July 2023.

dge DEPARTMENT GEO ENERGY

MONTAN UNIVERSITÄT LEOBEN

Influence of H_2 on Downhole Cements during Underground Hydrogen Storage

i) Introduction

Underground Hydrogen Storage (UGHS – Fig. 1) offers vast storage capacities, however, fundamentals research investigating the integrity of reservoir and cap rocks as well as downhole materials used in boreholes against hydrogen is essential.

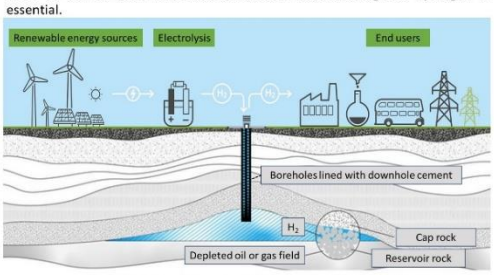

Figure 1: schematic concept of Underground Hydrogen Storage

ii) Project Description

The influence of hydrogen on the mineralogical phase composition and subsequently on physical and mechanical parameters of downhole cement is scarcely known. This study aims to contribute to a better fundamental understanding how hydrogen might influence the mineralogical phase composition of downhole cement and subsequently its physical and mechanical properties.

iii) Methodology

Hydrothermal autoclave experiments exposing hydrated cement pastes of class G cement to hydrogen in a defined but closed environment are carried out. Mineralogical investigations combined with nitrogen sorption/desorption experiments were performed before and after hydrogen treatment to evaluate any changes to the initial state of the investigated cement paste.

case	temperature	pressure	
i	-	-	Untreated reference
ii	-	-	Exposed to 10 wt% brine – wet reference
iii	22°C & 80°C	80 bars	Pure H_2 atmosphere – dry H_2
iv	22°C & 80°C	80 bars	H_2 and 10 wt% brine – wet H_2

iv) Results

X-ray diffraction analysis (Fig. 2) revealed only minor changes to the mineralogical phase composition of the investigated cement pastes, especially in the 5°-15° 2θ range. Decomposition of AFm and formation of ettringite were observed for low T treatment cases.

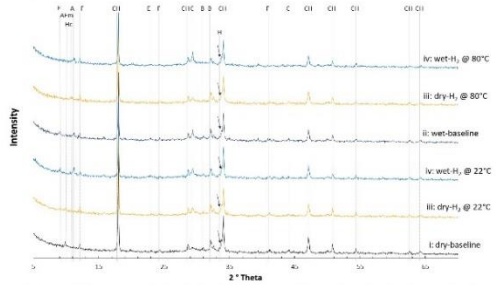

Fig. 2: X-ray diffractogram, E = Ettringite, AFm = Monosulphate, Hc = Hemicarbonate, A = Ca-Al-Hydrate, CH = Portlandite, C = Calcite, B = Belite, H = Hibschite

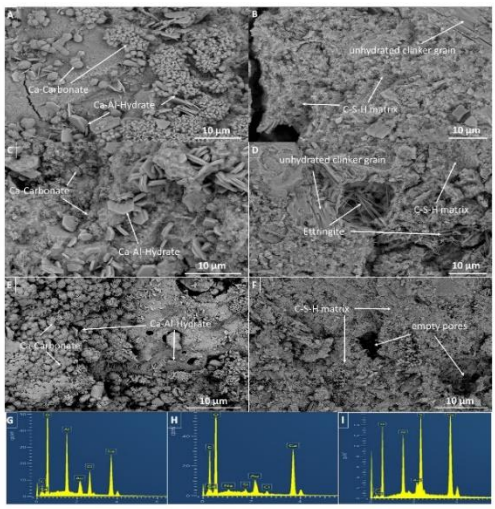

Fig. 3: Back scatter electron microphotographs obtained with a scanning electron microscope of samples of case ii (A and B) and iv @ 220°C (C and D) and @ 80°C (E and F); G-I: representative EDX spectra of Al-Ca-hydrate (G), Ca-carbonate (H) and ettringite (I) observed in the samples; the Au peak is from the coating.

The findings of XRD-analysis were confirmed by the observation of acicular ettringite crystals under the SEM (Fig. 3). At high T treatment, Ca-Al hydrates with hexagonal, platy shape did form. Nitrogen adsorption/desorption experiments delivered comparable results for the treated cement pastes and the baseline samples (Fig. 3).

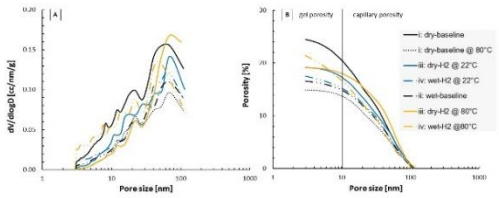

Fig. 4: results of nitrogen sorption experiments, A: pore size distribution, B: porosity vs. pore size in semi-logarithmic display.

v) Conclusion & Outlook

- Hydrogen does not influence the major phase composition of class G cement.
- Hydrogen and brine presence favour ettringite formation at low T.
- Microstructure and pore size distribution are not influenced by hydrogen.
- Very low permeable cement of class G shows low reactivity with hydrogen.
- Future research need to consider:
  - longer experimental durations.
  - Curing conditions at higher T & p
  - Different mix formulations and cement classes

Name: Thomas Sammer
thomas.sammer@unileoben.ac.at

WIP WELL INTEGRITY PLATFORM

Research Interests: Applied mineralogy
Downhole cements

www.dpe.ac.at
www.2023wip.ac.at

Poster presented at 4th annual Well Integrity Workshop of the Well Integrity Platform of the Drilling and Completion Engineering Chair, 23rd – 25th of April 2024.

Annex C

Cement and Concrete Research 182 (2024) 107555

Contents lists available at ScienceDirect

Cement and Concrete Research

journal homepage: www.elsevier.com/locate/cemconres

Influence of broad ion beam polishing on the surface roughness of hydrated cement paste and its implications on microstructural analysis

Thomas Sammer [a,*], Xiangyun Shi [a], Muhammad Zubair Khan [b], Aleksandar Matkovic [b], Christian Teichert [b], Johann G. Raith [a]

[a] Department Applied Geosciences and Geophysics, Montanuniversität Leoben, Peter Tunner Straße 5, 8700 Leoben, Austria
[b] Department Physics, Mechanic and Electrical Engineering, Montanuniversität Leoben, Franz Josef Straße 18, 8700 Leoben, Austria

ARTICLE INFO

Keywords:
Broad ion beam milling
Hydrated cement paste
Surface roughness analysis
Atomic force microscopy
Image processing

ABSTRACT

In recent years, the technical capabilities of high-resolution Scanning Electron Microscopes (SEM) improved significantly. To fully utilise their potential, it is crucial that also the preparation techniques are advanced to obtain a high-quality surface which preserves even nanometre sized microstructural features. In this study, state-of-the-art resin-embedded polishing, and novel Broad Ion Beam (BIB) milling of hydrated cement paste are compared. SEM microstructural investigations are aided by image processing to determine porosity and pore geometry factors. Additionally, a comprehensive quantitative surface roughness analysis based on Atomic Force Microscopy scans is carried out. BIB-milling enabled the study of nanoscale features such as gel porosity or the acicular morphology of calcium-silicate-hydrates. Pores exhibit increased aspect ratios whereas resin-embedded polishing results in higher circularity. However, a superior vertical surface roughness was achieved by the resin-embedded polishing approach. The research highlights the advantages and drawbacks of BIB-milling as a polishing method for hydrated cement pastes.

1. Introduction

High-resolution scanning electron microscopy (SEM) is an established method to carry out microstructural studies of cements and cementitious materials. It is also a common technique to visualize structures in the micro- to nanometre range [1]. To achieve this, fractured, or polished surfaces are investigated. However, due to rough surface characteristics of fractured surfaces only secondary electron imaging is possible limiting conclusions to morphological features only. Furthermore, fractured surfaces are considered non-representative since cracks propagate through the weakest portion of the material [2]. Therefore, to take full advantage of all capabilities that modern SEM instruments offer, smooth and flawless polished sample surfaces are a prerequisite. This allows collection of electron backscatter diffraction patterns, providing information about the crystallinity and crystal orientation of phases. Moreover, it facilitates chemical analysis through techniques such as energy dispersive spectroscopy (EDS) and wavelength dispersive spectroscopy (WDS) carried out by SEM and electron probe micro analysis (EPMA) as well as image analysis which can provide valuable information about porosity or pore size distribution (PSD) [3,4].

There is no normative procedure for the preparation of polished cement-based samples, but only common practice by impregnating the sample in resin followed by abrasive grinding and polishing using e.g., diamond pastes [4]. This is a very tedious task and prone to introduce preparation artefacts [2]. Achieving a sufficiently flat surface, a prerequisite for accurate chemical microanalysis, is particularly challenging due to the varying hardness and polishing behaviour of the various phases in cement-based sample material [5–7]. Consequently, this often results in the development of a surface with a certain microroughness, influencing quantitative chemical analyses with SEM and EPMA [4,8,9]. Quantitative image analysis for microstructural studies of cement pastes or cementitious materials to obtain porosity, pore size distributions or pore shapes is likely also to be affected by the slightest changes in surface irregularities [10].

Conventional polishing techniques limit the resolution of calcium silicate hydrates (C—S—H phases), ettringite and pores to about 100–200 nm [1]. Especially the phases, which are characterized by a nano-scale structure much smaller than that, cannot be differentiated in conventionally polished samples [3]. Modern diode backscatter electron

* Corresponding author.
E-mail address: thomas.sammer@gmx.net (T. Sammer).

https://doi.org/10.1016/j.cemconres.2024.107555
Received 20 March 2024; Received in revised form 6 May 2024; Accepted 23 May 2024
Available online 1 June 2024

(BSE) detectors allow SEM operation at low beam acceleration voltage (e.g., 1 kV) which reduces the penetration depth of the electron beam and allows improved image resolution [11]. These technical advances make it necessary to also improve the preparation techniques for cement pastes and cementitious materials to exploit the full potential of modern SEM instruments.

One advanced preparation method is broad ion beam (BIB) milling [12]. There, the sample is polished by ions, usually argon ions, which are shot onto the sample surface at a grazing angle of incidence. A sharp tungsten blade is employed to control the ion beam ensuring the controlled erosion of the material resulting in polished surface with minimal mechanical damage.

In the present study a resin-embedded, conventionally polished as well as a BIB-milled hardened cement paste are compared using SEM microstructural investigations extended by image processing. Additionally, a comprehensive quantitative characterization of the surface roughness is carried out using Atomic Force Microscopy (AFM) to provide a more detailed differentiation between the two polishing techniques.

2. Material and methods

2.1. Samples

For this study, an oil well cement of class G (ordinary portland cement) was used and mixed according to the specification 10A of the American Petroleum Institute (API Spec 10A [13]). The water to cement (w/c) ratio was 0.44 and the mixed slurry was poured into cylindrical brass moulds with 2.54 cm diameter and 5.08 cm length. After pouring the slurry was cured in a closed water bath container for 28 days. After 28 days the hardened paste was demoulded, cut into 5 mm slices using a water-cooled stone saw and placed in isopropanol for 24 h for solvent exchange to stop hydration. After that the slices were dried at 40 °C until constant mass was achieved and stored in a desiccator to limit carbonation.

2.1.1. Conventional resin-embedded polishing

For this study, a "best practice" procedure based on the preparation described in [2] with some adaption from [4,14] was performed. Therefore, a dried slice was first briefly manually dry grinded on a sandpaper with a grain size of 1000 grid followed by vacuum impregnation in EPO-TEK 301 resin. The resin was cured for 3 days at room temperature. After that, the top-part of the resin-impregnated surface was carefully removed by hand on a grinding disc to free the initial sample surface using ethylene glycol as lubricant. Here, extreme caution was taken to not remove too much sample material. Then the sample surface was lapped manually for several minutes using silicon carbide with a grain size of 1000 and isopropanol as lubricant. After that, automated polishing using a Struers Tegramin 30 grinding and polishing machine was performed. In total, five polishing steps using a water free alcohol based monocrystalline diamond suspension spray (DP-spray M) from Struers of 9, 6, 3, 1 and 0.25 μm diamond size were carried out. For the first three polishing steps, polishing disc MD-Plan, and for the last two steps MD-Dur from Struers were used. Each polishing step took about 3–4 min with the polishing disc rotating at 150 rounds per minute and a force of 15 N applied on the sample. After each polishing step the sample was cleaned ultrasonically in isopropanol.

2.1.2. Broad ion beam polishing (BIB-milling)

A dried slice was cut into roughly 7 × 5 mm^2 rectangles with defined sharp edges so that the sample fitted into the BIB-milling device. A Isomet low speed saw from Buehler and oil as lubricant was used for cutting. After that the sample was polished using an argon ion beam with a Hitachi ArBlade 5000 system operating in the cross-section milling mode using a tungsten blade. BIB-milling took 3 h at a milling energy of 8 keV.

2.2. Image acquisition with Scanning Electron Microscopy (SEM)

Samples prepared by both methods were imaged by a TESCAN CLARA field emission (FE) SEM. Before imaging, the polished samples were coated with an approximately 10 nm thick gold layer using a Cressington Sputter Coater 108 auto with 30 s sputtering time to obtain a conducting surface. The SEM was equipped with the TESCAN Essence Image Snapper software (version 1.0.8.0) which allows capturing and stitching of high-resolution images. Both BSE and secondary electron (SE) images were obtained. The acceleration voltage was set at 10 kV and the beam current at 1 nA.

2.2.1. Image processing

SEM images were processed using the open-source software ImageJ [15,16] and ilastik [17,18]. Image processing focused on segmentation of pore space and cracks, followed by statistical analysis of segmented areas to obtain pore space information such as porosity, pore size distribution, and pore geometry factors (e.g., aspect ratio, circularity). Pore space appears to be uniformly dark in BSE images, whereas in SE images pore space may occasionally be illuminated and appears bright, which complicates the segmentation process. Therefore, BSE images were used for segmentation while SE images were used to clarify any ambiguous pore boundaries. All images were first processed using the machine learning-based pixel classification workflow in ilastik to separate pore space from other phases [19]. The segmented images were then further converted into binary images using the global thresholding method in ImageJ. As all void space shows the same grey value, pores and cracks were barely distinguished by the automatized global thresholding method. Thus, large cracks that were only observed in the BIB-milled sample were manually selected and removed to correct for artefacts introduced by sample preparation. The occurrence of such large cracks in the BIB-milled sample is caused by the use of a low-speed saw during the pre-cutting of the sample to obtain defined edges to fit into the BIB-milling device (see Section 2.1.2). Example of pore segmentation and crack correction are shown in Fig. 1. Based on the segmented binary images, geometry information such as pore area, aspect ratio and circularity were extracted with the 'Analyze Particle' function in ImageJ.

2.3. Atomic force microscopy

AFM is a high-resolution scanning probe microscopy technique that provides a three dimensional (3D) topographical information of the sample surface on the nanometre scale [20]. AFM scans are obtained by a cantilever probe with a sharp tip at the free end which is moved across the surface of the sample using a high-precision piezoelectric stage. The deflection of the cantilever during the contact with the specimen surface is recorded, and a topographical representation of the surface as $z(x_i, y_j) = z(r)$ is generated.

In this study, AIST NT AFM system was used in tapping mode and under ambient conditions. Nu-Nano SCOUT probes were employed with nominal spring constant 42 N/m, resonant frequency ~ 350 kHz, and tip diameter < 20 nm.

The measured samples were polished as described in Section 2.1 and cut to size with a low-speed saw to fit into the sample holder of the AFM. AFM does not require a conducting surface in contrast to SEM. Hence only uncoated samples were measured. For each sample 16 areas with a size of 20 × 20 μm^2 were measured and topographical images recorded in high resolution. Pixel size was set to below 15 nm, so that the lateral resolution of the images is mainly probe limited. To avoid a selection bias and ensure a representative recording of the topographical surface the in total 16 areas of each sample were arranged in an artificial grit of 4 × 4 with a distance of 100 μm between the individual 20 × 20 μm^2 areas. The data processing of the recorded topographical images was carried out in the open-source software Gwyddion [21] delivering 16 datapoints of roughness parameters σ and ξ for each sample (for

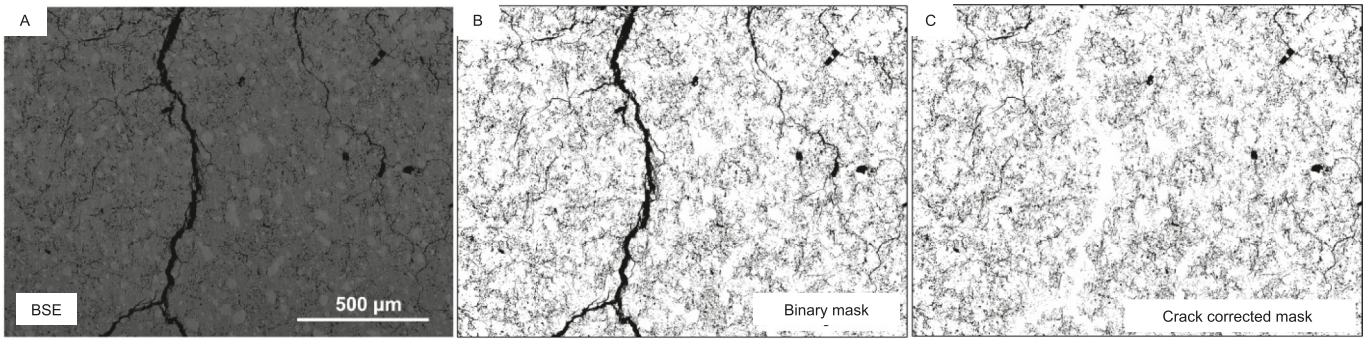

Fig. 1. Illustration of image processing applied in this study. A: Original BIB-SEM image in BSE mode. B: Segmented binary mask of void space (pore and crack) in A. C: Crack corrected pore mask in B.

description see Section 2.3.1.), and from which the arithmetic mean was calculated.

2.3.1. Height-difference function and height-height correlation function

The height-difference function and height-height correlation function analysis were applied to the AFM scans allowing a comprehensive, quantitative surface roughness evaluation on the nanometre scale [21,22]. For properly polished surfaces we can assume isotropic surface roughness, i.e., no preferential direction of surface features. Thus, it is sufficient to analyze the 1D height-difference function C(x) which is averaged over all scan lines. C(x) is defined as:

$$C(x) = < [z(x_0 + x) - < z >][z(x_0) - < z >] > \quad (1)$$

where <…> means the average over all possible point pairs in the line scan that are separated by a distance x and <z> is the average height. For polished cement pastes, a random rough surface is expected. If this lacks complete long-range order and shows a self-affine (e.g., the height fluctuations are much smaller than the lateral dimensions [22,23]) fractal behaviour on a short length scale and is smooth on a long length scale, the height-difference function can be simply approximated by:

$$C(x) = \sigma^2 \, exp.\left[- (|x|/\xi)^{2\alpha} \right]. \quad (2)$$

where σ, usually called rms roughness, denotes the root mean square of the deviations of the surface from the average height level < z>. σ is the most commonly used parameter to characterize vertical roughness of surfaces [23–25]. As can be seen from the approximation of Eq. (2), σ can be determined from the height-difference function, as σ^2 corresponds to C(0). However, in this study σ was obtained by using the "statistical quantities" function in Gwyddion [21] on the AFM scans. ξ represents the lateral correlation length and denotes the average length across which the heights between two surface points are correlated. It is a measure for the lateral roughness fluctuations. The lateral correlation length is characterized by the value of |x| at which C(x) decays to σ^2/e. α is called the roughness exponent or Hurst parameter [26]. It indicates how jagged a surface is and usually ranges between 0.5 and 1. Smaller values represent a very jagged surface with sudden fluctuations in height, whereas values close to 1 mean a less jagged surface. The roughness exponent can be determined by analysing the height-height correlation function H(x), (Eq. (3)) [25]:

$$H(x) = < [z(x_0 + x) - z(x_0)]^2 > . \quad (3)$$

For a surface with self-affine fractal behaviour, it can be shown that at small distances ($x \ll \xi$) H(x) has an asymptotic power-law form $H(x) \approx x^{2\alpha}$ and saturates at a value of $2\sigma^2$ for long distances ($x \gg \xi$). This allows the determination of α from the initial slope of the log-log plot of H(x). The determination of the set of roughness parameters σ, ξ, and α allows a comprehensive quantitative characterization of a random rough surface [26].

3. Results and discussion

3.1. Scanning electron microscopy imaging

Fig. 2 shows SEM images of the resin-embedded, conventionally polished sample in both SE and BSE modes. SE images reveal the topographic contrast while BSE images display compositional contrast. A general impression of a smooth surface with visually low relief is depicted (Fig. 2-A). However, it seems that a slight relief developed between residual clinker grains and the surrounding hydrated cement matrix indicated by the very fine but bright rim around some of the larger residual clinker grains (Fig. 2-A). This topographical effect can be explained due to the different response of the various phases in the hydrated cement paste to the mechanical forces applied during the grinding and polishing process of the conventional preparation method. Differences in hardness and grain size of the various phases might lead to different behaviour during polishing leading to, even though visually minor, topographical differences.

Some pores displayed in Fig. 2-A seem to be empty. Either the resin did not impregnate into them during the resin-impregnation, or the resin was chipped out during the mechanical polishing. Although the used resin of EPO-TEK 301 is a very low viscosity resin, a complete resin impregnation is challenging since hydrated cement pastes are characterized by very low permeability. To achieve a flat, polished surface with a conventional polishing approach, it is essential that the resin impregnates into the pores. Once cured, it preserves the pores to withstand the subsequent grinding and polishing. Insufficient resin impregnation would lead to a loss of microstructural detail and biased conclusions [2,4]. In general, the pores seem to have an irregular shape but with a general round morphology and are of several µm in size classifying them as capillary pores (Fig. 2-B, D, E).

BSE images (Fig. 2-B) allow to differentiate chemically different phases within the hydrated cement paste by their grey shades. Alite (C_3S) can be identified by its middle grey colours and its more angular shape compared to the rather rounded shape of belite (C_2S). In some belite grains, lamellas indicating solid solution of C_2S polymorphs can be observed. The ferrite phase (C_4AF) is characterized by the highest grey scale brightness and is often found as an interstitial phase between alite and/or belite grains or in their vicinity.

From these images one can conclude that the conventional polishing delivers relatively good surface quality especially for the larger residual clinker aggregates. Furthermore, the hydration frontline within residual clinker and developing hydration matrix can be seen (Fig. 2-C & D) allowing assumptions about inner and outer hydration products. However, detailed microstructural studies of the hydration products, e.g., such as C—S—H in its typical granular or acicular shape or gel porosity is not enabled in this sample. This is likely because such nano meter features are "buried" by the resin, limiting their investigation. Since nowadays SEMs equipped with a field emission gun as electron source, are capable of also resolving features down to a few nanometres, a

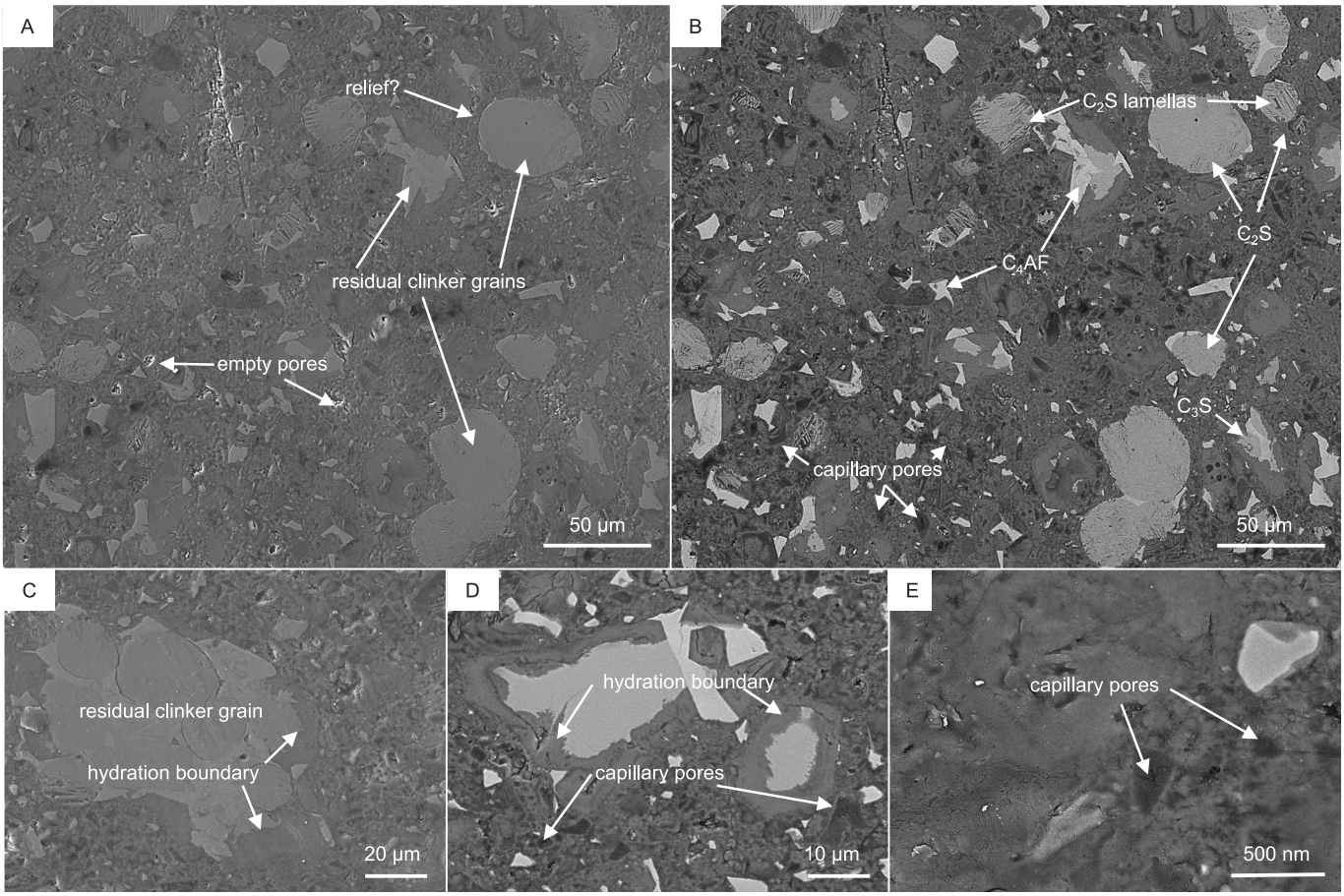

Fig. 2. SE and BSE images of the conventional resin-embedded polished sample. A: SE image illustrating the overall surface morphology. B: BSE of the same area as in A. C (SE), D & E (BSE) image at higher magnifications illustrating the roundish shape of pores. C_2S: belite, C_3S: alite, C_4AF: ferrite.

polishing process without the need for resin would be superior as it would not encounter such resin caused limitations.

Fig. 3 shows SEM images of the BIB-milled sample in both SE and BSE modes. Curtaining, i.e., the linear features caused by the argon ion beam oriented parallel to the BIB-milling direction [27] is visible in this sample. However, this artificial structure is no longer visible at higher magnifications (Fig. 3-D & E). There is no clearly visible relief difference between the residual clinker phases and the hydrated C—S—H matrix rather than the phase independent mentioned curtaining. At higher magnification in the nanoscale range, distinct features of the hydrated C—S—H matrix become visible, e.g., the acicular morphology (Fig. 3-C). Noticeable is the bending which was observed in real time during the SEM investigation of individual needles, which is caused by the interaction of the electron beam of the SEM. High water content, electrical non-conductivity and the general fineness of C—S—H needles can lead to electron beam induced bending, melting or general damage [3,4,28]. This phenomenon can develop already at low accelerating voltage and beam currents and short exposure times. The polishing obtained with BIB-milling moreover allows distinguishing capillary and gel porosity (e.g., pores <10 µm & <10 nm respectively; Fig. 3-D & E). Also, the shape of the capillary pores looks different compared to the roundish shape of the pores in the conventionally polished sample with a more natural angular and elongated shape. This difference can be explained by the lack of mechanical lateral forces which could cause the round character of pores in the conventional polished sample (Fig. 2).

In general, these SEM investigations demonstrate that BIB-milling leads to a surface with more natural characteristics enabling the study of nano scale features in hydrated cement pastes such as C—S—H needles or the nanometre sized gel porosity. It seems that the smallest pores are not affected by BIB-milling. This is not the case for the resin-embedded, and conventionally polished sample as these pores are covered by the resin and therefore not visible. On the other hand, it seems that the residual polyphase clinker grains can be much better studied in the conventionally polished sample. Features such as the typical lamellas in belite are not observed in the BIB-milled sample. The effects of curtaining seem to affect the smoothness and roughness of the BIB-milled surface (Fig. 3-A). However, these lines are only visible at low magnification. Another severe disadvantage of BIB-milling is the rather small area that can be polished. Only a few mm^2 can be polished in reasonable time. In contrast, resin-embedded, conventional polishing allows larger sample areas to be prepared and investigated. For thoroughness, one has to mention that the in this study used ion milling device from Hitachi (see Section 2.1.2.) can provide a second operation mode compared to the in this study applied cross section mode. The so called “Flat milling” mode allows the polishing of slightly larger areas by rotation the sample perpendicular to the ion beam compared to the cross-section mode. However, the size of such polished areas is still in the mm^2 range compared to cm^2 of conventional polishing. Furthermore, according to the manufacturer Hitachi, flat milling is mainly used for removing of surface layer artefacts and final polish after traditional mechanical polishing methods. Also, due to the rotation of the sample a bowl like shape of the surface is created, especially for larger polished areas. However, it would be interesting for future studies to evaluate flat milled cement pastes as this was not within the scope of this study.

Another drawback of BIB-milling is that the ion beam used for polishing must have a very high energy (>6 keV). This may induce a thermally damaged volume underneath the polished area corrupting microchemical analyses, e.g., EPMA. Also, redeposition of eroded

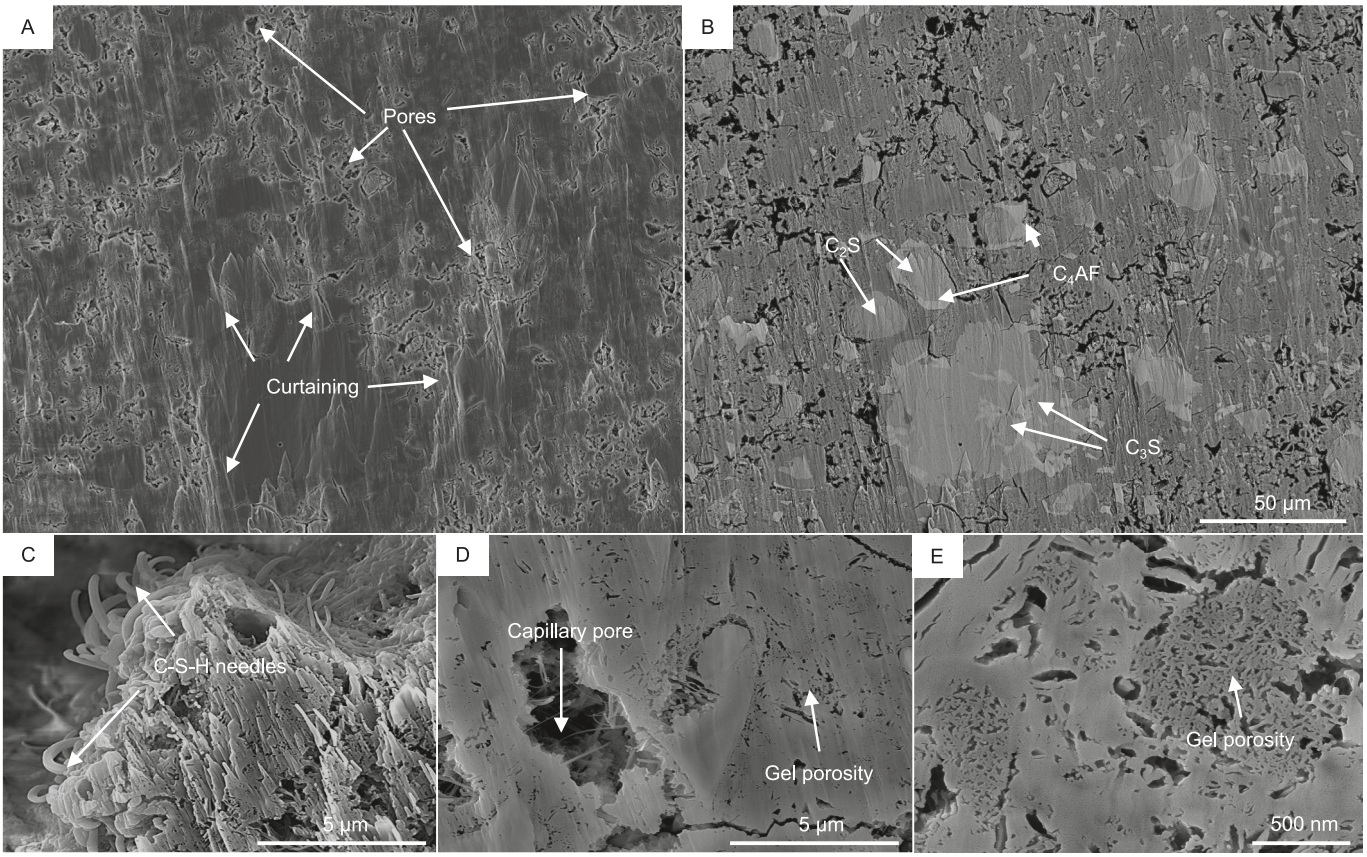

Fig. 3. SE and BSE images of the BIB-milled sample. A: SE image illustrating the surface morphology. B: BSE image of the same area as in A. C, D & E: SE image at higher magnification illustrating details such as acicular morphology of C—S—H phases and gel porosity. The bend characteristic of the C—S—H in C is not the natural appearance of C-S-H but caused by the energy of the electron beam during SEM investigation. C_2S: belite, C_3S: alite, C_4AF: ferrite, C—S—H: calcium silicate hydrate phases.

material and of material from the BIB-milling device itself, e.g., from the tungsten blade, may cause preparational induced artefacts on the surface.

In conclusion, the findings of the visual SEM investigation carried out in this study strikingly display the ability and advantages of the BIB-milling process to enable superior microstructural investigations such as gel porosity or nano features of C—S—H.

3.2. *Image processing and pore statistics*

To quantitatively compare the results of SEM imaging two different image processing approaches were applied: (i) the conventional global thresholding method in ImageJ was sufficient for segmenting void space in SEM images of the BIB-milled sample owing to the strong contrast between the solid phase and void space (Figs. 3-B, 4-A & B). Still, certain manual correction was necessary to obtain reliable porosity estimates due to the micro-cracks induced by the pre-cutting process required for BIB-milling using a low-speed precision saw (see Section 2.1.2). (ii) The more advanced machine learning-based pixel classification approach in ilastik was required for processing SEM images of the resin-embedded, conventionally polished sample. In the conventionally polished sample, a significantly less porous impression of the greyish matrix area is affirmed by the hindered segmentation of pore space with the thresholding method in ImageJ (Fig. 4-C). The grey areas appear to be mainly resin filled pores or other remnant phases of low atomic number or light element compounds e.g., polishing material such as silicon carbide or diamond paste smears. Moreover, the blurred pore edges and topographical differences in porous areas hamper the interpretation of true pore space in the conventionally polished sample (Fig. 4-E). The ImageJ thresholding method clearly underestimate the porosity, as it does not capture the complete pore area because of low contrast greyish areas. In contrast, the pixel classification method in ilastik delivers a better segmentation of the porous area (Fig. 4-G) based on not only the grey values but also the detected edge features. Although, this method has limitations as the resin in the pores often hides the real shape of the pores and covers the edges. Overall, the different surface polishing techniques result in different surface roughness that can influence image processing. In summary, images of BIB-milled samples are easier to segment because pore edges are better visualized in BIB-SEM images and not masked by resin.

Table 1 summarizes the information on porosity and pore geometry obtained from the SEM images processed for the conventionally polished and BIB-milled samples. The porosity of the two polishing techniques is significantly different, with the conventional polished sample having clearly lower porosity values compared to the BIB-milled one, i.e., 1.4–3.9 % vs. 12–14 %. This is explained by resin filled pore space not being able to be fully segmented by the applied image processing. The number of segmented pores is significantly lower for the conventionally polished sample in contrast the BIB-milled one (Table 1). Concerning the pore geometry factors, BIB-milling leads to lower circularity (roundness) and slightly higher aspect ratios of the segmented pores. The median and mean perimeter/area values are higher in the conventionally polished sample confirming what was stated before that the resin hinders the segmentation of especially smaller pores. It is noted that mean and median area and perimeter values are overall higher in larger sized images, indicating that the resolvability of pore features is mainly controlled by the pixel size of the images and not so much by the polishing technique. Nevertheless, similar sized images (e.g., con.-pol. 2 vs.

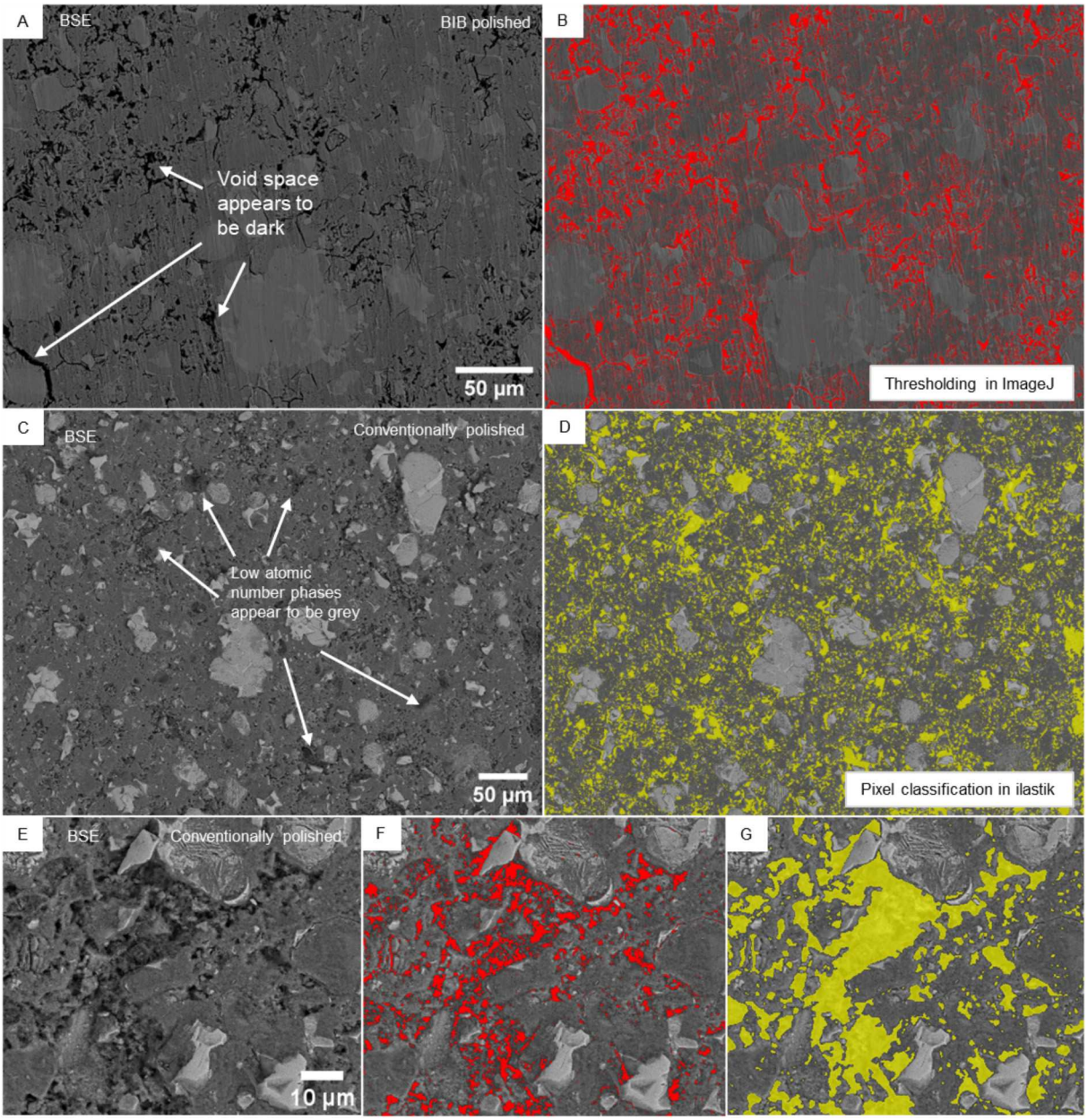

Fig. 4. Segmentation of pore space by thresholding in ImageJ versus pixel classification in ilastik. A: Exemplary SEM BSE image of BIB-milled sample. B: Pore space of A is shown in red, ImageJ thresholding. C: Exemplary SEM BSE image of conventionally polished sample. D: Pore space of C is shown in yellow, ilastik pixel classification. E-G: SEM BSE image at higher magnification of conventionally polished sample for comparison of thresholding (red) and pixel classification (yellow) results. (For interpretation of the references to colour in this figure legend, the reader is referred to the web version of this article.)

BIB-pol. 2 and BIB-pol. 3) of both polishing methods yield significant differences in porosity and pore geometry factors confirming a superior microstructural visualization by BIB-milling. All presented data in Table 1 for the BIB-milled sample is for manual crack-corrected images, as the presence of such larger artificial cracks (Fig. 1) significantly increased the porosity while the pore geometry factors were not affected by this correction.

Fig. 5 shows statistical distribution plots of the pore space analysis for all SEM images listed in Table 1. The pore frequency is plotted against the equivalent pore diameter in logarithmic scales, which typically follows a power law function indicating self-similar behaviour and allows distinguishing inherent pore characteristics resolved in SEM images (Fig. 5-A) [29,30]. The proximity of distribution lines for different images in log-log plots corresponds well with the pixel size of the SEM images (Fig. 5-A, Table 1). The processed images of the conventionally polished sample con.-pol. 1, con.-pol. 2 and especially con.-pol. 3 define separate lines in the log-log plot, displaying the influence of the different pixel size of the SEM images. The images of the BIB-milled sample BIB-pol. 2 and BIB-pol. 3 are of same size and mostly overlay on the log-log plot and are in close proximity to similar sized image con.-pol. 1 and con.-pol. 2. These distinct patterns in such log-log plots affirm that the resolvability of pore features is determined by the resolution and therefore the pixel size of the SEM images and not the polishing method.

The cumulative porosity and pore size distribution (Fig. 5-B) displays the significant difference in the segmented porosity values for the compared preparation techniques. In contrast to the BIB-milled sample, where the obtained porosity values decreased with decreasing pixel size, the conventional polished sample does not follow this trend. Here, the image with the largest pixel size has the lowest porosity.

Table 1
Information obtained from the SEM images used for processing and the calculated median and mean + standard deviation values for the pore geometry factors aspect ratio, circularity, perimeter, and area of the pore statistical analysis of both the conventionally polished and the BIB-milled sample, all images were obtained with a resolution of 2560 × 2219 pixels.

Sample	Image ID	Pixel size [nm/px]	Number of pores	Porosity [%]		Aspect ratio	Circularity	Perimeter [μm]	Area [μm^2]
Conventional polishing	Con.-pol. 1	220	2845	1.45	Median	1.92	0.72	2.78	0.43
					Mean	2.38 ± 1.69	0.67 ± 0.24	5.41 ± 7.09	1.99 ± 6.43
	Con.-pol. 2	110	1331	3.91	Median	1.87	0.71	2.97	0.49
					Mean	2.18 ± 0.98	0.71 ± 0.24	4.45 ± 4.83	1.42 ± 4.34
	Con.-pol. 3	55	1621	3.04	Median	1.95	0.79	0.89	0.05
					Mean	2.49 ± 1.72	0.73 ± 0.26	1.71 ± 3.10	0.32 ± 2.27
BIB-milling crack corrected	BIB-pol. 1	600	26,119	13.44	Median	2.03	0.57	8.85	3.54
					Mean	2.36 ± 1.10	0.58 ± 0.27	17.29 ± 38.18	13.93 ± 42.19
	BIB-pol. 2	136	19,091	13.65	Median	2.15	0.49	1.81	0.13
					Mean	2.52 ± 1.37	0.52 ± 0.25	3.92 ± 11.89	0.65 ± 4.41
	BIB-pol. 3	136	14,317	11.05	Median	2.07	0.59	1.70	0.15
					Mean	2.47 ± 1.35	0.60 ± 0.26	3.70 ± 9.71	0.70 ± 4.08

The BIB-milled sample has overall slightly higher aspect ratio values (Fig. 5-C, Table 1), which is probably due to better visualization of pore edges in the BIB-milled sample (Figs. 3 & 4). Also, during the conventional polishing process the presence of resin might cover the original pore structure as well as the mechanical grinding could destroy the original pore structure, resulting in rounder shaped pores as indicated by higher circularity values (Table 1).

3.3. Atomic force microscopy measurements

Surface topography images illustrating the surface morphology for both polishing methods were obtained by AFM (Fig. 6). The conventionally polished sample (Fig. 6-A) shows a more irregular surface with more sudden and spiky height changes. However, the absolute height differences between topographically lowest (dark blue in the artificial colour scale) and highest (bright in the artificial colour scale) areas seem to be less pronounced compared to the BIB-milled sample (Fig. 6-B). The spiky characteristics could resemble the maximum lateral smoothness and resolution that is achievable by using conventional diamond polishing pastes down to a size of 0.25 μm. The topographic hights could be due to residual clinker grains while topographic lows might develop in regions where the hydrated matrix or pores are predominant. Compared to the topographical illustration of the BIB-milled sample, a generally circular shape of the lowest areas (dark blue in Fig. 6-A) can be observed. This aligns with the SEM observations and results of image processing which indicate pronounced circularity and lower aspect ratio for the pores in the conventionally polished sample (Table 1). It indicates, that due to the resin impregnation or during the grinding and polishing, microstructural artefacts by the means of rounder shaped pores are introduced. The occurrence of artefacts caused by grinding and polishing has been discussed extensively in the literature [1–4]. Another explanation for such larger (e.g., several tenths of μm) round holes could be the occurrence of Hadley grains or hollow shell types even though such were not documented during the SEM investigation [31,32].

The BIB-milled sample shows larger differences in height. However, the high spots are more gradual and less sudden with a smoother peak compared to the spiky morphology in the conventional polished sample (Fig. 6-B). Linear features which are running parallel to the y axis can be interpreted as curtaining (Fig. 3, Section 3.1) and are visible in the 3D representations of the AFM scans (Fig. 6-B). Similar to the conventional polished sample, the striking height difference between certain regions can be attributed to the occurrence of different phases, e.g., residual clinker and hydrated matrix. Hydrated cement pastes are known for their complex microstructure and a variety in their mineralogical phase composition. The different phases, e.g., residual clinkers and hydrated amorphous phases, are characterized by different micro-hardness and grain sizes [33]. Likely, both these factors lead to the observed difference in polishing behaviour and development of a rough surface morphology at the nanometre scale. Nanoindentation could be a potential method to verify this assumption as it was previously successfully applied in combination with AFM on not just hydrated cement pastes but also other artificial materials [33–37]. However, this is beyond the scope of this study. Another explanation for areas with enhanced topographic height could be sample material that was eroded by the ion beam and later redeposited as this was observed previously [3].

In conclusion, AFM topographical images confirm that conventional polishing achieves a generally smoother surface while BIB-milling leads to pronounced height differences. However, BIB-milling also leads to partial areas that have no spiky irregularities and more gradual changes in height.

3.3.1. Height-difference function and height-height correlation function

The height-difference C(x) and the height-height correlation H(x) function were calculated from the AFM scans with the freeware Gwyddion (Section 2.3.1). Fig. 7 compares the height-difference functions and height-height correlation functions for one of the 16 20 × 20 μm^2 AFM scans for both polishing methods. Note that the data are plotted in the statistically significant range for small values in x. For Fig. 7-A, only the first part ($x < 5$ μm) of the curve, which is showing almost Gaussian decay ($\alpha = 1$) before the function reaches zero is relevant for the lateral correlation length (ξ) evaluation. In a similar manner, for the height-height correlation function only the initial slope of the log-log plot is evaluated (Fig. 7-B). For larger distances, e.g., $x \gg \xi$ the function saturates and forms a plateau which is disturbed for large x by less statistics (e.g., for larger x less data points are obtainable). The conventionally polished sample has a clearly lower rms roughness and therefore a lower σ^2 value which corresponds to C(0) (Fig. 7-A, see Section 2.3.1). The lateral correlation length ξ corresponds to the x-value at which the height-difference function C(x) falls off to a value σ^2/e (see black lines in Fig. 7-A). The α-parameter is easily determined from the height-height correlation function H(x) in double logarithmic presentation: the initial slope for $x \gg \xi$ corresponds to 2α.

Table 2 summarizes the results of this comprehensive surface roughness analysis. Arithmetic mean values are reported of σ, ξ, and α. The resin-embedded, conventionally polished sample has a lower average σ value with an average of (156 ± 114) nm compared to (388 ± 101) nm for the BIB-milled sample.

The lateral correlation length analysis yields an average ξ value of 1.47 μm for the conventionally polished sample and a higher average ξ of 2.12 μm for the BIB milled sample (Table 2). Since ξ is a measure for the lateral fluctuations of the surface roughness this means that, in the BIB-milled sample two points of equal height are further lateral apart compared to the conventionally polished sample. This can also be visually seen in Fig. 6. It should be noted that ξ corresponds to the minimum lateral feature size and is smaller than the average lateral feature size.

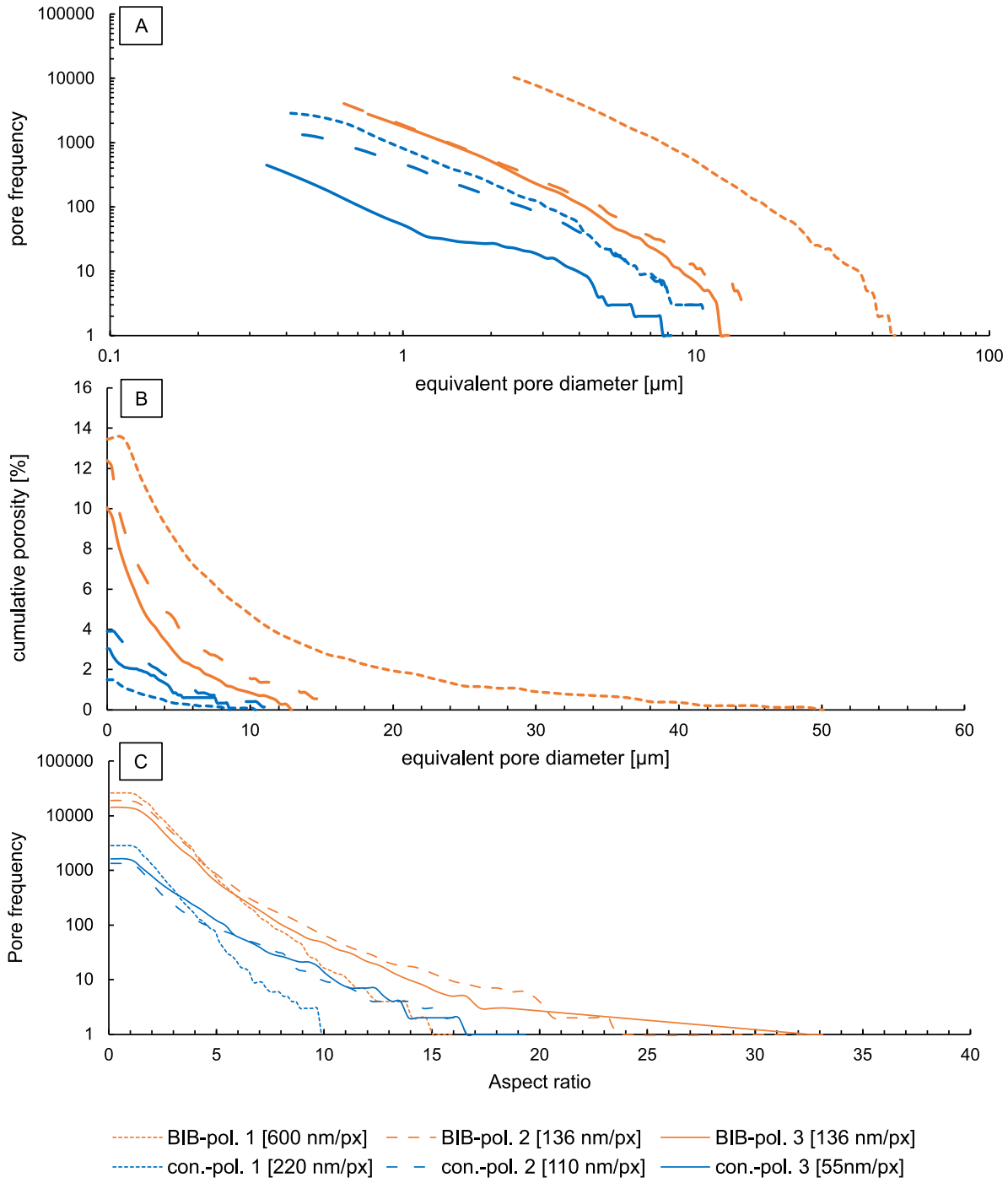

Fig. 5. Results of pore statistical analysis of segmented pore space of processed SEM images for conventionally polished (red) and crack-corrected BIB-milled (blue) samples. A: pore frequency vs equivalent pore diameter in a log-log presentation, B: cumulative porosity vs equivalent pore diameter, C: Aspect ratio plot in semi logarithmic presentation. (For interpretation of the references to colour in this figure legend, the reader is referred to the web version of this article.)

For the BIB-milled sample, an average Hurst parameter α of about 0.9 is obtained indicating an almost gaussian C(x) with gentle jaggedness. For the conventionally polished sample, an α value of 0.8 indicates slightly more abrupt heights changes.

4. Conclusion

To fully utilise the potential of modern SEMs, it is crucial that also the preparation techniques are improved since defects in polishing can result in misconceptions during microstructural studies. This is even more important since the technical capabilities of modern high-resolution SEM instruments equipped with a field emission gun improved significantly over the last decade, now allowing a more detailed study of even nanometre sized features. In this paper, state-of-the-art resin-embedded polishing of hydrated cement paste was compared with a novel BIB-milling process. SEM microstructural investigations enhanced with image processing were employed to determine key parameters such as porosity, pore size distribution, pore circularity and aspect ratio.

SEM investigations of the BIB-milled sample facilitated the detailed study of nano-microstructural features such as gel porosity and the acicular morphology of C—S—H, a level of detail not achievable in the

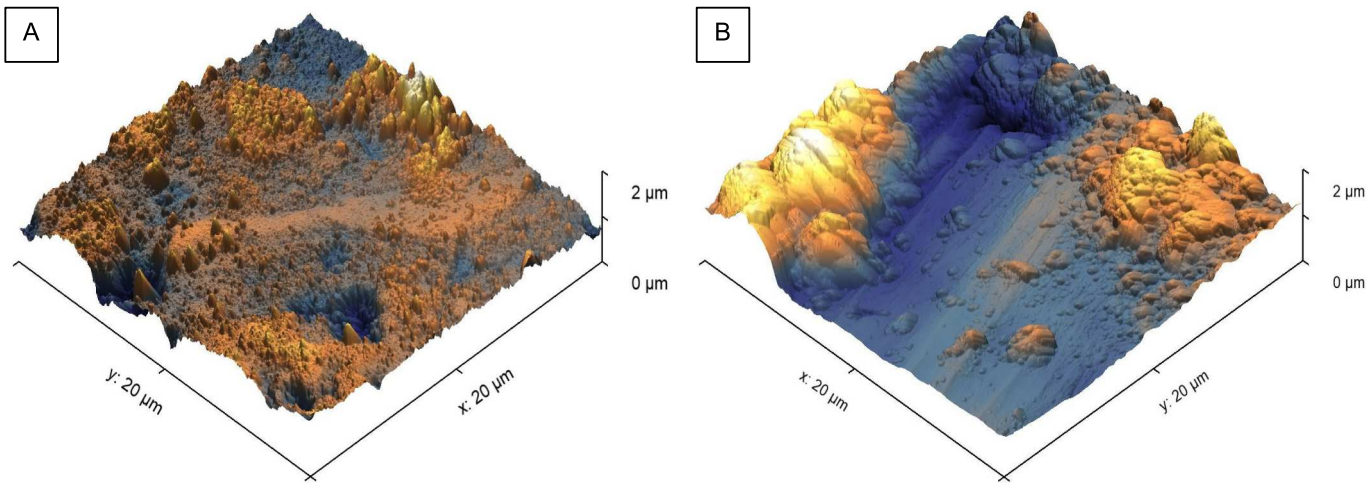

Fig. 6. 3D representation of 20 × 20 µm^2 AFM topography scans illustrating the surface morphology obtained with the two polishing techniques. A: resin-embedded, conventionally polished, B: BIB-milled. Both 3D topographies are presented in the same z scale.

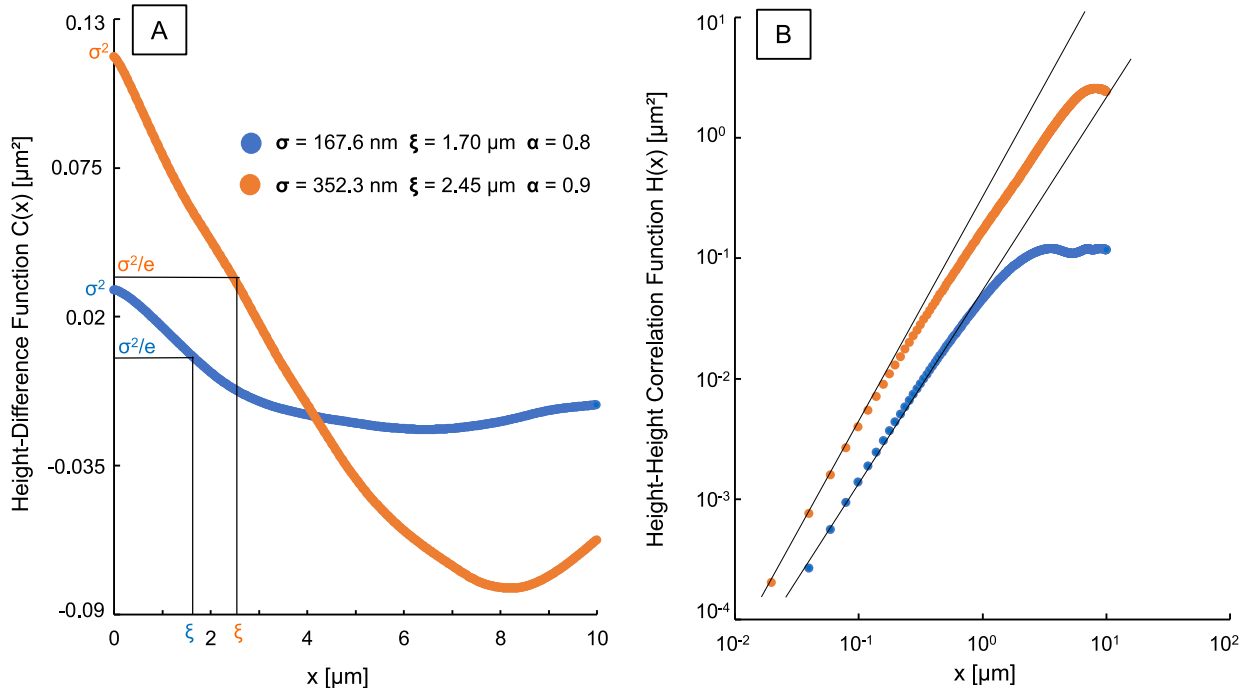

Fig. 7. Height-difference functions (A) and height-height correlation functions (B) obtained for one of the 20 × 20 µm^2 areas of the investigated samples. Blue line: resin-embedded, conventionally polished sample, orange line: BIB-milled sample. For further explanation see text. Please note the double-logarithmic presentation in B. The black lines in B represent the initial slopes which correspond to 2α. (For interpretation of the references to colour in this figure legend, the reader is referred to the web version of this article.)

Table 2
Results of the comprehensive surface roughness analysis performed on the obtained AFM scans using the freeware Gwyddion. For each sample the arithmetic mean and single standard deviation are displayed which were calculated from datasets of in total 16 20 × 20 µm^2 areas arranged in a 4 × 4 grid.

$n = 16$	σ (nm)	ξ (µm)	α
Resin-embedded and conventionally polished sample	156 ± 114	1.47 ± 0.47	0.8 ± 0.1
BIB-milled sample	388 ± 101	2.12 ± 0.68	0.9 ± 0.5

resin-embedded sample. Furthermore, the BIB-milled sample exhibited enhanced visualization of pore shapes and edges, making SEM images easier to process in subsequent image processing and analysis. In contrast, the resin-embedded, conventionally polished sample presented very low porosity values, making it challenging for image processing. This was mainly caused by the presence of resin causing difficulties in the segmentation of pore space and masking the true shape of the pores. This emphasizes the necessity and advantages of a resin free polishing process that enables the study of fragile samples without the hazard of modifying the microstructure by vacuum or pressure impregnation.

Pores segmented from BIB-SEM images exhibit increased aspect ratios compared to those of the resin-embedded polished sample, where higher circularity of the pores appears to be artefact. It should be noted

that the pre-preparation of BIB-milled samples, including the use of a low-speed saw to cut out small cuboidal sample pieces with well-defined edges often introduces cracks in the sample due to the brittle characteristics of hydrated cement pastes which can introduce bias and affect the accuracy of image processing results.

Surface roughness analysis applying height-difference and height-height correlation function analysis on AFM scans revealed that conventional polishing leads to an overall much smoother vertical surface roughness (156 nm) compared to BIB-milling (388 nm). The level of lateral fluctuations indicated by the lateral correlation lengths is also increased by the BIB-milled method (e.g., 1.47 compared to 2.12 μm). The jaggedness of the conventionally polished surface, indicated by the roughness parameter α is only slightly decreased when changing from conventional polishing to BIB-milling.

In conclusion, this study highlights the advantages and drawbacks of the BIB-milling method, compared to the resin-embedded, conventional polishing, especially for SEM microstructural investigations. Surface roughness was found to be higher in the BIB-milled sample. This emphasizes the imperative need for an improved polishing technique for cementitious materials and highlights the importance of a resin free polishing process. The study confirms that BIB-milling stands as a suitable and effective method for polishing hydrated cement pastes allowing enhanced microstructural investigations.

CRediT authorship contribution statement

Thomas Sammer: Writing – original draft, Methodology, Conceptualization. **Xiangyun Shi:** Writing – original draft, Resources, Formal analysis. **Muhammad Zubair Khan:** Resources, Investigation, Formal analysis. **Aleksandar Matkovic:** Writing – review & editing, Writing – original draft, Resources, Investigation. **Christian Teichert:** Writing – review & editing, Supervision. **Johann G. Raith:** Writing – review & editing, Supervision.

Declaration of competing interest

The authors declare that they have no known competing financial interests or personal relationships that could have appeared to influence the work reported in this paper.

Data availability

Data will be made available on request.

Acknowledgements

This research activity has received funding from Montanuniversität Leoben and is part of the Strategic Core Research Area SCoRe A^{+} Hydrogen and Carbon. The authors would like to thank David Misch, Lukas Skerbisch and Gerhard Hawranek for assistance during SEM investigations. A. M. acknowledges the support of the Austrian Science Fund via Y1298-N START Prize.

References

[1] K.L. Scrivener, Backscattered electron imaging of cementitious microstructures: understanding and quantification, Cem. Concr. Compos. 26 (2004) 935–945.
[2] K. Kjellsen, A. Monsøy, K. Isachsen, R. Detwiler, Preparation of flat-polished specimens for SEM-backscattered electron imaging and X-ray microanalysis—importance of epoxy impregnation, Cem. Concr. Res. 33 (2003) 611–616.
[3] F. Kleiner, C. Matthes, C. Rößler, Argon broad ion beam sectioning and high resolution scanning electron microscopy imaging of hydrated alite, Cem. Concr. Res. 150 (2021) 106583.
[4] V. Thiery, E. Dubois, S. Bellayer, The good, the bad and the ugly polishing: effect of abrasive size on standardless EDS analysis of Portland cement clinker's calcium silicates, Micron 158 (2022) 103266.
[5] C.J. Evans, E. Paul, D. Dornfeld, D.A. Lucca, G. Byrne, M. Tricard, F. Klocke, O. Dambon, B.A. Mullany, Material removal mechanisms in lapping and polishing, CIRP Ann. 52 (2003) 611–633.
[6] G. Rémond, C. Nockolds, M. Phillips, C. Roques-Carmes, Implications of polishing techniques in quantitative X-ray microanalysis, J. Res. Natl. Inst. Stand. Technol. 107 (2002) 639–662.
[7] G. Ji, Z. Tan, R. Shabadi, Z. Li, W. Grünewald, A. Addad, D. Schryvers, Di Zhang, Triple ion beam cutting of diamond/Al composites for interface characterization, Mater. Charact. 89 (2014) 132–137.
[8] D.E. Newbury, N.W.M. Ritchie, Is scanning electron microscopy/energy dispersive X-ray spectrometry (SEM/EDS) quantitative? Scanning 35 (2013) 141–168.
[9] D.E. Newbury, N.W.M. Ritchie, Performing elemental microanalysis with high accuracy and high precision by scanning electron microscopy/silicon drift detector energy-dispersive X-ray spectrometry (SEM/SDD-EDS), J. Mater. Sci. 50 (2015) 493–518.
[10] M. Yio, H.S. Wong, N.R. Buenfeld, 3D Monte Carlo simulation of backscattered electron signal variation across pore-solid boundaries in cement-based materials, Cem. Concr. Res. 89 (2016) 320–331.
[11] D.C. Bell, N. Erdman, Low Voltage Electron Microscopy: Principles and Applications, Wiley published in association with the Royal Microscopical Society, Chichester, West Sussex, 2013.
[12] J.M.E. Harper, J.J. Cuomo, Material processing with broad-beam ion sources, Annu. Rev. Mater. Sci. 13 (1983) 413–439.
[13] American Petroleum Institute, API SPEC 10A, 2022.
[14] F. Georget, W. Wilson, K.L. Scrivener, Edxia: microstructure characterisation from quantified SEM-EDS hypermaps, Cem. Concr. Res. 141 (2021) 106327.
[15] J. Schindelin, I. Arganda-Carreras, E. Frise, V. Kaynig, M. Longair, T. Pietzsch, S. Preibisch, C. Rueden, S. Saalfeld, B. Schmid, J.-Y. Tinevez, D.J. White, V. Hartenstein, K. Eliceiri, P. Tomancak, A. Cardona, Fiji: an open-source platform for biological-image analysis, Nat. Methods 9 (2012) 676–682.
[16] J. Schindelin, C.T. Rueden, M.C. Hiner, K.W. Eliceiri, The ImageJ ecosystem: an open platform for biomedical image analysis, Mol. Reprod. Dev. 82 (2015) 518–529.
[17] C. Haubold, M. Schiegg, A. Kreshuk, S. Berg, U. Koethe, F.A. Hamprecht, Segmenting and tracking multiple dividing targets using ilastik, Adv. Anat. Embryol. Cell Biol. 219 (2016) 199–229.
[18] S. Berg, D. Kutra, T. Kroeger, C.N. Straehle, B.X. Kausler, C. Haubold, M. Schiegg, J. Ales, T. Beier, M. Rudy, K. Eren, J.I. Cervantes, B. Xu, F. Beuttenmueller, A. Wolny, C. Zhang, U. Koethe, F.A. Hamprecht, A. Kreshuk, ilastik: interactive machine learning for (bio)image analysis, Nat. Methods 16 (2019) 1226–1232.
[19] X. Shi, D. Misch, S. Vranjes-Wessely, A comprehensive assessment of image processing variability in pore structural investigations: conventional thresholding vs. machine learning approaches, Gas Sci. Eng. 115 (2023) 205022.
[20] G. Binnig, C.F. Quate, C. Gerber, Atomic force microscope, Phys. Rev. Lett. 56 (1986) 930–933.
[21] D. Nečas, P. Klapetek, Gwyddion: an open-source software for SPM data analysis, Open Phys. 10 (2012).
[22] B.B. Mandelbrot, The Fractal Geometry of Nature, W. H. Freeman and Company, New York, 1983.
[23] P. Meakin, Fractals, Scaling and Growth Far from Equilibrium, 1st ed., Cambridge University Press, Cambridge, 1998.
[24] S.K. Sinha, E.B. Sirota, S. Garoff, H.B. Stanley, X-ray and neutron scattering from rough surfaces, Phys. Rev. B Condens. Matter 38 (1988) 2297–2311.
[25] H.-N. Yang, G.-C. Wang, T.-M. Lu, Diffraction From Rough Surfaces and Dynamic Growth Fronts, World Scientific, Singapore, 1993.
[26] C. Teichert, Self-organization of nanostructures in semiconductor heteroepitaxy, Phys. Rep. 365 (2002) 335–432.
[27] G. Desbois, J.L. Urai, P.A. Kukla, U. Wollenberg, F. Pérez-Willard, Z. Radí, S. Riholm, Distribution of brine in grain boundaries during static recrystallization in wet, synthetic halite: insight from broad ion beam sectioning and SEM observation at cryogenic temperature, Contrib. Mineral. Petrol. 163 (2012) 19–31.
[28] J.E. Rossen, Composition and Morphology of C-A-S-H in Pastes of Alite and Cement Blended With Supplementary Cementitious Materials, Lausanne, École Polytechnique Federale de Lausanne, 2014.
[29] J. Klaver, G. Desbois, R. Littke, J.L. Urai, BIB-SEM characterization of pore space morphology and distribution in postmature to overmature samples from the Haynesville and Bossier Shales, Mar. Pet. Geol. 59 (2015) 451–466.
[30] D. Misch, W. Siedl, M. Drews, B. Liu, J. Klaver, M. Pupp, R.F. Sachsenhofer, Mineralogical, BIB-SEM and Petrophysical data in seal rock analysis: a case study from the Vienna Basin, Austria, J. Pet. Geol. 44 (2021) 25–46.
[31] K.O. Kjellsen, E.H. Atlassi, Pore structure of cement silica fume systems: presence of hollow-shell pores, Cem. Concr. Res. 29 (1999) 133–142.
[32] K.O. Kjellsen, H.M. Jennings, B. Lagerblad, Evidence of hollow shells in the microstructure of cement paste, Cem. Concr. Res. 26 (1996) 593–599.
[33] K.J. Krakowiak, W. Wilson, S. James, S. Musso, F.-J. Ulm, Inference of the phase-to-mechanical property link via coupled X-ray spectrometry and indentation analysis: application to cement-based materials, Cem. Concr. Res. 67 (2015) 271–285.
[34] M. Sebastiani, R. Moscatelli, F. Ridi, P. Baglioni, F. Carassiti, High-resolution high-speed nanoindentation mapping of cement pastes: unravelling the effect of microstructure on the mechanical properties of hydrated phases, Mater. Des. 97 (2016) 372–380.

[35] S. Parveen, S. Rana, R. Fangueiro, A review on nanomaterial dispersion, microstructure, and mechanical properties of carbon nanotube and nanofiber reinforced cementitious composites, J. Nanomater. 2013 (2013) 1–19.
[36] Y. Sáez de Ibarra, J.J. Gaitero, E. Erkizia, I. Campillo, Atomic force microscopy and nanoindentation of cement pastes with nanotube dispersions, Phys. Status Solidi A 6 (2006) 1076–1081.
[37] M. Mozetič, A. Vesel, G. Primc, C. Eisenmenger-Sittner, J. Bauer, A. Eder, G. Schmid, D.N. Ruzic, Z. Ahmed, D. Barker, K.O. Douglass, S. Eckel, J.A. Fedchak, J. Hendricks, N. Klimov, J. Ricker, J. Scherschligt, J. Stone, G. Strouse, I. Capan, M. Buljan, S. Milošević, C. Teichert, S.R. Cohen, A.G. Silva, M. Lehocky, P. Humpoliček, C. Rodriguez, J. Hernandez-Montelongo, D. Mercier, M. Manso-Silván, G. Ceccone, A. Galtayries, K. Stana-Kleinschek, I. Petrov, J.E. Greene, J. Avila, C.Y. Chen, B. Caja-Munoz, H. Yi, A. Boury, S. Lorcy, M.C. Asensio, J. Bredin, T. Gans, D. O'Connell, J. Brendin, F. Reniers, A. Vincze, M. Anderle, L. Montelius, Recent developments in surface science and engineering, thin films, nanoscience, biomaterials, plasma science, and vacuum technology, Thin Solid Films 660 (2018) 120–160.

C Journal of Carbon Research

MDPI

Article

Insight into Carbon Black and Silica Fume as Cement Additives for Geoenergy Wells: Linking Mineralogy to Mechanical and Physical Properties

Thomas Sammer [1,*], Arash Nasiri [2], Nikolaos Kostoglou [3], Krishna Ravi [2] and Johann G. Raith [1]

[1] Department of Applied Geosciences and Geophysics, Montanuniversität Leoben, 8700 Leoben, Austria
[2] Department Geoenergy, Montanuniversität Leoben, 8700 Leoben, Austria
[3] Department of Materials Science, Montanuniversität Leoben, 8700 Leoben, Austria
* Correspondence: thomas.sammer@stud.unileoben.ac.at

Abstract: The geoenergy industry has challenging demands on cements used as downhole materials. Once placed in the annular space, the cement sheath must be very low permeability and mechanically durable. Its characteristics are strongly influenced by its microstructure. A holistic approach, including combined mineralogical, physical, and mechanical investigations, provides a better understanding of how these characteristics interplay. Class G cement was investigated and compared to cement formulations containing carbon black or silica fu me, trying to tailor its performance. The addition of carbon black and silica fume has some effect on the modal and chemical phase composition and results in a much denser microstructure. Furthermore, porosity is reduced while the pore size distribution remains similar. Samples containing carbon black have a reduced Young's modulus, indicating a more plastic behavior. The addition of silica fume increased both mechanical strength and permeability. However, comparable results can also be achieved by carefully tuning the water/cement ratio of the initial slurry.

Keywords: geoenergy well cement; mineralogy; carbon black; silica fume; microstructure; mechanical properties; physical properties

Citation: Sammer, T.; Nasiri, A.; Kostoglou, N.; Ravi, K.; Raith, J.G. Insight into Carbon Black and Silica Fume as Cement Additives for Geoenergy Wells: Linking Mineralogy to Mechanical and Physical Properties. *C* **2024**, *10*, 71. https://doi.org/10.3390/c10030071

Academic Editors: Lok Kumar Shrestha and Rekha Goswami Shrestha

Received: 6 July 2024
Revised: 4 August 2024
Accepted: 6 August 2024
Published: 8 August 2024

1. Introduction

Today, cement, in various compositions, is one of the most consumed construction materials, also finding application in the geoenergy industry. In oil, gas, H_2-storage, carbon sequestration, and geothermal wells, cement, most commonly Portland-type cements, is applied to fill the so-called annular space between the steel casing and the surrounding rock formations, providing not just mechanical strength for the borehole infrastructure but also ensuring tightness against migrating fluids. This is crucial for ensuring the safe and environmentally friendly production of hydrocarbons, the underground storage of H_2 and CO_2, or the extraction of geothermal energy [1]. On the one hand, to provide tightness, also called zonal isolation, the installed cement sheaths need to have very low permeability, even at higher pressure-temperature conditions of up to 200 MPa and 150 °C, as realized in the subsurface formations encountered in the geoenergy industry. Zonal isolation is the exclusion of fluids such as water; e.g., groundwater in one zone, from oil or gas in another zone [2–5]. On the other hand, due to the geothermal gradient and potential movements of the subsurface, e.g., earthquakes or induced seismicity, the cement sheath must also be mechanically durable and withstand a wide range of thermal and mechanical loads [5–7]. These characteristics are important in a cement sheath to operate a well safely and economically during its lifetime.

The physical and mechanical properties of hardened cement sheaths are dependent on their microstructure [8]. Cement sheaths exhibit a complex and, due to the hydration

process, somewhat dynamic microstructure, which highly depends on the slurry formulation and the curing conditions [9,10]. Mineralogical investigations can provide additional information and help to better understand the characteristics of cement sheaths and their physical and mechanical suitability and durability [11–14]. In recent years, a lot of effort has been made to improve cement sheaths for geoenergy wells [7,15,16]. Often, additives or supplementary cementitious materials (SCMs) are added to the cement slurry to enhance certain properties [17–20]. Commonly used SCMs and additives are silica fume, fly ash, ground granulated blast furnace slag, and limestone powder [21]. However, ongoing research has led to the emergence of novel additives, such as carbon black, which show promising potential for enhancing certain properties of the cement sheath [22,23]. Chemically pure, non-reactive nanoparticles of carbon black are added to decrease the porosity of the cement sheath and prevent gas migration through the cement slurry during the placement and curing of the mixture in the wellbore, thus acting as a fluid-migration blocking additive. Fluid-migration blocking additives are very important for well integrity because, during the placement and curing of the cement slurry, downhole fluids might migrate upwards, causing channels, fissures, or cracks in the later hardened cement sheath. Thus resulting in a poor cementing job and an increased risk of well integrity failure. However, the influence of carbon black on the microstructure and especially on the properties of the hardened cement sheath has yet to be fully resolved [23].

Silica fume, which is composed of nanoparticles of amorphous SiO_2, is a so-called pozzolanic material, inducing a pozzolanic reaction within the cement slurry [24,25]. This chemical reaction between the pozzolan and Ca^{2+} or calcium hydroxide ($Ca(OH)_2$) in the presence of water means that the addition of silica fume reduces the portlandite content in the cement sheath and increases the calcium silicate hydrate (C-S-H) content. This leads to advanced mechanical performance and a modified microstructure [19,26–29]. However, it is also known that the addition of silica fume increases the desiccation of the curing cement slurry because of the increased water consumption of the pozzolanic reaction, therefore enhancing the risk of autogenous shrinkage of the cement sheath [30,31].

Other benefits of adding additives to the cement slurry include economic and environmental aspects. By adding low-cost additives such as carbon black, the total costs of cementing during the construction of the well can be lowered [22]. Moreover, another beneficial aspect is the reduction of greenhouse gases. It is commonly known that the cement industry is one of the major contributors to greenhouse gas emissions, resulting from the calcination during the manufacturing process of the raw materials needed for cement. One ton of cement releases roughly an equivalent amount of CO_2 into the atmosphere [32,33]. By substituting cement with, for example, silica fume, a by-product from the production of elemental silicon and its alloys, the amount of cement can be reduced.

Therefore, understanding how the physical and mechanical properties of geoenergy well cement sheaths can be tailored in an optimal way is of utmost importance. As physical and mechanical properties are also dependent on the mineralogical phase composition of the hardened cement sheath, studies need to be complemented by mineralogical investigations. An inclusive approach combining in-depth mineralogical studies with mechanical and physical investigations of downhole cements is a rather novel approach, but vital to better understanding their mechanical and physical performance.

In this study, we present the results of integrated mineralogical and microstructural investigations together with the physical and mechanical characterization of geoenergy well cement sheaths. The purpose of this study is to investigate the impact of incorporating carbon black and silica fume as additives in cement slurries on the phase composition, microstructure, and resultant physical and mechanical properties of geoenergy well cement sheaths. By comprehensively analyzing these changes through advanced techniques such as scanning electron microscopy, mercury intrusion porosimetry, nitrogen gas adsorption, and mechanical strength testing, we aim to establish a clear correlation between the microstructural modifications and the enhanced or diminished performance of the cement. The significance of this study lies in its potential to improve the reliability and durability of

well cementing in geoenergy applications. Understanding how specific additives affect the microstructure and mechanical properties of the cement can lead to the development of optimized cement formulations. An interdisciplinary approach with mineralogical methods and mechanical and physical characterizations allows an integrated and holistic evaluation. In this paper, we present comprehensive data from scanning electron microscopy, mercury intrusion porosimetry, nitrogen gas adsorption, and permeability measurements. Additionally, the uniaxial compressive strength (UCS) and tensile strength of the investigated cement sheaths were determined, and mineral chemical investigations using an electron microprobe were performed.

2. Materials and Methods

2.1. Sample Materials

In total, four different cement sheath mixtures were investigated. A high sulfate-resistant Class G cement, which is an ordinary Portland cement according to API Spec 10A [34] with a gypsum and aluminate (C_3A) content lower than 3 mass%, was used. Sample G-1 was mixed with the recommended water to the cement (w/z) ratio of the manufacturer, G-2 was mixed with a reduced water content, G-1-CB had added carbon black of the quality N326, G-1-SF had added silica fume with a purity of 97 mass% amorphous SiO_2 (particle size below 1 µm). For samples G-1-CB and G-1-SF, a sulfonated organic polymer acting as a dispersant was added to achieve a mixable slurry. All samples were mixed according to and with equipment compliant with API Spec 10A. The exact mixture formulations for each sample are listed in Table 1. After mixing, the cement slurries were poured into cylindrical molds (2.54 cm in diameter, 5.08 cm in length) made out of brass and left for curing for 28 days in a water bath at room temperature (~22 °C). After 28 days, the cylinders containing the cured cements were demolded and further processed as needed for the follow-up investigations. For all mineralogical and some physical properties investigations (Mercury Intrusion Porosimetry (MIP), N_2 adsorption), the cylinders were cut into 5-mm slices, placed in 99.9% isopropanol for 24 h for solvent exchange to prevent further hydration, and finally dried at 40 °C until constant mass was achieved. After drying and additional further preparation steps (e.g., milling to obtain analytical fine powder for X-ray diffraction (XRD), Simultaneous Thermal Analysis (STA), and N_2 adsorption), the samples were stored in a desiccator to limit the carbonation of the powders. For permeability testing, the initial cylinders were dried at 40 °C until they reached a constant mass. For uniaxial compressive strength (UCS) testing, the initial cylinders were demolded after 28 days and immediately tested according to ASTM C39. Tensile strength cylinders with a 5.08 cm diameter and 2.54 cm length were cast, cured, and demolded in the same way as the samples for UCS were. Tensile strength was then determined according to ASTM C496.

Table 1. Exact mixture formulation of the four investigated samples, BWOC = by weight of cement.

Sample		G-1	G-1-CB	G-1-SF	G-2
Formulation (BWOC %)	Cement	100	100	100	100
	Water	44	46	46	35
	Carbon black	-	5	-	-
	Silica fume	-	-	10	-
	Dispersant	-	1	1.5	-
Density of slurry (g/cm^3)		1.9	1.9	1.9	2.0

2.2. Scanning Electron Microscopy (SEM)

The dried slices were crushed into small pieces using a hand mortar, and SEM image acquisition on a fresh fractured surface was carried out using a TESCAN CLARA field emission (FE) microscope located at the Chair of Functional Materials and Materials Systems, Montanuniversität Leoben, Austria, equipped with TESCAN Essence Image Snapper software, version 1.0.8.0, allowing for the capture and stitching of high-resolution images.

Both backscattered (BSE) and secondary (SE) electron images were obtained. The acceleration voltage was set at 10 kV and the beam current at 1 nA. To obtain a conducting surface and minimize charging effects, the samples were coated with gold using a Cressington Sputter Coater 108 Auto with a 30 s sputtering time.

2.3. X-ray Diffraction (XRD)

To obtain the powdered sample material needed for XRD measurements, the dried sample slices were first ground and then milled using a hand mortar until an analytically fine powder was achieved. A hand mortar was used to ensure a delicate sample preparation and avoid the additional amorphization of certain phases in the hardened paste. Apart from preparation and measurement, the powders were stored in a desiccator to limit carbonation. The measurements were carried out with a Panalytical XPert 3 Powder Diffractometer located at the Chair of Petroleum Geology, Montanuniversität Leoben, Austria, operating at 40 kV and 40 mA, using Cu Kα (1.5 Å) as a radiation source at a step size of 0.004° per second in the 2θ range of 2.5°–70°. The qualitative identification of the phases was carried out manually by comparing the interlayer distance (d) values of the major peaks with the database table presented in [35].

2.4. Simultaneous Thermal Analysis (STA)

For STA, the dried sample slices of the cement sheaths were ground and milled using a hand mortar to obtain an analytically fine powder. Between all sample preparation steps and the measurement, the samples were stored in a desiccator to prevent carbonation of the samples. A combined measurement of thermogravimetry (TG) and differential scanning calorimetry (DSC) was carried out using a TG-DSC Apparatus STA 449 C from Netzsch located at the Chair of Process Technology and Industrial Environmental Protection, Montanuniversität Leoben, Austria. TG is a method in which the change in mass of a material during progressive heating is recorded as a function of temperature. Changes in mass are a result of degradation, the removal of water (e.g., dehydration), and the oxidation of components within the material. DSC is a thermo-analytical technique in which the difference in the amount of heat required to increase the temperature of a sample is measured as a function of temperature, allowing for differentiation between exothermal and endothermal reactions recorded via TG. For hardened cement pastes, three major weight losses can be differentiated during an STA experiment [7,35]:

- up to 350 °C: dehydration of C-S-H and AFm, AFt (aluminium-iron sulphates)
- 400–550 °C: dehydroxylation of portlandite ($Ca(OH)_2$)
- above 600 °C: decarbonation of $CaCO_3$

Roughly 25 mg of powdered sample material was placed in a cylindrical corundum crucible (6.8 mm diameter) and heated up to 1400 °C at a rate of 10 °C/min under constant argon flow (42 mL/min) to provide an inert atmosphere and prevent carbonation of the samples.

Due to the dehydroxylation of portlandite in a well-defined temperature interval, the portlandite content of the investigated sample can be calculated using the following Equation (1):

$$Ca(OH)_{2,\,measured} = L_{Ca(OH)2} \times M_{Ca(OH)2}/M_{H2O} + L_{CaCO3} \times M_{Ca(OH)2}/M_{CO2} \quad (1)$$

where $Ca(OH)_2$ is the measured mass fraction of portlandite and $L_{Ca(OH)2}$ and L_{CaCO3} are the weight losses attributed to portlandite and carbonates in their respective decomposition temperature domains and M_x the molar mass of substance x. The weight loss of carbonates was accounted for under the assumption that all carbonates present in the sample result from the carbonation of portlandite during the sample preparation, which supposedly cannot be fully prevented. The C-S-H content is quite difficult to calculate from STA results due to the fact that, in the temperature range, sulfate-bearing phases such as monosulfate or ettringite decompose, and the molar mass of C-S-H is also unknown due to the unknown

ratio of Ca and Si ions and water content [35]. In this study, the C-S-H + AFm content was calculated under the assumption that no ettringite should be present after 28 days of curing due to hydration kinetics [36] and the AFm content should be below 3% due to the low concentration of gypsum and aluminate (C_3A) in the used class G cement [7]. Furthermore, no hydrogarnet is assumed to be present due to the minor amount of C_3A since it was not detected with XRD. Based on these assumptions, the C-S-H + AFm content was calculated using Equation (2):

$$C\text{-}S\text{-}H_{\ measured} = L_{C\text{-}S\text{-}H} \times M_{C\text{-}S\text{-}H}/M_{H2O} \quad (2)$$

where $C\text{-}S\text{-}H_{\ measured}$ is the mass fraction of C-S-H and AFm under the assumption that the majority is indeed C-S-H and only minor amounts of AFm contribute. Also, the molar mass of C-S-H was assumed to be 180 for Ca-rich C-S-H, which is typically found in hydrated Portland cement pastes. Both, portlandite and C-S-H + AFm content were calculated from the TG graphs using the stepwise method [35].

2.5. Electron Probe Micro Analysis (EPMA)

EPMA measurements were carried out to investigate the mineral chemical composition of the C-S-H matrix of the samples, mainly the Ca/Si ratio and the influence of added silica fume. To obtain the well-polished and flat surface required for EPMA measurements, a special preparation technique was needed. The surface of the dried sample slices was briefly manually dry ground on sandpaper with grain sizes of 1000 µm and, after that, vacuum impregnated in a low-viscosity resin (EPO-TEK 301). The resin was cured for 3 days at room temperature. Afterwards, the upper-most part of the resin was carefully removed by hand with a grinding disc to free the initial sample surface. Here, extreme caution was taken to not remove too much of the sample material. Then, the sample surface was lapped for several minutes using SiC with a grain size of 1000. After that, automated polishing using a Tegramin 30 grinding and polishing machine from Struers, was performed. In total, four polishing steps using a monocrystalline diamond paste spray of 9, 6, 3, and 1 µm with polishing discs from Struers, namely MicroTex 900 for the first two steps and MD Dur for the last two steps, were performed. Each polishing step took about 3–4 min with the polishing disc rotating at 120 rpm and a force of 20 N applied to the samples. After each polishing step, the samples were cleaned in an ultrasonic bath.

The polished samples were carbon coated with a 15 nm thin layer to ensure a conductive surface and allow wavelength dispersive spectrometry (WDS) analysis of the material. A JEOL superprobe JXA 8200 located at the Chair of Resource Mineralogy, Montanuniversität Leoben, Austria, equipped with 5 spectrometers and a tungsten cathode, was used. The acceleration voltage and beam current were set at 15 kV and 10 nA with a beam diameter of 1 µm. Further measurement parameters, the measured elements, and the used crystals and minerals for standardization of the respective elements, are reported in Table 2. The measurement points were selected within the middle grey matrix areas, obtaining total values for the oxides of 72–78 mass% due to the inability of the device to measure elements as light as oxygen or hydrogen. For every measurement, background correction and ZAF correction were applied, and the detection limit (D.L.) for each measured element was calculated with Equation (3) automatically by the software.

$$\mathbf{D.L.} = \frac{\mathbf{z}}{\mathbf{m}}\sqrt{2 \times \frac{\mathbf{Ibg}}{\mathbf{tbg}}} \quad (3)$$

With z and m being factors for confidence levels and calculation in mass%, respectively, and I_{bg} and t_{bg} being the intensity of the background in counts per second and the time of background counting.

The obtained mass% values were transferred into mole% using the molecular weight of the elements and their respective oxides, followed by normalization to 100%. The mole ratios were then calculated and plotted. Based on these values, arithmetic mean values were determined.

Table 2. Measurement conditions of EPMA.

Element	X-ray Line	Crystal	Peak Position	Measurement Duration Peak/Background (s)	Standard	D.L. (ppm)	ZAF Factor
Mg	Kα	TAP	107.927	20/10	Biotite	107	4.5861
Al	Kα	TAP	90.376	20/10	Biotite	106	3.6217
S	Kα	PETJ	171.832	60/30	Barite	123	2.1296
Fe	Kα	LIFH	134.434	20/10	Biotite	253	0.1968
Ca	Kα	PETH	107.548	20/10	Wollastonite	90	0.8795
Si	Kα	TAP	77.046	20/10	Wollastonite	149	3.4362

2.6. Mercury Intrusion Porosimetry (MIP)

MIP measurements are often applied to investigate the pore size distribution and porosity of hardened cement pastes and cementitious materials due to their broad and relatively simple applicability and wide range of pore size detectability. Particularly when it comes to the comparison of different cementitious materials, MIP delivers meaningful results. However, it is also important to note that the so-called ink bottle effect and accessibility problems can result in an underestimation of macropores (e.g., pores larger than 50 nm according to the IUPAC classification), and the characterization of cementitious materials is not always straight-forward [35,37].

In this study, MIP measurements were conducted at the Chair of Geology, Friedrich-Alexander-Universität Erlangen. A Quantachrome Poremaster for Windows Data Report, version 8.00, was used. The mercury surface tension was 0.485 N/m and the contact angle to the pore surface was 140°. The samples were treated as described in Section 2.1, then the dried slices were crushed, and approximately 1.3 g of fractured pieces were placed in the sample chamber and analyzed by increasing the pressure gradually up to a maximum pressure of 410 MPa. Using the Washburn equation [38], the pore size distribution from pores of sizes of mm down to 3 nm was obtained. Additionally, total porosity, density, and surface area were recorded.

2.7. N_2 Adsorption at 77 K

Low pressure gas sorption experiments were executed with an Autosorb iQ^3 gas sorption analyzer from Anton Paar Quanta Tec located at the Chair of Physics, Montanuniversität Leoben, using N_2 of ultra-high purity (99.999%) as adsorbate. The samples were cast and treated as described in Section 2.1. Then, the dried slices were milled with a hand mortar to obtain a fine powder suitable for analytics. Before the actual measurement, 0.4 g of the powdered sample was outgassed under vacuum (10^{-6} mbar) for 24 h at 40 °C. To reduce the dead volume of the sample cell, which was automatically evaluated before each run using helium (99.999% purity), non-porous glass filling rods were placed inside the sample cells alongside the sample powder. N_2 adsorption/desorption isotherms were recorded at 77 K in a relative pressure (P/P_0) range from 10^{-3} to 0.99. The pore volume, pore size distribution from 3 nm to 100 nm, using the Barrett-Joyner-Halenda (BJH) method, and surface area using the multi-point BET method, of the samples were obtained. The porosity of the samples was calculated based on the measured pore volume by N_2 adsorption and skeletal density (e.g., ratio of the mass of the solid material to the sum of the volume of the solid material) of the samples determined using Helium Pycnometry using the following Equation (4):

$$\textbf{Porosity} = \frac{\textbf{skeletaldensity} \times \textbf{Vpores}}{1 + \textbf{skeletaldensity} \times \textbf{Vpores}} \quad (4)$$

In contrast to MIP measurements, gas sorption is only able to detect pores of up 200 nm. However, since a significant number of pores in cement sheaths are below this value and the macropores (>50 nm, IUPAC classification) obtained by MIP are often

underestimated, it is a vital tool for enhanced porosity investigation and quality control of MIP measurements [35,38].

2.8. Permeability Measurements

N_2 gas permeability was determined to occur at 2.54 cm in diameter and 5.08 cm in length in the cylindrical samples at ambient temperature. A Gasperm Steady State Gas Permeameter from Vinci Technologies, located at the Chair of Applied Geophysics, Montanuniversität Leoben, Austria, was used with low flow and high-pressure measurement conditions and a radial confining pressure of 0.8 MPa. For each cement sheath formulation, three cylindrical samples were measured, and, for each cylinder, the N_2 gas flow was constantly increased manually until a constant flow was established. After achieving constant flow for the first time, the flow was then increased four more times, recording the pressure every time the flow became constant again. Considering the non-Darcy flow in tight cement sheaths, the effect of gas slippage was accounted for through Klinkenberg correction, while Forschheimer permeability was considered irrelevant, noting the very small scale of pore sizes (<100 nm) in cement sheaths. Permeability was calculated by the corresponding software from Vinci Technologies for every constant gas flow and corresponding pressure, assuming laminar flow of the gas within the sample, resulting in five constantly increasing permeability values obtained per cylinder. Linear regression was performed to observe if a clear linear correlation between increased gas flow (e.g., permeability) and increased pressure could be observed. The total permeability of the sample obtained was calculated by taking the mean arithmetic value of the five permeability values of each cylinder and the three cylinders for each cement sheath formulation.

2.9. Uniaxial Compressive Strength (UCS) and Tensile Strength

For investigating the mechanical properties of the cement sheaths, uniaxial compressive and tensile strengths were investigated using a Quasar 200 machine from Galdabini located at the Chair of Drilling and Completion Engineering, Montanuniversität Leoben, Austria. The samples were prepared as described in Section 2.1. The mode of the measurement was axial displacement control (API RP 10B) with a speed of 0.5 mm/min until the samples failed. The load and deformation of the samples were recorded and converted into stress and strain. Three measurements for each cement sheath formulation were carried out to account for the reproducibility of the data. The average value plus standard deviation was calculated and is reported in Section 3.3. Additionally, the stress/strain curve was displayed for evaluating the mechanical behavior of the sample and for calculating Young's modulus.

3. Results and Interpretation

3.1. Mineralogical Investigations

3.1.1. Scanning Electron Microscopy (SEM)

Figure 1 shows back scatter electron (BSE) images of a fractured surface of the four investigated cement sheaths. Figure 1A–D display details at higher magnification, E and F show an overview of samples G-1-CB and G-1-SF at lower magnification. Sample G-1 (Figure 1A) shows the typical microstructure of a class G cement sheath. Thin, needle-like structures can be identified as C-S-H phases. Also, larger particles of non-hydrated clinker phases are visible. Sample G-2 (Figure 1B) shows a similar microstructure. Needles of C-S-H and non-hydrated clinker phases are clearly visible. Compared to G-1, the C-S-H phases tend to be more acicular, with the development of slightly larger and thicker needles. However, aggregates of C-S-H of granular, undefined shape are also present in both samples, making up the majority of the cement sheath matrix. Samples G-1-CB and G-1-SF show a denser microstructure. Especially in G-1-SF, the development of C-S-H needles seems to be suppressed. The majority of the C-S-H form a dense, granular microstructure. Occasionally, larger euhedral crystals of portlandite with hexagonal platy morphology can be observed in all samples. From SEM images, one can also draw first conclusions about

the porosity and pore size. G-1 and G-2 show capillary porosity between C-S-H needles and non-hydrated clinker grains, as well as gel porosity within the C-S-H matrix. Both capillary and gel porosity are terms from cement and concrete science describing pores with sizes of 2.5 nm up to 10 µm for capillary porosity and 0.5 nm up to 10 nm for gel porosity. Samples G-1-CB and G-1-SF, however, show a clearly denser microstructure. Especially in G-1-SF, capillary porosity is scarce.

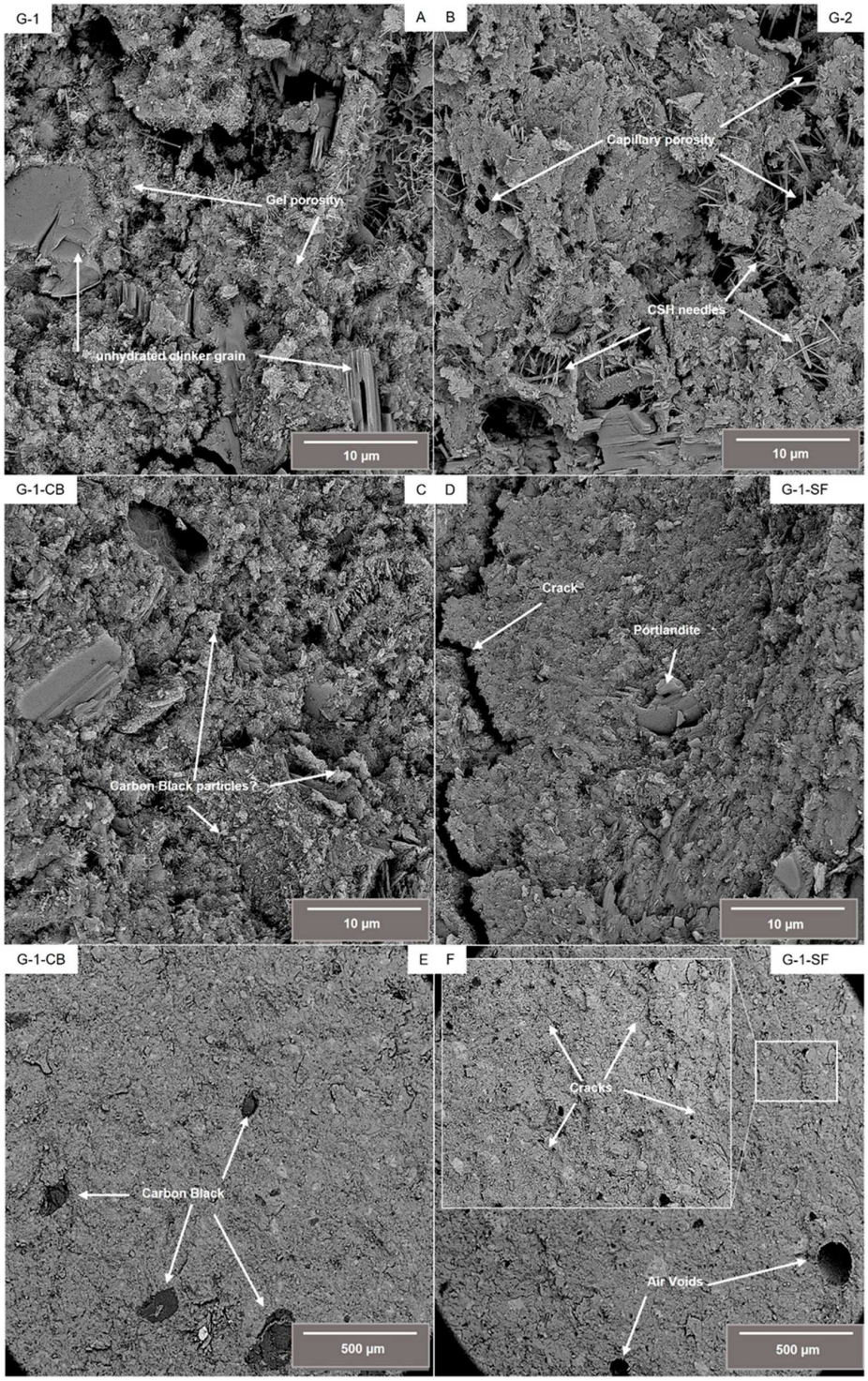

Figure 1. Backscatter electron (BSE) images of the investigated samples at higher magnification (**A**–**D**) as well as an overview of samples G-1-CB and G-1-SF at lower magnification, illustrating the occurrence of agglomerated carbon black particles (**E**) and cracks (**F**).

As can be seen in Figure 1E, the added carbon black is not homogeneously distributed within the cement slurry. Even though the used carbon black (N326) was very fine grained with a grain size in the nm range, apparently some larger agglomerated particles did form. It is known from the literature that the addition of carbon black to cement slurries can be tricky due to the hydrophobic character of carbon black [22,23,39]. A surfactant was used to overcome this issue (Table 1). To obtain an improved distribution of carbon black within the slurry, further experiments perfecting the mixture formulation seem to be needed. Maybe the creation of a suspension of carbon black ahead of time, which is then later added to the slurry, can lead to a better distribution within the cement slurry. These, up to several hundred µm, large carbon black particles could act as weak points within this cement sheath, potentially deteriorating mechanical and physical properties.

Sample G-1-SF shows significantly more air voids, e.g., large, round-shaped pores with sizes up to several hundred micrometers (Figure 1F). These voids are formed during the mixing of the slurry due to the entrapment of air. This observation is a good indicator regarding the fluid-migration-blocking property of this mixture, which is crucial for cements used in the geoenergy industry [2,40]. During the placement of the cement slurry within the borehole, fluid migration might cause the up-well movement of fluids through the cement slurry, resulting in the formation of channels, fissures, or cracks, limiting the mechanical and physical resistance of the cement sheath against the forces initially placed. Obviously, the addition of silica fume decreases the permeability of the slurry, limiting its ability to outgas air and trapping it. Additionally, the sample with the added silica fume shows promoted crack formation. Occasionally, FE-SEM investigation has indicated that all samples have some small (~1 µm) microcracks. However, sample G-1-SF shows significantly more of these microcracks, which are homogeneously distributed over the investigated fractured surface (Figure 1F). This might indicate the much more brittle mechanical behavior of this cement sheath mixture (Section 3.3). Although the addition of silica fume resulted in a much denser-looking microstructure with suppressed capillary porosity, indicating a decreased matrix permeability, the bulk permeability of the hardened cement sheath compared to the decreased permeability of the cement slurry might be significantly increased due to the crack formation.

In summary, it can be concluded that high-resolution FE-SEM is a powerful tool by which to obtain a first, quick overview of the characteristics of the microstructure and a first qualitative estimation regarding porosity, pore sizes, and even permeability behavior. However, it is impossible to make reasonable, quantitative assumptions about these properties based on BSE or SE images. Furthermore, one has to consider that the investigation of a fractured surface might not be representative due to the fact that a fractured surface always develops in a weakened area of the sample; therefore, interpretation has to be cautious.

3.1.2. X-ray Diffraction (XRD)

Figure 2 shows the powder diffraction patterns of tested cement sheaths and the original non-hydrated cement (G-0). The main peaks of the major phases present in the initial cement and cement sheath are marked. The main crystalline phase formed during the hydration of the cement paste is portlandite (CH). The formation of monosulfoaluminate (AFm) can be clearly seen in sample G-1, with the major peak of this phase at a 2θ angle of ~9.8°. In the three other cement sheaths, this peak is not so clearly developed. Especially in sample G-1-SF, it seems to be missing, indicating that the addition of silica fume suppresses the formation of AFm. However, ettringite, a crystalline tri-sulfate phase usually forming in the early hydration states of cement pastes and later transforming into AFm, was also not detected by XRD. This absence can be explained by the curing duration of 28 days. After this time span and the low amounts of gypsum and aluminate (C_3A) in the initial cement class G, all the formed ettringite should have transformed into AFm [36]. Thus, it is unclear in which phases the sulfur is incorporated in sample G-1-SF. C-S-H has been discussed as a potential phase that can incorporate SO_3^{-} ions either between the layers of the C-S-H crystal structure or substituting for silicon ions [41–43].

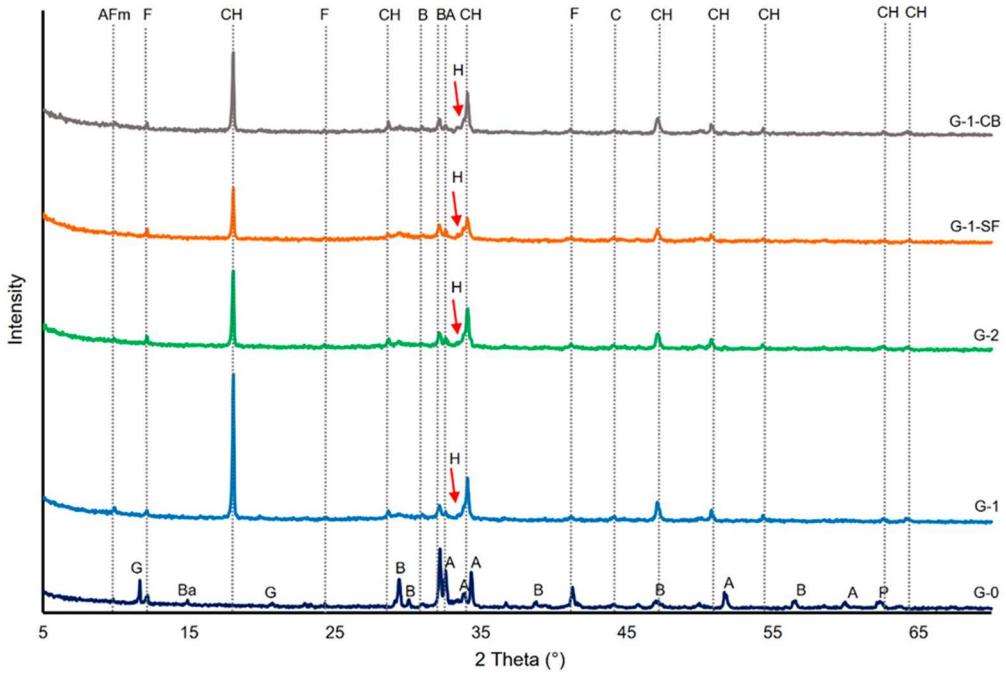

Figure 2. X-ray diffractograms of the investigated cement sheaths and the initial cement (G-0). AFm: Monosulfoaluminate, CH: Portlandite, Ba: Badellite, A: Alite, B: Belite, C: Calcite, F: Ferrite, G: Gypsum, H: Hibschite, P: Periclase.

The residual clinker phases detected by XRD are ferrite (C_4AF) and belite (C_2S). This is in accordance with the relative slower hydration reactions of these two clinker phases compared to alite (C_3S) and aluminate (C_3A). Compared to the XRD pattern of the initial clinker (G-0), alite peaks disappeared in contrast to a few peaks of ferrite and belite (Figure 2). The formation of hibschite, a hydrated variety of grossular, can be assumed, as indicated by the non-symmetric part on the left side of the third portlandite reflection peak. Since portlandite is assumed to be a highly crystalline phase, a symmetric reflection peak would be expected, as can be seen for all the other portlandite refection peaks (Figure 2). By comparing the intensities of the portlandite reflection peaks, an estimation of the quantitative proportions can be drawn. G-1 seems to have the highest portlandite content, and G-1-SF the lowest. Other common hydration products, especially C_4AF, such as hydrogarnet, despite the indication of hibschite, could not be detected, maybe due to their absence or poor crystalline structure. In general, no striking difference in the qualitative phase composition of the four cement sheath samples due to the addition of chemically non-reactive carbon black and pozzolanic silica fume was observed. The slightly elevated, plateau-like area in the 2θ range of ~27° and 35° is due to the amorphous C-S-H phases [35].

3.1.3. Simultaneous Thermogravimetric Analysis (STA)

The results obtained from STA are presented in Figure 3. The x-axis shows an increasing temperature during the experiment. The y-axes, on the left side, show the thermogravimetric weight loss (TG) in mass% and, on the right side, the differential scanning calorimetry (DSC) in µV/mg, indicating an exothermal or endothermal reaction for the observed weight loss. Table 3 summarizes the quantitative phase contents obtained from STA. All four samples show very similar behavior during heating. However, the calculated quantitative portions of portlandite and C-S-H differ (Table 3). The curves show four rapid weight losses. The first loss in a temperature range of 100–200 °C is mainly due to the dehydration of C-S-H and AFm, or ettringite. However, since the cement pastes were cured for 28 days, all ettringite should have transformed into AFm due to the kinetics of the hydration reactions [36]. The AFm content should also be minor due to the low gypsum and aluminate portions in the initial class G cement (Table 1) and the determined phase

composition of hydrated cement class G from other studies [7]. Therefore, it was concluded that the majority of this low-T weight loss can be accounted for by C-S-H. The second major weight loss at 450–500 °C is due to the dehydroxylation of portlandite. A third and fourth weight loss can be observed at 650 °C and 800 °C. These are due to the release of CO_2 from carbonates. The third peak is caused by the decarbonation of allotropic forms of calcite, namely vaterite and aragonite, while the fourth peak is due to the decarbonation of well-crystallized calcite [44,45]. The existence of carbonates in cement sheaths can be explained by the carbonation of the samples during preparation and storage. Especially when the cement pastes are milled, the powder is likely to react with the CO_2 in the atmosphere, resulting in minor carbonation. In the literature, different explanations have been given for whether portlandite, C-S-H, or both react with CO_2 to form carbonates [44–47]. Some studies have suggested that both phases undergo carbonation simultaneously, while others indicate that portlandite is carbonated first. Despite this discussion, a consensus has been reached that, at the onset of carbonation, the carbonation of portlandite is dominant.

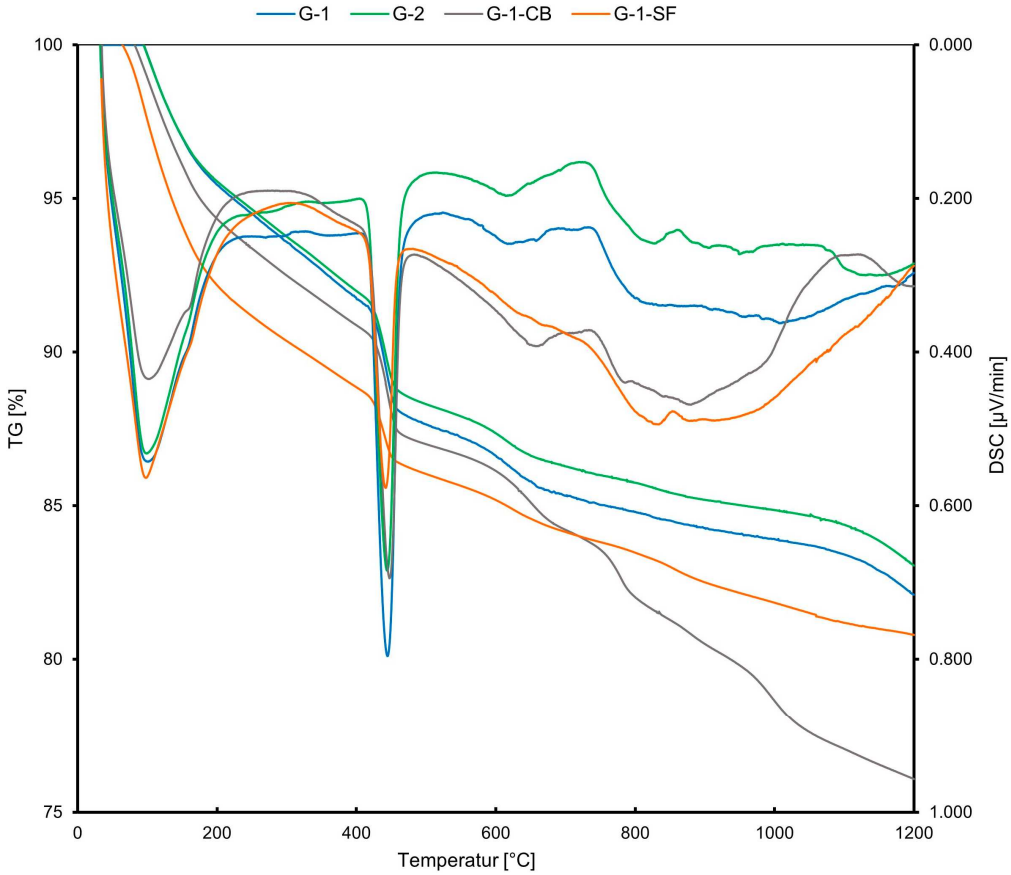

Figure 3. STA curves displaying the weight loss of the samples (TG in %) and the exothermic or endothermic character of the reaction (DSC).

Table 3. Quantitative contents (mass%) of portlandite, C-S-H (+AFm), and carbonates as obtained by STA.

	G-1	G-2	G-1-CB	G-1-SF
Portlandite	19.4	17.3	19.8	12.3
C-S-H + AFm	42.5	44.5	45	50
Carbonates	2.9	2.9	3.4	2

Concerning our case, the G-1-SF sample has a lower portlandite content (Table 3) due to the added silica fume, which acts as pozzolanic material, forming C-S-H from portlandite

and silica fume. Also, the weight loss due to the release of CO_2 is lower compared to the other samples (Figure 3), indicating a lower carbonate content compared to the other three samples. This strengthens the conclusion that portlandite plays a more prolonged role during the early carbonation of cements. However, it is clearly visible from the TG data that the samples underwent some carbonation, which is nearly inevitable during preparation and storage [35].

In samples G-1, G-2, and G-1-SF, the fourth weight loss peak is very minor compared to sample G-1-CB, indicating a higher calcite content and maybe a higher degree of carbonation in the sample with added carbon black. Also, a fifth peak at ~1000 °C developed in this sample. This peak is due to the release of CO, which comes from an equilibrium reaction with CO_2 when carbon is present at high temperatures (Boudouard Reaction).

G-1 and G-2 show similar weight loss in the 100–200 °C temperature range, indicating a similar quantitative amount of C-S-H + AFm. G1-CB and especially G-1-SF show a significantly higher weight loss in this range, indicating higher C-S-H + AFm content. Since the added carbon black is assumed to be chemically non-reactive during the hydration of the cement paste, the observation of a slightly increased C-S-H content for sample G-1-CB compared to G-1 and G-2 is not fully understood. The addition of carbon black should reduce the total amount of cement clinker phases in the initial slurry and, therefore, one would expect a lower C-S-H content in the cement sheath. This leaves room for speculation and further investigation. The DSC curve shows a less pronounced first peak (at about 100 °C) compared to the other three samples (Figure 3). Maybe carbon black causes an exothermic reaction at this temperature, reducing the endothermic dehydration peak of C-S-H and contributing to the increased TG loss.

3.1.4. Electron Probe Micro Analysis (EPMA)

The results of the chemical EPMA analyses are summarized in Figure 4. In total, 20–30 measurement points were carefully selected within the C-S-H matrix area for each sample. The mole fractions of Ca vs. Si are plotted in Figure 4A, illustrating the change of Ca/Si by adding silica fume to the cement paste mixture, indicating not just a change in the quantitative portion of the C-S-H (Table 3), but also a change in the mineral chemical composition of the C-S-H phase. Additionally, the mean average Ca/Si ratio of all measurements plus the standard deviation are given on the graph. Sample G-1-SF clearly shows a lower average Ca/Si ratio of 1.61 compared to the other three samples, which have Ca/Si ratios of 1.91 to 2.02 for G-1, G-2, and G-1-CB. These values are slightly higher than the average reported value of 1.75 for pure C-S-H [10,42,48,49], but are still in the range reported by various studies of Ca/Si ratios [15,42]. Also, one has to consider that the investigated C-S-H phases are not pure calcium silicon hydrate; other elements such as Al and Mg or even sulfate anions are likely to be incorporated, influencing the measured Ca/Si ratio.

A lower Ca/Si ratio usually means a higher density of the C-S-H phase with a high polymerization of silicate ions, potentially increasing the mechanical strength, although this effect is not yet fully understood [50]. However, EPMA data clearly show that the addition of silica fume changes the mineral chemistry of the most important phase when it comes to the mechanical strength of cement sheaths. Additionally, FE-SEM imaging supports the development of a denser microstructure in sample G-1-SF (Figure 1).

Sample G-1-CB shows a slightly increased Ca/Si ratio compared to G-1 and G-2. Since carbon black is assumed to be chemically non-reactive, this observation is surprising, as is the increased C-S-H content determined by STA (Section 3.1.3). Maybe the presence of nanoparticles of carbon black physically hinders the growth of C-S-H crystallites, not just affecting the morphology (Figure 1), but also the chemical composition. A higher Ca/Si ratio means a less dense structure of the C-S-H phase with a lower degree of silicon ion polymerization [15,50].

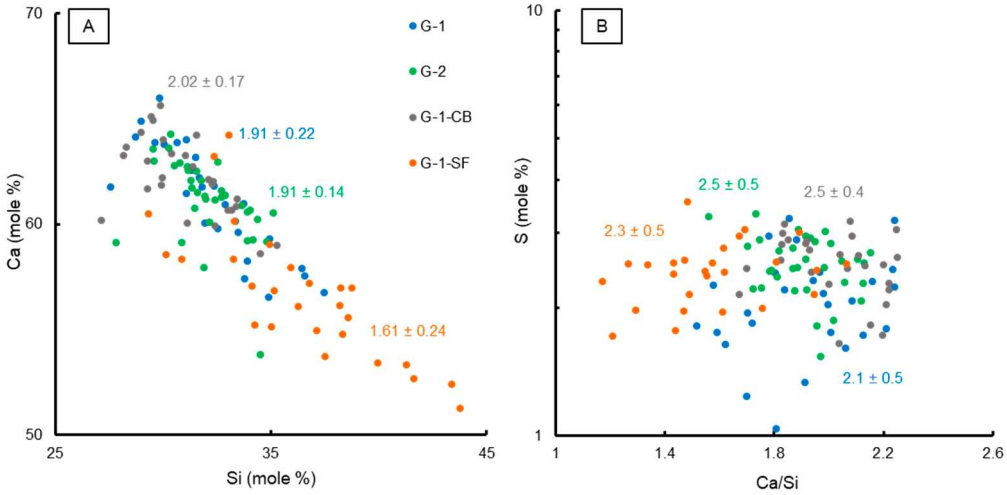

Figure 4. Binary plots showing chemical characteristics of C-S-H phases based on EPMA analyses. (**A**) Ca vs. Si (mole %) with the calculated mean Ca/Si ratios. (**B**) Ca/Si vs. S content (mole %) with the mean S value of the C-S-H matrix for each sample.

In Figure 4B, the Ca/Si ratio is plotted against the mole fraction of S together with the mean mole fraction of S plus the standard deviation of all measurements. Sample G-1 shows a slightly lower S content compared to the other three samples. G-1 also shows a clearly developed AFm peak in the XRD pattern (Figure 2) compared to the other three samples. This could indicate that, in the samples with a changed mix formulation, the formation of sulfur-bearing phases (e.g., AFm) could be hindered or limited, leading to the enhanced incorporation of sulfate in the C-S-H phase, potentially substituting silicon [43]. However, these are only vague indications. As can be seen from Figure 4B, many EPMA analyses of G-1 yield a very similar S content to the other three samples. Only a few measurements yield lower contents. Further investigations on the atomic scale of C-S-H using TEM could help to confirm these observations.

3.2. Physical Properties

3.2.1. Porosity and Pore Size Distribution

Determining the porosity and pore size distribution of cement pastes is not straightforward, as various evaluation methods (e.g., MIP, gas adsorption, or drying methods) can yield different results [35]. Differences are due not only to the effects of sample preparation, but also to the complex cement microstructure. Cement pastes are characterized by an enormous pore size range, from the nm scale to the mm scale. Evaluating the entire pore size distribution is rather complicated and is mainly carried out by MIP, which has limitations at the nm scale. However, the pore space in the nm range, e.g., the gel porosity, is also very important, since it makes up a large part of the porosity and strongly influences the microstructure of the major phase in cement pastes, the C-S-H. Therefore, additional N_2 adsorption/desorption at 77 K measurements were performed in this study to attain a more complete insight into the range of nanopore sizes.

Mercury Intrusion Porosimetry (MIP)

The cumulative porosity and pore size distribution obtained by MIP measurements are presented in Figure 5. The measured total porosity, density, and surface area are presented in Table 4. The results show one dominant class of pore size in all four samples, with pore sizes ranging from 20 nm to 60 nm with a mean diameter of 43 nm, 39 nm, 34 nm, and 37 nm for G-1, G-2, G-1-CB, and G-1-SF, respectively. This shows that the reduction of the water/cement ratio and the addition of carbon black and silica fume did decrease the mean pore size diameter slightly. Sample G-1-SF shows a possible second population, with pore sizes smaller than 5 nm (Figure 5A). This second population is missing in the

other three samples. The dominating pore population is in the range of 20–60 nm and can be classified as capillary porosity [35,38,51]. Therefore, this study confirms that mercury intrusion porosimetry is a suitable method to measure the capillary porosity of cement pastes [7].

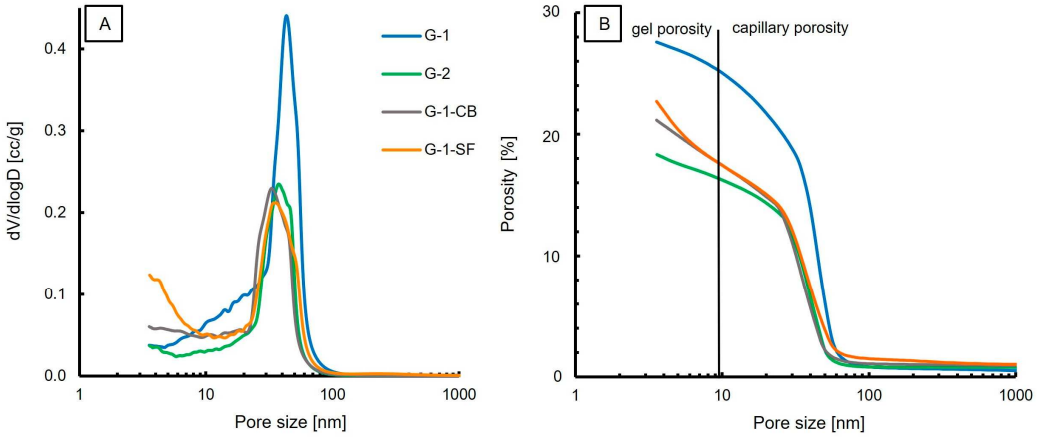

Figure 5. MIP results; (**A**) Pore size distribution with one dominating population in the range of 30–60 nm. (**B**) Porosity vs. Pore size.

Table 4. Physical parameters of the investigated cement sheaths obtained by MIP, N_2 adsorption, and permeability measurements. The porosity for the N_2 adsorption experiment was calculated using the determined pore volume and skeletal density obtained from He-pycnometry.

	G-1	G-2	G-1-CB	G-1-SF
MIP				
Intruded volume (cc/g)	0.22	0.14	0.16	0.22
Porosity (%)	25.9	17.5	20.2	21.9
Pore diameter range (µm)	0.0036–214	0.0036–222	0.0036–214	0.0036–222
Mean pore diameter (µm)	43	39	34	37
Surface area (m^2/g)	31.7	19.7	29.7	39.8
Bulk density (g/cc)	1.62	1.87	1.78	1.70
N_2 adsorption at 77 K				
Intruded volume BJH (cc/g)	0.14	0.09	0.10	0.09
Porosity (%)	24.5	17.3	19.8	17.6
Mean pore diameter (µm)	61	57	68	69
Surface area multipoint BET (m^2/g)	22.9	12.1	17.8	11.6
Skeletal density (g/cc)	2.37	2.39	2.37	2.28
Permeability (mD)	0.08	0.09	0.18	1.26

Minor amounts of the total porosity are attributed to gel porosity (Figure 5B); the dominant porosity is capillary porosity. However, MIP might underestimate the volume of bigger pores in a material [35] as these larger pores might only be accessible through small pore throats (i.e., the ink-bottle effect), resulting in the dimension of the pore throats being the reported pore size.

The amount of gel porosity is comparable for G-1, G-2, and G-1-CB. Sample G-1-SF shows a higher value of gel porosity (Figure 5B). This is supported by the obtained surface area values (Table 4); G-1-SF shows the largest surface area of 39 m^2/g. Typically, the surface area increases with decreasing grain size. G-1 and G-1-CB have similar surface area values. Sample G-2 yields the smallest surface area (19 m^2/g). G-2 also has the lowest total porosity, at 17.59%. The addition of carbon black and silica fume did decrease the porosity by about 6% and 4%, respectively, compared to the total porosity of 26% of G-1.

N_2 Adsorption at 77 K

In contrast to MIP measurements, nitrogen adsorption/desorption measurements at 77 K can accurately determine the volume of the nanopores (<100 nm). Causes for differences in the porosity and pore size distribution measurements of these two methods have been discussed in the literature [52–54]. The dominant pore diameter for each sample, porosity, and surface area are reported in Table 4. Figure 6A shows the pore size distribution. In general, a similar trend compared to the MIP results is observed. One dominant population in the range of 50–70 nm is observed in all samples. This pore size range is slightly larger compared to the MIP measurements, but is in accordance with the MIP results. Additionally, at about 20 nm, a second, minor pore population is clearly visible in all samples. The smallest pore size obtained by N_2 adsorption is around 3 nm. However, one has to mention that, due to the limitations of the employed BJH method, it is not possible to detect pores that are significantly smaller than 3 nm. Also, the observation of decreasing pore volume by changing the slurry formulation is in accordance with MIP results. The measured porosity values are slightly lower compared to the MIP values (Table 4). However, both methods list G-1 as the sample with the highest porosity, with values of 25.9% and 24.5%, respectively. G-2 shows the lowest porosity values, with 17% for each method. Sample G-1-SF shows significant differences in the obtained porosity values. MIP yielded a porosity of 22%, whereas nitrogen adsorption yielded only 17.5%.

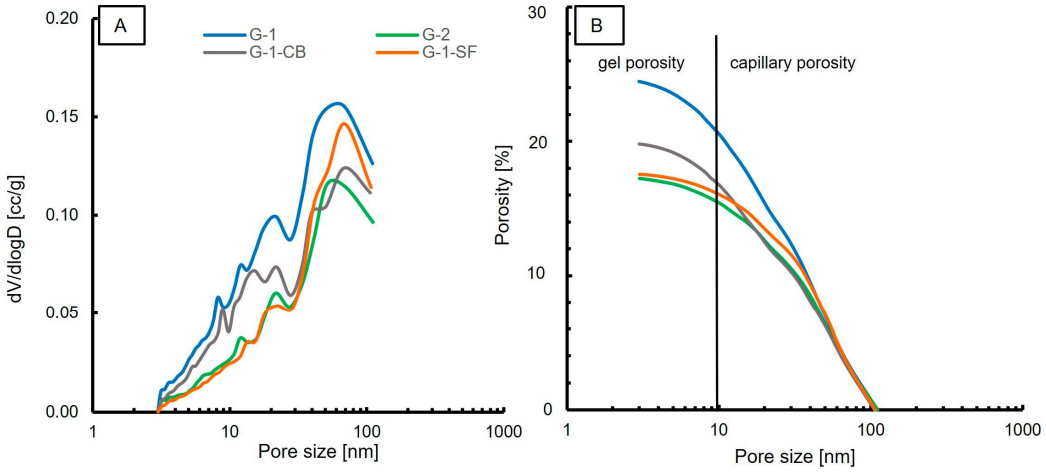

Figure 6. Results of N_2 adsorption experiments. (**A**) Pore size distribution; (**B**) Porosity vs. Pore size.

Figure 6B displays the porosity versus the pore size. Similar to MIP, the majority of measured porosity values fall in the range of capillary porosity. Roughly 8–10% of the total porosity is attributed to gel porosity. G-2 and G-1-SF show a lower gel porosity content compared to samples G-1 and G-1-CB. This is in contrast to what MIP indicated. The obtained surface area values are lower for all samples compared to the MIP results, but the same trend is observed for samples G-1, G-1-CB, and G-2. The results of G-1-SF are contradictory. It shows the lowest surface area of all four samples in the N_2 adsorption experiment, whereas MIP indicated the highest surface area.

Also, the indication of a second population in G-1-SF with a pore size of 3 nm as displayed by MIP (Figure 5A) is not confirmed in the N_2 adsorption experiment. To explain this discrepancy, one has to consider the different working principles and interaction mechanisms of the two techniques, as well as the employed models for data analysis. Other factors could be the sample preparation and sample drying process. For MIP, small, fractured pieces were analyzed, whereas for N_2 adsorption, a grinded powder was used. We can speculate that mechanical forces applied during milling in a hand mortar caused a reduction of the smallest pores. Also, the drying process may have led to a change in microstructure, since it is known that temperature has a significant influence on cement

paste microstructures [7]. However, the drying temperatures for both methods were the same at 40 °C, so we exclude this explanation.

3.2.2. Permeability

The measured nitrogen gas permeability of the investigated cement sheaths is reported in Table 4. G-1 and G-2 show a very similar permeability of 0.08 and 0.09 mD, respectively, which is in accordance with values reported in other studies [16]. G-1-CB shows a slightly higher permeability of 0.18 mD, G-1-SF shows a significantly higher permeability of 1.26 mD.

Figure 7 displays the raw data obtained during the permeability measurements. It illustrates the applied differential pressure of the measuring device plotted against the permeability calculated by the software. For each sample, five permeability values were recorded, while the applied differential pressure of the permeating nitrogen gas was increased (Section 2.8). As can be seen, the linear correlation fits nearly perfectly with correlation values of R^2 higher than 0.9. This acts as a quality control for the measurement and allows for the calculation of the mean permeability values, presented in Table 4.

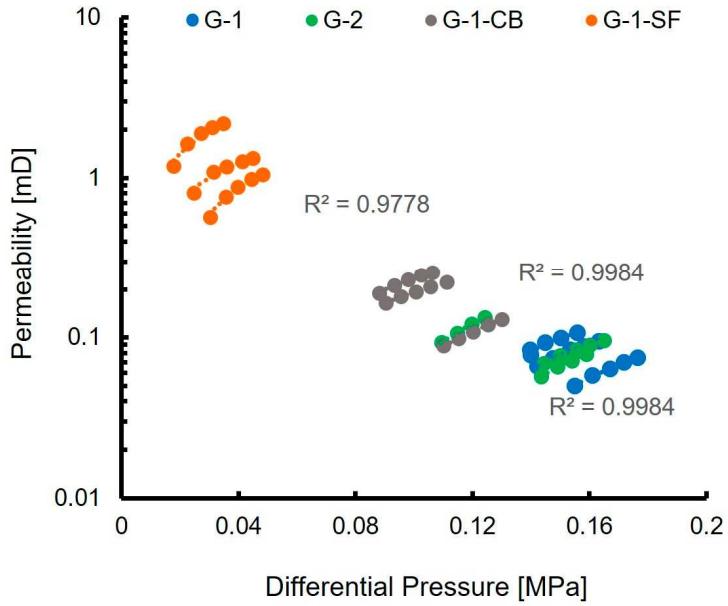

Figure 7. Results of nitrogen permeability measurements. The nominal minimum permeability the equipment is able to measure is 0.01 mD.

One aspect of the initial idea of adding carbon black and silica fume to the cement slurry was to reduce the permeability of the hardened cement sheath. Carbon black was added with the intention of filling the pore space and reducing it, thereby lowering the ability of gases to permeate through. As pointed out, silica fume additionally causes pozzolanic reactions, increasing the amount of C-S-H phases and also changing the microstructure of the cement paste (see Sections 3.1 and 3.2). The increased permeability of G-1-SF observed in this study can be explained by the formation of shrinkage cracks due to the higher water consumption caused by the pozzolanic reaction and the mechanically more brittle behavior of the sample (Section 3.3). This effect has been documented before [19,27,55,56]. The agglomeration of aggregated carbon black particles (Figure 1) might cause heterogeneity within the cement paste, also affecting its physical and mechanical performance.

3.3. Mechanical Properties

The results of uniaxial compressive strength (UCS) and tensile strength testing are reported in Table 5. In total, three measurements of each slurry formulation were carried out. An increase in the UCS was observed for G-2 and G-1-SF (Figure 8A), corresponding

to the reduction of the w/c ratio and the addition of silica fume, respectively. This can be explained by the reduced porosity, which was also documented with SEM and is reflected in the physical properties (Figure 1, Table 4). The increased number of C-S-H phases in sample G-1-SF is another major cause for the increase in UCS values, since this phase is mainly responsible for late strength development in cement sheaths. G-1-CB shows decreased UCS compared to G-1, while its tensile strength increases slightly. G-1-CB shows reduced porosity and slightly increased C-S-H content compared to G-1; why the UCS value is reduced is not fully understood. One hypothesis could be that the reduction is caused by the prolonged formation of low-density C-S-H relative to high density C-S-H phases. This is supported by the higher Ca/Si ratio obtained by EPMA measurements (Section 3.1.4; Figure 4) and the lower Young's modulus (Table 5). Such a correlation between the development of low-density C-S-H and the deterioration of concrete stiffness (e.g., effective reduction of Young's modulus) has been observed before [57]. Another possible explanation could be the presence of large, aggregated carbon black particles (Figure 1E), creating weak spots within the sample.

Table 5. Results of mechanical testing.

n = 3	G-1	G-2	G-1-CB	G-1-SF
UCS [MPa]	44.5 ± 1.3	51.3 ± 2	38.4 ± 2.2	56.5 ± 1.5
Tensile Strength [MPa]	1.2 ± 0.01	1.6 ± 0.09	1.3 ± 0.02	2.2 ± 0.06
Young's modulus [GPa]	4.8 ± 0.21	6.0 ± 0.13	4.4 ± 0.16	6.1 ± 0.11

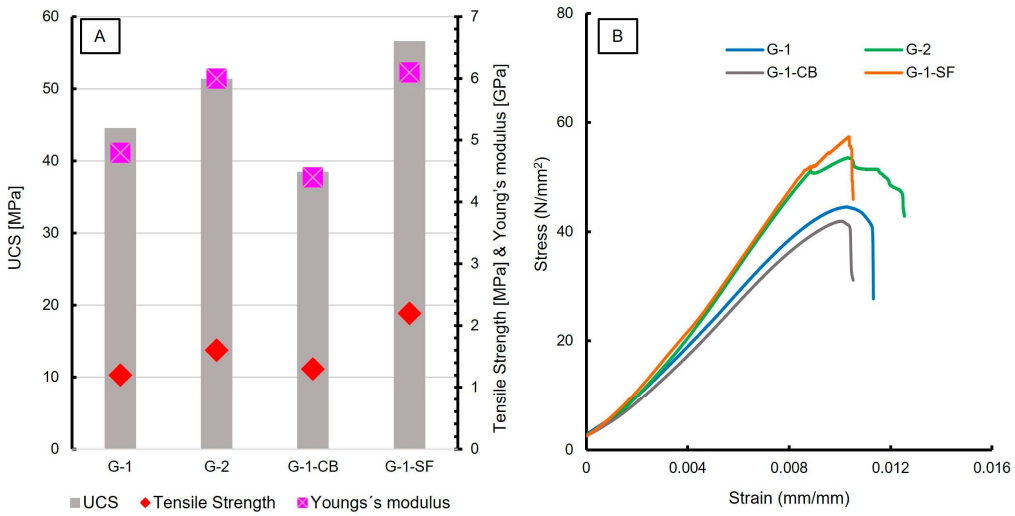

Figure 8. (**A**) Diagram showing results of UCS, Tensile Strength, and Young's modulus measurements; (**B**) stress—strain curves of the investigated cement sheaths. Young's modulus was calculated from the initial slope of the linear part of the stress—strain curves.

Figure 8B shows the stress vs. strain curves of UCS testing, displaying the mechanical behavior. G-1 and G-1-CB show a very similar behavior, as do G-2 and G-1-SF. All four samples show a quasi-linear rise in the beginning, indicating the elastic area where the Young's modulus values were calculated. After reaching maximum stress, G-1 and G-1-CB show somewhat plastic behaviors, with a vaulted curve before failure, displayed in a rapid and steep decline in stress. G-2 and G-1-SF show two linear areas. The first one makes up the majority of the curve up to a stress of 52 N/mm^2 followed by a small but sharp decrease and a shorter second linear trend before the material fails. This indicates the compression of pore space with a short failure. Once the compressible pore space is reduced, the sample still holds mechanical strength, which increases further. However, for G-2, the second linear part of the curve has a very flat rise compared to G-1-SF. Also, the behavior of G-2 at maximum strain looks like vaulted steps. This can be interpreted as plastic behavior as well.

G-1-SF, however, shows a very rapid decline after the second linear increase, indicating the very brittle behavior of the sample. Both G-2 and G-1-SF show very similar values for the Young's modulus at around 6 GPa. The very brittle behavior of G-1-SF might also be an explanation for the increased crack formation observed by SEM studies of this sample. G-1-CB shows the lowest Young's modulus, with a value of 4.4 GPa. When combined with the increased tensile strength, carbon black seems to be an additive that increases the ductile behavior of cement sheaths. This can be very beneficial in a geoenergy well to resist any bending or lateral forces once the infrastructure is in place. Otherwise, too brittle behavior might have negative consequences, resulting in failure of the applied cement sheath and endangering well integrity.

4. Discussion

Due to the variety of methods applied, careful and adequate sample preparation was of utmost importance to obtain reliable and reproducible results. Since different mixture formulations were compared, unintended artifacts or sample manipulations during sample preparation and storage are not considered to have a severe influence on the findings of this study, bearing in mind that all samples were treated the same way. However, concerning the investigation of physical properties, the addition of additives could hinder the removal of water during the solvent exchange, drying, or degassing of the samples. This could influence the results of porosity obtained by N_2 adsorption. Especially, sample G-1-SF showed significant differences concerning pore size, porosity, and surface area obtained by the two methods applied (Table 4).

The addition of silica fume clearly affects the microstructure of the C-S-H phase. This has been observed before [20,27,58]. Due to the small particle size and high surface area of silica fume, the hydration kinetics of the cement paste are enhanced at an early stage, promoting C-S-H nucleation. Also, the rate of capillary water consumption is increased, affecting the hydration process of the C-S-H due to the lack of water-filled space for C-S-H growth. This could explain the observed change in crystallite morphology (Figure 1) and the promoted granular C-S-H shape compared to the C-S-H needles present in samples G-1 and G-2. Similar conclusions can be drawn for the microstructure of sample G-1-CB. Even though the added carbon black is assumed to be chemically inert, it might physically block the free water-filled space, preventing the growth of a needle-like C-S-H microstructure and reducing porosity.

Mineral chemical analysis (Figure 4A) showed that the Ca/Si ratio of the C-S-H matrix decreased due to the addition of silica fume and increased slightly in sample G-1-CB. Previous studies found that the Ca/Si ratio directly correlates with increased polymerization of the silicate chains, constituting the layers inside the nanometric units of C-S-H [42,59,60]. It was revealed previously [42,57] that there are two forms of C-S-H, namely low density or inner product and high density or outer product with dissimilar mechanical properties. However, the way the Ca/Si ratio or the degree of polymerization affects the mechanical properties is not fully understood due to the difficulties to decouple this effect from other parameters such as bulk chemistry, porosity, degree of hydration, C-S-H content, portlandite content, and the intermixing of these phases [50]. The results of our study suggest that an increase in Ca/Si ratio leads to a decrease in UCS (Figure 4A; Figure 8). This could offer a potential explanation for the contradictory observation of sample G-1-CB, which shows slightly increased C-S-H content but decreased UCS and Young's modulus values. Yet, one has to consider that the mechanical properties investigated in this study are bulk parameters of the entire cement sheath. Therefore, conclusions about the mechanical behavior of a single phase, even though C-S-H is considered the most significant phase in cement sheaths when it comes to mechanical strength, have to be made delicately. Perhaps further investigations of, for example, nanoindentation experiments [61] combined with high-resolution in-situ chemical analysis (e.g., FE-EPMA), could contribute to a more ultimate conclusion. Samples G-1 and G-2 show the same Ca/Si ratio; however, G-2 has

elevated UCS. This can be explained by the decreased porosity of the sample due to the lower water content in the mix formulation.

Our study highlights the complexity of cement sheaths and their characterization, considering that the before-mentioned factors have a mutual influence. Only a holistic and interdisciplinary approach with the application of a wide spectrum of different methods can lead to a reasonable interpretation of the results. Figure 9 illustrates the most important findings of this study and their interplay. It can be seen that samples with increased mechanical strength (G-2, G-1-SF) also have a higher C-S-H content (e.g., a higher ratio of C-S-H/portlandite), increased bulk density, decreased porosity, and smaller mean pore diameters. Additionally, the C-S-H in G-1-SF has a decreased Ca/Si ratio. G-1-CB, of which C-S-H has the highest observed Ca/Si ratio, also has reduced porosity, but its UCS and Young's modulus have decreased. However, tensile strength did increase. In general, for the geoenergy industry, an additive that increases tensile strength and reduces the Young's modulus of the cement sheath is highly valuable. When placed in the annular space, it is less brittle and therefore more resistant against lateral forces within the well. To increase the tensile strength of a material, some sort of bonding/adhesion must appear.

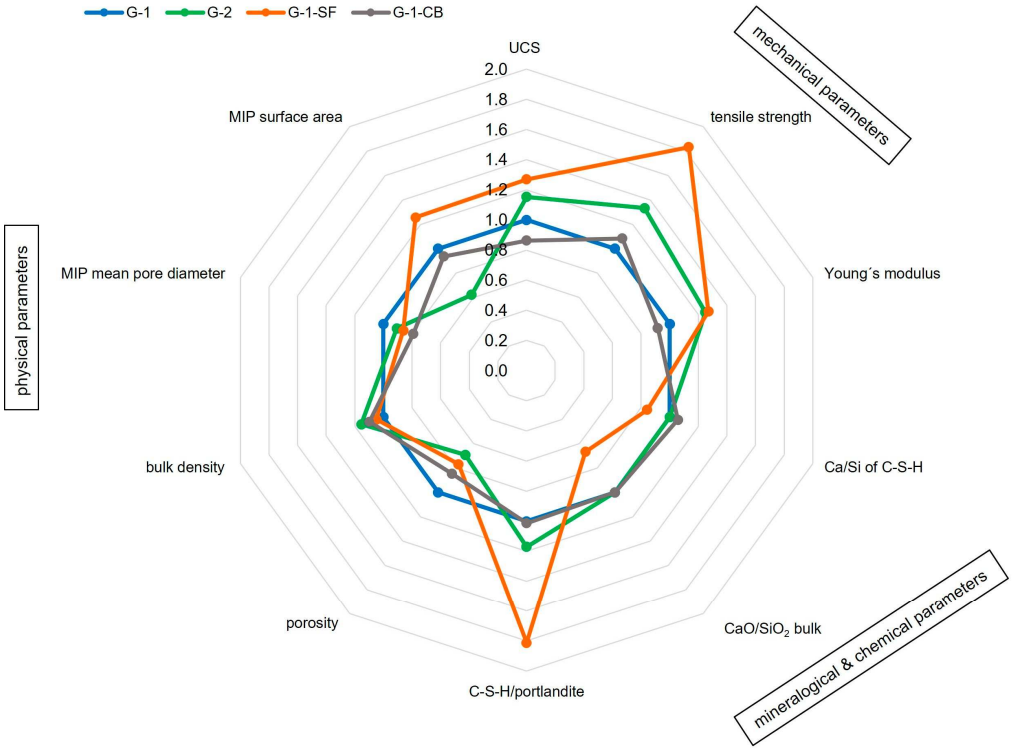

Figure 9. Illustration of the interplay of various parameters obtained in this study that affect well integrity. The parameters are displayed as ratios compared to baseline sample G-1; a value greater than 1 means an increase in the parameter compared to G-1, a value lower 1 implies a decrease.

The surfactant used for samples G-1-CB and G-1-SF to make the formulation mixable could also have an influence on the mechanical properties. However, since only small amounts of surfactant were added (Table 1), its influence is assumed to be negligible. Also, the amount of carbon black added to the mix formulation, as well as the quality, grain size, or degree of agglomeration of carbon black particles, might have an influence on the hardened cement sheath [23]. As shown in Figure 8B, the addition of silica fume makes the cement sheath more brittle. Thus, adding too much silica fume might have negative consequences for the tensile strength of the cement sheath. Silica fume might also have negative effects on the viscosity of the cement slurry. Too high amounts of silica fume make the slurry very viscose, which would lead to a slurry that is no longer pumpable in the field during the cementing of a geoenergy well.

Though the porosity was reduced by adding additives or reducing the w/c ratio (Table 4), the permeability was not tailored beneficially by these measures. But permeability is also dependent on the connectivity, shape, and tortuosity of the pores. Since porosity did decrease in samples G-1-CB and G-1-SF, the assumption can be drawn that matrix permeability for samples containing carbon black or silica fume did decrease. However, due to the higher brittleness and, therefore, the increased occurrence of fractures or heterogeneous distribution of the additive within the sample, higher bulk permeability was observed. Since lower porosity and especially lower pore sizes mean higher capillary forces, it is generally harder for fluids to permeate through the cement. However, future research focusing on permeability aspects within this context is necessary.

5. Conclusions

Four cement sheath samples for geoenergy wells with different mix formulations were characterized regarding mineralogical, physical, and mechanical properties, as well as their interplay. Two samples contained the additives carbon black and silica fume. One sample had a reduced w/c ratio. The addition of carbon black and silica fume led to a visible (under the SEM) change in the microstructure and had some effect on the modal and chemical phase composition.

Adding silica fume increases the content of C-S-H phases and reduces the portlandite content. The disappearance of the specific AFm sulfate phase indicates minor changes in the mineralogical phase composition. EPMA measurements indicate increased S incorporation into the C-S-H phase and a decreased Ca/Si ratio. Additionally, the addition of silica fume results in a much denser and more granular microstructure of the C-S-H matrix, suppressing the formation of phases with acicular morphology. Moreover, the mechanical strength increased, but a more brittle behavior of the cement sheath was also observed.

The addition of carbon black results in a higher Ca/Si ratio of the C-S-H phase, indicating the prolonged stability of the low-density C-S-H phases within this sample. Also, UCS and Young's modulus decreased, but tensile strength increased. This observed change in mechanical behavior can be beneficial for geoenergy well cement sheaths to withstand lateral stress.

Changing the w/c ratio of the cement slurry mixture does not visibly change the microstructure, but leads to a decrease in porosity and an increase in mechanical strength. Permeability was highest in the cement sheath containing silica fume, likely due to the formation of microcracks. These cracks are potentially caused by shrinkage during the curing of the sample due to the higher amount of water required for the pozzolanic reaction. Additionally, the observed increase in brittle mechanical behavior might lead to enhanced crack formation.

The findings of this study highlight the complexity of cement sheaths and their challenging characterization. Only a holistic and interdisciplinary approach with the application of mineralogical methods allows for an integrated evaluation of their physical and mechanical behaviors.

Author Contributions: Conceptualization, T.S.; methodology, T.S.; investigation, T.S. and N.K.; resources, A.N. and N.K.; writing—original draft preparation, T.S., A.N. and N.K.; writing—review and editing, A.N., N.K., K.R. and J.G.R.; supervision, K.R. and J.G.R. All authors have read and agreed to the published version of the manuscript.

Funding: This research activity has received funding from Montanuniversität Leoben, Austria, and is part of the Strategic Core Research Area SCoRe A^+ Hydrogen and Carbon.

Data Availability Statement: Data available upon request.

Acknowledgments: The authors would like to thank Friedrich Kittinger for performing TGA experiments, David Misch, Lukas Skerbisch and Gerhard Hawranek for providing assistance during SEM investigations.

Conflicts of Interest: The authors declare that they have no known competing financial interests or personal relationships that could have appeared to influence the work reported in this paper.

References

1. Nelson, E.B. *Well Cementing*, 1st ed.; Elsevier Science: Amsterdam, The Netherlands, 1990.
2. Carter, G.; Slagle, K. A Study of Completion Practices to Minimize Gas Communication. *J. Pet. Technol.* **1972**, *24*, 1170–1174. [CrossRef]
3. Levine, D.C.; Thomas, E.W.; Bezner, H.P.; Tolle, G.C. Annular Gas Flow After Cementing: A Look at Practical Solutions. In Proceedings of the SPE Annual Technical Conference and Exhibition, Las Vegas, NV, USA, 23–26 September 1979.
4. Cheung, P.R.; Beirute, R.M. Gas Flow in Cements. *J. Pet. Technol.* **1985**, *37*, 1041–1048. [CrossRef]
5. Bois, A.-P.; Vu, M.-H.; Ghabezloo, S.; Sulem, J.; Garnier, A.; Laudet, J.-B. Cement Sheath Integrity for CO_2 Storage—An Integrated Perspective. *Energy Procedia* **2013**, *37*, 5628–5641. [CrossRef]
6. Ghabezloo, S.; Sulem, J.; Guédon, S.; Martineau, F.; Saint-Marc, J. Poromechanical behaviour of hardened cement paste under isotropic loading. *Cem. Concr. Res.* **2008**, *38*, 1424–1437. [CrossRef]
7. Bahafid, S.; Ghabezloo, S.; Duc, M.; Faure, P.; Sulem, J. Effect of the hydration temperature on the microstructure of Class G cement: C-S-H composition and density. *Cem. Concr. Res.* **2017**, *95*, 270–281. [CrossRef]
8. Verbeck, G.J. Structures and Physical Properties of Cement Paste. *Proc. Int. Symp.* **1968**, *13*, 1–32.
9. Kjellsen, K.O.; Detwiler, R.J.; Gjørv, O.E. Pore structure of plain cement pastes hydrated at different temperatures. *Cem. Concr. Res.* **1990**, *20*, 927–933. [CrossRef]
10. Taylor, H.F.W. *Cement Chemistry*, 2nd ed.; Thomas Telford Ltd.: London, UK, 2003.
11. Kjellsen, K.O.; Detwiler, R.J.; Gjørv, O.E. Backscattered electron imaging of cement pastes hydrated at different temperatures. *Cem. Concr. Res.* **1990**, *20*, 308–311. [CrossRef]
12. Famy, C.; Brough, A.; Taylor, H. The C-S-H gel of Portland cement mortars: Part I. The interpretation of energy-dispersive X-ray microanalyses from scanning electron microscopy, with some observations on C-S-H, AFm and AFt phase compositions. *Cem. Concr. Res.* **2003**, *33*, 1389–1398. [CrossRef]
13. Scrivener, K.L. Backscattered electron imaging of cementitious microstructures: Understanding and quantification. *Cement Concrete Compos.* **2004**, *26*, 935–945. [CrossRef]
14. Stutzman, P.E. 3. Microscopy of Clinker and Hydraulic Cements. In *Applied Mineralogy of Cement & Concrete*; Broekmans, M.A., Pöllmann, H., Broekmans, M.A., Eds.; De Gruyter: Berlin, Germany, 2012; pp. 101–146.
15. Krakowiak, K.J.; Thomas, J.J.; Musso, S.; James, S.; Akono, A.-T.; Ulm, F.-J. Nano-chemo-mechanical signature of conventional oil-well cement systems: Effects of elevated temperature and curing time. *Cem. Concr. Res.* **2015**, *67*, 103–121. [CrossRef]
16. Qin, J.; Pang, X.; Cheng, G.; Bu, Y.; Liu, H. Influences of different admixtures on the properties of oil well cement systems at HPHT conditions. *Cem. Concr. Compos.* **2021**, *123*, 104202. [CrossRef]
17. Zyganitidis, I.; Stefanidou, M.; Kalfagiannis, N.; Logothetidis, S. Nanomechanical characterization of cement-based pastes enriched with SiO2 nanoparticles. *Mater. Sci. Eng. B* **2011**, *176*, 1580–1584. [CrossRef]
18. Cuesta, A.; Santacruz, I.; De la Torre, A.G.; Dapiaggi, M.; Zea-Garcia, J.D.; Aranda, M.A. Local structure and Ca/Si ratio in C-S-H gels from hydration of blends of tricalcium silicate and silica fume. *Cem. Concr. Res.* **2021**, *143*, 106405. [CrossRef]
19. Yajun, J.; Cahyadi, J.H. Effects of densified silica fume on microstructure and compressive strength of blended cement pastes. *Cem. Concr. Res.* **2003**, *33*, 1543–1548. [CrossRef]
20. Liao, W.; Sun, X.; Kumar, A.; Sun, H.; Ma, H. Hydration of Binary Portland Cement Blends Containing Silica Fume: A Decoupling Method to Estimate Degrees of Hydration and Pozzolanic Reaction. *Front. Mater.* **2019**, *6*, 78. [CrossRef]
21. Juenger, M.C.G.; Siddique, R. Recent advances in understanding the role of supplementary cementitious materials in concrete. *Cem. Concr. Res.* **2015**, *78*, 71–80. [CrossRef]
22. Calloni, G.; Moroni, N.; Miano, F. Carbon Black: A Low Cost Colloidal Additive for Controlling Gas-Migration in Cement Slurries. In Proceedings of the SPE International Symposium on Oilfield Chemistry, San Antonio, TX, USA, 14–17 February 1995.
23. Zhang, Q.; Luan, C.; Yu, C.; Huang, Y.; Zhou, Z. Mechanisms of carbon black in multifunctional cement matrix: Hydration and microstructure perspectives. *Constr. Build. Mater.* **2022**, *346*, 128455. [CrossRef]
24. Snellings, R.; Mertens, G.; Elsen, J. Supplementary Cementitious Materials. *Rev. Mineral. Geochem.* **2012**, *74*, 211–278. [CrossRef]
25. Massazza, F. Pozzolana and Pozzolanic Cements. In *Lea's Chemistry of Cement and Concrete*; Elsevier: Amsterdam, The Netherlands, 1998; pp. 471–635.
26. Lu, P.; Sun, G.; Young, J.F. Phase Composition of Hydrated DSP Cement Pastes. *J. Am. Ceram. Soc.* **1993**, *76*, 1003–1007. [CrossRef]
27. Muller, A.; Scrivener, K.; Skibsted, J.; Gajewicz, A.; McDonald, P. Influence of silica fume on the microstructure of cement pastes: New insights from 1H NMR relaxometry. *Cem. Concr. Res.* **2015**, *74*, 116–125. [CrossRef]
28. Mueller, D.T.; Dillenbeck, R.L. The Versatility of Silica Fume as an Oilwell Cement Admixture. In Proceedings of the SPE Production Operations Symposium, Oklahoma City, OK, USA, 7–9 April 1991.
29. Bhanja, S.; Sengupta, B. Influence of silica fume on the tensile strength of concrete. *Cem. Concr. Res.* **2005**, *35*, 743–747. [CrossRef]
30. Lura, P.; Jensen, O.M.; van Breugel, K. Autogenous shrinkage in high-performance cement paste: An evaluation of basic mechanisms. *Cem. Concr. Res.* **2003**, *33*, 223–232. [CrossRef]

31. Jensen, O.; Hansen, P.F. Autog enous Deformation and Change of the Relative Humidity in Silica Fume-Modified Cement Paste. *Mater. J.* **1996**, *93*, 539–543.
32. Barcelo, L.; Kline, J.; Walenta, G.; Gartner, E. Cement and carbon emissions. *Mater. Struct.* **2014**, *47*, 1055–1065. [CrossRef]
33. Amato, I. Green cement: Concrete solutions. *Nature* **2013**, *494*, 300–301. [CrossRef]
34. American Petroleum Institute, API SPEC 10A. 2022. Available online: https://shop.standards.ie/en-ie/standards/api-spec-10a-2019-add-2-2022-96776_saig_api_api_3182225/ (accessed on 5 July 2024).
35. Scrivener, K.; Snellings, R.; Lothenbach, B. (Eds.) *A Practical Guide to Microstructural Analysis of Cementitious Materials*; CRC Press: Boca Raton, FL, USA; Taylor & Francis Group: London, UK, 2016.
36. Lea, F.M.; Hewlett, P.C. *Lea's Chemistry of Cement and Concrete*; Elsevier: Amsterdam, The Netherlands, 1998.
37. Diamond, S. Mercury porosimetry: An Inappropriate Method for the Measurement of Pore Size Distributions in Cement-Based Materials. *Cem. Concr. Res.* **2000**, *30*, 1517–1525. [CrossRef]
38. Aligizaki, K.K. *Pore Structure of Cement-Based Materials*; CRC Press: Boca Raton, FL, USA, 2005.
39. Li, X.; Li, M. Multifunctional self-sensing and ductile cementitious materials. *Cem. Concr. Res.* **2019**, *123*, 105714. [CrossRef]
40. Sutton, D.L.; Faul, R.; Sabins, F. Annular gas flow theory and prevention methods described. *Oil Gas J.* **1984**, *82*, 50.
41. Richardson, I.G.; Groves, G.W. Microstructure and microanalysis of hardened cement pastes involving ground granulated blast-furnace slag. *J. Mater. Sci.* **1992**, *27*, 6204–6212. [CrossRef]
42. Richardson, I.G. The calcium silicate hydrates. *Cem. Concr. Res.* **2008**, *38*, 137–158. [CrossRef]
43. Lamberet, S. *Durability of Ternary Binders Based on Portland Cement, Calcium Aluminate Cement and Calcium Sulfate*; EPFL: Lausanne, Switzerland, 2005.
44. Šauman, Z. Carbonization of porous concrete and its main binding components. *Cem. Concr. Res.* **1971**, *1*, 645–662. [CrossRef]
45. Morandeau, A.; Thiéry, M.; Dangla, P. Investigation of the carbonation mechanism of CH and C-S-H in terms of kinetics, microstructure changes and moisture properties. *Cem. Concr. Res.* **2014**, *56*, 153–170. [CrossRef]
46. Branch, J.; Kosson, D.; Garrabrants, A.; He, P. The impact of carbonation on the microstructure and solubility of major constituents in microconcrete materials with varying alkalinities due to fly ash replacement of ordinary Portland cement. *Cem. Concr. Res.* **2016**, *89*, 297–309. [CrossRef]
47. Sevelsted, T.F.; Skibsted, J. Carbonation of C–S–H and C–A–S–H samples studied by 13 C, 27 Al and 29 Si MAS NMR spectroscopy. *Cem. Concr. Res.* **2015**, *71*, 56–65. [CrossRef]
48. Allen, A.J.; Thomas, J.J.; Jennings, H.M. Composition and density of nanoscale calcium-silicate-hydrate in cement. *Nat. Mater.* **2007**, *6*, 311–316. [CrossRef]
49. Chatterji, S. CaO/SiO2 mole ratio of calcium silicate hydrate in fully hydrated tricalcium silicate paste. *Cem. Concr. Res.* **1980**, *10*, 783–787. [CrossRef]
50. Sebastiani, M.; Moscatelli, R.; Ridi, F.; Baglioni, P.; Carassiti, F. High-resolution high-speed nanoindentation mapping of cement pastes: Unravelling the effect of microstructure on the mechanical properties of hydrated phases. *Mater. Des.* **2016**, *97*, 372–380. [CrossRef]
51. Jennings, H.M.; Thomas, J.J.; Rothstein, D.; Chen, J.J. Cements as Porous Materials. In *Handbook of Porous Solids*; Schth, F., Sing, K.S.W., Weitkamp, J., Eds.; Wiley-VCH Verlag GmbH: Weinheim, Germany, 2002; pp. 2971–3028.
52. Hansen, W.; Almudaiheem, J. Pore Structure of Hydrated Portland Cement Measured by Nitrogen Sorption and Mercury Intrusion Porosimetry. *MRS Proc.* **1986**, *85*, 105. [CrossRef]
53. Midgley, H.; Illston, J. Some comments on the microstructure of hardened cement pastes. *Cem. Concr. Res.* **1983**, *13*, 197–206. [CrossRef]
54. Valckenborg, R.M.E.; Pel, L.; Hazrati, K.; Kopinga, K.; Marchand, J. Pore water distribution in mortar during drying as determined by NMR. *Mater. Struct.* **2001**, *34*, 599–604. [CrossRef]
55. Bhanja, S.; Sengupta, B. Modified water–cement ratio law for silica fume concretes. *Cem. Concr. Res.* **2003**, *33*, 447–450. [CrossRef]
56. Maruyama, I.; Teramoto, A. Temperature dependence of autogenous shrinkage of silica fume cement pastes with a very low water–binder ratio. *Cem. Concr. Res.* **2013**, *50*, 41–50. [CrossRef]
57. Constantinides, G.; Ulm, F.-J. The effect of two types of C-S-H on the elasticity of cement-based materials: Results from nanoindentation and micromechanical modeling. *Cem. Concr. Res.* **2004**, *34*, 67–80. [CrossRef]
58. Muller, A.C.A.; Scrivener, K.L.; Gajewicz, A.M.; McDonald, P.J. Densification of C–S–H Measured by 1 H NMR Relaxometry. *J. Phys. Chem. C* **2013**, *117*, 403–412. [CrossRef]
59. Chiang, W.-S.; Ferraro, G.; Fratini, E.; Ridi, F.; Yeh, Y.-Q.; Jeng, U.-S.; Chen, S.-H.; Baglioni, P. Multiscale structure of calcium- and magnesium-silicate-hydrate gels. *J. Mater. Chem. A* **2014**, *2*, 12991. [CrossRef]
60. Cappelletto, E.; Borsacchi, S.; Geppi, M.; Ridi, F.; Fratini, E.; Baglioni, P. Comb-Shaped Polymers as Nanostructure Modifiers of Calcium Silicate Hydrate: A 29Si Solid-State NMR Investigation. *J. Phys. Chem. C* **2013**, *117*, 22947–22953. [CrossRef]
61. Renuka, V.; Venkateswara Rao, S.; Tadepalli, T. Nanoindentation technique in characterizing cementitious materials—A review. *Mater. Today Proc.* **2023**, *in press*. [CrossRef]

International Journal of Hydrogen Energy 89 (2024) 1166–1175

Contents lists available at ScienceDirect

International Journal of Hydrogen Energy

journal homepage: www.elsevier.com/locate/he

Hydrogen induced changes in the phase composition and micro-structure of downhole cements: Fundamental research within the context of underground hydrogen storage

Thomas Sammer [a,*], Nikolaos Kostoglou [b], Krishna Ravi [c], Johann G. Raith [a]

[a] Department of Applied Geosciences and Geophysics, Montanuniversität Leoben, Leoben, 8700, Austria
[b] Department of Materials Science, Montanuniversität Leoben, Leoben, 8700, Austria
[c] Department of Geoenergy, Montanuniversität Leoben, Leoben, 8700, Austria

ARTICLE INFO

Handling Editor: Dr A Bhatnagar

Keywords:
Underground hydrogen storage
Cement sheath integrity
Cement-hydrogen interaction
Mineralogical phase analysis

ABSTRACT

Underground hydrogen storage (UHS) promises great storing potential for energy produced from renewables. To make UHS a feasible and safe process, fundamental research investigating the integrity of the cement sheath applied in boreholes against hydrogen exposure is essential. In this study, hydrothermal autoclave experiments are conducted to evaluate hydrogen induced changes in the mineralogical phase composition and the micro-structure of a class G cement. X-ray diffraction and scanning electron microscopy combined with nitrogen adsorption/desorption experiments are carried out. Only minor mineralogical changes are observed such as the decomposition of monosulphate and the formation of ettringite. Nitrogen adsorption/desorption experiments reveal comparable pore size distributions with minor differences in porosity and surface area. The findings of this study suggest that hydrogen does not substantially affect the phase composition and microstructure of the investigated low permeable class G cement sheath emphasizing the relatively unreactive nature of downhole cements of this type against hydrogen.

1. Introduction

Current energy politics aim for a substitution of conventional fossil fuels by renewable energy sources to reduce anthropogenic CO_2 emissions combating climate change [1–3]. To overcome weather and seasonal fluctuations in the energy production of e.g., wind or solar sources and thus addressing a significant challenge of the broad implementation of a sustainable energy transition, hydrogen is becoming the centre of interest. Nowadays, hydrogen is considered a promising way of storing energy from renewable energy sources. However, to store hydrogen in a feasible way, vast storage volumes are needed [4–7]. Underground hydrogen storage (UHS), e.g., the concept of using natural geological bodies in the subsurface like depleted oil or gas fields as potential storage volumes, promises exactly that [8–15].

The storage of hydrogen containing gas mixtures in geologic formations is not a new concept as “town gas” has been stored in the subsurface during the last century [7]. However, the application of UHS in the context of renewable energy storage is a more recent development [16]. In recent years, various UHS pilot plants were conducted in e.g. Germany [4,5,17,18], Poland [19,20], China [21], Spain [22], Romania [23], France [24], the United States of America [25] and the United Kingdom [10] with most of them using salt caverns as storage volume [26].

However, for UHS to become a sustainable reality, environmental considerations and the environmental footprint of UHS infrastructure including wells, pipelines and surface facilities on local ecosystems and landscapes have to be evaluated and considered as well [8,27]. One significant concern is hydrogen leakage as the H_2 molecule might be able to diffuse through narrowest gaps and fractures that are impermeable for other gases due to its very small molecule size [11,13,26]. Such hydrogen leakage into e.g., the groundwater can disrupt chemical balances and influence or even enhance microbial activity and processes as there is a variety of hydrogen metabolizing bacteria [8,10,28]. Such microbial process can cause methane production or interactions with subsurface minerals altering the geochemistry [8]. Also, the injection and withdrawal of hydrogen can induce seismic activity causing

* Corresponding author. Chair of Resource Mineralogy, Department of Applied Geosciences and Geophysics, Montanuniversität Leoben, Peter-Tunner-Straße 5, 8700, Leoben, Austria
E-mail address: thomas.sammer@stud.unileoben.ac.at (T. Sammer).

https://doi.org/10.1016/j.ijhydene.2024.09.449
Received 19 January 2024; Received in revised form 23 September 2024; Accepted 30 September 2024

environmental and safety hazards [26,27].

From an operational point of view, depleted gas and oil reservoirs are preferred for the geologic storage of H_2 due to their abundancy compared to salt caverns and already existing infrastructure [5]. Further advantages of depleted fields are that (a) the reservoirs are already fairly well understood and (b) the usage of existing infrastructure like boreholes and surface handling facilities can prevent high initial investment costs. Boreholes provide access to geological reservoirs but are also the bottleneck of any production or storage operation. Simplified, boreholes are lined with downhole materials, consisting of a steel casing surrounded by a cement sheath filling the so-called annular space. The cement sheath, as a key element for well integrity, acts as a bonding component between the steel casing and wallrock ensuring mechanical stability and tightness of the hole.

However, the unique physical and chemical properties of hydrogen might cause potential integrity issues during a UHS operation. Despite integrity issues of the reservoir and cap rock caused by potential hydrogen induced chemical or biochemical reactions, especially the effect that hydrogen might have on the mineralogical phase composition and subsequently on the physical and mechanical parameters of downhole cement, potentially deteriorating the integrity of the cement sheath, is still very scarcely known [5,26,29]. To make UHS a feasible process, fundamental research investigating not just the integrity of reservoir and cap rocks [7,30–34], but also downhole cements applied in boreholes during the storage life of the well are essential, also from a safety perspective [5,35–37]. Borehole integrity is particularly important once the injection scale is industrial, as there is a severe knowledge gap regarding the interaction of hydrogen with downhole cement, which is a significant barrier element for the well integrity and therefore safety [38–42].

Usually, Portland type cements containing the four main clinker phases alite (C_3S or Ca_3SiO_5), belite (C_2S or Ca_2SiO_4), ferrite (C_4AF or $Ca_2(Al,Fe)_2O_5$) and aluminate (C_3A or $Ca_3Al_2O_6$) are applied during well cementing jobs. Once the initial cement is mixed with water, the above-mentioned phases react with water at different rates to develop the binding and a solidified hydrated cement paste. Calcium silicate hydrates (C–S–H) with an amorphous and layered crystal structure are the main hydration products responsible for the mechanical strength of the cement sheath [43]. Other phases formed during the hydration process include portlandite ($Ca(OH)_2$), the aluminium-iron trisulphate ettringite (AFt, $Ca_6Al_2(SO_4)_3(OH)_{12}\bullet 26H_2O$) and the aluminium-iron monosulphate (AFm, $Ca_6Al_2(SO4)(OH)_{12}\bullet 12H_2O$).

Even though the effect hydrogen might have on downhole cement is still very scarcely known and only limited experimental results are published so far [16,35,44], some studies were carried out in recent years performing thermodynamic modelling on this system [45,46]. These models indicate that certain redox-sensitive phases within the hardened cement sheath are susceptible to hydrogen alteration caused by the strong reducing character of hydrogen. Especially ferric iron and sulphate bearing phases like ferrite (C_4AF), AFm and ettringite are altered, resulting in the formation of native iron, magnetite, iron sulphides and Al-hydrates.

However, modelling results need to be expanded by experimental work. Studies, conducting short term, long term or even cyclic hydrogen exposure to cement sheaths are crucial for understanding well integrity during UHS. Short term experiments with a hydrogen exposure of class H cement for 7 days conducted by Hussain et al. (2022) showed a decrease in compressive strength over time, linked to the reductive dissolution of hematite (Fe_2O_3) and the subsequent formation of mackinawite (FeS). CT scans confirmed an increase in hydrogen bubbles within the cement matrix, correlating with the observed strength reduction [47]. Ugarte et al. (2023) conducted hydrogen exposure experiments on cements of class H cured under different environments and for different time periods of up to 168 days. They observed minor changes in mechanical and physical properties as well as the formation of portlandite and ettringite [44]. Al-Yaseri et al. (2023) investigated the effects of hydrogen on cement of class G under reservoir conditions after 125 days. The results indicate low reactivity of the cement with hydrogen, however an increase in cement weight and density was observed [35]. Shi et al. (2020) exposed cements to hydrogen for 3 months, however the results indicated relatively small changes in porosity and mineralogy and more sever changes in permeability [16]. Maury et al. (2023) evaluated the influence of hydrogen on mechanical and physical properties of class H cement under reservoir conditions for different time periods. The results revealed an increase in porosity and permeability and a change in the elastic properties of the cement [48].

This study aims to contribute to a better fundamental understanding on how hydrogen might influence the mineralogical phase composition of downhole cement class G and its implications on physical and mechanical properties of the cement sheath. To do so, the rationale of this study was to compare baseline samples to samples exposed to various hydrogen containing atmospheres. Therefore, hydrothermal autoclave experiments exposing hydrated cement pastes to hydrogen gas in a defined but closed environment were carried out. Mineralogical investigations combined with nitrogen adsorption/desorption experiments were performed before and after hydrogen treatment to evaluate any changes to the phase composition and microstructure of the investigated cement paste.

2. Materials and methods

2.1. Cement sample preparation and hydrogen treatment

Oil well cement of class G was used and mixed according to the specification 10A of the American Petroleum Institute (- API Spec 10A [49]). The water to cement (w/c) ratio was 0.44 and the mixed slurry was poured into cylindrical brass moulds with 2.54 cm diameter and 5.08 cm length. After pouring, the cement paste was left for curing in a water bath for 28 days. After 28 days the hardened cement paste was demoulded, and 5 mm thick slices were cut from the initial cylinder using a water-cooled stone saw. To stop hydration, the slices where then placed in isopropanol for 24 h for solvent exchange, followed by drying at 40 °C in a compartment dryer until constant mass was achieved. To limit carbonation in between experiments, the slices were placed in a desiccator. Table 1 lists the formulation of the mixed paste along with basic physical and chemical properties of the hardened cement paste and the cement class G used.

Table 1
Formulation of the cement slurry as well as chemical and physical data, BWOC = by weight of cement. The chemical bulk composition was analysed by X-ray fluorescence (XRF).

		Hydrated cement paste	Cement Class G
Formulation (BWOC %)	Cement	100	100
	Water	44	–
Physical properties (g/cm^3)	Density of slurry	1.9	–
	Bulk density	1.62	–
	Skeletal density	2.37	3.18
Chemical composition obtained by XRF (Mass%)	SiO_2	18.21	21.15
	TiO_2	0.17	0.18
	Al_2O_3	4.07	4.65
	Fe_2O_3	3.64	4.06
	MnO	0.11	0.11
	CaO	54.45	63.23
	MgO	0.82	0.95
	Na_2O	0.1	0.1
	K_2O	0.58	0.76
	P_2O_5	0.1	0.11
	SO_3	3.1	2.7
	LOI	14.41	1.4
	Total	99.76	99.4

After one year, the following experimental runs were then applied to the hydrated cement paste (Table 2): (i) untreated (dry-baseline sample, e.g., Portland cement of class G), (ii) 10 wt% synthetic NaCl brine treated (wet-baseline sample), (iii) hydrogen gas treated (dry-H_2), and (iv) hydrogen and 10 wt% synthetic NaCl brine treated (wet-H_2). Even though case (iii) is unlikely to be reflective of real in-situ UHS conditions, it was still considered insightful for a better fundamental understanding of the so far completely unknown system hydrogen-cement sheath. For cases (iii) and (iv), specially designed autoclaves (high-pressure cells, see Fig. 1) were used to allow treatment of the cement at a hydrogen pressure of 80 bar. Autoclave experiments of cases (iii) and (iv) were conducted once at room temperature (22 °C) and once at 80 °C, with the later experiment representing more realistic in-situ pressure-temperature conditions of a UHS process. For the experiment involving synthetic brine, the autoclave was filled up half with brine and then the sample was placed in the brine before filling up the autoclave with hydrogen until a pressure of 80 bar was reached. Case (ii) was carried out at room temperature and atmospheric pressure, allowing to evaluate the influence the synthetic brine had on the hydrated cement paste for better comparison. All experimental runs lasted for 28 days. The samples then underwent mineralogical and microstructural investigations to study the impact of hydrogen gas exposure.

2.2. Mineralogical and microstructural investigation

To obtain powdered sample material needed for X-ray diffraction (XRD) measurements, the hydrated cement paste was first ground and then milled using a hand mortar to ensure a delicate sample preparation and avoid additional grinding-induced amorphization of certain phases in the hardened cement paste. XRD measurements were done with a Panalytical XPert 3 Powder Diffractometer located at the Chair of Energy Geosciences, Montanuniversität Leoben, operating at 40 kV and 40 mA, using Cu Kα (1.5 Å) as radiation source at a step size of 0.004° per second in the 2θ range of 2.5°–70°. The qualitative identification of the phases was done manually by comparing the interlayer distance (d) values of the major peaks with the database table presented in Ref. [50].

For visual investigation of the microstructure slices of baseline and autoclave treated samples were crushed into small pieces using a hand mortar. Scanning electron microscope image acquisition was done using a TESCAN CLARA field emission scanning electron microscope (FE-SEM) instrument located at the Chair of Functional Materials and Materials Systems, Montanuniversität Leoben, equipped with the TESCAN Essence Image Snapper software, version 1.0.8.0, allowing capturing and stitching of high-resolution images. Both backscattered (BSE) and secondary (SE) electron images were obtained, and qualitative chemical information was gathered with an energy dispersive X-ray spectroscopy (EDX) system from Oxford Instruments. The acceleration voltage was set at 10 kV and the beam current at 1 nA. To obtain a conducting surface and minimize charging effects, the samples were coated with gold using a Cressington Sputter Coater 108 Auto with 30 s sputtering time.

Table 2
Experimental conditions of the treatment cases applied to the investigated cement class G paste conducted within this study.

case	H_2-treatment	Involvement of brine	T [°C]	p [bar]	comment
(i)			22	atmospheric pressure	dry-baseline
(ii)		x	22	atmospheric pressure	wet-baseline
(iii)	x		22	80	dry-H_2 @ 22 °C
			80		dry-H_2 @ 80 °C
(iv)	x	x	22	80	wet-H_2 @ 22 °C
			80		wet-H_2 @ 80 °C

Low-pressure gas sorption experiments were conducted with an Autosorb iQ^3 gas sorption analyser from Anton Paar QuantaTec located at the Chair of Physics, Montanuniversität Leoben, using N_2 of ultra-high purity (99.999%) as adsorbate. This allowed to quantify basic physical parameters of the hydrated cement paste such specific surface area, specific pore volume and pore size distribution. Therefore, in the same way as for the XRD studies, the samples were ground with a hand mortar to obtain a fine powder suitable for analytics. Before the actual measurement, 0.4 g of powdered sample were outgassed under vacuum (10^{-6} mbar) for 24 h at 40 °C. To reduce the dead volume of the sample cell, which was automatically evaluated before each run using helium (99.999% purity), non-porous glass filling rods were placed inside the sample cells alongside the sample powder. Nitrogen adsorption/desorption isotherms were recorded at 77 K in a relative pressure (P/P_0) range from 10^{-3} to 0.99. Pore volumes and pore size distribution from 3 to 100 nm were estimated using the Barrett-Joyner-Halenda (BJH) method while the surface area was calculated using both the BJH and the multi-point Brunauer-Emmett-Teller (BET) methods. One has to mention that in principle the BJH method approach is not suitable to determine pore size distributions of heterogenous mesoporous (IUPAC classification [51]) materials with a low surface area. However, in a qualitative or semi-quantitative manner the BJH derived data can be used as a relative comparison between samples of the same batch with similar adsorption characteristics. Porosity of the samples was based on the estimated pore volume by nitrogen adsorption data and the skeletal density determined of sample powders with a helium Ultrapycnometer 1000 from Quantachrome using the following equation (1):

$$\text{Porosity} = \frac{\text{skeletal density}^*\text{Vpores}}{1 + \text{skeletal density}^*\text{Vpores}} \quad (1)$$

In general, hardened cement paste is heterogenous due to its nature of being a mix of cement powder and water hardened by chemical reactions. This leads to the composure of different mineral phases that make up the hardened paste. To ensure comparability of different samples from the same batch, mixing and curing procedures were developed within cement sciences [50]. One such procedure for downhole cements is API Spec 10A [49] which was implemented within this study to limit the influence of the heterogeneity and to ensure comparability of the samples. Additionally, the sample preparation for e.g., XRD or N_2 sorption, where the cement gets milled up into a fine powder, acts as a homogenisation process further eliminating the influence of initial heterogeneity.

3. Results and discussion

3.1. Mineralogical investigation: AFm decomposition and Al–Ca-hydrate formation

Fig. 2 displays the results of X-ray diffraction analysis of the cases runs described above, with the main peaks of the identified major phases marked. A consistent and similar phase composition is observed in the diffractograms of all samples. The main crystalline phase is portlandite (CH) in all treated samples and the baseline sample, accompanied by remnants of the initial clinker phases belite and ferrite, in agreement with their slower hydration reaction rate than alite and aluminate [52,53]. While a symmetric reflection peak is expected for the highly crystalline phase portlandite, the non-symmetric peak of portlandite at ~34.7° 2θ suggests the presence of hibschite, a hydrated member of the Ca-garnet grossular, i.e. a hydrogarnet. Despite indications of hibschite, other common hydration products, especially from the ferrite clinker phase, were not detected, possibly due to their poor crystallinity rendering them undetectable by XRD. The elevated, plateau-like area in the 2θ range of ~27°–35° is attributed to amorphous C–S–H phases [54]. The calcite peak at 27° indicates some carbonation of the cement

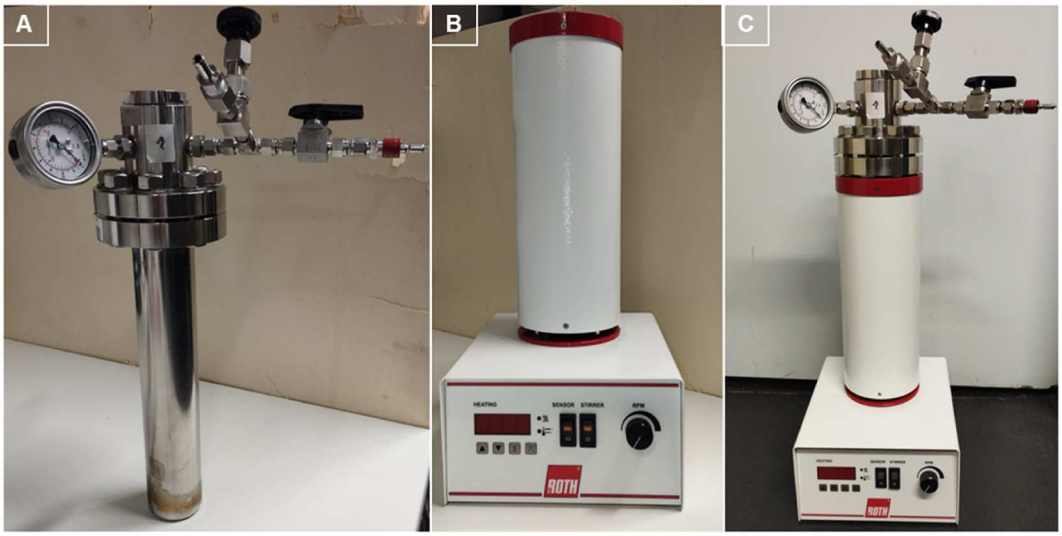

Fig. 1. A) hydrothermal autoclave used in this study; B) heating system for temperature control during experimental runs; C) assembled autoclave and heating system.

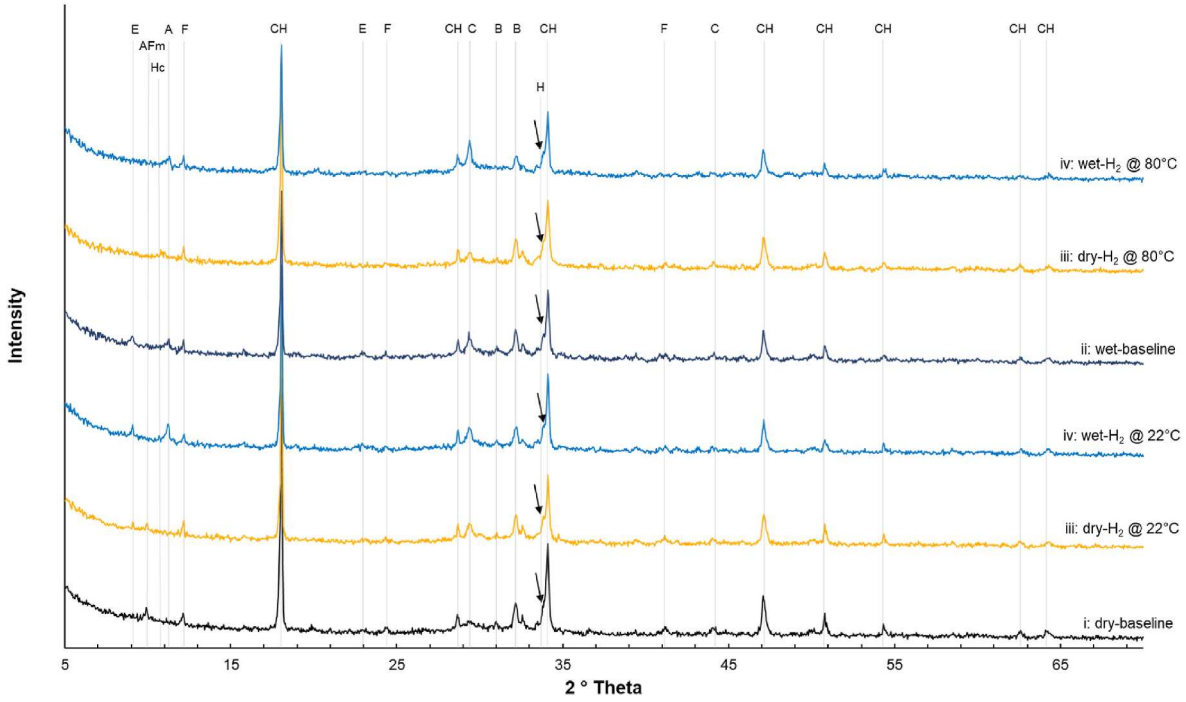

Fig. 2. X-ray diffractograms of samples from the different investigated cases as well as the baseline samples, E = ettringite, AFm = monosulphate, Hc = hemicarbonate, A = C_4AH_{13} phase, CH = portlandite, C = calcite, B = belite, H = hibschite.

samples. Despite precautions to prevent carbonation by storing the samples in tubs and in a desiccator to minimize exposure to CO_2 in ambient air, complete prevention of carbonation remains challenging [50,54].

Nevertheless, certain distinctions, particularly in the initial segment of the diffractograms (5°–15° for 2θ), were noted, indicating subtle alterations in the mineralogical phase composition of the examined cement pastes due to the applied experimental runs. The most prominent difference is the absence of the most significant peak of the AFm (monosulphate) phase at a 2θ angle of 9.8° [55]. AFm is a common hydration product in cement pastes which forms out of the initial hydration product ettringite (trisulphate) as the hydration process progresses [38,40]. Since the investigated cement paste was cured for 28 days and then stored in a desiccator for one year, the presence of AFm in the baseline sample is to be expected.

However, the introduction of hydrogen (case (iii) @ 22 °C) and hydrogen-brine (case (iv) @ 22 °C), as well as brine alone (case (ii), wet-baseline), induces the decomposition of AFm and the re-formation of ettringite (Fig. 2). This observation aligns with previously published results of thermodynamic modelling [45,46], suggesting that the introduction of the potent reducing agent H_2 triggers redox reactions especially within redox-sensitive phases, particularly those incorporating oxidized species of iron (e.g., Fe^{3+} in AFm) and sulphate (SO_4^{2-}). However, the formation of completely reduced phases like sulphides or hematite and the complete absence of sulphate-containing phases as predicted by thermodynamic modelling [33], were not observed.

It is important to remember that thermodynamic modelling assumes equilibrium; however, during the experimental runs, equilibrium may not have been reached, potentially resulting in intermediary products such as ettringite. Also, the results of thermodynamic modelling heavily depend on the quality of the underlying database. AFm and ettringite are known to have a variable chemical composition enabling the substitution of various ions (e.g., Al^{3+}, Fe^{3+}, Cr^{3+}, CO_3^{2-}, SO_4^{2-}, SeO_4^{2-}, CrO_4^{2-}) in the crystal structures [56]. This makes it difficult to obtain good and reliable thermodynamic data for these phases. Additionally, the kinetics governing these redox reactions may extend the duration of the four-week experiments, despite previous studies on the kinetics of hydrogen-induced pyrite reduction suggest a rapid reaction occurring within hours to days [57,58].

Given that ettringite is also forming in the baseline sample of case (ii), other factors such as the presence of fluids (e.g., brine) or humidity may also control ettringite formation. Previous studies having investigated the stability of ettringite come to the conclusion that a more humid environment favours ettringite formation and stability [56]. In samples of case (iii) @ 80 °C and case (iv) @ 80 °C, ettringite was not observed. This aligns with the decomposition of ettringite at higher temperatures [59,60]. Instead, in case (iii) @ 80 °C a hemicarbonate phase (Hc, $Ca_4Al_2(CO_3)_{0.5}(OH)_{13} * 5.5H_20$)) [61] was observed, while in case (iv) @ 80 °C, C_4AH_{13}, a calcium-aluminium hydrate, was identified. The occurrence of these phases is consistent with the modelling predicted by Zeng et al. [45]. Given that case (iii) @ 80 °C and especially case (iv) @ 80 °C closely resemble more realistic conditions for underground hydrogen storage in geological reservoirs, an important insight from this study is that the introduction of hydrogen does not severely affect the major mineralogical phase composition of the investigated class G cement paste. Although minor changes were observed, these changes can also be ascribed to the presence and interaction of brine with the cement paste, as evidenced by similar observations in the mineralogical phase composition of the baseline sample (case (ii)).

3.2. Mineralogical investigation: high-resolution scanning microscopy

Microphotographs illustrating fractured surfaces of the examined cement pastes for each case are presented in Figs. 3 and 4. In Fig. 3, fractured surfaces of cases (i) and (iii), at both 20 °C and 80 °C, are showcased. Fig. 4 provides insights into observations for cases (ii) and (iv) at both 20 °C and 80 °C. Here both internal surfaces and external surfaces have been imaged; the latter are surfaces of the sample that had been in direct contact with the respective treatment case's atmosphere. This approach enhances the comprehension of how the permeability of the cement paste may contribute to any discernible changes.

As depicted in Fig. 3, the surface characteristics exhibit strikingly

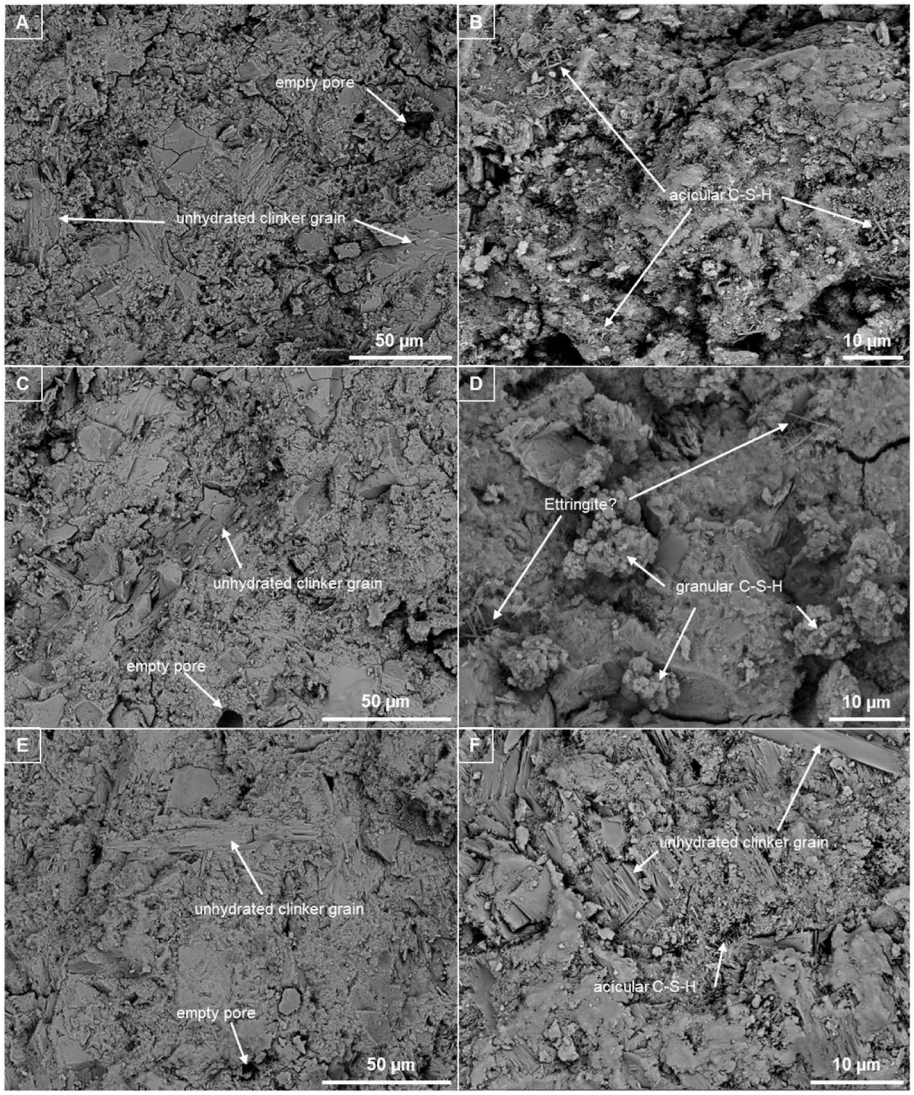

Fig. 3. BSE microphotographs obtained with a FE-SEM of samples of case (i) and (iii) @ both 22 °C and 80 °C, at lower (A, C, E) and higher (B, D, F) magnification.

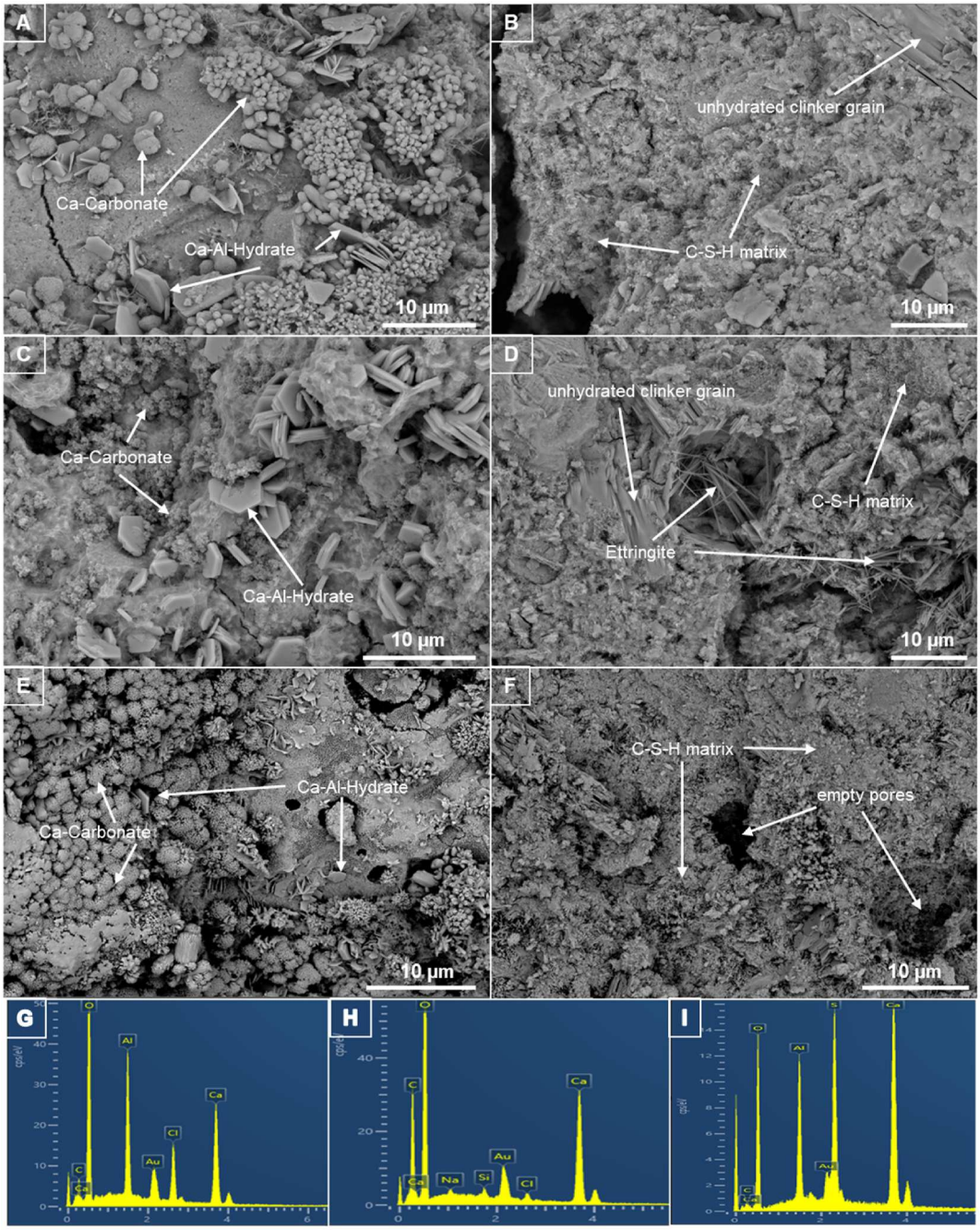

Fig. 4. BSE images obtained with a FE-SEM of samples of case (ii) (A and B) and (iv) @ 22 °C (C and D) and @ 80 °C (E and F); G-I) representative EDX spectra of Al–Ca-hydrate (G), Ca-carbonate (H) and ettringite (I) observed in the samples; the Au peak is from the coating.

similar appearances across all cases. Occasionally, non-hydrated clinker grains are visible, along with some larger pores (capillary pores, approximately several µm in size). The predominant phase constituting the cement paste matrix, namely the C–S–H, displays both acicular and granular morphologies [52,62]. However, the C–S–H exhibits exceedingly fine-grained structures in the nanometre range and its amorphous nature precludes the observation of a distinct crystal structure [52]. Notably, in the microphotographs of case (iii) @ 22 °C, some larger needles, approximately 1 µm in size, are seen (Fig. 3-D). Drawing insights from XRD data and the distinctive acicular morphology, this phase could potentially be identified as ettringite [56,60].

Cases (ii) and (iv) exhibit a comparable microstructure on the inner surfaces (fractured surfaces not in direct contact with the atmosphere of the corresponding case) of the samples (Fig. 4 -B, D, E). Here, non-hydrated clinker grains and a C–S–H matrix with a very fine-grained (in the nanometre range) acicular or granular morphology are the predominant observable features. However, in the case of (iv) @ 22 °C, the formation of needles with a size in the micrometre range within pores is evident. EDX spectra acquired from these needles (Fig. 4-I) validate their identification as ettringite. The EDX spectra reveal a higher S peak than Al peak, a characteristic signature of ettringite [63]. The filling of pore space by ettringite, for example, could contribute to the beneficial effect of reduced permeability and increased mechanical strength of the cement sheath, as observed in prior studies [44]. However, it is crucial to note that delayed ettringite formation (DEF) could pose challenges when the crystallization pressure, induced by ettringite formation within the pores, exceeds the mechanical strength of the cement sheath. This situation may lead to expansion, followed by internal damage, thereby

weakening the cement sheath [64,65]. In contrast, the pores of case (iv) @ 80 °C (Fig. 4-F) are empty, and no ettringite needles are observed. This aligns with the results of the XRD measurements and underscores the instability of ettringite at elevated temperatures [59,60]. The hemicarbonate phase identified by XRD could not be discerned during the SEM investigations of this sample.

On the external surfaces (those directly exposed to the fluids and atmosphere of the corresponding case), a markedly distinct appearance is evident (Fig. 4-A, 4-C and 4-E). Here, micrometre-sized hexagonal and platy-shaped crystals have formed. Morphologically, these crystals closely resemble portlandite [66]. However, EDX analysis indicates that chemically these crystals are chlorine, calcium and aluminium-bearing hydrate (Fig. 4-G). C_4AH_{13} is known to typically develop such structures [67]. As mentioned earlier, both thermodynamic modelling [45] and XRD measurements of this study confirm the presence of such a phase.

Since these crystals also form in the baseline sample (case (ii), Fig. 4-A), it can be inferred that the formation of this phase is not attributed to hydrogen but is instigated by the presence of brine. The observation that these hexagonal platy crystals are exclusively found on the external surface and not the internal surface suggests that solid-fluid interaction between cement and brine (leaching and precipitation mechanisms) drive their formation. Initially, calcium, aluminium and most likely other elements are leached out of the cement when exposed to the brine and hydrogen atmosphere. As the autoclave experiments are characterised by a closed system with no fresh brine supply, saturation is eventually reached. This leads to the precipitation of the chlorine-bearing calcium-aluminium hydrate on the surface with the chlorine being up taken from the initial artificial brine. Since the investigated class G cement paste is low permeable due to the slurry formulation with a w/c ratio of 0.44 the absence of these phases on the internal surfaces can also be a result of the low porosity and low permeability and therefore the inability of the saturated fluid to permeate into the cement paste. Similar observations are noted for Ca-carbonates in both cases (ii) and (iv) (Fig. 4-A, 4-C, 4-E and 4-H). Notably, the Ca-carbonates exhibit diverse morphologies, encompassing rounded and edgy shapes, as revealed at higher magnification (Fig. 5). It is concluded that the underlying mechanism for this carbonate formation is once again precipitation. The tap water used, is assumed to contain bicarbonate as a potential carbon source, which likely contributes to this process. Upon contact with brine, leaching followed by precipitation may occur. This assumption is supported by the absence of carbonates on the interior of the cement (Fig. 4-B, 4-D, and 4-E), restricting this observation to a surface precipitation process, similar to the chlorine-bearing C_4AH_{13}.

In cases where hydrogen is introduced into the system, the carbonates exhibit smaller and less defined structures with a markedly distinct granular and irregular morphology, indicative of dissolution. This suggests that hydrogen may lead to the dissolution of carbonates, a topic currently under discussion, especially in the context of the integrity of cap rock and reservoir rocks during the UHS process [34,68]. However, this is a preliminary observation, and the primary focus of this study does not centre on carbonate dissolution. Further experiments are imperative to gain deeper insights into this aspect.

High-resolution BSE images of the aforementioned Ca-carbonates are illustrated in Fig. 5. Fig. 5-A showcases carbonate aggregates composed of prismatic to acicular individual crystals, which exhibit undefined rounded morphologies. A distinct steep rhombohedral-scalenohedral shape of individual crystals is evident (Fig. 5-B), suggesting a morphological resemblance to calcite which crystallizes in the trigonal crystal system [69].

3.3. Pore structure characterization: nitrogen adsorption experiments

The pore size distribution obtained by nitrogen adsorption/desorption measurements at 77 K for the conducted experimental runs, reveals a consistent general trend across all samples (Fig. 6-A). In each case, a predominant pore family with a mean pore diameter (D1) of approximately 69 nm is evident (Table 3). At around 20 nm (D2), a second, albeit minor, pore family can be distinguished. Notably, the sample of case (iii) @ 22 °C (depicted by the blue solid line in Fig. 6-A) displays a slightly different pattern with more humps and lacking the second minor pore family. Moreover, the mean pore diameter of the dominant pore family (D1) is marginally larger for this sample compared to the others (Table 3). However, this deviation is minimal and lacks statistical significance. It is noteworthy that the pore size distribution of case (i), representing the baseline sample, also exhibits a slightly more varied pattern. Remarkably, the sample of case (iv) @ 80 °C (depicted by the yellow dotted line in Fig. 6-A) displays a relatively higher volume content of the smallest pores, suggesting the potential presence of pores smaller than 3 nm. However, the applied BJH method does not enable the detection of pores smaller than 3 nm. The remaining pore size distribution of this sample is comparable to the other samples.

In Fig. 6-B, the porosity versus pore size is presented in a semi-logarithmic format. Samples from case (i) (baseline) and case (iv) @ 80 °C exhibit a higher content of gel porosity (pore sizes <10 μm), leading to a steeper decline of the curve and consequently a lower percentage of capillary porosity. This contrasts with the flatter to sub-horizontal gel porosity patterns observed for the other samples. Capillary and gel porosity are terms from cement and concrete science that describe pores with sizes ranging from 2.5 nm up to 10 μm for capillary porosity and 0.5 nm up to 10 nm for gel porosity, respectively [50]. However, there is no distinct trend in porosity across the samples. The baseline sample of case (i) demonstrates the highest porosity (24.5%), while the baseline sample @ 80 °C exhibits the lowest one (14.9%). It appears that temperature and the presence of brine already influence the physical properties such as porosity, making it challenging to draw clear assumptions about the impact of hydrogen [54,70]. However, it is crucial to note that the BJH method applied in this study only allows the

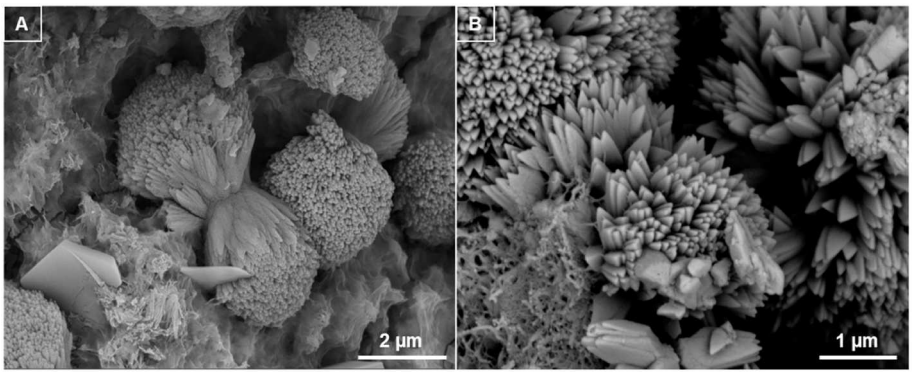

Fig. 5. BSE images of the Ca-carbonates of the case (iv) sample obtained with a FE-SEM; A) @ 22 °C, B) @ 80 °C.

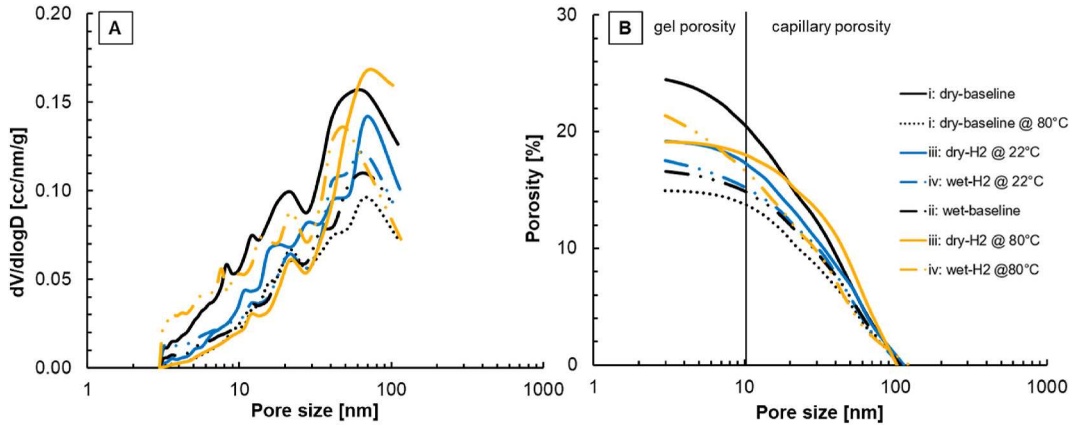

Fig. 6. Results of nitrogen adsorption/desorption experiments at 77 K as deduced by the BJH method, A) pore size distribution of the investigated samples in semi-logarithmic display, B) porosity vs. pore size in semi-logarithmic display.

Table 3
Physical data obtained by N_2 adsorption/desorption experiments at 77 K of hydrated cement pastes for the investigated experimental runs (case i) to (case iv). mPD (D1) = mean pore diameter of the dominating main pore family, mPD (D2) = mean pore diameter of the second, minor pore family.

Multi-point Brunauer-Emmet-Teller (BET) method	Barrett-Joyner-Halenda (BJH) method				
Surface area	Surface area	Porosity	mPD D1	mPD D2	
m^2/g	m^2/g	%	nm	nm	
before H_2-treatment					case
22.9	24.9	24.5	69.2	21.8	i: dry-baseline
11.3	10.5	14.9	69.2	21.5	i: dry-baseline @ 80 °C
13.5	12.9	16.5	70.1	21.7	ii: wet-baseline
after H_2- treatment					case
14.6	14.8	19.1	96.5	18.1	iii: dry-H2 @ 22 °C
20.5	15.5	17.4	67.2	21.6	iv: wet-H2 @ 22 °C
11.1	11.3	19.1	68.8	21.7	iii: dry-H2 @ 80 °C
35.5	26.6	21.4	49.2	21.8	iv: wet-H2 @ 80 °C

investigation of pore sizes down to 3 nm reliably and the maximum pore size that can be explored with the nitrogen adsorption/desorption method is limited to values slightly above 100 nm. Additionally, the observed differences in the smallest pores in the gel porosity range could also be attributed to the milling process preceding the nitrogen adsorption/desorption experiments, where a hand mortar was used instead of an automated milling device to prevent overgrinding of the delicate sample material [50]. Thus, these variations might be explained by a higher degree of milling, resulting in a finer powder.

Table 3 summarizes the values of the surface areas and mean pore diameters obtained through the nitrogen adsorption/desorption experiments at 77 K. The surface areas obtained with the BET method characterize the investigated cement paste as low-surface area samples with obtained values ranging between 10 and 20 m^2/g for most samples. No clear differentiation can be observed between baseline samples (case (i) and (ii)) and samples exposed to H_2 containing environments (case (iii) and (iv)). Only samples of case (i) and case (iv) @ 80 °C have slightly higher values with 22.9 m^2/g and 35.5 m^2/g respectively. However, since case (i) as baseline sample has slightly elevated BET surface area, the slightly increased BET area for case (iv) can be neglected to be caused by the presence of H_2. For pore surface characterization the BET method is considered the "gold standard" for determining the total sum of the surface area (e.g., both internal and external surface area) [71]. However, also the cumulative surface areas obtained with the BJH method show similar surface area values compared to the BET values. Slight differences in surface areas, especially for such low-surface area samples could be related to contributions to the surface area not only related to the presence of nanopores (mostly mesopores and macropores in this samples according to the IUPAC classification [51]) but also the particle size itself, i.e. the finer is the powder, the higher will be the external surface area.

In general, it can be concluded that the addition of hydrogen does not significantly alter the pore structure of the investigated cement paste, which is in agreement with the observed minor changes in mineralogical phase composition. Similar to the mineralogical reactions, it can be inferred that other factors, such as the presence of brine or increased temperature, seem to have a more substantial impact on the cement sheath compared to hydrogen. This underscores the unreactive behaviour of hydrogen with the low permeable class G cement under the conditions investigated within this study aligning with the findings of other researchers [16,35,44,72]. The experiments conducted over the 28-day period within this research give an initial insight into the integrity of cement sheaths against hydrogen. However, UHS systems are intended for cyclic storage periods from weeks to months [29]. Therefore, it is necessary to conduct long term, experiments lasting for months or even years to fully assess the integrity of cement sheaths. Such future experiments have to also consider aging effects of the cement as well as the impact of cyclic loading. Cyclic loading leads to changes in the stress regime, potentially causing deformations within the cement sheath weakening its sealing capacity [26]. Al-Yaseri et al. (2023) conducted experiments lasting for 125 days. They concluded overall low reactivity of the investigated cement, however they did not consider the impact a cyclic change of the stress regime might have on mechanical properties of the cement [35]. The variation in pressure, gas volume and thermal expansion during cyclic storage of hydrogen could cause mechanical degradation of the cement sheath as it might not be designed for such specific and sever loading conditions [73]. Furthermore, UHS will most likely include the presence of methane as so-called cushion gas, e.g., the amount of gas that is permanently stored in natural gas storages. The presence of cushion gas leads to the formation of a hydrogen containing gas mixtures. However, methane containing cushion gas should not pose an issue as methane is very low reactive and there are decades of practical experience regarding the influence of methane on downhole cements coming from natural gas production.

4. Conclusions

Underground hydrogen storage promises great potential for storing energy from renewable energy sources, hence increasing their efficiency, and overcoming seasonal limitations. However, to make underground hydrogen storage a feasible process, fundamental research should not just focus on the integrity of the reservoir and cap rocks but also on the cement sheath applied in the annular space of boreholes upon interaction with hydrogen. Still there is a severe knowledge gap regarding the possible deteriorating effect that hydrogen might have on the cement sheath and therefore on the well integrity and safety. This experimental study evaluates.

1) the changes in the mineralogical phase composition of a hydrated cement paste of class G exposed to different hydrogen containing environments for a time span of 4 weeks and
2) the influence of changes in the phase composition on the physical properties of the cement.

X-ray diffraction (XRD) analysis revealed some minor changes to the phase composition, with portlandite and some residual non-hydrated clinker phases being the dominant crystalline phases in all samples. The decomposition of the AFm phase and the formation of ettringite were observed in autoclave experiments involving hydrogen and hydrogen-brine at room temperature.

In experimental runs done at 80 °C ettringite was absent due to its thermal decomposition at higher temperatures and a hemi-carbonate phase was observed instead. On surfaces which were in direct contact with the hydrogen-brine atmosphere hexagonal, platy crystals of a chlorine bearing Ca–Al-hydrate formed. Similarly, Ca-carbonates were observed with different morphology in the experimental runs with hydrogen. These findings agree with XRD measurements and published thermodynamic modelling results.

Nitrogen adsorption/desorption measurements were carried out at 77 K to identify potential changes in the pore structure due to the interaction with hydrogen. They revealed comparable pore size distributions in all samples. The higher percentage of gel porosity (pore size $<$10 nm) and surface area in cements exposed to hydrogen-brine at various temperatures are rather due to the influence of brine and not of the hydrogen. In general, it can be concluded that hydrogen does not significantly affect the pore structure, emphasizing the relatively unreactive nature of hydrogen-downhole cement systems.

In summary, this study confirms that the exposure of cement sheath to hydrogen does not lead to substantial changes in the mineralogical phase composition and its pore structure. Other factors such as the absence/presence of brine and elevated temperature seem to have a more significant impact. However, these findings are only valid for the investigated low permeable class G cement under the experimental conditions. Further research considering longer (e.g., months, or even years instead of the 4 weeks in this study) experimental durations, curing conditions at higher T and p, cyclic loading or even other slurry formulations which would result in a cement sheath with higher porosity and permeability and therefore better ability for hydrogen to permeate into it, needs to be evaluated.

CRediT authorship contribution statement

Thomas Sammer: Writing – review & editing, Writing – original draft, Methodology, Investigation, Conceptualization. **Nikolaos Kostoglou:** Writing – review & editing, Writing – original draft, Resources, Investigation. **Krishna Ravi:** Writing – review & editing, Supervision, Resources. **Johann Raith:** Writing – review & editing, Supervision.

Declaration of competing interest

The authors declare that they have no known competing financial interests or personal relationships that could have appeared to influence the work reported in this paper.

Acknowledgements

This research has received funding from Montanuniversität Leoben and is part of the Strategic Core Research Area SCoRe A^+ Hydrogen and Carbon. The authors would like to thank David Misch and Lukas Skerbisch for providing assistance during SEM investigations and Eva Wegerer and Franz Seidl for assistance during XRD measurements. N.K. is grateful to Christian Mitterer and Oskar Paris from the Montanuniversität Leoben for providing access to the gas sorption analyser.

References

[1] European Commission. European green deal: delivering on our targets. Luxembourg: Publications Office of the European Union; 2021.
[2] Williams JH, Jones RA, Haley B, Kwok G, Hargreaves J, Farbes J, Torn MS. Carbon-neutral pathways for the United States. AGU Adv 2021;2.
[3] Wen L, Li Z. Provincial-level industrial CO2 emission drivers and emission reduction strategies in China: combining two-layer LMDI method with spectral clustering. Sci Total Environ 2020;700:134374.
[4] Pudlo D, Ganzer L, Henkel S, Kühn M, Liebscher A, de Lucia M, Panfilov M, Pilz P, Reitenbach V, Albrecht D, Würdemann H, Gaupp R. The H2STORE project: hydrogen underground storage – a feasible way in storing electrical power in geological media? In: Hou MZ, Xie H, Were P, editors. Clean energy systems in the subsurface: production, storage and conversion. Berlin, Heidelberg: Springer Berlin Heidelberg; 2013. p. 395–412.
[5] Reitenbach V, Ganzer L, Albrecht D, Hagemann B. Influence of added hydrogen on underground gas storage: a review of key issues. Environ Earth Sci 2015;73:6927–37.
[6] Züttel A. Hydrogen storage methods. Naturwissenschaften 2004;91:157–72.
[7] Carden P, Paterson L. Physical, chemical and energy aspects of underground hydrogen storage. Int J Hydrogen Energy 1979;4:559–69.
[8] Amid A, Mignard D, Wilkinson M. Seasonal storage of hydrogen in a depleted natural gas reservoir. Int J Hydrogen Energy 2016;41:5549–58.
[9] Flesch S, Pudlo D, Albrecht D, Jacob A, Enzmann F. Hydrogen underground storage—petrographic and petrophysical variations in reservoir sandstones from laboratory experiments under simulated reservoir conditions. Int J Hydrogen Energy 2018;43:20822–35.
[10] Heinemann N, Booth MG, Haszeldine RS, Wilkinson M, Scafidi J, Edlmann K. Hydrogen storage in porous geological formations – onshore play opportunities in the midland valley (Scotland, UK). Int J Hydrogen Energy 2018;43:20861–74.
[11] Muhammed NS, Haq B, Al Shehri D, Al-Ahmed A, Rahman MM, Zaman E. A review on underground hydrogen storage: insight into geological sites, influencing factors and future outlook. Energy Rep 2022;8:461–99.
[12] Muhammed NS, Haq MB, Al Shehri DA, Al-Ahmed A, Rahman MM, Zaman E, Iglauer S. Hydrogen storage in depleted gas reservoirs: a comprehensive review. Fuel 2023;337:127032.
[13] Perera M. A review of underground hydrogen storage in depleted gas reservoirs: insights into various rock-fluid interaction mechanisms and their impact on the process integrity. Fuel 2023;334:126677.
[14] Pfeiffer WT, Bauer S. Subsurface porous media hydrogen storage – scenario development and simulation. Energy Proc 2015;76:565–72.
[15] Tarkowski R. Underground hydrogen storage: characteristics and prospects. Renew Sustain Energy Rev 2019;105:86–94.
[16] Shi Z, Jessen K, Tsotsis TT. Impacts of the subsurface storage of natural gas and hydrogen mixtures. Int J Hydrogen Energy 2020;45:8757–73.
[17] Ganzer L, Reitenbach V, Pudlo D, Panfilov M, Albrecht D, Gaupp R. The H2STORE project - experimental and numerical simulation approach to investigate processes in underground hydrogen reservoir storage. In: All days, SPE; 2013.
[18] Bauer S, Dahmke A, Kolditz O. Subsurface energy storage: geological storage of renewable energy—capacities, induced effects and implications. Environ Earth Sci 2017;76.
[19] Tarkowski R. Perspectives of using the geological subsurface for hydrogen storage in Poland. Int J Hydrogen Energy 2017;42:347–55.
[20] Tarkowski R, Czapowski G. Salt domes in Poland – potential sites for hydrogen storage in caverns. Int J Hydrogen Energy 2018;43:21414–27.
[21] Bai M, Song K, Sun Y, He M, Li Y, Sun J. An overview of hydrogen underground storage technology and prospects in China. J Petrol Sci Eng 2014;124:132–6.
[22] Sainz-Garcia A, Abarca E, Rubi V, Grandia F. Assessment of feasible strategies for seasonal underground hydrogen storage in a saline aquifer. Int J Hydrogen Energy 2017;42:16657–66.
[23] Iordache I, Schitea D, Gheorghe AV, Iordache M. Hydrogen underground storage in Romania, potential directions of development, stakeholders and general aspects. Int J Hydrogen Energy 2014;39:11071–81.
[24] Le Duigou A, Bader A-G, Lanoix J-C, Nadau L. Relevance and costs of large scale underground hydrogen storage in France. Int J Hydrogen Energy 2017;42:22987–3003.
[25] Lord A. Overview of geologic storage of natural gas with an emphasis on assessing the feasibility of storing hydrogen. 2009.

[26] Zeng L, Sarmadivaleh M, Saeedi A, Chen Y, Zhong Z, Xie Q. Storage integrity during underground hydrogen storage in depleted gas reservoirs. Earth Sci Rev 2023;247:104625.
[27] Taiwo GO, Tomomewo OS, Oni BA. A comprehensive review of underground hydrogen storage: insight into geological sites (mechanisms), economics, barriers, and future outlook. J Energy Storage 2024;90:111844.
[28] Heinemann N, Scafidi J, Pickup G, Thaysen EM, Hassanpouryouzband A, Wilkinson M, Satterley AK, Booth MG, Edlmann K, Haszeldine RS. Hydrogen storage in saline aquifers: the role of cushion gas for injection and production. Int J Hydrogen Energy 2021;46:39284–96.
[29] Zivar D, Kumar S, Foroozesh J. Underground hydrogen storage: a comprehensive review. Int J Hydrogen Energy 2021;46:23436–62.
[30] Hashemi L, Blunt M, Hajibeygi H. Pore-scale modelling and sensitivity analyses of hydrogen-brine multiphase flow in geological porous media. Sci Rep 2021;11:8348.
[31] Bo Z, Zeng L, Chen Y, Xie Q. Geochemical reactions-induced hydrogen loss during underground hydrogen storage in sandstone reservoirs. Int J Hydrogen Energy 2021;46:19998–20009.
[32] Hassannayebi N, Azizmohammadi S, de Lucia M, Ott H. Underground hydrogen storage: application of geochemical modelling in a case study in the Molasse Basin, Upper Austria. Environ Earth Sci 2019;78.
[33] Henkel S, Pudlo D, Werner L, Enzmann F, Reitenbach V, Albrecht D, Würdemann H, Heister K, Ganzer L, Gaupp R. Mineral reactions in the geological underground induced by H2 and CO2 injections. Energy Proc 2014;63:8026–35.
[34] Bensing JP, Misch D, Skerbisch L, Sachsenhofer RF. Hydrogen-induced calcite dissolution in Amaltheenton Formation claystones: implications for underground hydrogen storage caprock integrity. Int J Hydrogen Energy 2022;47:30621–6.
[35] Al-Yaseri A, Fatah A, Zeng L, Al-Ramadhan A, Sarmadivaleh M, Xie Q. On hydrogen-cement reaction: investigation on well integrity during underground hydrogen storage. Int J Hydrogen Energy 2023;48:35610–23.
[36] Angst UM, Geiker MR, Michel A, Gehlen C, Wong H, Isgor OB, Elsener B, Hansson CM, François R, Hornbostel K, Polder R, Alonso MC, Sanchez M, Correia MJ, Criado M, Sagüés A, Buenfeld N. The steel–concrete interface. Mater Struct 2017;50.
[37] Nasiri A, Ravi K, Prohaska-Marchried M, Feichter M, Raith J, Coti C, Baronio E, Busollo C, Mantegazzi A, Pozzovivo V, Pruno S. An interdisciplinary approach to investigate the cement integrity for underground hydrogen storage wells. 2023. Day 1 Mon, June 05, 2023, SPE.
[38] Nelson EB, editor. Well cementing. New York, USA: Elsevier; 2010.
[39] Carter G, Slagle K. A study of completion practices to minimize gas communication. J Petrol Technol 1972;24:1170–4.
[40] D.C. Levine, E.W. Thomas, H.P. Bezner, G.C. Tolle, Annular gas flow after cementing: a look at practical solutions, in:.
[41] Bois A-P, Vu M-H, Ghabezloo S, Sulem J, Garnier A, Laudet J-B. Cement sheath integrity for CO2 storage – an integrated perspective. Energy Proc 2013;37:5628–41.
[42] Kiran R, Teodoriu C, Dadmohammadi Y, Nygaard R, Wood D, Mokhtari M, Salehi S. Identification and evaluation of well integrity and causes of failure of well integrity barriers (A review). J Nat Gas Sci Eng 2017;45:511–26.
[43] Battocchio F, Monteiro PJ, Wenk H-R. Rietveld refinement of the structures of 1.0 C-S-H and 1.5 C-S-H. Cement Concr Res 2012;42:1534–48.
[44] Ugarte ER, Tetteh D, Salehi S. Experimental studies of well integrity in cementing during underground hydrogen storage. Int J Hydrogen Energy 2023.
[45] Zeng L, Sarmadivaleh M, Saeedi A, Al-Yaseri A, Dowling C, Buick G, Xie Q. Thermodynamic modelling on wellbore cement integrity during underground hydrogen storage in depleted gas reservoirs. 2022. Day 2 Tue, October 18, 2022, SPE.
[46] Jacquemet N, Chiquet P, Grauls A. Hydrogen reactivity with (1) a well cement - PHREEQC geochemical thermodynamics calculations. In: 1st geoscience & engineering in energy transition conference. European Association of Geoscientists & Engineers; 2020. p. 1–5.
[47] Hussain A, Al-Hadrami H, Emadi H, Altawati F, Thiyagarajan SR, Watson M. Experimental investigation of wellbore integrity of depleted oil and gas reservoirs for underground hydrogen storage. 2022. Day 2 Tue, May 03, 2022, OTC.
[48] Maury Fernandez D, Emadi H, Thiyagarajan S, Hussain A, Ispas I. Effects of hydrogen on class H well cement's properties under geological storage conditions. 2023. All Days, ARMA.
[49] American Petroleum Institute. Api spec 10A. 2022.
[50] Scrivener K, Snellings R, Lothenbach B, editors. A practical guide to microstructural analysis of cementitious materials. Boca Raton, London, New York: CRC Press Taylor & Francis Group; 2016.
[51] Sing KS. Characterization of porous solids: an introductory survey. In: Characterization of porous solids II, proceedings of the IUPAC symposium (COPS 11). Elsevier; 1991. p. 1–9.
[52] Scrivener KL, Juilland P, Monteiro PJ. Advances in understanding hydration of Portland cement. Cement Concr Res 2015;78:38–56.
[53] Taylor HFW. Cement chemistry. second ed. London: Telford; 1997.
[54] Bahafid S, Ghabezloo S, Duc M, Faure P, Sulem J. Effect of the hydration temperature on the microstructure of Class G cement: C-S-H composition and density. Cement Concr Res 2017;95:270–81.
[55] Matschei T, Lothenbach B, Glasser FP. The AFm phase in Portland cement. Cement Concr Res 2007;37:118–30.
[56] Fridrichová M, Dvořák K, Gazdič D, Mokrá J, Kulísek K. Thermodynamic stability of ettringite formed by hydration of ye'elimite clinker. Adv Mater Sci Eng 2016;2016:1–7.
[57] Truche L, Berger G, Destrigneville C, Guillaume D, Giffaut E. Kinetics of pyrite to pyrrhotite reduction by hydrogen in calcite buffered solutions between 90 and 180°C: implications for nuclear waste disposal. Geochem Cosmochim Acta 2010;74:2894–914.
[58] Truche L, Jodin-Caumon M-C, Lerouge C, Berger G, Mosser-Ruck R, Giffaut E, Michau N. Sulphide mineral reactions in clay-rich rock induced by high hydrogen pressure. Application to disturbed or natural settings up to 250 °C and 30 bar. Chem Geol 2013;351:217–28.
[59] Zhou Q, Glasser FP. Thermal stability and decomposition mechanisms of ettringite at <120°C. Cement Concr Res 2001;31:1333–9.
[60] Afflerbach S, Pritzel C, Hartwich P, Killian MS, Krumm W. Effects of thermal treatment on the mechanical properties, microstructure and phase composition of an Ettringite rich cement. Cement 2023;11:100058.
[61] Georget F, Lothenbach B, Wilson W, Zunino F, Scrivener KL. Stability of hemicarbonate under cement paste-like conditions. Cement Concr Res 2022;153:106692.
[62] Richardson IG. The calcium silicate hydrates. Cement Concr Res 2008;38:137–58.
[63] Diamond S. The microstructure of cement paste and concrete—a visual primer. Cement Concr Compos 2004;26:919–33.
[64] Kawabata Y, Ueda N, Miura T, Multon S. The influence of restraint on the expansion of concrete due to delayed ettringite formation. Cement Concr Compos 2021;121:104062.
[65] Joshi NR, Matsumoto A, Asamoto S, Miura T, Kawabata Y. Investigation of the mechanical behaviour of concrete with severe delayed ettringite formation expansion focusing on internal damage propagation under various compressive loading patterns. Cement Concr Compos 2022;128:104433.
[66] Galmarini S, Aimable A, Ruffray N, Bowen P. Changes in portlandite morphology with solvent composition: atomistic simulations and experiment. Cement Concr Res 2011;41:1330–8.
[67] García Giménez R, La Vigil de Villa R, Frías M. From coal-mining waste to construction material: a study of its mineral phases. Environ Earth Sci 2016;75.
[68] Zeng L, Keshavarz A, Xie Q, Iglauer S. Hydrogen storage in Majiagou carbonate reservoir in China: geochemical modelling on carbonate dissolution and hydrogen loss. Int J Hydrogen Energy 2022;47:24861–70.
[69] Zhang C, Li F, Lv J. Morphology and formation mechanism in precipitation of calcite induced by Curvibacter lanceolatus strain HJ-1. J Cryst Growth 2017;478:96–101.
[70] Aligizaki KK. Pore structure of cement-based materials: testing, interpretation and requirements. London: Taylor & Francis; 2006.
[71] Thommes M, Kaneko K, Neimark AV, Olivier JP, Rodriguez-Reinoso F, Rouquerol J, Sing KS. Physisorption of gases, with special reference to the evaluation of surface area and pore size distribution (IUPAC Technical Report). Pure Appl Chem 2015;87:1051–69.
[72] Corina AN, Soustelle V, ter Heege J. HyUSPRe Report & Data on 'New experimental data on reactions between H2 and well cement and effects on fluid flow and mechanical properties of well cement. Zenodo; 2023.
[73] Ugarte ER, Salehi S. A review on well integrity issues for underground hydrogen storage. J Energy Resour Technol 2022;144.